Universidade de Aveiro
2014
Departamento de Engenharia de Materiais e Cerâmica

Allu Amarnath Reddy

Selantes vítreo e vitrocerâmico à base de aluminosilicatos alcalino-terrosos para aplicações funcionais

Alkaline-earth aluminosilicate-based glass and glass-ceramic sealants for functional applications

Universidade de Aveiro
2014

Departamento de Engenharia de Materiais e Cerâmica

Allu Amarnath Reddy

Selantes vítreos e vitrocerâmicos à base de aluminosilicatos alcalino-terrosos para aplicações funcionais

Alkaline-earth aluminosilicate-based glass and glass-ceramic sealants for functional applications

Tese apresentada à Universidade de Aveiro para cumprimento dos requisitos necessários à obtenção do grau de Doutor em Ciência e engenharia de materiais, realizada sob a orientação científica do Doutor José Maria da Fonte Ferreira, Professor Associado com Agregação do Departamento de Engenharia de Materiais e Cerâmica da Universidade de Aveiro e do Doutor Dilshat U. Tulyaganov, Professor do Turin Polytechnic University in Tashkent (Tashkent, Uzbequistao).

Apoio financeiro da FCT e do FSE no âmbito do III Quadro Comunitário de Apoio.

to my friend (*HarshaVardhan Reddy Maraka*), parents and supervisors

o júri

Presidente

Prof. Doutor **Fernando Joaquim Fernandes Tavares Rocha**
Professor Catedrático da Universidade de Aveiro

Vogais

Prof. Doutor **Jorge Ribeiro Frade**
Professor Catedrático, Universidade de Aveiro

Prof. Doutor **Rui Manuel Amaral de Almeida**
Professor Catedrático, Instituto Superior Técnico, Universidade de Lisboa

Prof. Doutor **José Maria da Fonte Ferreira**
Professor Associado com agregação, Universidade de Aveiro (orientador)

Prof. Doutora **Maria Margarida Rolim Augusto Lima**
Professora Auxiliar, Faculdade de Ciências e Technologia, Universidade Nova de Lisboa

Prof. Doutor **Luís Filipe da Silva dos Santos**
Professor Auxiliar, Instituto Superior Técnico, Universidade de Lisboa

Acknowledgements

First of all, I would like to express my sincere thanks to Professor José M.F. Ferreira, who has been the best possible guide I could ever hope to have, not only scientifically also I am grateful for his encouragement, guidance and support from the initial level to final level which enabled me to develop an understanding of the subject. Without his support and encouragement during tough times it would not be possible to complete this PhD dissertation in time. I appreciate all his contributions of time and ideas to make my PhD experience productive and stimulating.

I gratefully acknowledge my co-supervisor Professor Dilshat U. Tulyaganov, who taught me the fundamentals of glass and glass-ceramics and design of glass compositions, investigating and analysing the properties of glass and glass-ceramics and his moral support throughout my PhD dissertation time. In the absence of his scientific guidance, it would have been really difficult to complete this Odyssey with success.

I would like to thank to Dr. Ashutosh Goel, who introduced me to Professor José M.F. Ferreira. He has always been my role model as a researcher since I met him first time in 2011, University of Aveiro. His valuable suggestions and constructive discussions at different stages of my PhD improved the quality of my thesis. His moral support has never failed to give me hope.

Sincere thanks are extended to Dr. V.V. Kharton for his superb experimental work on electrical conductivity measurements, thermal shock resistance studies and oxygen leakage measurements discussed in this dissertation. These studies would not have been possible without his support and his research group. I very much appreciate their enthusiasm, intensity and willingness to perform these experiments for me in their laboratory.

I am much indebted to Dr. María Jesús Pascual Francisco for hot-stage microscopy measurements which are helped in understanding the sintering and crystallization behaviour of studied glasses in this dissertation. Thanks are also extended to her strong support in getting JECS-trust 2012 (201242-2) project. Sincere thanks are also going to Glenn C. Mather and Francisco for valuable suggestions and constructive discussion in understanding the glass science during my stay at Campus de Cantoblanco, Madrid.

I would like to thank Professor Luis Mafra, Department of Chemistry, University of Aveiro, for his great help concerning Magic Angle Spinning-Nuclear Magnetic Resonance (MAS-NMR) measurements.

I am much indebted to Professor Gaddam Vijaya Prakash for introducing me to the fascinating field of glass science and research. It was during my stay at Indian Institute of Technology (IIT) Delhi, that I learnt the basics of materials science which further played a significant role while accomplishing my PhD work.

I am grateful to Dr. Surendra Babu who taught me the fundamentals of rare-earth spectroscopy in phosphate glasses during my stay at IIT Delhi.

I would like to thank Dr. Pradeesh Kannan who taught me the basics and making of glass. I strongly appreciate his continuous moral support, not only scientifically, since 2008. Sincere thanks are also extended to Dr. Subratha Das for his moral support during my PhD dissertation.

A special thanks to all the technical staff in Department of Materials and Ceramic Engineering, University of Aveiro for their unceasing support. Without them it would not have been possible to finish my experimental task.

I thank to all my colleagues with whom I worked for the last six years.

Financial support of the Portuguese Foundation for Science and Technology for the fellowship grant SFRH/BD/89915/2012 is gratefully acknowledged. Support by the JECS-trust (201242-2) is also gratefully acknowledged.

palavras-chave

Vidros; Vitrocerâmicos; Selantes; SOFCs, Bi-camadas; Auto-reparação.

Resumo

A concepção planar de células de combustível de óxido sólido (SOFC) é a mais promissora devido a sua fabricação mais fácil, um melhor desempenho e uma densidade de potência relativamente elevada. Nas SOFCs planares e outros dispositivos de electrólitos sólidos são necessárias vedações estanques ao gás ao longo das arestas de cada uma das células e entre os tubos de distribuição de gás e de pilha. Materiais vítreos e vitrocerâmicos (GC), em particular com composições baseadas em aluminosilicatos alcalino-terrosos, estão entre os materiais mais promissores para aplicações de vedação à prova de gás em SOFCs. Além do desenvolvimento de novos materiais à base de vidros e vitrocerâmicos, são também necessários novos conceitos para superar os desafios enfrentados pela tecnologia selante atualmente existente. O presente trabalho visa dar um contributo nesse sentido, propondo soluções de vedação para SOFCs e outras aplicações electroquímicas. Para o efeito, foram sintetizados vários vidros e GCs à base de diópsido, os quais foram caracterizados por recurso a uma grande variedade de técnicas. Todos os vidros foram preparados por fusão, enquanto os GCs foram produzidos por sinterização (tratamento térmico) de compactos de pó de vidro nas faixas de temperatura de 800 – 900 ºC por 1 – 1000 h. Além disso, foram estudados os efeitos de diversas substituições iónicas, especialmente de CaO por SrO, e de MgO + SiO_2 por Ln_2O_3 (Ln = La, Nd, Gd, e Yb), em composições de aluminosilicatos à base de diópsido na estrutura, sinterização e cristalização dos vidros e nas propriedades dos GCs resultantes com particular relevância para as propriedades de vedação em SOFCs. Com base nos resultados obtidos neste estudo, foi possível propor um novo conceito de selante vritrocerâmico em bi-camadas que visa ultrapassar os desafios enfrentados pelos vedantes actualmente usados em SOFCs. Os sistemas designados por Gd–0,3 (em % molar: 20,62 MgO–18,05 CaO–7,74 SrO–46,40 SiO_2–1,29 Al_2O_3–2,04 B_2O_3–3,87 Gd_2O_3) e Sr–0,3 (em % molar: 24,54 MgO–14,73 CaO–7,36 SrO–0,55 BaO–47,73 SiO_2–1,23 Al_2O_3–1,23 La_2O_3–1,79 B_2O_3–0,84 NiO) foram seleccionados para realizar o conceito de bi-camada. Ambos os GCs exibem propriedades térmicas semelhantes, e excelente estabilidade térmica ao longo de um período de 1.000 horas, mas diferem nas suas fracções vítreas/cristalinas. Eles revelaram também elevada aptidão para se ligarem à interconexão metálica (Crofer22APU) e ao electrólito sólido (zircónia estabilizada com 8 mol% de ítria (8YSZ) sem a formação de camadas interfaciais indesejáveis entre os diferentes componentes das SOFCs. Duas camadas separadas compostas pelos vidros (Gd–0,3 e Sr–0.3) foram preparadas e depositadas sobre as interconexões metálicas através de uma abordagem *tape casting*. As bi-camadas vitrocerâmicas mostram boa capacidade de molhamento e ligação à placa Crofer22APU, coeficientes de expansão térmica adequados (9,7–11,1 $\times$ 10^{-6} K^{-1}), confiabilidade mecânica, elevada resistividade eléctrica, e uma forte adesão aos componentes da SOFC. Todas estas características confirmam a boa adequação do sistema selante bi-camadas investigado para aplicações em SOFCs.

Keywords

Glasses; Glass-ceramics; Sealants; SOFCs; Bi-layer; Self-healing.

abstract

The planar design of solid oxide fuel cell (SOFC) is the most promising one due to its easier fabrication, improved performance and relatively high power density. In planar SOFCs and other solid-electrolyte devices, gas-tight seals must be formed along the edges of each cell and between the stack and gas manifolds. Glass and glass-ceramic (GC), in particular alkaline-earth alumino silicate based glasses and GCs, are becoming the most promising materials for gas-tight sealing applications in SOFCs. Besides the development of new glass-based materials, new additional concepts are required to overcome the challenges being faced by the currently existing sealant technology. The present work deals with the development of glasses- and GCs-based materials to be used as a sealants for SOFCs and other electrochemical functional applications. In this pursuit, various glasses and GCs in the field of diopside crystalline materials have been synthesized and characterized by a wide array of techniques. All the glasses were prepared by melt-quenching technique while GCs were produced by sintering of glass powder compacts at the temperature ranges from 800–900 ºC for 1–1000 h. Furthermore, the influence of various ionic substitutions, especially SrO for CaO, and Ln_2O_3 (Ln=La, Nd, Gd, and Yb), for MgO + SiO_2 in Al-containing diopside on the structure, sintering and crystallization behaviour of glasses and properties of resultant GCs has been investigated, in relevance with final application as sealants in SOFC. From the results obtained in the study of diopside-based glasses, a bi-layered concept of GC sealant is proposed to overcome the challenges being faced by (SOFCs). The systems designated as Gd–0.3 (in mol%: 20.62MgO–18.05CaO–7.74SrO–46.40SiO_2–1.29Al_2O_3 – 2.04 B_2O_3–3.87Gd_2O_3) and Sr–0.3 (in mol%: 24.54 MgO–14.73 CaO–7.36 SrO–0.55 BaO–47.73 SiO_2–1.23 Al_2O_3–1.23 La_2O_3–1.79 B_2O_3–0.84 NiO) have been utilized to realize the bi-layer concept. Both GCs exhibit similar thermal properties, while differing in their amorphous fractions, revealed excellent thermal stability along a period of 1,000 h. They also bonded well to the metallic interconnect (Crofer22APU) and 8 mol% yttrium stabilized zirconium (8YSZ) ceramic electrolyte without forming undesirable interfacial layers at the joints of SOFC components and GC. Two separated layers composed of glasses (Gd–0.3 and Sr–0.3) were prepared and deposited onto interconnect materials using a tape casting approach. The bi-layered GC showed good wetting and bonding ability to Crofer22APU plate, suitable thermal expansion coefficient (9.7–11.1 $\times$ 10^{-6} K^{-1}), mechanical reliability, high electrical resistivity, and strong adhesion to the SOFC componets. All these features confirm the good suitability of the investigated bi-layered sealant system for SOFC applications.

Contents

List of tables

List of figures

List of abbreviations

BO	Bridging oxygen
CCD	Charge coupled device
CTE	Coefficient of Thermal Expansion
DC	Diffusion coefficient
Di	Diopside
DTA	Differential thermal analysis
E_a	Electrical activation energy
EDS	Energy dispersive spectroscopy
emf	Electro motive force
ESEM	Environmental scanning electron microscopy
FC	Fuel Cell
GC	Glass-ceramic
HSM	Hot-stage-microscope
HT	High temperature
Ln	Lanthanide
MAS-NMR	Magic angle nuclear magnetic resonance
NBO	Non bridging oxygen
RF	Radio frequency
RIR	Reference intensity ratio
S_c	Sintering ability parameter
SD	Standard deviation
SE	Solid-electrolyte
SEM	Scanning electron microscopy
SH	Self-healing
SMA	Shape memory alloy
SOFC	Solid Oxide Fuel Cell
XRD	X-ray diffraction
YSZ	Yttria-stabilized zirconia

List of Symbols

α	CTE
β	Heating rate
V_m	Molar volume
ρ	Density
$\varnothing$	Diameter
F	Probability of failure
j	Flux density
m	Weibull modulus
R	Resistance
σ	Mechanical strength
σ_e	Electrical conductivity
σ_O	Weibull characteristic strength
T_g	Glass transistion temperature
T_c	Onset of crystallization temperature
T_p	Peak crystallization temperature
T_s	Softening temperature
T_{FS}	First shrinkage temperature
T_{MS}	Maximum sintering temperature
T_D	Deformation temperature
T_{HB}	Half-Ball temperature
T_F	Flow temperature

List of publications

1. Sintering behaviour of lanthanide-containing glass-ceramic sealants for solid oxide fuel cells.
   Ashutosh Goel, **Allu Amarnath Reddy**, Maria J. Pascual, Laurent Gremillard, Annie Malchere, José M.F. Ferreira.
   Journal of Materials Chemistry 22 (2012) 10042-10054

2. Diopside - Mg orthosilicate and Diopside - Ba disilicate glass-ceramics for sealing applications in SOFC: sintering and chemical interactions studies.
   Allu Amarnath Reddy, Dilshat U. Tulyaganov, Ashutosh Goel, Maria J. Pascual, Vladislav V. Kharton, Ekaterina V. Tsipis, José M.F. Ferreira.
   International Journal of Hydrogen Energy 37 (2012) 12528-12539

3. Study of melilite based glasses and glass-ceramics nucleated by Bi_2O_3 for functional applications.
   Allu Amarnath Reddy, Dilshat U. Tulyaganov, Saurabh Kapoor, Ashutosh Goel, Maria J. Pascual, Vladislav V. Kharton, and José M.F. Ferreira.
   RSC Advances 2 (2012) 10955–10967

4. Diopside–Ba disilicate glass–ceramic sealants for SOFCs: enhanced adhesion and thermal stability by Sr for Ca substitution.
   Allu Amarnath Reddy, Dilshat U. Tulyaganov, Maria J. Pascual, Vladislav V. Kharton, Ekaterina V. Tsipis, Vladislav A. Kolotygin, José M.F. Ferreira.
   International Journal of Hydrogen Energy 38 (2013) 3073-3086

5. Study of calcium–magnesium–aluminum–silicate (CMAS) glass and glass–ceramic sealant for solid oxide fuel cells.
   Allu Amarnath Reddy, Ashutosh Goel, Dilshat U. Tulyaganov, Saurabh Kapoor, K. Pradeesh, Maria J. Pascual, and José M.F. Ferreira.
   Journal of Power Sources 231 (2013) 203-212.

6. Sintering and devitrification of glass-powder compacts in the akermanite - gehlenite system.
   Allu Amarnath Reddy, Dilshat U. Tulyaganov, Ashutosh Goel, Saurabh Kapoor, Maria J. Pascual, José M.F. Ferreira.
   Journal of Materials Science 48 (2013) 4128–4136

7. Melilite glass–ceramic sealants for solid oxide fuel cells: effects of ZrO_2 additions assessed by microscopy, diffraction and solid-state NMR.
   Allu Amarnath Reddy, Dilshat U. Tulyaganov, Ashutosh Goel, Mariana Sardo, Paul V. Wiper, Maria J. Pascual, Vladislav V. Kharton, Ekaterina V. Tsipis, Vladislav A. Kolotygin, Luís Mafra, José M.F. Ferreira.
   Journal of Materials Chemistry A 1 (2013) 6471–6480

8. Aluminosilicate-based sealants for SOFCs and other electrochemical applications - A brief review.
   Dilshat U. Tulyaganov, **Allu Amarnath Reddy**, Vladislav V. Kharton, José M.F. Ferreira.
   Journal of Power Sources 242 (2013) 486-502.

9. SrO–Containing Diopside Glass–Ceramic Sealants for Solid Oxide Fuel Cells: Mechanical Reliability and Thermal Shock Resistance.
   Allu Amarnath Reddy, Dilshat U. Tulyaganov, Maria J. Pascual, Vladislav V. Kharton, Ekaterina V. Tsipis, Vladislav A. Kolotygin, José M.F. Ferreira.
   Fuel Cells 13 (2013) 689–694.

10. Effect of strontium to calcium ratio on the structure, crystallization behaviour and functional properties of diopside based glasses.
    Allu Amarnath Reddy, Dilshat U. Tulyaganov, Maria J. Pascual, Vladislav V. Kharton, Sergey I. Bredikhin, Vladislav A. Kolotygin, José M.F. Ferreira.
    International Journal of Hydrogen Energy 39 (2014) 3552-3563.

11. Thermal and mechanical stability of lanthanide–containing glass–ceramic sealants for solid oxide fuel cells.
    Allu Amarnath Reddy, Ashutosh Goel, Dilshat U. Tulyaganov, Mariana Sardo, Luís Mafra, Maria J. Pascual, Vladislav V. Kharton, Ekaterina V. Tsipis, Vladislav A. Kolotygin, and José M.F. Ferreira.
    Journal of Materials Chemistry A 2 (2014) 1834-1846.

12. Bi-layer glass-ceramic sealant for solid oxide fuel cells.
    Allu Amarnath Reddy, Neda Eghtesadi, Dilshat U. Tulyaganov, Maria J. Pascual, Luis F. Santos, Surendran Rajesh, Fernando M.B. Marques, and José M. F. Ferreira.
    Journal of European Ceramic Society 34 (2014) 1449–1455

Others

13. $KCa_4(BO_3)_3:Ln^{3+}$ (Ln=Dy, Eu, Tb) phosphors for near UV excited white-light-emitting diodes.
    Allu Amarnath Reddy, Subrata Das, Ashutosh Goel, Rupam Sen, Renée Siegel, Luís Mafra, G Vijaya Prakash, José M.F. Ferreira.
    AIP Advances 3 (2013) 022126.

14. Structure, biodegradation behaviour and cytotoxicity of alkali-containing alkaline-earth phosphosilicate glasses.
    Ishu Kansal, **Allu Amarnath Reddy**, Francisco Muñoz, Hae-Won Kim, Dilshat U. Tulyaganov, Seong-Jun Choi, José M.F. Ferreira.
    Materials Science and Engineering C 44 (2014) 159–165.

1. Introduction

The depletion of fossil fuel reserves and the emission of greenhouse gases constitute a menace to the present and the future generations in terms of energy availability, environmental pollution, global warming and health hazards. Therefore, finding alternative energy resources and efficient production methods for electricity is a fundamental requirement for the modern world [1-3]. Among the various technologies, fuel cell (FC) is the most widely adopted one owing to a promising and viable alternative for large scale generation of electricity, with minimal undesirable chemical, thermal and acoustic emissions [4-7]. Therefore, the development of FC technology is one such attempt to cater the rising energy demands in the coming era.

A FC is an electrochemical device that converts the stored chemical energy directly into electrical energy. Simple FC essentially consists of an anode and a cathode separated by an electrolyte. There are several types of FCs, named after the type of material used for the electrolyte, currently under development, each with its own advantages, limitations, and potential applications [4-7]. Among various FCs, solid oxide fuel cells (SOFCs) offer important advantages: (i) the most electrically efficient one with 45–65% efficiency (total system efficiency ~85%, including the thermal component – unheard of by any other technology) in the conversion of chemical energy to electricity; (ii) capable of operating with various fuels, for ex. natural gas, gasoline, hydrogen and bio–fuels; (iii) low cost and environmental friendly nature (e.g., low emissions NO_x [<0.5 ppm)]; (iv) because of high operation temperatures SOFCs do not need highly expensive catalyst such as platinum; and (v) high stability of electrolyte, flexibility of cell design, and long stack–life because all the components are solid [2, 8-10]. All of the above advantages make SOFCs a “highly efficient future technology” that is currently in demand among different categories of FC. Because of these reasons and motivations, tremendous research and development efforts in this area have been made along the last two decades, especially through specific programs supported by various Governmental and private agencies across the world, solely dedicated towards finding feasible solutions to various technical challenges which acted as major roadblocks for the commercialization of SOFC technology. For example: In 1997 a pilot project started with

a 100 kW SOFC cogeneration plant in The Netherlands, which achieved 46% electrical efficiency and 25% thermal efficiency [11, 12]. Based on geometry, tubular and planar deigns are the two most popular SOFCs. However, the current path lengths are typically longer in tubular cells, compared to planar cells. This significantly limits their performance beyond a certain radial extension over planar cells. Planar design is the most promising due to its cheap and simple fabrication along with improved performance and power density relative to other designs. Among the various developments in planar–SOFCs (p–SOFC), advances in interconnect components have increased the SOFCs' electrical efficiency up to 65%. The use of metallic interconnects instead of ceramic bipolar plates makes it possible to lower the SOFC temperature from 1000 ºC to 700–800 ºC and to increase power density [1, 8, 13].

A single SOFC comprises, at least, one dense solid–electrolyte (SE) membrane in contact with porous cathode and anode, onto which a gaseous oxidant (usually atmospheric oxygen) and a fuel are continuously supplied; the power is generated due to oxidant reduction at the cathode and fuel oxidation by the O^{2-} anions diffused through the electrolyte, at the anode. The SOFC performance is primarily governed by electrical and electrochemical properties of the electrodes and solid electrolyte, compositions of the fuel and oxidant gas mixtures and current collection. The ideal absence of gas leakages is also essential to grant its ingegrity and functioning [14-20]. In general, the ceramics used in SOFCs do not become electrically and ionically active until they reach relatively high temperatures and, as a consequence, the cell has to run at temperatures ranging from 600–1,000 ºC.

Of critical importance for the SOFC efficiency and durability are also the properties of sealants used to prevent gas mixing between the anode and cathode compartments, to bond the cell stacks, and also to provide electrical insulation. Whilst the negative impact of minor leakages in the SOFC stacks can often be neglected, any leak may critically increase the contamination of high–purity gases produced using the solid–electrolyte membranes and induce measuring errors in the electrochemical sensors. Therefore, one major hurdle that still proves to be an arduous task for the researchers worldwide is the development of a hermetic high temperature sealing [2, 21-26] .

To date, a number of sealants have been proposed and studied extensively for their physical, thermal, mechanical and electrical properties and also tested in real SOFCs stacks. Among the various types of sealant materials, glass and glass–ceramics (GCs) materials are considered as the most efficient and attractive sealing materials for SOFCs due to their ability to form hermetic seals at high temperatures, low costs and durability [21-26]. A principal advantage of the glass seals is that their chemical composition and molecular structure can be tailored to optimize properties like coefficient of thermal expansion (CTE), mechanical strength, sintering behaviour, chemical and electrical resistance, etc. A vast amount of specialised literature available in this area (reviewed in Chapter 2) reveals that currently used SOFCs sealant materials based glass and GC are not completely satisfactory towards their commercialization in open market. Therefore, still there is a need to develop suitable sealant materials along with new concepts and or proposals. The aim of this study was to develop new glass based sealant materials and to evaluate their suitability for application in different technological areas with emphasis on sealing in SOFCs. The aim of this study also includes the development of Bilayer sealant material in order to overcome the challenges being faced by the present glass based seal materials.

In the light of the above mentioned perspective, this dissertation comprises five chapters. The first chapter, i.e. Introduction provides the basics of SOFCs and highlights the necessity of an efficient sealant material. The second chapter provides an overview about the current status of sealing technology in SOFC, and draws attention towards the lacuna in the existing glass/GC seals. In other words, chapter two lays the foundation of our work. The third chapter deals with the experimental procedure and methodology used in accomplishing this work. It provides details about all the experimental techniques and procedures employed in order to synthesize, characterize and test our samples. Chapter four is the most important part of this work as it presents all the experimental results obtained on newly designed glass and GCs based sealant material developed for the realization of bi-layer seal during past 3–4 years along with pertaining discussion while, in chapter five we have tried to conclude all the results obtained during this work and provide future directions in order to produce technologically useful materials.

2. State of the art

2.1 Key requirements for seals in SOFCs and other devices

Fig. 2.1 and 2.2 present several typical examples illustrating the use of high-temperature sealants in various SOFCs [27-32]. The seal optimization requires always a multifactor analysis; in addition to the materials science–related aspects and sealing configuration, the variables include, at least, contact area with other components of the electrochemical device, compression, exposure to oxidizing and reducing atmospheres, seal formation conditions, and prospective startup/shutdown regimes. Nonetheless, the general requirements to the GC sealants, irrespective of the stack configuration and fabrication technologies, involve [15-17, 33-36]:

(i) Nearly zero gas permeability;

(ii) Good adhesion to the solid electrolyte interconnects, electrodes, current collectors and/or other interfacing materials;

(iii) Chemical inertness with respect to these materials under the stack fabrication and operation conditions;

(iv) Coefficients of thermal expansion (CTE) compatible with those of the electrochemical cell constituents and other construction materials;

(v) High electrical resistivity (>10^5 Ohm cm) under operating conditions;

(vi) Minimum volatilization and diffusion of the sealant components;

(vii) No tendencies to bulk reduction, oxidation, hydration, carbonate formation, and reactions with other gaseous species such as SO_x and H_2S;

(viii) Thermal and morphological stability at the cell operation temperatures and during startup/shutdown;

(ix) Compatibility of the characteristic temperatures, primarily glass transition, crystallization, softening and maximum shrinkage temperature, with the limitations arising from properties of the electrochemical device components and target operation regimes;

(x) Superior thermal shock resistance and high mechanical strength;

(xi) Good sinter ability, easy processing, and an absence of seal defects such as

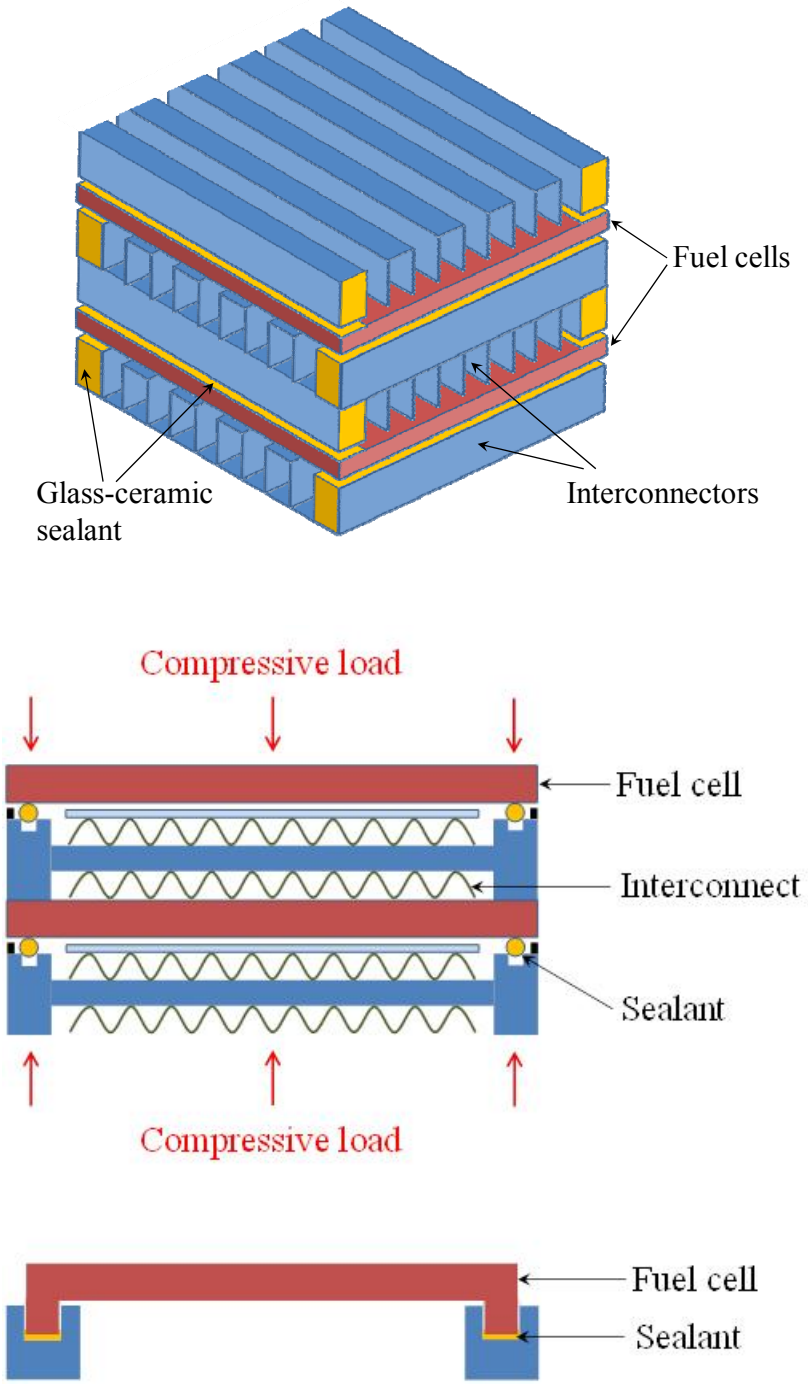

Fig. 2.1: Typical sealing configurations in planar SOFCs.

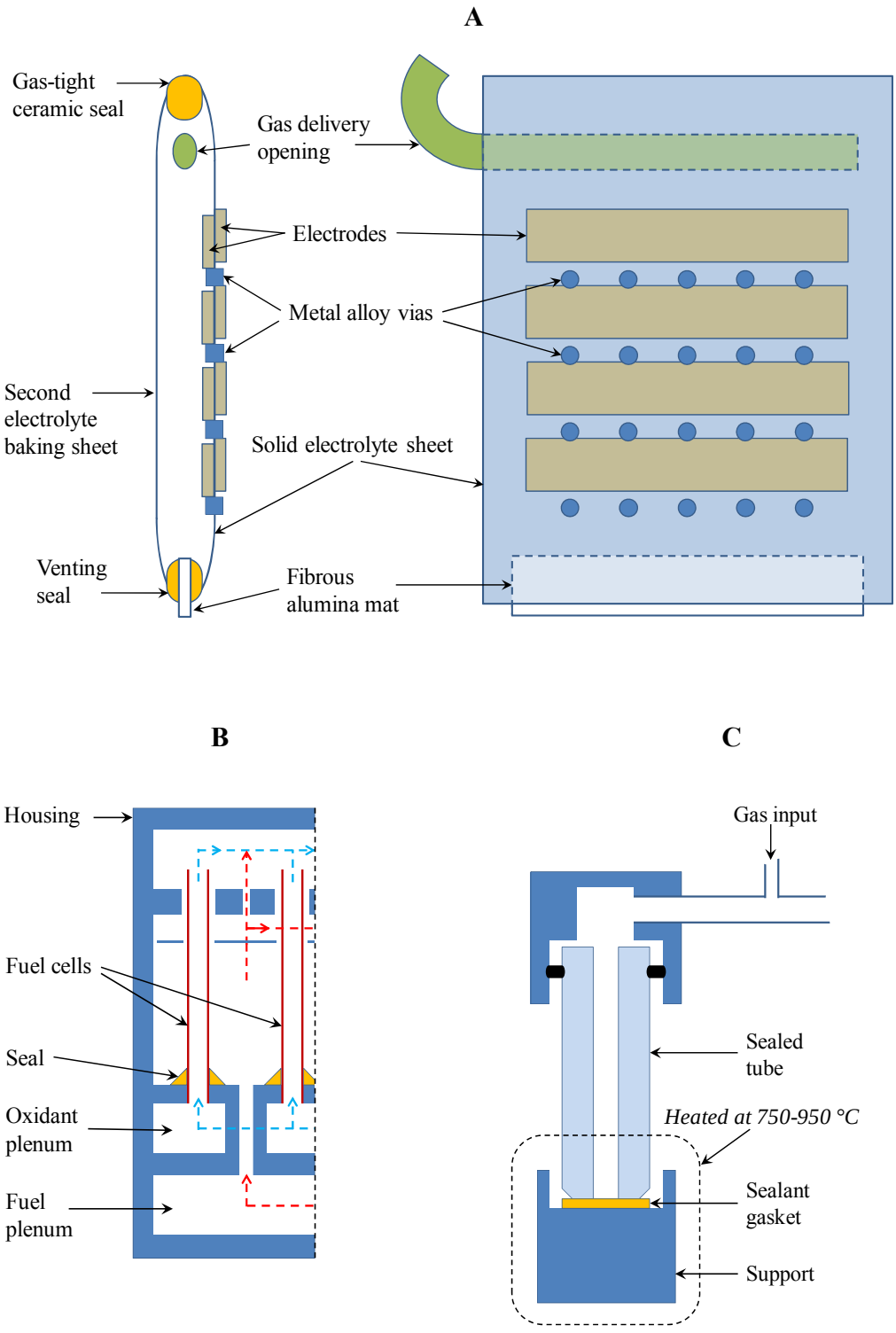

Fig. 2.2: Examples of seal configurations: (a), planar SOFCs; (b) tubular SOFCs; (c) cell for sealant testing.

pores, bubbles or micro cracks;

(xii) Stability with respect to local heating, high applied voltage, flame, carbon deposition and other parasitic phenomena;

(xiii) Self–healing ability originating from viscous flow of the seal glass;

(xiv) Availability of the seal components and low costs.

2.2 Families of glass and glass-ceramic sealants

Through literature survey has evidenced that the majority of SOFC seals are primarily glasses and GCs. A glass is a super cooled liquid having no periodicity and symmetry in the network. All oxide or fluoride materials will not form a glass. To identify a glass forming oxide material Zacharaisen has proposed selection rules [37]. According to Zacharaisen an oxide glass may be formed *(1)* if *the sample contains a high percentage* of *cations which are surrounded by oxygen tetrahedra or by oxygen triangles; (2) if these tetrahedra or triangles share only corners with each other and; (3)* if *some oxygen atoms are linked to only two such cations and do not form further bonds with any other cations*. From these considerations one could conclude that the following oxides should be glass formers: B_2O_3, SiO_2, GeO_2, P_2O_5, As_2O_3, Sb_2O_3, In_2O_5, Tl_2O_3, SnO_2, PbO_2, and SeO_2.

Most of the glass and GC based sealants proposed so far are silicate; borate, phosphate or borosilicates (e.g., [23, 38]). However, every material has some advantages which are coupled along with some drawbacks. Alkali silicate glasses or GCs, in principle are not suitable as sealants because alkali cations tend to react with other components of the electrochemical devices [39], form volatile oxides and stable hydroxides and carbonates, and can lead to chromium poisoning. Further, most of the researchers have searched sealing materials on Ba–aluminosilicate GC system and its derivatives [23, 39-42]. The majority of these glass compositions contain high amount of BaO (30–35 mol%), leading to the crystallization of monoclinic celsian ($BaAl_2Si_2O_8$) after long term heat treatments [23] and formation of detrimental crystalline phase $BaCrO_4$ when interfacing with Cr–based metallic interconnect materials in air at operating temperatures [43]. Significant content of BaO may also promote interaction with water vapour, leading to sealant degradation under SOFC operating conditions. For

example, Pacific Northwest National Laboratory (PNNL) patented a glass–based sealant named as G18 (15CaO–35BaO–5Al_2O_3–10B_2O_3–35SiO_2 (mol%)) [44]; the proneness of G18 glass for crystallizing the low thermal expansion monoclinic $BaAl_2Si_2O_8$ phase during long term SOFC operation, its high content of BaO that might also react with water vapour and Cr–containing gaseous species (CrO_3 or $CrO_2(OH)_2$) diffused to the glass surfaces to form $BaCrO_4$, constitute the most serious drawbacks as SOFC sealant. The large CTE differences between this chromate ((18–20) × 10^{-6} K^{-1}), the sealing glass (CTE of (10–13) × 10^{-6} K^{-1}) and the metallic interconnects ((11−13) × 10^{-6} K^{-1}) lead to significant losses in bonding strength between SOFC glasses and interconnect materials or to their physical separation.

Also, B_2O_3 forms volatile compounds with water vapour leading to seal degradation [23]. Glasses with B_2O_3 as the only glass former have shown up to 20% weight loss in the humidified H_2 environment and extensive interactions with cell component materials both in air and wet fuel gas [45]. Thus, high amount of B_2O_3 in the sealants is not seen with alacrity. Some P_2O_5–based glasses have also been investigated for sealing purposes. Again, these compositions face a severe problem of volatilization of phosphate component leading to easy crystallization of pyro– or meta–phosphates. These phases show poor stability at high temperature in wet fuel gas atmosphere [38, 46]. The difficulties in meeting all the requirements in a given material stimulated many research groups throughout the world searching for alternative glass sealants [21, 25, 26, 34-36, 47-56]. Previous review articles on sealant materials for SOFCs have evidenced that aluminosilicate–based materials constitute the most promising family for the rigid GC sealants [21, 23, 25, 26, 57]. Therefore, in the current chapter an attempt was undertaken to analyse the compositional range and properties of aluminosilicate–based sealants aiming at their further improvements. Selection of the references for this review is focused on the last 10–15 years, with the main emphasis on the newly reported materials.

2.3 Aluminosilicate based glass and glass–ceramic sealants

The thermodynamic properties of aluminosilicate glasses are mainly determined by their composition and the network connectivity. When introducing Al_2O_3 in the fully

connected corner–sharing tetrahedral network of amorphous silicates, the Al atoms substitute for the Si atoms in the centre of the tetrahedra thus leading to charged $(AlO_4)^{5-}$ units. In order to maintain local charge neutrality, $(AlO_4)^{5-}$ units can be charge–compensated by alkali cations (K, Li) which must be present in the vicinity of each such tetrahedron. Therefore, the $(AlO_4)^{5-}$ tetrahedra substitute directly into the network for silicon–oxygen tetrahedra, and simultaneously tend to suppress the immiscibility while raising the T_g and decreasing the CTE of glasses [58]. However, if the concentration of these cations becomes larger than needed for a full compensation of the $(AlO_4)^{5-}$ units, then the cations play the role of modifiers. Namely, these create non–bridging oxygens (NBO) by breaking T–O–T linkages (T=Si/Al) and/or play the role of charge balancing, by neutralizing the AlO_4 entities.

Considering the above mentioned features, alkali or alkaline earth oxides such as Na^+, K^+, Ca^{2+}, Mg^{2+}, Sr^{2+}, Ba^{2+} etc., can serve both as charge compensators and/or as network modifiers in aluminosilicate glasses. These cations perturb silicate frameworks linked by bridging oxygen (BO) and by forming NBO, which play essential roles in many dynamic properties of melts. In principle, the number of NBO atoms in a glass is directly related to the viscosity of the glass forming liquid [59]. The types of cations in oxide glasses certainly can cause different states of disorder depending on their characteristics, such as ionic radius, charge, field strength, and on their local environments.

2.3.1 Alkali containing aluminosilicate glass/ glass–ceramic sealants

Alkali oxides involved in the batch as a modifier contribute to get homogeneous melt at moderate temperatures, to decrease the glass transition temperature, to adjust glass viscosity and to improve the wettability of glasses. Chemical compositions of some alkali containing glasses employed as sealants in SOFC are summarized in Table 2.1[34, 35, 60-67]. Alkali alkaline–earth aluminosilicate seal glasses generally contain 20–45 mol% of network modifiers with the molar ratio $(Na_2O+K_2O)/(CaO+MgO)$ varied in the range 0.03–1.8. Recently D. Coillot et al. [63] reported on alkali aluminosilicate glasses free from alkaline–earth oxides. Properties of some alkali containing aluminosilicate

Table 2.1: Some alkali alkaline earth aluminosilicate glass compositions (%) investigated for SOFCs.

	Na_2O/K_2O	*CaO/MgO/BaO*	*Al_2O_3*	*SiO_2*	*Others*	*Ref.*
Mol	10-25	15.0	10.0	45-60	5.0 TiO_2	[60]
Wt	9.6- 23.8	12.9-13	15.7	41.5-55.6	6.1-6.2 TiO_2	
Mol	7.3/10	3.34/-/8.23	2.80	66.9	1.43	[61, 62]
Wt	6.2/13	2.6/-/17.4	3.9	55.4	1.43	
Wt	-/5-10	-/-/10-15	0-15	20-25	5-10 ZnO 45-50 Bi_2O_3	[34]
Mol	13/4	-	-	65-75	0-10 B_2O_3 1 La_2O_3 7 ZrO	[63]
Wt	11.6/5.4 11.7/5.5	-	-	56-65.5	0-10 B_2O_3 4.7 La_2O_3 12.4 ZrO	
Mol	9-12	24-26	16-18	53-58	-	[35, 64, 65]
Wt	9.4-11.3	20.4-22.1	24.8-27.8	48.4-52.8	-	
Mol	1.3 6.2 1.3	39.7/0.5 40.9/- 36.8/0.4	13.4 11.2 12.4	45 36 41.8	- 1La_2O_3/4.7ZnO 7.3 ZnO	[65]
Wt	1.3 5.7 1.2	34.8/0.3 34.2/- 31.6/0.27	21.4 17.1 19.4	42.2 32.3 38.4	- 5La_2O_3/ 5.7ZnO 9.1 ZnO	
Mol	10-12.1	22.2-25.6	6.1-7.3	51.7-57	8-10	[68]
Wt	10-12	20-23	10-12	50-55	8-10	
Mol	18-23	18	9	40-45	10 B_2O_3	[64]
Wt	17.3-22.1	15.6-15.7	14.2	37.2 -42	10.8 B_2O_3	

Table 2.2: Properties of some aluminosilicate glass and glass–ceramic compositions

T_g, ºC	T_s, ºC	T_p, ºC	*Density (gcm^{-3}): Glass/GC*	*CTE (10^{-6} K^{-1}): Glass/GC*	*Ref.*
Alkali alkaline earth silicate					
562-654	589-709	T_{p1}:705-831 T_{p2}:864-965	-	8.19-8.88/8.27 (200-550)	[60]
468-486	540-600	-	-	11	[61, 62]
470-480	530-575	-	-	9.41-11.2 (50-460)	[34]
610-630	675-692	-	-	7.5-8.3	[63]
670	740	T_{p1}:830 T_{p2}:940	-	-/10.7	[35] [22,73,74]
700-780	-	T_{p1}:780-1020 T_{p2}:900	-	7.8-9.7(200-400)/ 10 (RT-800)	[65]
670	740	-		9.4-9.8(300-500)/ 10.7(RT-800)	[68]
545-580	680-740	-		9.3-11.2 (200-400)	[64]
Alkaline earth silicate					
730	750	-	-/3-3.10	11.2	[69]
619	682	-	-	10.5 (RT-500 ºC) 11.8 (200-800 ºC)	[47, 70-72]
666-699	-	780-833	-	8-8.3	[73]
627-730	657-765	844-903	-	7.9-8.3 (200-600)	[74]
645	693	-	-	11.76/11.68	[75]
685	741	-	-	11.87/11.63 (RT-680)	[76]
630	685	-	-	11.80/12.40 (RT-630)	[76]
685	741	-	-	11.6/11.9 (RT-T_s)	[77]
712-800	748-838	-	3.6-4.19	8.4-10.7/8.5-10.1	[78]
584-650	-	779-789	-	11.4-13/12-13	[79]
640-722	664-745	T_{p1}:820-890 T_{p2}:860-930	3.6-3.8	10.5-11.5 (200-650)	[80]

635-653	673-683	730	-	9.9-11.8/11.3-12.5 (30-500)	[81]
611-672	660-712	720-785	3.89	9.9-12.4 (RT-610)	[39]
Boron containing alkaline earth silicate					
678-718	701-748	775-858	3.69-3.86	-/9.1-10.8 (100-650)	[82]
710-724	-	760	-	7.94-8.06/ 8.05-8.43	[83]
690-720	-	807-825	3.4-3.8	7.5-8.5	[84]
650-690	-	766-1074	-	6.84-7.71/ 7.67-8.10	[85]
620	620-735	-	-	4.7-7.76	[86]
554-659	660-709	T_{p1}:821-913 T_{p2}:1092-1021	2.67-3.32	8.29-9.72	[87]
775	815	965	-	10.8	[88]
635-775	670-815			10.8 (50-775)	[89, 90]
668	745	T_{p1}:820 T_{p2}: 864	-	9-12/11	[36, 91-93]
-	645-781	655-745	-	9.23-11.17 (200-650)	[94]
595-620	-	760-808	3.4-3.8	-/9.5-13.2 (100-750)	[95]
-	912-937	-	3.24-4.54	4.1-8.1	[96]
601-622	-	T_{p1}:762-838 T_{p2}:896-907		10.34-10.83	[97]
-	656-854	-	2.61-3.92	4.92-10.98	[98]
575-633	628-685	-	-	11.2-11.8 (RT-630)/ 10.8-12.5 (RT-1000)	[41]
Others					
655	-	790	-	-	[55]
576	-	-	-	9.4	[99]
552	558	-	-	11.9 ((275-550)/ 10.1-13.0	[100]

glass sealants are shown in Table 2.2 [34, 35, 60-68]. Values of T_g (545–780 ºC) and T_s (680–740 ºC) were obtained when Na_2O introduced in the amount of 1.3–18 mol% whilst 7 mol% K_2O containing glasses demonstrated T_g of 470 ºC and T_s of 530 ºC [34]. Substitution of 5 mol% of Na_2O for SiO_2 in calcium aluminosilicate glass reduced T_g and T_s by 35 and 60 ºC, respectively, and also increased CTE from 9.2×10^{-6} up to 11.2×10^{-6} K^{-1} [64]. On the other hand, the substitution of 15 mol% Na_2O for SiO_2 in calcium aluminosilicate glasses was found to increase T_g and T_s by 92 ºC and 120 ºC respectively, whilst CTE decreased from 8.9×10^{-6} down to 8.2×10^{-6} K^{-1} [60]. Values of T_g (468–630 ºC) and T_s (540–692 ºC) were obtained in Na_2O (7.3–13 mol%) and K_2O (4–10 mol%)–containing glasses [61-63]. Additionally, lowest values of T_g and T_s were revealed when low field strength K^+ ion was incorporated in silicate glasses. Generally, it is well known that incorporation of alkali ions at the expense of glass formers resulted in disruption of silicate network owing to the increasing number of NBO. Fewer changes in silicate network will occur when alkali ions substitute for alkaline–earth ions. Nevertheless, network disorder increases with growing $(Na_2O+K_2O)/(CaO+MgO)$ molar ratio causing T_g and T_s diminishing (Fig. 2.3a). Consequently, with increasing $(Na_2O+K_2O)/(CaO+MgO)$ molar ratio T_g decreases from 780 to 562 ºC and T_s from 740 to 600 ºC.

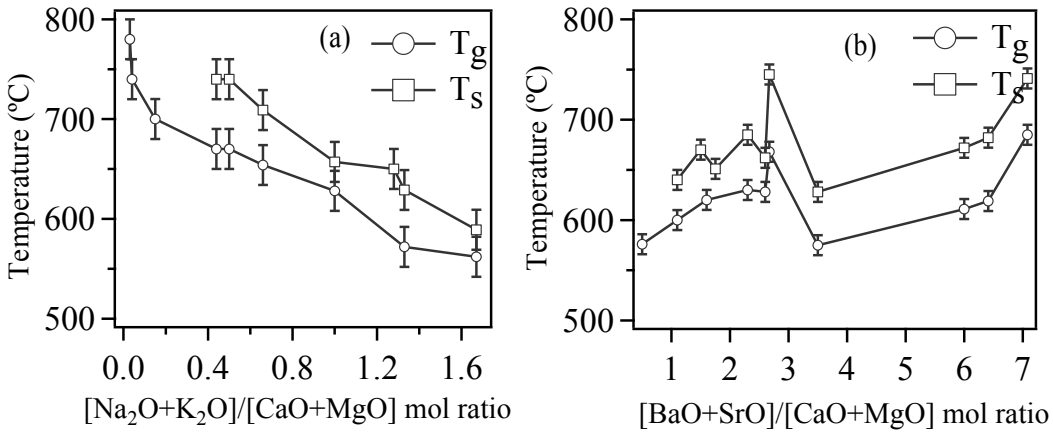

Fig. 2.3: Variation of glass transition (T_g) and glass softening point (T_s) with respect to (a) $(Na_2O+K_2O)/(CaO+MgO)$ (b) $(BaO+SrO)/(CaO+MgO)$ molar ratio in some alkali alkaline earth aluminosilicate glass compositions (see Tables 2.1,2.2 and 2.3).

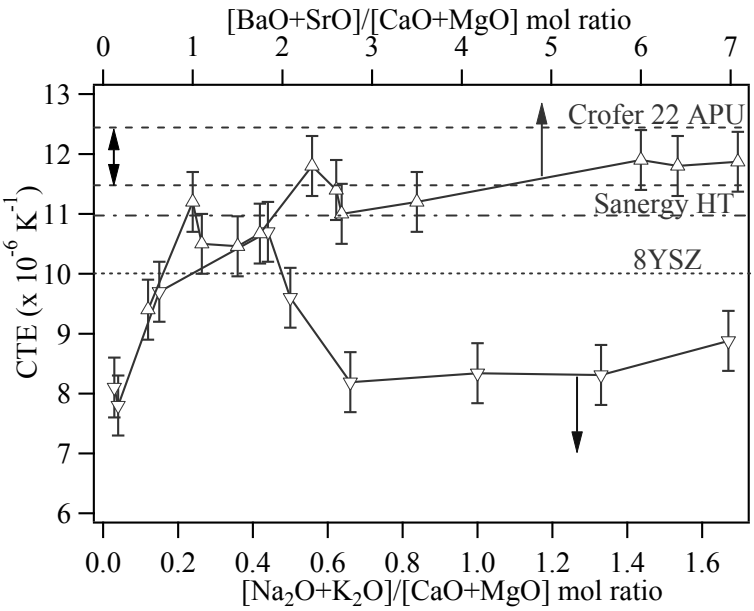

Fig. 2.4: Variation of the coefficients of thermal expansion (CTE) as function of the $(Na_2O+K_2O)/(CaO+MgO)$ molar ratio in some alluminosilicate glass compositions and (BaO+SrO)/(CaO+MgO) ratio in alluminosilicate compositions investigated for SOFCs (based on the data from Tables 2.2, 2.3 and 2.4).

Fig. 2.4 shows the variation in CTE of alkali containing alkaline–earth aluminosilicate glasses with respect to $(Na_2O+K_2O)/(CaO+MgO)$ molar ratio. CTE of glasses increased from 7.8 to 10.7 $\times$ 10^{-6} K^{-1} when $(Na_2O+K_2O)/(CaO+MgO)$ ratio changes in the range 0 to 0.4, and then decreased down to about 8.2 $\times$ 10^{-6} K^{-1}. CTE values are stabilized with the further increase in $(Na_2O+K_2O)/(CaO+MgO)$ molar ratio, between 0.6 to 1.7. This anomalous behaviour can be explained on the basis of mixed modifier ions presence and their distribution in the glasses. When mixing the high– and low–field–strength cations (e.g., Mg^{2+} and K^+, respectively) to the aluminosilicate, the high field–strength cation is consistently favoured to form the NBO's while low field strength ions behave as charge compensators. On the other hand, when pair of cations with the similar ionic radii but different charges (e.g., Ca^{2+} and Na^+, respectively) is mixed, the charge difference apparently plays an important role in the preference to the formation of dissimilar pairs primarily in order to maximize a homogeneous distribution of charges in the glasses. Non–random distributions of modified cations in Ca–Na silicate glasses due to the similar ionic radii affect the dynamics of Na^+ and related

properties in the glass [101]. The desired CTEs, (9–11) × 10^{-6} K^{-1}, have been obtained when the glasses featured (Na_2O+K_2O)/(CaO+MgO) ratio in the range 0.1–0.5 (Fig. 2.4).

As a matter of fact, most of the glass/glass–ceramic candidates investigated up to now contain no alkali metals and the impact of alkali appears unclear. Some alkali metal–containing glasses used for sealants in SOFC enhance the chromium vaporization from metallic interconnects by the formation of very volatile Na_2CrO_4 and K_2CrO_4 species [23]. Chou et al. [61, 62] discussed the compatibility between Crofer22APU interconnects and potassium oxide containing glasses. The addition of K_2O in the parent glass sealant led to de–bonding of the sealant from Crofer22APU due to alkaline–earth chromates formation. No discussion about corrosion mechanism, like alkali chromates formation and their volatility, on as–received Crofer22APU has been presented. Kaur et al. [60] studied the microstructure at the interfaces of Crofer22APU and glass with varying Na_2O content from 10 to 25 mol%. The diffusion couple between Crofer and glass (10 mol % Na_2O) was found to show a good and smooth interface; no traces of Na^+ were observed. Several investigations [35, 60, 61, 63] stated that alkali metals role is still unclear, and thus their drawbacks may be smaller than expected and it may be advantageous to keep them in glass seal composition. For instance, Smeacetto et al. [67] have extensively studied alkali–containing alkaline earth aluminosilicate glasses and found that glasses containing a low amount of sodium oxide can be used as sealing material for SOFCs. Further, Smeacetto et al. [67] have also evaluated the performance of Na_2O–containing GC sealant in two SOFC short stack configurations. The GC sealant was reported to have a good chemical and thermo mechanical compatibility with both Crofer22APU and yttria–stabilized zirconia (YSZ) components. At the same time, one should note that potential effects of Na^+ presence are not limited to the GC|YSZ and GC|interconnect interfaces. In particular, high surface diffusivity of Na^+ may cause poisoning of the electrodes; sodium incorporation in the solid electrolyte grain boundaries may lead to worse mechanical strength and, often, higher electrical resistivity of stabilized zirconia (e.g., [102] and references cited). These effects associated with a slow degradation in the SOFC performance with time cannot be ignored in the seal developments and require long–term testing of such sealants.

2.3.2 Alkaline earth aluminosilicate glass/glass–ceramic sealants

A number of alkaline earth aluminosilicate glass sealants have been apprised for SOFCs and other solid–electrolyte devices. Knowing the fact that alkaline earth metals have different chemical properties such as field strength, ionic radius, and electro negativity those can have strong influence on T_g, T_s, CTE, crystallization behaviour, electrical conductivity as well as the reactivity of glasses. To date, the most well–known systems that have been widely used for sealing applications are the BaO/SrO–Al_2O_3–SiO_2–based, BaO/SrO–CaO–Al_2O_3–SiO_2–based and BaO/SrO–CaO/MgO–Al_2O_3–SiO_2–B_2O_3–based glass systems. Some compositions of alkaline earth and boron containing aluminosilicate glasses employed as sealants in SOFCs are summarized in Tables 2.3 and 2.4 whilst their properties are provided in Table 2.2 [36, 39, 41, 47, 55, 70, 71, 74-82, 84-100, 103-109]. Relatively wide ranges of T_g, T_s and CTE were obtained in the alkaline–earth metals containing boron/alumino silicate glasses. Those are as follows:

(i) for MgO containing glasses T_g varied in the range of 620–700 ºC, T_s changed between 620 and 735 ºC, and CTE varied in the range of (4.7–8.1)× 10^{-6} K^{-1}[86];

(ii) for CaO containing glasses T_g varied in the range of 710–724 ºC, T_s is close to740 ºC, and CTE changed in the interval 7.9× 10^{-6} to 8.1× 10^{-6} K^{-1}[83];

(iii) for SrO containing glasses T_g varied in the range of 660–800 ºC, T_s changed in the range of 660–838 ºC and CTE varied in the range of (6.8–11.5) × 10^{-6} K^{-1}[78, 80, 84, 88, 89, 110, 111];

(iv) finally for BaO containing glasses T_g varied in the range of 601–789 ºC, T_s changed in the interval 656–937 ºC, and CTE was (4.1–11.8)× 10^{-6} K^{-1} [73, 74, 85, 97, 98, 112].

Barium–containing aluminosilicate glasses demonstrated lowest T_g and T_s (Table 2.2) and highest CTE values (Table 2.2) as compared to other alkaline earth containing glasses, for instance CaO and SrO containing glasses. This behaviour can be explained on the basis of field strength values. The field strength of alkaline earth modifier cations fallows this trend: Mg^{2+} (045–0.51) > Ca^{2+} (0.33–0.35) > Sr^{2+} (0.27) > Ba^{2+} (0.24). Since the force characteristic of Mg^{2+} cations is highest among alkali and alkaline–earth cations

and lowest among network–former ions, one can assume that the Mg^{2+} cations in the glass network can exist as both modifiers and network formers [113]. CTE increased with increasing BaO contents from 20 to 40 mol% and achieved a maximum of approximately 11×10^{-6} K^{-1} at 40 mol% BaO in the $BaO–Al_2O_3–La_2O_3–SiO_2–B_2O_3$ system [114]. CTE also increased with increasing SrO content, with a maximum of 9.7×10^{-6} K^{-1} at 25.7 mol% SrO in the $SrO–Al_2O_3–La_2O_3–SiO_2–B_2O_3$ system [87]. However, increasing SrO and decreasing B_2O_3/SiO_2 ratio resulted in growing of the glass transition temperature (T_g) and softening temperature (T_s) as the structure becomes inverted and rigid [87]. Hence, the CTE increases directly with the decreasing the field strength of alkaline earth cations due to the weaker bonding at lower field strength.

However, the effect of the network modifier on the T_g, T_s and CTE of a seal glass is complex and is related to the field strength, to the amount of a network modifier, and also to the presence of other concomitant components in the glass. Thus:

(i) T_g of 575–668 ºC, T_s of 558–781 ºC and CTE range $(9.9–12.0) \times 10^{-6}$ K^{-1} were revealed for CaO–BaO containing glasses [36, 39, 47, 70, 71, 77, 81, 91-93, 106];

(ii) T_g of 630–735 ºC, T_s of 721–768 ºC and CTE of$(11.2–12.1) \times 10^{-6}$ $K^{-1}$are found for CaO–SrO containing glasses [69, 77];

(iii) T_g of 584–650 ºC and CTE in the range of $(11.4–13.0) \times 10^{-6}$ K^{-1} are characteristic of SrO–BaO containing glasses [79];

(iv) T_g range of 624–715 ºC, T_s of 665–750 ºC and CTE of $(8.6–10.1) \times 10^{-6}$ K^{-1}were obtained for MgO–BaO containing boron–aluminosilicate glasses. BaO and SrO as modifiers increase the CTE as compared to CaO and MgO due to their low field strength values [86]. The lowest T_g of 584 ºC and highest CTE of 13×10^{-6} K^{-1}were obtained for 18.5 mol% SrO and 33.3 mol% BaO containing aluminosilicate glasses [79].

Table 2.3: Some alkaline earth aluminosilicate glass compositions (%) investigated for SOFCs

	CaO	*SrO/BaO*	*Al_2O_3/La_2O_3*	*SiO_2*	*B_2O_3*	*Others*	*Ref.*
Mol	26.48	26.48/-	1.96	41.16	1.92	2 TiO_2	[103]
Wt	20.6	38.1/-	2.8	34.4	1.9	2.2 TiO_2	
Mol	23.4	23.4	-	39.6	3.6	10 ZnO/10 MnO_2/10La_2O_3	[105]
Wt	13.6-18.3	25.2-33.8	-	24.7-33.1	2.6-3.5	11.3 ZnO/12 MnO_2/33.9La_2O_3	
Mol	19.2	18.5	2.9	42.2	1.9	13.2 ZnO/2.1 TiO_2	[104, 115]
Wt	15	26.6	4.1	35.2	1.8	14.9 ZnO/2.3 TiO_2	
Mol	15	-/35	5	35	10	-	[47, 70, 72]
Wt	8.8	-/56.4	5.4	22.1	7.3	-	
Mol	-	-/30	-	40	0-7.5	20 ZnO 2.5-10 Mn_2O_3	[73]
Wt	-	-/45.1-48.2	-	23.5-25.2	0-5.5	15.9 -17.0ZnO 4.1-15.5 Mn_2O_3	
Mol	-	-/30	0-10	40	0-10	20 ZnO	[74]
Wt		-/47.7-49.3	0-10.6	24.9-25.8	0-7.5	16.9-17.5 ZnO	
Mol	5	43.5 ($SrCO_3$)	-	34	10	5 Y_2O_3 2.5 ZnO	[75]
Wt	2.6	59.6	-	19	6.5	10.5 Y_2O_3 1.9 ZnO	
Mol	6	42.5	-	37.0	8.5	6 Y_2O_3	[76]
Wt	3.8	49.4	-	25	6.6	15.2 Y_2O_3	
Mol	15	-/35	5	35	10	-	[76]
Wt	8.8	-/56.4	5.4	22.1	7.3	-	
Mol	-	20-40	4-12.5	34-48	-	6-29 ZnO 3-10 TiO_2	[78]
Wt	-	19.05-46.21	2.82-12.98/ 7.45-24.8	14.52-28.17	-	4.24-25.89 ZnO 13.01-33.42 TiO_2	
Mol	-	18.5-20/30-33.3	4.6-5/4.6-5	27.7-30	9.2-10	0-1.8 P_2O_5	[79]
Wt	-	16.5-	4-4.5/12.9-	14.4-	5.5-	0-2.2 P_2O_5	

		18.3/44.1-40.7	14.4	15.9	6.2		
Mol	-	38.8	-	52.5	-	8.7 ZnO	[80]
		39.5	-	40.1	11.5	8.9 ZnO	
		38.8	-	40.9	9.4	9.1ZnO/1.8V_2O_5	
		40.5	2.4	41.0	5.9	9.1ZnO/1.1Cr_2O_3	
Wt	-	51	-	40-x	0-10	9 ZnO X=4V_2O_5, 3Al_2O_3, 2Cr_2O_3	
Mol	21.6	-/18.3	0.5	59.6	-	-	[107]
Wt	15.8	-/36.7	0.7	46.8	-	-	
Mol	15	-/35	5	32-37	8	0-5 P_2O_5	[81]
Wt	8.5-8.9	-/54.2-56.5	5.1-5.4	19.4-23.4	5.6-5.9	0-7.2 P_2O_5	

Table 2.4: Boron–containing alkaline earth aluminosilicate glass compositions (%) investigated for SOFC

	CaO /MgO	*SrO/ BaO*	*Al_2O_3/ La_2O_3*	*SiO_2*	*B_2O_3*	*Others*	*Ref.*
mol	-	23.7	-/2.4	52.3	22.6	-	[82]
		16.6	-/2.6	56.4	24.4		
Wt	-	30	10	40	20	-	
		30	10	40	20		
mol	30	-	-	40	20	10 Y_2O_3/10 La_2O_3	[83]
Wt	21.7	-	-	31.1	18	29.2 Y_2O_3/	
	19.3			27.5	15.9	37.3 La_2O_3	
mol	-	-/30	-	40	20	10 Al_2O_3/10 Y_2O_3/ 10 La_2O_3	[84]
Wt	-	-/48.9	-	25.5	14.8	10.8 Al_2O_3	
		-/43.2		22.6	13.1	21.2 Y_2O_3	
		-/39.5		20.6	11.9	28 La_2O_3	
mol	-	30	-	40	20	10 Al_2O_3/10 Cr_2O_3/	[85]

						10 Y_2O_3/10 La_2O_3	
Wt	-	39.2 36.9 33.9 30.6	-	30.3 28.5 26.2 23.6	17.6 16.5 15.2 13.7	12.9 Al_2O_3 18.0 Cr_2O_3 24.6 Y_2O_3 32.1 La_2O_3	
mol	-/30	-	-	40	20	10 Al_2O_3/10 Y_2O_3/ 10 La_2O_3	[86]
Wt	-/20.1 -/16.6 -/14.6	-	-	39.9 33.1 29.1	23.1 19.2 16.9	16.9 Al_2O_3 31.1 Y_2O_3 39.4 La_2O_3	
mol	-	7.9-25.7	12.1-13.1/3.8-4.1	40.9-44.4	12.8-35.3	-	[87]
Wt	-	10-30	15/15	30	10-30	-	
mol	-	13.3	13.3/13.4	25-60	0-35	-	[90, 108]
Wt		12.5-12.9	12.3-12.7/39.5-40.8	13.6-33.7	0-22.1	-	
mol	0-15	-/0-40	0-10/0-15	0-40	0-15	0-5 (ZrO_2)	[36, 91-93]
Wt	0-6.9	-/0-50.7	0-8.4/0-40.4	0-19.9	0-8.6	0-5.1	
mol	16-24 - 16	-/16-24 36-44/- 16-28/-	6/6 5/5 5/5	30-42 30-30 31-43	10-14 13-16 15	-	[94]
Wt	9.5-13.3 - 10.1-10.8	-/26.1-36.5 40.4-47.4/- 19.9-32.8/-	6.1-6.5/ 19.4-20.8 5.3-5.5/ 16.9-17.6 5.8-6.1/ 18.4-19.6	17.9-26.8 18.7-26.7 21.1-31	6.9-10.4 9.8-11.6 11.8-12.5	-	
mol	-	-/47.62	4.76	26.67	20.95	-	[113]
Wt	-	-/67.3	4.5	14.8	13.4	-	
mol	-	-/40	0-10	33.3-40	16.7-20	-	[97]
Wt	-	-/59.5-61.8	0-9.9	19.4-24.2	11.3-14	-	
mol	-	-/12.62-50	5-7.59	15-63.2	16.67-30	-	[98]
Wt		-/25.2-68.7	4.6-10.1	8.1-49.5	15.2-18.7	-	

mol	-	20/20	-	40	20	-	[104]
Wt	-	23.2/34.3	-	26.9	15.6	-	
mol	10-15	-/32.5-35	2.5-5/0-5	30-39	10-15	-	[41]
Wt	6-8.8	-/47.3-56.4	2.4-5.4/0-15.5	19.4-23.2	6.9-11.3	-	

Fig. 2.3b displays the variation in T_g and T_s as function of the (BaO+SrO)/(CaO+MgO) molar ratio. These variations are rather discontinuous: (i) when the ratio (BaO+SrO)/(CaO+MgO) ranges from 0.50 to 2.67 T_g and T_s vary in the intervals of 575–650 ºC and 640–750 ºC, respectively; (ii) T_g and T_s both show an abrupt decrease at the molar ratios from 2.67 to 3.5; (iii) continuous increase in T_s and T_g were observed in the interval 3.5–6; and finally,(iv) significant increase of T_g and T_s were revealed when the molar ratio ranged from 6.50–7.08. A general trend to growing CTE has been observed with increasing molar ratio (BaO+SrO)/(CaO+MgO), Fig. 2.4.

Highly suitable values of T_g, T_s and CTE have been achieved in the barium containing boron aluminosilicate glasses (Table 2.2). However, poor thermal stability and unwanted chemical interaction with the SOFC components limit the application of BaO– and B_2O_3–containing glasses. B_2O_3 works well for decreasing the viscosity of the glass but at the same time it decreases seal thermal stability owing to lowering network connectivity. On the other hand, the compositions that contain large amounts of boron can react in overtime with water vapour and produce gaseous $B_2(OH)_2$ or $B(OH)_3$. This can decompose the seal glass and limit the life span. Notice that Zhang et al. [104] discussed the borate volatility issues in their report.

Glass–ceramics (GCs), formed by the controlled crystallization of glasses, exhibit superior properties with respect to glasses. The performance of GCs can be controlled by proper controlling of the nature and amount of crystalline components. Crystallization typically increases the strength and CTE [92, 93]. The higher CTEs of GCs are however entirely consistent with the relative CTE variations of the crystalline phases developed in the glasses. The resultant CTE can be estimated using the standard additive rule $\alpha=\Sigma m_i\alpha+a_i$ where α is the CTE of the glass ceramics, m_i and α are the mole fraction and CTE of each phase present in the matrix, respectively, and a_i is a constant factor for phase

i [116]. Significant content of BaO in the aluminosilicate glasses can lead to formation of the following crystalline phases: (i) Barium silicate ($BaSiO_3$; CTE (9–13) × 10^{-6} K^{-1}), (ii) Barium orthosilicate ($BaSi_2O_5$; CTE≈14 × $10^{-6}K^{-1}$), (iii) Hexacelsian ($BaAl_2Si_2O_8$; CTE=(7–8) × 10^{-6} K^{-1}), (iv) Monocelsian ($BaAl_2Si_2O_8$; CTE= (2–3) × 10^{-6} K^{-1}), and (v) Orthocelsian ($BaAl_2Si_2O_8$; CTE= (7–8) × 10^{-6} K^{-1}) [23]. The activation energy for crystal growth is very low for the BaO–containing glass (206–300 $kJmol^{-1}$) as compared to CaO–containing (413 $kJmol^{-1}$) and MgO–containing (340–420 $kJmol^{-1}$) aluminosilicate glasses, and thus causes rather poor thermal stability [117]. Consequently, due to low activation energy there is a strong tendency for celsian formation in BaO–containing glasses. The celsian ($BaAl_2Si_2O_8$) crystalline phase having a low CTE value reduces thermal expansion of the resultant GCs. On the other hand, significant content of BaO in the glasses can also lead to formation of $BaCrO_4$ on the sealant surfaces due to the transport of volatile Cr–containing species, such as CrO_3 or $CrO_2(OH)_2$. The high CTE of $BaCrO_4$ (~18 × 10^{-6} K^{-1}), contributes to the physical separation of the sealing glass from the stack components where the CTEs are (10–13) × 10^{-6} K^{-1} [23]. Thus, the formation of low expansivity $BaAl_2Si_2O_8$ phase due to high BaO content in these glasses makes them unsuitable for the SOFC sealants.

2.4 The problem and the possible solution

The above literature survey evidenced that many compositions of glass sealants for p–SOFCs have been developed and extensively studied for their thermal and chemical properties. However, no specific sealant developed so far is offering a great promise for the planar–SOFC applications. There are several ways in which a rigid glass/GC SOFC seal can fail during operation, including: i) failure by fracture under pressurization, ii) failure during rapid thermal cycling, and iii) failure upon thermal aging. Self–healing (SH)–glasses/GCs would be one viable option to overcome the drawbacks presented by the rigid glass/GC seals. SH–glasses/GCs ideally have the ability to effectively “repair” any cracks developed during thermal cycling when heated to a sufficiently high temperature. The advantage of this approach is that materials with significantly different CTE values could potentially be used as seals because at FC operating

temperatures−induced, the thermo−mechanical stresses could be relaxed. Until now, very few related studies have been reported in literature [48, 53, 118]. However, most of the proposed solutions still have some lacunas or challenges to be further addressed. For instance, the SH glass seal proposed by Singh et al. [53, 54] experienced a continuous creep deformation at FC operating temperature, therefore, resulting in a possible overflow of the sealant material. Further, SH shape memory alloy (SMA)/glass composite seal designed by Story et al. [119] is unsuitable due to its high electrical conductivity and low transformation temperature of the SMA. Concerning SH−glass seals, the following challenging issues still need to be fully demonstrated by researches/technicians: i) the ability to SH at the cell operating temperature 700−800^{o}C, ii) the thermal stability of the seal against crystallization for long durations, and iii) the maintainance of the sealing capability [54]. In the light of the above mentioned state−of−art, it is evident that there is a need for the development of new sealing and/or bonding materials for FCs, in particular materials that can have high flexibility and also higher mechanical, chemical and thermo−physical stability. In this regard, SH glasses have the potential to remove the main difficulties being faced by SOFC community relatively to the use of rigid glass/GC seals. A careful design and synthesis of suitable SH−glass seals along with optimization of their properties with respect to final application in SOFC will be a valuable contribution in this field. In addition, additional new concepts/modifications are required to conquer the challenges being faced by the existing sealing technology.

3. Experimental

3.1 Glass preparation

High purity powders of SiO_2 (>99.5%), Al_2O_3 (Sigma Aldrich, >98%), $MgCO_3$ (BDH chemicals, UK, >99%), $CaCO_3$ (>99.5%), $SrCO_3$ (Sigma Aldrich, 99.9%), $BaCO_3$ (Sigma Aldrich, 99.9%), La_2O_3 (Sigma Aldrich, 99.9%), H_3BO_3 (>99.5%), and NiO (Sigma Aldrich, 99.9%) were used. Homogeneous batch mixtures of 100 g in accordance with the designed compositions, obtained by ball milling were preheated in temperature ranges 800–1100 ºC for 2 h for decarbonisation. The decarbonized mixture was then melted in Pt crucibles in temperature ranges 1550–1585 ºC for 2 h, in air. Glasses in bulk form were produced by pouring the melts on preheated bronze moulds followed by annealing at around T_g for 1 h. The glasses in frit form were obtained by quenching of glass melts in cold water. The frits were dried at 100 ºC for 24 h and then milled in a high–speed agate mill resulting in fine glass powders with mean particle sizes of 10–15 μm (determined by light scattering technique; Coulter LS 230, UK; Fraunhofer optical model). The amorphous nature of glasses was confirmed by X–ray diffraction (XRD) analysis (Rigaku Geigerflex D/Max, Tokyo, Japan; C Series; Cu K_α radiation; 2θ range 10º–80º; step 0.02 $^o s^{-1}$).

3.1.2 Density and Molar volume

Archimedes' method (i.e. immersion in diethyl phthalate) was employed to measure the apparent density of the bulk annealed glasses. Molar Volume (V_m), was calculated using the density data for the bulk glasses using following relations:

$$V_m = \frac{M}{\rho} \qquad 3.1$$

where M is the molar mass of the glass and ρ is the apparent density of the bulk glasses.

3.2. Thermal analysis of glasses

3.2.1 Sintering behaviour – hot stage microscope (HSM)

The sintering behaviour of the glass powders was investigated using a side–view hot stage microscope (HSM) EM 201 equipped with image analysis system and 1750/15

Leica electrical furnace. The cylindrical shaped samples with height and diameter of ~3 mm were prepared by cold–pressing the glass powders. The cylindrical samples were placed on a 10 × 15 × 1 mm alumina (>99.5 wt. % Al_2O_3) support. The temperature was measured with a Pt/Rh (6/30) thermocouple contacted under the alumina support. The microscope projects the image of the sample through a quartz window and onto the recording device. The computerized image analysis system automatically records and analyses the geometry changes of the sample during heating. The image analyser takes into account the thermal expansion of the alumina substrate while measuring the height of the sample during firing, with the base as a reference. The HSM software calculates the percentage of decrease in height, width and area of the sample images. The measurements were conducted in air with a heating rate of 5 $Kmin^{-1}$. The temperatures corresponding to the characteristic viscosity points (first shrinkage (FS), maximum shrinkage (MS), deformation (D), softening point (S), hemi–sphere (HS) and flow point (F)) were obtained from the photographs taken during the hot–stage microscopy experiment following Scholze's definition [120, 121].

3.2.2 Differential thermal analysis (DTA)

The values of the glass transition temperature (T_g), crystallization onset temperature (T_c) and peak temperature of crystallization (T_p) were obtained by differential thermal analysis (DTA) using a Setaram LabSys TG–DTA16 instrument (Setaram Instrumentation, France) calibrated in the temperature range 25–1000 ºC. The measurements were performed using powdered glass samples (50 mg) in an alumina crucible and α–alumina powder as reference at a heating rate (β) of 5 $Kmin^{-1}$ and 20 $Kmin^{-1}$.

3.2.3 *In situ*–hot stage scanning electron microscopy

The environmental scanning electron microscopy (ESEM, FEIXL30, Eindhoven, Netherlands), with an *in situ* heating stage was employed to shed some more light on the sintering behaviour of glasses. Due to the highly expensive and time consuming nature of this study, three glasses with similar lanthanide content (Nd–0.2, Gd–0.2 and Yb–0.2) (Chapter 4.4) were only selected for this analysis. Small amounts of glass powder were

introduced in an MgO crucible plated with Pt (platinum plating is used to connect electrically the inside of the crucible to the SEM, so that a potential can be applied to the inside of the crucible). Since the glass grains were large enough to be manipulated with tweezers, a few grains were arranged in contacting pairs so as to facilitate the formation of necks during sintering. Observations were made in environmental mode with a water vapor pressure of 2 Torr. The samples were heated to 500 ºC at 30 $Kmin^{-1}$, and then until 1000 ºC at 10 $Kmin^{-1}$ (with several pauses to take pictures at different temperatures). The formation of a neck between two glass particles was followed as a function of temperature.

3.2.4 *In situ* High Temperature X–ray diffraction (HT–XRD)

The phase transformations occurring in glass powders over increasing temperature from room temperature to 850 ºC were monitored by *in situ* high temperature X–ray diffraction (HT–XRD) analysis (Philips, X'pert, The Netherlands, equipped with a Pt hot stage). The schedule of the hot stage was as follows: Step 1: Room temperature to 500 ºC at β of 30 $Kmin^{-1}$; Step 2: 500 ºC to 850 ºC at β of 5 $Kmin^{-1}$; Step 3: dwell at 850 ºC for 1 h. The XRD data was collected at the following temperatures: (i) room temperature; (ii) 500 ºC; (iii) 700 ºC; (iv) 750 ºC; (v) 800 ºC; and (vi) 850 ºC without any significant dwell. Further XRD data was also collected at 850 ºC after dwell of 1 h.

3.2.5 Dilatometry

Dilatometry measurements were done with prismatic samples with cross section of 4×5 mm^2 (Bahr Thermo Analyse DIL 801 L, Hüllhorst, Germany GmbH; β=5 $Kmin^{-1}$). The mean values and the standard deviations (SD) presented for coefficient of thermal expansion (CTE) (both glasses and GCs), and softening temperature (T_s) have been obtained from (at least) three different samples for each glass and GC.

3.3 Structural characterization of glass

3.3.1 Magic angle spinning – Nuclear magnetic resonance (MAS–NMR)

^{29}Si, ^{27}Al, and ^{11}B 1D magic–angle spinning (MAS) nuclear magnetic resonance (NMR) spectra were recorded for all the glasses and GCs. The spectra were acquired on a

Bruker Avance III 400 spectrometer operating at a B_0 field of 9.4 T with ^{29}Si, ^{27}Al and ^{11}B Larmor frequencies of 79.5, 104.3 and 128.4 MHz, respectively. ^{29}Si MAS NMR spectra were recorded using a 7 mm probe employing a rotation speed of 5 kHz, using a 4.5 μs radio–frequency (RF) excitation pulse length with a RF field strength of 56 kHz (90º flip–angle) and 60 s recycle delay. Kaolinite was used as the chemical shift reference. ^{27}Al and ^{11}B MAS NMR spectra were recorded using a 4 mm probe using a spinning rate of 14 kHz, 1 s recycle delay, 0.5 μs RF excitation pulse (equivalent to a $\pi/18$ flip angle) for ^{27}Al and 0.9 μs (equivalent to a $\pi/12$ flip angle) for ^{11}B. The flip angle pulses used for ^{27}Al and ^{11}B were optimized using an aqueous solution of $Al(NO_3)_3$ and H_3BO_3.

3.4 Glass–ceramic preparation

The GCs were produced by sintering and heattreatment of glass powder compacts. Rectangular bars with dimensions of 4×5×50 mm^3 or circular disc shaped pellets with Ø 20 mm and thickness ~3 mm were prepared from fine glass powders by uniaxial pressing (80 MPa). The glass powder compacts were sintered in the temperature ranges of 850–900 ºC for 1 h. Slow β of 5 $Kmin^{-1}$ was maintained for all the samples in order to prevent deformation of the samples. Further, glass powder compacts already sintered at 900 ºC for 1 h, were heat treated under isothermal conditions at 850 ºC for different time durations varying between 1 h – 1000 h. GCs were produced after prolonged heattreatment, up to 1000 h, in order to evaluate their thermal expansion behaviour and stability of crystalline phase assemblage during long term operation at SOFC operation temperature.

3.5 Characterization of glass–ceramics

3.5.1 Linear shrinkage, density and Mechanical strength

The linear shrinkage during sintering and after the prolong heat treatment was calculated from the difference of the diameter/length between the green and the sintered pellets. Archimedes' method (i.e. immersion in diethyl phthalate) was also employed to measure the apparent density of the GCs. The mechanical properties of GCs were

evaluated by measuring the three–point bending strength of rectified parallelepiped bars (Shimadzu Autograph AG 25 TA, Columbia, MD with 0.5 mmmin^{-1} displacement). The mean values and the standard deviation presented for the linear shrinkage, density and mechanical strength have been obtained from five different samples.

The mechanical reliability was tested by applying the well–known Weibull statistics to the experimental data [122]. According to Weibull statistics, the increasing probability of failure (F) for a brittle material can be expressed by $F=1–exp\ (–\sigma/\sigma_0)^m$, where F is the failure probability for an applied stress (σ), σ_0 is a normalizing parameter known as Weibull characteristic strength, and m is the Weibull modulus. Here, the Weibull modulus m is a measure of the degree of strength data dispersion.

3.5.2 Qualitative and quantitative crystalline phase evaluation

The crystalline phases in GCs were determined by XRD analysis (Rigaku Geigerflex D/Max, C Series; CuKα radiation; 2θ angle range 10º–80º; step 0.02 deg s^{-1}). The quantitative analysis of crystalline phases in GCs (crushed to particle size < 25 μm) were determined by XRD analysis using a conventional Bragg–Brentano diffractometer (Philips PW 3710, Eindhoven, The Nederlands) with Ni–filtered Cu–Ka radiation. The quantitative phase analysis of the GCs was made by combined Rietveld–Reference intensity ratio (RIR) method. A 10 wt.% of corundum (NIST SRM 674a, annealed at 1500 ºC for 1 day to increase the crystallinity to 100%) was added to all the GC samples as an internal standard. The mixtures, ground in an agate mortar, were side loaded in aluminium flat holder in order to minimize the preferred orientation problems. Data were recorded in 2θ range = 5–140º (step size 0.02º and 6 seconds of counting time for each step). The phase fractions were extracted by Rietveld–RIR refinements, using GSAS software [123] and EXPGUI [124] as graphical interface, were rescaled on the basis of the absolute weight of corundum originally added to their mixtures as an internal standard, and therefore, internally renormalized. The background was successfully fitted with a Chebyshev function with a variable number of coefficients depending on its complexity. The peak profiles were modelled using a pseudo–Voigt function with one

Gaussian and one Lorentzian coefficient. Lattice constants, phase fractions, and coefficients corresponding to sample displacement and asymmetry were also refined.

3.6 Joining behaviour and chemical interactions between electrolyte/seal and interconnect/seal diffusion couples

In order to investigate the adhesion and chemical interaction of the glasses with SOFC components, wetting experiments between glass (powder) – 8YSZ (Tosoh, Japan) and glass (powder) – metallic interconnect were carried out under different conditions. Two different metallic interconnect materials, namely, Crofer22APU (Thyssen Krupp, VDM, Werdohl, Germany) and SanergyHT (Sandvik AB, Sandviken, Sweden) were employed for wetting and interaction experiments with the glasses [125, 126]. The glass powders, 40 % solid content mixed with 5 vol% solution of polyvinyl alcohol (PVA) prepared by dissolution of PVA in warm water, were deposited on SOFC components by slurry coating. The diffusion couples were heated to 900 ºC with a relatively slow β of 2 $Kmin^{-1}$ and kept at that temperature for 1 h. Heat treatment was performed without applying any dead load. The adhesion and chemical interactions of the glasses with SOFC components, were also tested in humidified $10\%H_2$–$90\%N_2$ gas mixture atmosphere at 850 ºC temperature for 250 h at 2 $Kmin^{-1}$ (chapter 4.2).

3.7 Microstructural characterization– SEM and EDS

Microstructural observations were made on polished surfaces of the sintered and heat treated glass powder compacts (chemically etched by immersion in 2 vol % HF solution for duration of 2 min) by scanning electron microscopy (SEM; SU–70, Hitachi). In addition, energy dispersive spectroscopy (EDS; Bruker Quantax, Germany) has been utilized to study the distribution of elements along the interface of glass–interconnect/ceramic plate.

3.8 Electrical characterization

The total conductivity (σ) was determined by AC impedance spectroscopy, using P4284A precision LCR meter, 20 Hz – 1 MHz, and Gamry PCI4/750 instruments using

dense disk– or bar–shaped samples with porous Pt electrodes. In the course of impedance measurements, the magnitude of AC voltage was fixed at 1.00 V; the equilibration time after each temperature change was 2–4 h. the measurements were performed as function of temperature at 620–850 ºC and time (1–300 h) in flowing atmospheric air, dry Ar, argon humidified at room temperature, and 10% H_2–90% N_2 gas mixture. The water vapour partial pressures, determined by a Jumo humidity transducer in air, dry Ar, and humidified Ar flow, were 0.006 atm, 10^{-4} atm and 0.03 atm, respectively.

Seal glass/8YSZ diffusion couples had prepared (section 3.6) after that used for the electrical measurements in order to test possible degradation processes in the course of annealing/heat treatment at SOFC operation temperature. In the latter case, porous Pt electrodes were deposited onto both GC and 8YSZ surfaces, and then fired at 870–880 ºC during 15 min.

3.9 Ion transference number (electro motive force method)

The ion transference numbers, which show the contribution of all mobile ions to the total conductivity, were determined by the modified electromotive–force (e.m.f.) technique, as described elsewhere [127, 128]. Gas mixtures of 10% H_2–90% N_2 were supplied at the anode of a Pt|GC|Pt cell, where the oxygen partial pressure ($p1$) was determined using a 8YSZ sensor. The cathode was exposed to atmospheric air ($p2$ = 21 kPa). The e.m.f. of the cell was measured at 820–860 ºC as a function of an external resistance, R_M. The ion transference numbers were calculated using regression model of eq. (3.2) in combination with eq. (3.3):

$$\frac{E_{th}}{E_{obs}} - 1 = A\left(\frac{1}{R_M}\right) + B \qquad R_e = \frac{A}{B} \qquad 3.2$$

$$t_i = 1 - \frac{R_{bulk}}{R_e} \qquad 3.3$$

where A and B are regression parameters, E_{obs} the measured e.m.f., E_{th} the theoretical Nernst voltage, R_{bulk} the bulk resistance determined from the impedance spectra, and R_e the partial electronic resistance of the sample. In all cases, porous Pt electrodes deposited onto the surfaces of dense GC disks or bars were used; the partial pressures of oxygen

and water vapour in the gas mixtures were controlled employing 8YSZ solid–electrolyte sensors and Jumo humidity transducers, respectively.

3.9 Oxygen leakage measurements

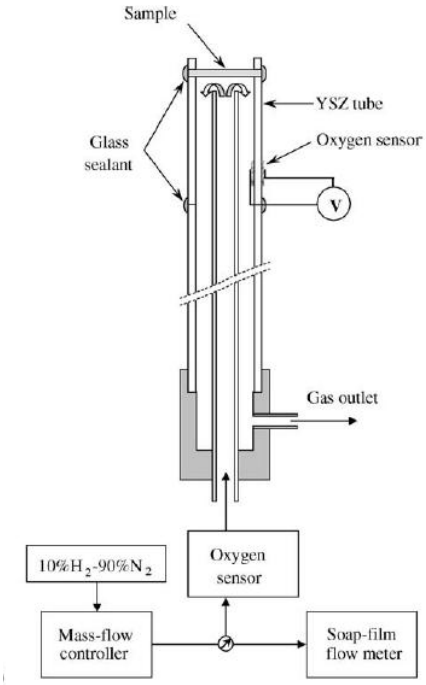

Fig. 3.1: Schematic diagram of experimental set–up for oxygen leakage measurements

The oxygen leakage measurement was performed by the determination of oxygen permeation fluxes through GCs under air/H_2–H_2O gradients. The experimental setup, sketched in Fig. 3.1, comprises a dense membrane disk (0.65 mm thickness) hermetically sealed onto an YSZ tube, and two oxygen sensors at the inlet and outlet of the cell. Gas mixture of H_2–H_2O–N_2 (10.3 cm^3min^{-1}) with controllable flow rate (V) was supplied to the membrane permeate side, where hydrogen interacted with oxygen permeating through the GCs. The oxygen permeation flux density (j) through a membrane under steady–state conditions was calculated from eq. (3.4):

$$j = \frac{V}{RST_V}\frac{p(H_2)_{in} - p(H_2)_{out}}{2} \qquad 3.4$$

where T_V is the flow meter temperature, S the membrane surface area, and $p(H_2)_{in}$ and $p(H_2)_{out}$ are the hydrogen partial pressures at the inlet and outlet of the measuring cell, respectively. The hydrogen pressure was calculated by from eq. (3.5)

$$p(H_2) = \frac{CP_{total}}{1+K\times p(O_2)^{1/2}} \qquad 3.5$$

where C is the volume fraction of H–containing species (H_2 +H_2O) in the gas determined by its initial composition, P_{total} the total pressure, K the equilibrium constant of the H_2 oxidation reaction calculated using thermodynamic data [129], and $p(O_2)$ the oxygen partial pressure in the gas flow determined by the oxygen sensor [128].

3.10 Thermal shock resistance

In order to evaluate thermal shock stability of the sealant in contact with various solid oxide electrolyte (SOE) ceramics, a series of dense electrolyte membranes made of 8 mol% yttria–stabilized zirconia, $Ce_{0.8}Gd_{0.2}O_{2-\delta}$ (CGO, Rhodia) and $(La_{0.9}Sr_{0.1})_{0.98}Ga_{0.8}Mg_{0.2}O_{3-\delta}$ (LSGM, Praxair) were sealed onto YSZ tubes (Tosoh) at 900±10 ºC during 30 min. Gas–tight SOE disks of YSZ, CGO and LSGM were sintered at 1600, 1500 and 1400 ºC, respectively; their density was higher than 95% of theoretical. After sealing of the electrolyte assemblies and one gas–tightness test at room temperature, each cell was heated up to T_{max} = 800 ºC, kept at this temperature during 10–15 min, quenched in air, and then checked for gas–tightness again. This procedure was repeated several times. The cells made of YSZ were successfully tested in 15 air–quenching cycles; for LSGM and CGO disks sealed onto YSZ, cracking and resultant physical leakages were observed after 3 and 4 cycles. SEM analysis of the SOE and GC interfaces was carried out using various combinations of the SOE disks, sealed one to another and quenched in air under identical conditions.

3.11 Bilayer Synthesis

Bi–layered compacts were prepared from 0.75 g of Gd–0.3 (composition referred in Chapter 4.4 and 4.5) and 0.75 g of Sr–0.3 (composition referred in Chapter 4.2) glass powders by depositing them in two uniform successive layers in a rectangular mould having dimensions of 4 mm × 5 mm × 50 mm and then uniaxial pressure (80 MPa) was applied to obtain rectangular bars. Cylindrical discs with 10 mm diameter were also prepared following the same procedure but using 0.3 g of each glass powder to study the interface between two layers and to determine the electrical conductivity of the bi–layers.

The as obtained green bodies were sintered at 850 ºC for 1 h and further heat treated for 100 h at a heating rate, β = 5 Kmin^{-1}.

To investigate the adhesion of the bilayered glasses to the SOFC components wetting experiments between the powdered glasses and ceramics/interconnects (Crofer22APU and Crofer22H) were carried out. The separated layers were deposited using a tape casting approach. They were then superimposed and thermocompressed onto the ceramics/interconnects. The diffusion couples were heated up to 850 ºC at a relatively slow β = 2 Kmin^{-1} and kept at that temperature for 100 h. The heat treatment was performed without applying any deadload.

3.12 Raman spectroscopy

Raman spectra for Bi–layer GC were obtained using a Horiba LabRam HR 800 Evolution confocal Raman microscope, with a 532 nm excitation laser and a 100x objective lens (NA = 0.9). The incident laser power on the samples was ~10 mW and the spot size was ~3.14 square micron. The collected Raman radiation was dispersed with a 600 lines mm^{-1} grating and focussed on a Peltier–cooled charge–coupled device (CCD) detector allowing a spectral resolution of *ca* 5 cm^{-1}. All spectra were recorded in the 100–4000 cm^{-1} range with an integration time of 1 s and 3 accumulations per spectrum.

4. Results and Discussion

In recent years, our research group has investigated a few series of alkaline–earth aluminosilicate glasses and GCs aiming sealing SOFC's components [117, 130-135]. Parent glass compositions have been selected in the primary crystallization field of Al–containing diopside ($CaMgSi_2O_6$; hereafter refereed as Di). The major attribute of Di based GCs is their good sinter ability and the ability to accommodate various cations (Ba^{2+}, Sr^{2+}, La^{3+}, Cr^{3+}, Al^{3+}, B^{3+}, etc.) in their structure or amorphous glassy phase, thus leading to the formation of mono–mineral GCs [33, 133, 135, 136] which renders them high mechanical strength and low porosity; two essential traits expected from a robust sealing material. Furthermore, strong adhesion, and high chemical stability with metallic interconnect and ceramic electrolyte (ZrO_2 stabilized with 8 mol% Y_2O_3, 8YSZ) even after 300 h of heat treatment and low leak rate [117, 131, 134, 135, 137] are some other attributes which make them an interesting candidate for this job. However, still there is a need to improve the CTE and study the thermal stability of Di based GC sealants during long term heat treatments (at least up to 1000 h) in order to qualify them for final application in SOFC stack. In addition, due to the known background about the diopside based glass and GC we intended to develop SH glass and GCs sealant.

4.1 Diopside – Ba disilicate glass–ceramics for sealing applications in SOFC: sintering and chemical interactions studies

4.1.1 Introduction

The chemical composition of a glass for a suitable and compliant seal for SOFC or other high temperature electrochemical applications should be chosen considering: (i) the various thermal and chemical environments to which the seal will be exposed during its operation; (ii) the role of each chemical constituent in the glass towards rendering the thermal and chemical stability along with mechanical integrity to the seal in hostile high temperature working environment, including minimum surface diffusion and poisoning phenomena, and; (iii) basic requirements such as good electrical insulating properties. For instance the glass compositions investigated in our previous studies [131, 137, 138], were designed in the primary crystallization field of Di owing to their high chemical resistance, good sintering ability and relatively high coefficients of thermal expansion (CTE). A minor amount of B_2O_3 was added along with lanthanide oxides in order to tailor the viscosity and flow behaviour. The GC seals demonstrated high mechanical properties, phase stability at elevated temperatures, good wetting abilities and minimal chemical interaction with other SOFC components. However, thermal stability of these GC seals during long term operation is still a matter of concern. Therefore, further experimentation is required in terms of tailoring glass chemistry so as to achieve a stable seal with appropriate CTE matching and minimal reactivity with SOFC components during long run.

In this regard designing of GC compositions with combination of Di with the crystalline phases exhibiting substantially high CTE, such as barium aluminosilicates might be feasible solution of the problem [21, 23]. As it was recently demonstrated [139], barium silicates exhibit CTEs in a range suitable for components of sealing materials which implies that if the respective crystalline phases are combined with other crystalline or amorphous phases, an appropriate CTE can be adjusted. Since the glass forming ability is higher for molar ratios $[BaO]/[SiO_2] \leq 1$, the BaO concentration should be chosen low enough to allow good densification of glass powders and avoid the formation of any undesirable crystalline phase with low CTE [139]. The same requirement is critically

important to improve sealant stability in steam–containing environments necessary for the SOFC anode operation.

The present study is an attempt to design some new Di based glass compositions in order to tailor the CTE and flow properties of the Di based GC sealants. The glass composition $Ca_{0.9}MgAl_{0.1}La_{0.1}Si_{1.9}O_6$, investigated in our previous study [117], was chosen as the starting point and three new glass compositions by introducing different concentrations of barium disilicate ($BaSi_2O_5$) were derived. Table 4.1.1 presents the detail composition of the glasses. Additionally 2 wt. % B_2O_3 was added to glasses in order to tailor their flow behaviour whilst NiO (1 wt %) was introduced to improve their adhesion to the metallic SOFC components; as confirmed in the present study, this small amount of nickel oxide has no detectable effects on the conductivity and chemical expansivity.

Table 4.1.1: Nominal batch compositions of the glasses

	CaO	*MgO*	*BaO*	*Al_2O_3*	*La_2O_3*	*SiO_2*	*B_2O_3*	*NiO*
Di–Ba–1								
Wt%	21.09	16.84	1.36	2.13	6.81	48.77	2.00	1.00
Mol%	22.14	24.60	0.52	1.23	1.23	47.79	1.69	0.79
Di–Ba–2								
Wt%	20.55	16.41	2.72	2.08	6.63	48.61	2.00	1.00
Mol%	21.77	24.19	1.05	1.21	1.21	48.06	1.71	0.80
Di–Ba–3								
Wt%	19.47	15.55	5.44	1.97	6.28	48.29	2.00	1.00
Mol%	21.01	23.34	2.15	1.17	1.17	48.62	1.74	0.81

4.1.2 Results

The competitive process between sintering and crystallization affect the microstructure of sintered GCs by means of porosity, crystallization fractions and their corresponding properties. This can be accessed through DTA and HSM measurements on glass powder compacts as seal glasses are usually applied on the ceramic or metallic plate

of SOFC components in the form of glass powders. In general, two different trends can be observed: (i) sintering precedes crystallization – in this case sintering and crystallization are independent processes and the overall effect is a dense GC material; (ii) crystallization precedes sintering – in this case a fully/partially crystallized porous GCs results [138].

The process of formation of GCs via sintering of glass powders involves sintering and crystallization. Both of these processes take place either simultaneously or independently. In general, the sintering phenomena occur in three steps: (i) inter–particle neck formation and growth; (ii) densification and shrinking of the pores; and (iii) disappearance of the isolated pores resulting in a fully dense or partially dense glass–ceramic [140, 141]. Hot–stage microscopy (HSM) is an interesting technique for studying the sintering process of dry–pressed compacts [138, 142] since it permits a continuous record of the contraction process of the material (Fig. 4.1.1). HSM also enables the competition between densification and crystallization upon sintering the glass–powder compacts to be assessed by comparing DTA and HSM curves recorded under the same heating conditions.

Fig. 4.1.1 presents variation in the relative area and heat flow with respect to temperature as obtained from HSM and DTA, respectively at a β of 5 $Kmin^{-1}$. Table 4.1.2 summarizes the values of the temperature of first shrinkage (T_{FS}; $\log\eta = 9.1 \pm 0.1$; η is viscosity in dPa s), temperature for maximum shrinkage (T_{MS}; $\log \eta = 7.8 \pm 0.1$) and ratio of the final area/initial area of the glass powder compact (A/A_0), as obtained from the HSM data at T_{MS} (Fig. 4.1.1), along with temperature for onset of crystallization (T_c), and peak temperature of crystallization (T_p) as received from DTA of the glasses.

The following observations can be made from the DTA and HSM results:

1. The temperature of first shrinkage, $T_{FS,}$ increased from 770 to 774 ºC with increasing $BaSi_2O_5$ amount.
2. Two stage sintering was observed for all the investigated compositions, evidenced from Fig. 4.1.1. The second stage of densification occurred in competition with devitrification, but accomplished before T_p. Only in Di–Ba–3 glass the second T_{MS2} is attained slightly after the T_P.

3. Values of A/A_0 (obtained at T_{MS1}) correspond to the ratio of final area to initial area of the glass–powder compact at T_{MS1} (as presented in Table 4.1.2), ranging from 0.65 to 0.67 implies towards good densification (95–98%) [143].
4. The DTA thermographs of all the three glasses exhibited single crystallization exothermic curves. This signifies that the GC is formed either as a result of single phase crystallization or of an almost simultaneous precipitation of more than one crystalline phase.

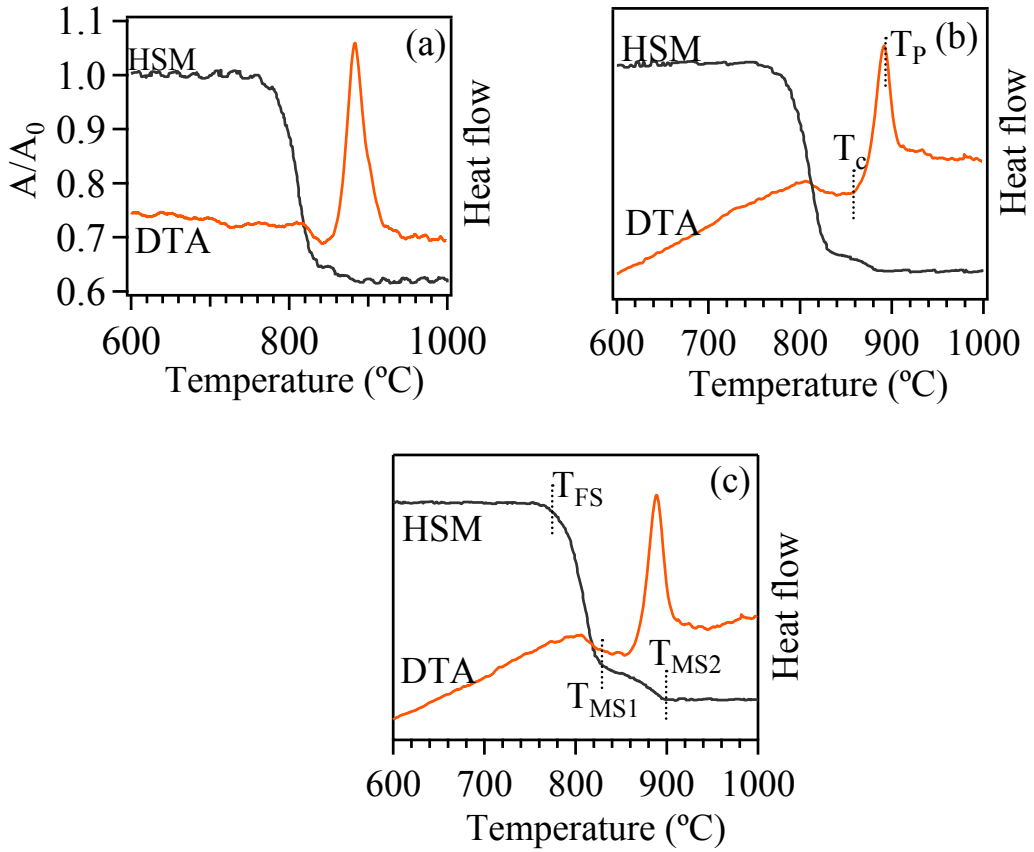

Fig. 4.1.1: Comparison of DTA and HSM curves on the same temperature scale for compositions (a) Di–Ba–1 (b) Di–Ba–2 and (c) Di–Ba–3

Table 4.1.2: Thermal parameters of the glasses obtained from DTA and HSM at β=5 $Kmin^{-1}$.

	Di–Ba–1	*Di–Ba–2*	*Di–Ba–3*
T_{FS} ±5 (ºC)	770	771	774
T_{MS1} ±5 (ºC)	837	832	830
T_{MS2} ±5 (ºC)	882	886	900
T_c ±2 (ºC)	844	859	856
T_P ±2 (ºC)	883	892	889
A/A_0 at T_{MS1}	0.65	0.67	0.65

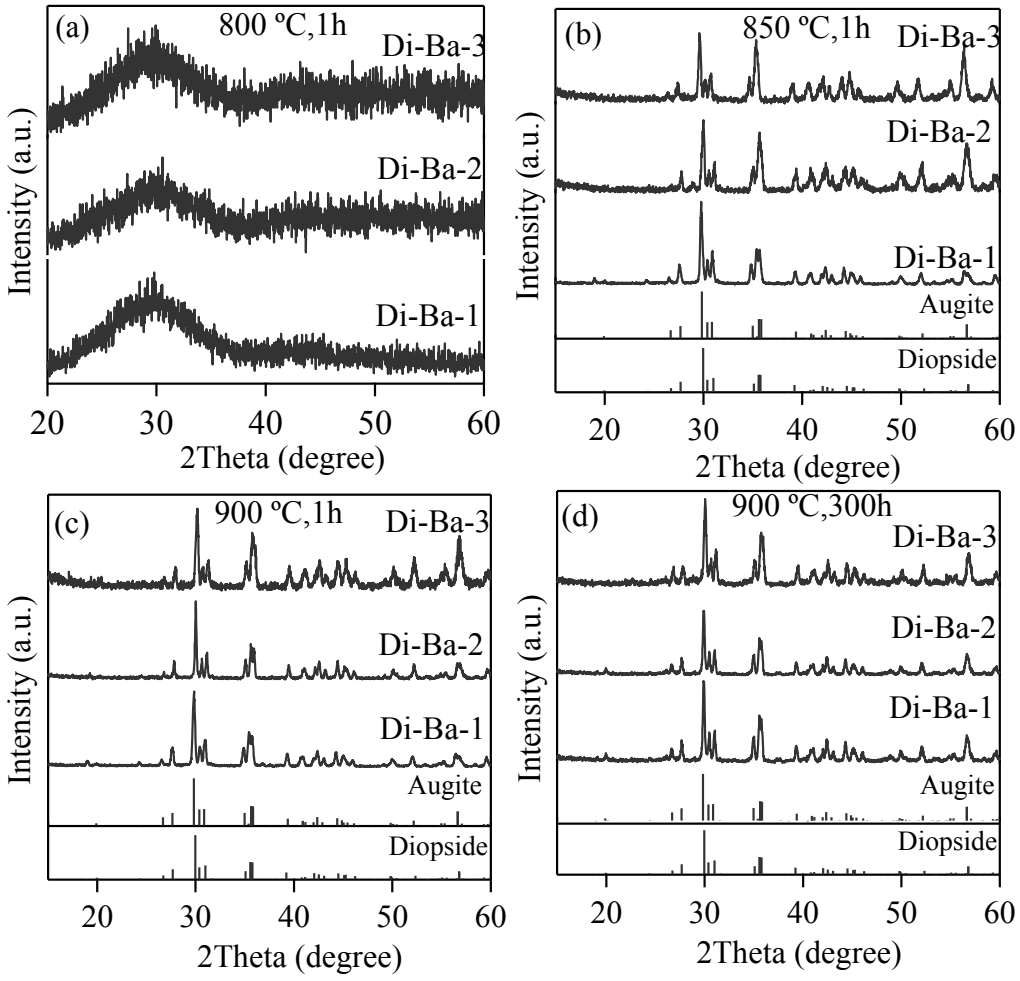

Fig.4.1.2: XRD spectra of the investigated glass powders at different temperatures (a) 800 ºC for 1 h, (b) 850 ºC for 1 h, (c) 900 ºC for 1 h, (d) 900 ºC for 300 h

Well–sintered dense glass–powder compacts were obtained after heat treatment at 800 ºC. There were no evidences of deformation or formation of open porosity on further heat treatment in the interval 800–900 ºC, as confirmed by the steady increases in density, shrinkage and bending strength (Table 4.1.3). Fig. 4.1.2 presents X–ray diffractograms of the sintered glass powder compacts depicting the evolution of crystalline phases after with change in temperature. The samples were still amorphous after heat treatment at 800 ºC (Fig. 4.1.2a). Diopside (Di: $CaMgSi_2O_6$) solid solution crystallized as the only phase in all the GCs at both 850 ºC (Fig. 4.1.2b) and 900 ºC for 1 h (Fig. 4.1.2c). The standard diffraction patterns of Augite ($CaMg_{0.7}Al_{0.6}Si_{1.77}O_6$, ICDD: 78–1392) and diopside ($CaMgSi_2O_6$; ICDD: 078–1390) are presented for comparison in Fig. 4.1.2. Fig. 4.1.2d presents XRD diffractograms of the glass powder compacts at 900 ºC for 300 h suggesting a relatively good stability of phases upon prolonged isothermal heat treatment.

Table 4.1.3: Properties of sintered glass–ceramics produced from glass–powder compacts after heat treatment at different temperatures for 1 h.

	800 ºC	*850 ºC*	*900 ºC*
	Shrinkage (%)		
Di–Ba–1	14.96±0.2	15.09±0.1	15.85±0.1
Di–Ba–2	15.08±0.3	15.51±0.2	15.31±0.1
Di–Ba–3	16.11±0.2	16.29±0.2	16.53±0.1
	Density (gcm^{-3})		
Di–Ba–1	2.98±0.005	2.99±0.003	3.08±0.006
Di–Ba–2	3.01±0.002	3.13±0.001	3.13±0.003
Di–Ba–3	3.04±0.001	3.19±0.002	3.19±0.002
	Mechanical strength (MPa)		
Di–Ba–1	81±8	123±12	172±4
Di–Ba–2	80±12	141±3	164±1
Di–Ba–3	99±5	148±9	184±9

The CTE values of the GCs sintered at 900 ºC for 1 h and 300 h are presented in Table 4.1.4. In general, the CTE of GCs sintered at 900 ºC for 1 h varied in the range (9.7–10.9) × 10^{-6} K^{-1} while after long heat treatment at 900 ºC for 300 h it changed in the interval (9.7–10.6) × 10^{-6} K^{-1}. The GCs Di–Ba–1 and Di–Ba–2 exhibited trend towards decreasing CTE while CTE of the Di–Ba–3 increased after isothermal heat treatment at 900 ºC for 300 h.

Table 4.1.4: CTE (±0.1) × 10^{-6} K^{-1} (200 – 700 ºC) of the glass–ceramics produced at different conditions.

	900 ºC, 1h	*900 ºC, 300h*
Di–Ba–1	10.4	9.8
Di–Ba–2	10.9	9.7
Di–Ba–3	9.7	10.6

Fig. 4.1.3a and 4.1.3b shows the SEM images of the interfaces between Crofer22APU/glass for Di–Ba–1 and Di–Ba–2 glasses along with the corresponding EDS mappings of the relevant elements existing at the interface after heat treatment at 900 ºC for 1 h in air. All the GC seals bonded well to Crofer22APU metallic interconnect, no gaps were observed, and the investigated interfaces showed homogeneous microstructures over their entire cross–sections of the joint. Fig. 4.1.3 (down figures) presents the elemental distribution profiles for Cr, Fe, Si, Al, La, Ca and Mg elements along the interface of Di–Ba–1 GC/Crofer22APU and Di–Ba–2 GC/Crofer22APU. The analysis of element mapping and elemental profiles confirmed formation of a smooth interface between investigated GC seals and SOFCs Crofer22APU metallic plate. Neither spinal nor chromium oxide layers were detected at the interfaces by SEM/EDS analyses, within the limits of experimental uncertainty.

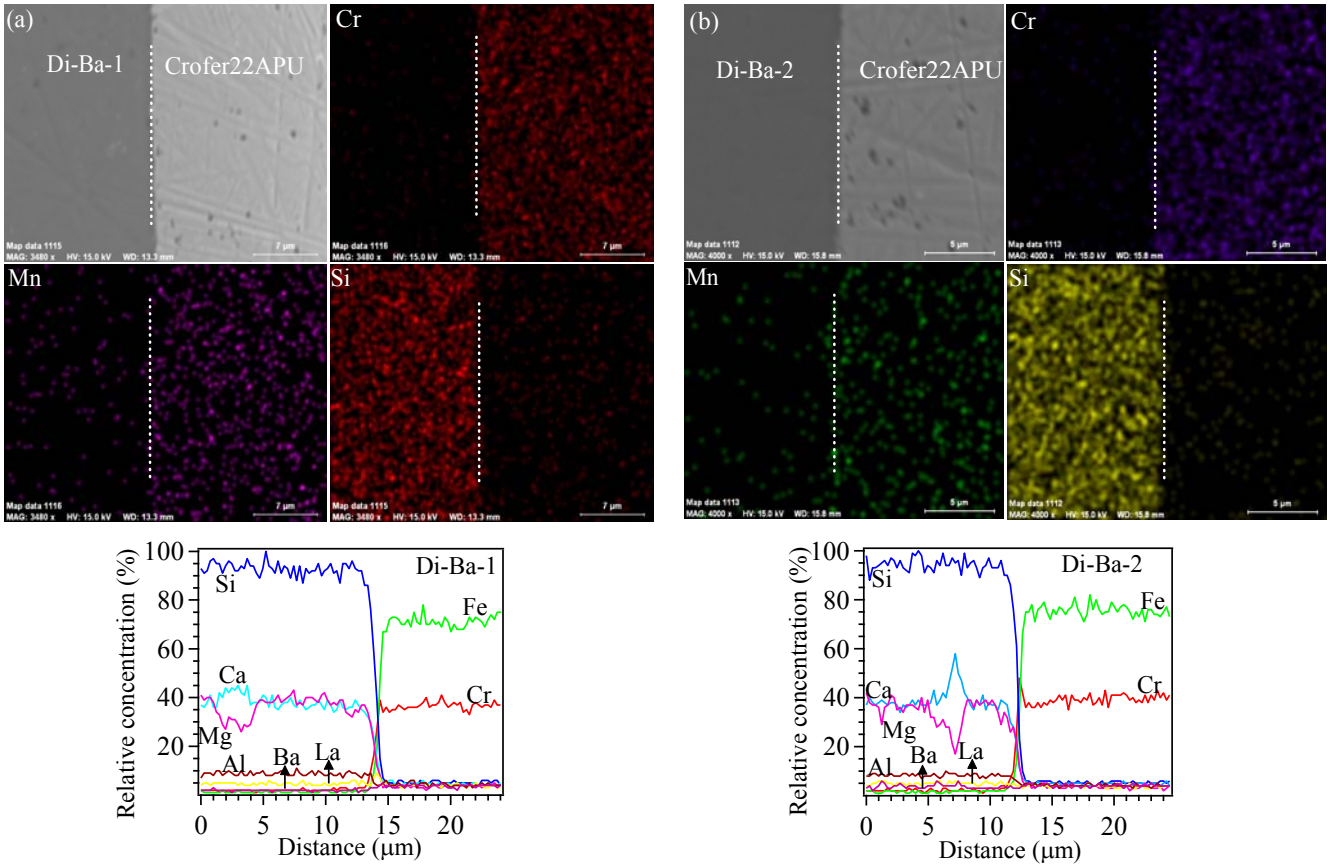

Fig.4.1.3: (a) Microstructure (SEM) and EDS element mapping of Cr, Mn, and Si at interface between (a) Di–Ba–1glass & Crofer22APU and (b) Di–Ba–1glass and Crofer22APU. Down figures represents EDS line profile for diffusion of Cr, Fe, Ca, Mg, Si, La, Al and Ba at the interface between glass Di–Ba–1 & Crofer22 APU and glass Di–Ba–2 & Crofer22 APU developed after heat treatment at 900 ºC for 1 h. (White dotted line indicates the interface between the Croffer22APU and the glass–ceramics).

The impedance spectra of the studied GC materials (Fig. 4.1.4) are more complex with respect to other candidate sealants tested in previous works (e.g. [128]). The form of the spectra, their characteristic frequencies and estimated capacitances suggest the presence of two contributions attributed to the crystalline and glassy phases; a small electrode tail is also visible in the low–frequency limit. The total electrical resistivity corresponds therefore to the sum of the bulk contributions. Although more detailed

studies focused on dielectrical properties of the GC constituents and relevant interfacial phenomena are necessary, the observed behaviour indicates, in general, substantial compositional differences between the crystallized and glassy phases in the GCs. On the other hand, whatever the microscopic mechanisms, the impedance spectra unambiguously showed that the electrical resistivity of the studied GCs is high enough for the SOFC applications. For example, at 1073 K the resistivity varies in the range 5 – 10 MOhm × cm, enabling good isolation between the fuel cell components. Comparison of the impedance spectroscopy data collected in different atmospheres showed also that the conductivity is independent of the oxygen partial pressure and humidity, again in accordance with the general requirements to the SOFC sealants.

As for other GCs, the temperature dependencies of electrical conductivity of the studied materials (Fig. 4.1.5) are described by a standard Arrhenius model:

$$\sigma = \frac{A_0}{T}\exp\left(\frac{E_a}{RT}\right) \qquad 4.2.1$$

where E_a is the activation energy and A_0 is the pre–exponential factor. The calculated activation energies are listed in Table 4.1.5. Increasing content of $BaSi_2O_5$ leads to lower conductivity values and higher activation energy. Irrespectively of the role of alkaline–earth cations, comparison of the conductivity values observed for these three of GCs shows that the effect of NiO additive on the electrical properties is negligible, as expected due to very low concentration of nickel.

Table 4.1.5: Activation energies for the total conductivity of glass–ceramics sealants in air, and their statistical errors

	T, K	E_a, *kJmol*$^{-1}$
Di–Ba–1	973–1123	140±2
Di–Ba–2	873–1123	178±3
Di–Ba–3	973–1123	173±3

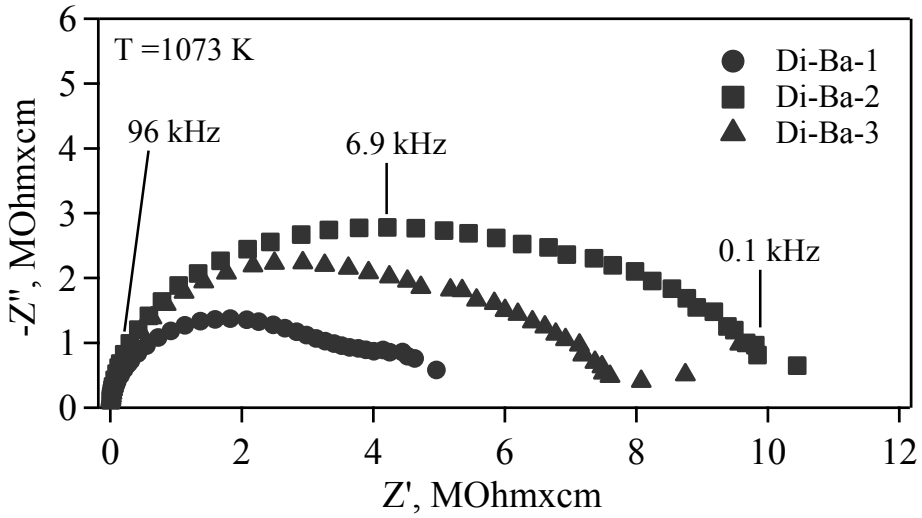

Fig. 4.1.4: The impedance spectra of the studied glass–ceramics materials

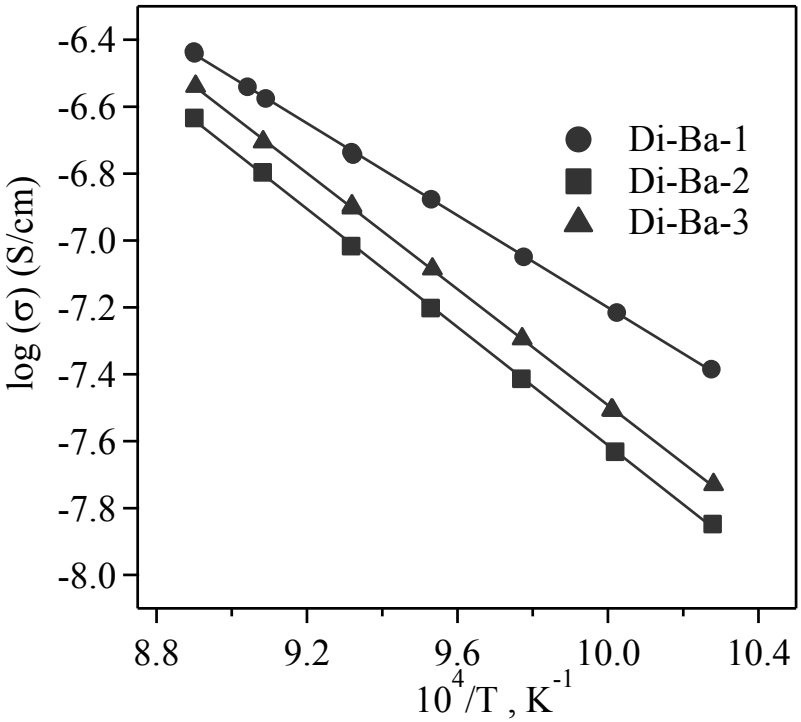

Fig. 4.1.5: The temperature dependencies of electrical conductivity of the studied materials

4.1.3 Discussion

In the present study particular attention has been focused on the determination of CTE of GC seals at different heat treatment conditions and the interaction of seal glass with the metallic interconnect–Crofer22APU. No specific trends were observed in the variation of CTE with glass composition. Composition Di–Ba–1 demonstrated relatively good stability in the CTE values during long term exposition at 900 ºC for 300 h although a slightly decreasing trend was observed. More significant changes were revealed in other investigated compositions (Table 4.1.4). In general, CTE of investigated GCs is correlated quite well with those of ceramic electrolyte, 8YSZ (~10 × 10^{-6} K^{-1}) and metallic interconnect, Crofer22APU (~11.4–12.5 × 10^{-6} K^{-1}) [21, 23, 137]. Further, relatively higher CTE values of GCs were recorded in this work compared to CTE of similar GCs synthesized previously [33, 117, 131, 137].

Regarding the chemical interactions of seals with interconnect, it is known that GCs generally show higher chemical stability than the glasses. Indeed, no appreciable diffusion of elements from the investigated GCs towards the Crofer22APU and vice versa was detected (Figs. 4.1.3). No interfacial layers, especially either Cr– or Ba–rich, that are detrimental due to their high CTE, were observed. Further, the investigated interfaces showed a homogeneous microstructure over the entire cross–section of the joint without gaps formation.

Additionally, all experimental GCs featured high density and mechanical strength (Table 4.1.3) due to desired sequence of events when sintering precedes the crystallization that was confirmed by HSM and DTA results (Fig. 4.1.1). Generally, the sintering in all experimental glass powders proceeded in two stages, but the main stage with densification level 95–98% was accomplished at $T_{MS1,}$ i.e., before the onset of crystallization and therefore, resulted in well sintered and dense glass powder compacts. Overal, better properties were achieved for Di-Ba-1 glass compared to the G-10 glass. In addition Di-Ba-1 glass exhibited stable CTE values during prolonged heat treatment and bonded well without forming any interfacial reactions. Therefore, Di-Ba-1 glass was selcted for further experiments as a sealant for SOFCs.

4.2 Diopside – Ba disilicate glass–ceramic sealants for SOFCs: enhanced adhesion and thermal stability by Sr for Ca substitution

4.2.1 Introduction

A choice of an appropriate GC sealant material is essential for developing reliable planar SOFCs. In this regard special attention was drawn to CTE of a parent glass that should be nearly equal to CTE of respective crystallized material. This would ensure appropriate adhesion of glass powder to anode, cathode and interconnect material during cell stack sealing procedure. Another critical issue is achieving stability GC's phase composition at prolonged heat treatment to get mechanical integrity of a pSOFC stack at operating conditions.

The literature survey evidenced that changing the thermal properties might be achieved by introducing SrO oxide in the silicate glass network. Ojha *et al.*[87] reported that SrO modified the network of Al_2O_3–B_2O_3–SiO_2–La_2O_3 glasses resulting in CTE 9 × 10^{-6} K^{-1}. Kumar *et al.*[86] studied the MgO/SrO–based borosilicate glasses and observed that SrO containing glasses exhibited higher CTE in comparison to MgO–based glasses. Mahapatra *et al.*[144] developed SrO–La_2O_3–Al_2O_3–SiO_2 (SABS–0) based glass with all the desired thermo physical properties. Kaur *et al.* [82] studied SrO/BaO–B_2O_3–La_2O_3–SiO_2 system and reported that SrO contain glass seals have shown high hermeticity and structural integrity with Crofer 22APU even after prolonged heat–treatment duration of 750 h at 850 ºC whereas BaO glass seal exhibited substantial number of pores after prolonged heat–treatment. In a more recent study, Sherma *et al.* [79] evaluated SrO–BaO based aluminosilicate glasses with P_2O_5 as a nucleating agent and claimed that Ba_2SiO_4, $BaAl_2Si_2O_8$, and Sr_2SiO_4 crystalline phases developed at 800 ºC were not detrimental for high temperature sealing applications.

The very promising glass composition Di−Ba−1 discussed in previous section was adopted as the starting point for synthesis new series of glasses and was developed by partial substitution Sr for Ca in the same composition aiming at (i) tailor CTE of parent glass and crystallized material; (ii) improving the wetting behaviour of the sealants via reducing viscosity of the glasses in the deformation temperature interval; and (iii) achieving stable thermo–mechanical properties of sintered glass–powder compacts. A

more in deep study was also performed at evaluating their suitability for applications as sealants for SOFCs by evaluating the thermal shock resistance of the sealant/oxide electrolyte (SOE) pair joints, using various SOE ceramic compositions.

4.2.2 Results and discussion

4.2.2.1 XRD analysis and thermal properties

Table 4.2.1 presents the detail composition of the glasses. All the five glass compositions were prone for easy casting after 2 h of melting at 1580 ºC, resulting in homogeneous and transparent glasses. With respect to the colour, the glasses exhibited dark honey colour due to the presence of NiO. The XRD amorphous nature of the quenched glasses and frits was confirmed by XRD analysis.

Table 4.2.1: Chemical composition of glasses

	CaO	*MgO*	*BaO*	*SrO*	Al_2O_3	La_2O_3	SiO_2	B_2O_3	*NiO*
Sr–0.0									
Wt%	21.09	16.84	1.36	0.00	2.13	6.81	48.77	2.00	1.00
Mol%	22.14	24.60	0.52	0.00	1.23	1.23	47.79	1.69	0.79
Sr–0.1									
Wt%	18.36	16.5	1.36	4.24	2.09	6.67	47.79	2.00	1.00
Mol%	19.67	24.58	0.53	2.46	1.23	1.23	47.77	1.73	0.80
Sr–0.2									
Wt%	15.74	16.17	1.36	8.31	2.04	6.53	46.84	2.00	1.00
Mol%	17.19	24.56	0.54	4.91	1.23	1.23	47.75	1.76	0.82
Sr–0.3									
Wt%	13.23	15.85	1.36	12.22	2.00	6.40	45.94	2.00	1.00
Mol%	14.73	24.54	0.55	7.36	1.23	1.23	47.73	1.79	0.84
Sr–0.4									
Wt%	10.81	15.54	1.36	15.98	1.97	6.28	45.07	2.0	1.00
Mol%	12.26	24.52	0.56	9.81	1.23	1.23	47.71	1.83	0.85

The density and molar volume of glasses (Table 4.2.2) increased with additions of SrO. The values changed from 2.990 to 3.167 gcm^{-3}, with minimum and maximum values being registered for the parent and Sr–0.4 glass compositions, respectively (Table 4.2.2), i.e. variations are composition dependent and can be explained by atomic weight considerations. Due to the larger size of Sr ions (1.32 Å) as compared to Ca ions (1.14 Å), the substitution of SrO for CaO results in a larger cell volume and consequently large molar volume of the glasses. Sr is heavier than Ca (with atomic weights of 87.62 and 40.078 $gmol^{-1}$, respectively) and, therefore, the weight of the cell also increases with the increasing substitution of SrO in the glasses. In the present case, the increase in cell weight seems to dominate over the increase in cell volume, leading to higher density values for the SrO–substituted glasses.

Table 4.2.2: Density (gcm^{-3}), molar volume (MV) (cm^3mol^{-1}), and CTE ($\pm 0.1\times10^{-6}$ K^{-1}) (200–500 ºC) of glasses

	Density	*MV*	*CTE*
Sr–0.0	2.990±0.003	19.69±0.02	7.1
Sr–0.1	3.045±0.006	19.72±0.04	10.0
Sr–0.2	3.088±0.001	19.82±0.01	11.3
Sr–0.3	3.134±0.005	19.92±0.03	11.2
Sr–0.4	3.167±0.005	20.06±0.03	10.2

The CTE values for SrO–containing glasses varied in the interval (10.0–11.3) × 10^{-6} K^{-1} indicating that Sr for Ca substitution in pyroxene glasses enhances the CTE. This effect can be explained by the differences in bond lengths of Ca–O (2.38 Å) and Sr–O (~2.60 Å) groups [145]. The CTE significantly increased at first addition of SrO reaching the maximum when Sr replaced 20 and 30% of Ca with some decline at further SrO increment (Table 4.2.2).

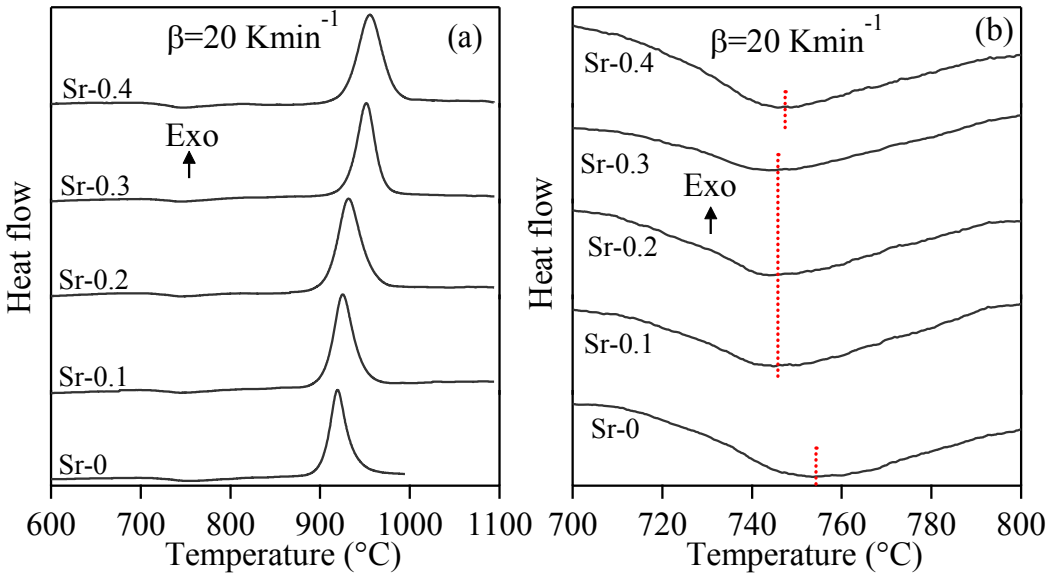

Fig. 4.2.1: DTA thermographs of investigated glasses at 20 $Kmin^{-1}$ within different temperature intervals: (a) 600–1100 ºC; (b) 700–800 ºC.

T_g of glasses presented in the Table 4.2.3 were obtained from the DTA thermographs (Fig. 4.2.1a and 4.2.1b) as the mid–point of the endothermic dip. Heating rate of 20 $Kmin^{-1}$ was used since T_g could not be accurately recorded at 5 and 10 $Kmin^{-1}$. T_g as a parameter related to the system viscosity [146], decreased in all the investigated SrO–containing compositions when compared to the parent glass (Table 4.2.3, Fig. 4.2.1). In general, strontium is a slightly larger ion than calcium, thus its incorporation expands the glass network and lowers the energy barrier for the glass to super cooled liquid transition, which results in T_g drop. Earlier Fujikura *et al.* [147] revealed non–linear variation T_g with substitution of Sr for Ca while O'Donnell *et al.* [148] revealed a linear trend.

4.2.2.2 Structure of glass: MAS–NMR

Fig. 4.2.2a shows ^{29}Si MAS–NMR spectra of the glass samples. All spectra had a broad peak centred at 81 ppm indicative of Q^2 silicate species, with Q^0, Q^1, Q^3 and Q^4 being below detectable levels. The chemical shift of the peak is invariant with increasing Sr substitution for Ca in the present glasses. Fig. 4.2.2b shows ^{27}Al MAS–NMR spectra of the glass samples, all of which had a broad, slightly asymmetric peak with a tail towards more negative ppm indicating existence of ^{IV}Al, ^{V}Al and ^{VI}Al coordination.

However, the signals originated from ^{IV}Al species at 55 ppm are dominating making ambiguous existence of ^{V}Al and ^{VI}Al groups. Fig. 4.2.2c shows ^{11}B MAS–NMR spectra of the glass samples, all of which had a broad resonance bands observed within the chemical shift range between 10 and –35 ppm. The peaks were centred at ca. –19, –14 and –9 ppm indicative of the majority of the boron atoms in three fold coordination, i.e. in the form of BO_3 triangles [135]. With respect to the structural changes of glass K. Fujikura *et al.*, investigated ^{29}Si MAS–NMR spectra of SrO containing glasses [147] and demonstrated that only 50 % Sr for Ca substitution influenced the silicate network. Similarly in the present study ^{29}Si MAS–NMR and ^{27}Al MAS–NMR spectra revealed no variation in the chemical shifts for silicon and aluminium atoms in all SrO–containing glasses including composition Sr–0.4 with 40 % Sr for Ca substitution. Therefore, further substitutions of Sr for Ca in the pyroxene structure will be attempted to reveal any possible effects occurred in the glass structure.

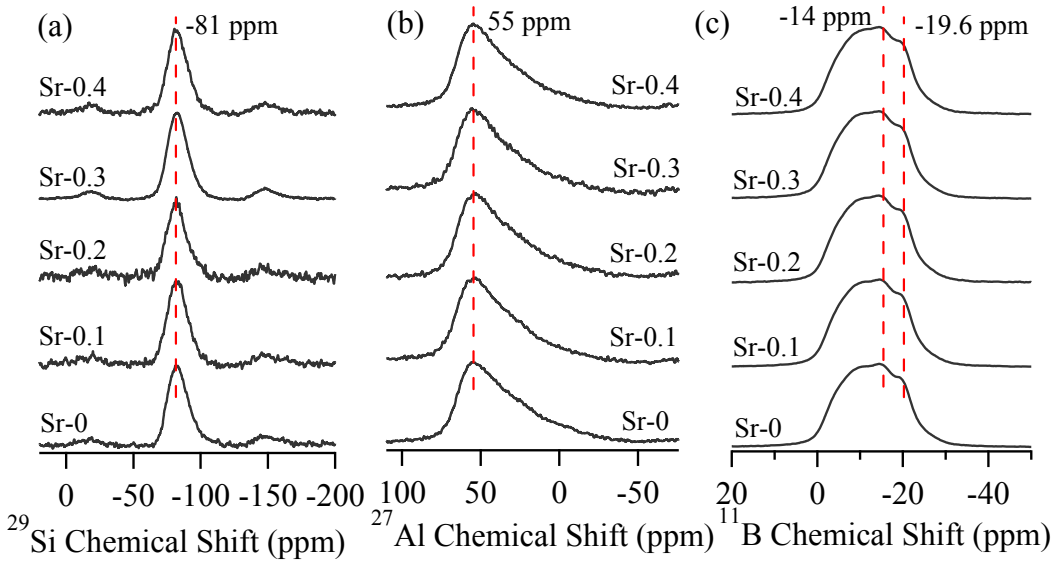

Fig. 4.2.2: MAS–NMR Spectra for (a) ^{29}Si; (b) ^{27}Al; and (c) ^{11}B Nuclei

4.2.2.3 Sintering and crystallization behaviour: DTA and HSM

Fig. 4.2.3 shows variation in the relative area and heat flow with respect to temperature as gained from HSM and DTA measurements, respectively at a heating rate of 5 Kmin^{-1}. Table 4.2.3 summarizes the values of the temperature of first shrinkage

(T_{FS}; $\log\eta = 9.1 \pm 0.1$; η is viscosity in dPa.s), temperature for maximum shrinkage (T_{MS}; $\log \eta = 7.8 \pm 0.1$), temperature for deformation (T_D; $\log \eta = 6.3 \pm 0.1$), temperature for half–ball (T_{HB}; $\log \eta = 4.1 \pm 0.1$), temperature for flow (T_F; $\log \eta = 3.4 \pm 0.1$), and ratio of the final area/initial area of the glass powder compact (A/A_0), as obtained from the HSM data at T_{MS} (Fig. 4.2.3), along with temperature for onset of crystallization (T_c), peak temperature of crystallization (T_p) as received from DTA of the glasses. The data as obtained from HSM and DTA (β=5 $Kmin^{-1}$) pertaining to sintering and devitrification behaviour of glasses that allow observation of the following trends:

1. With the initial replacement of SrO for CaO T_{FS} decreased from 770 to 761 ºC whilst increased from 761 to 781 ºC with further replacement.
2. All glasses exhibited two stage of sintering: the first sintering stage is accomplished at T_{MS1} while the second one at T_{MS2}. In all the compositions $T_{MS1}<T_c$, so that sintering precedes crystallization. This feature will ensure production of well sintered and mechanically strong glass powder compacts. The second stage of densification occurred in competition with crystallization but ended very close to T_p, i.e. peak temperature of crystallization.
3. The values of sintering ability S_c for the SrO containing glasses varied in the interval 19–35 ºC and those are considerably higher compared to SrO–free parent glass (S_c = 7 ºC).
4. The DTA thermographs of the experimental glasses exhibited single crystallization exothermic curve. This signifies that the GC is formed either as a result of single phase crystallization or of an almost simultaneous precipitation of more than one crystalline phase. Moreover, values of T_c and the peak temperature of crystallization (T_p) exhibited a tendency to increase with increasing strontium content in the glasses.
5. Fig. 4.2.4 presents the photomicrographs of all the investigated glasses depicting the changes in geometric shape of the glasses with respect to temperature as obtained from HSM. The deformation temperature (T_D) of the glasses show linear trend to decrease from 900 to 855 ºC with introduction SrO.

6. SrO content in the glasses significantly influenced on the half–ball (T_{HB}) and flow (T_F) temperatures. With increasing SrO content T_{HB} and T_F reduced from 1305 to 1207 ºC and from 1341 to 1228 ºC, respectively.
7. Values of A/A_0 ranged from 0.64 to 0.71 (Table 3) implying towards good densification level (95–98%) [128].

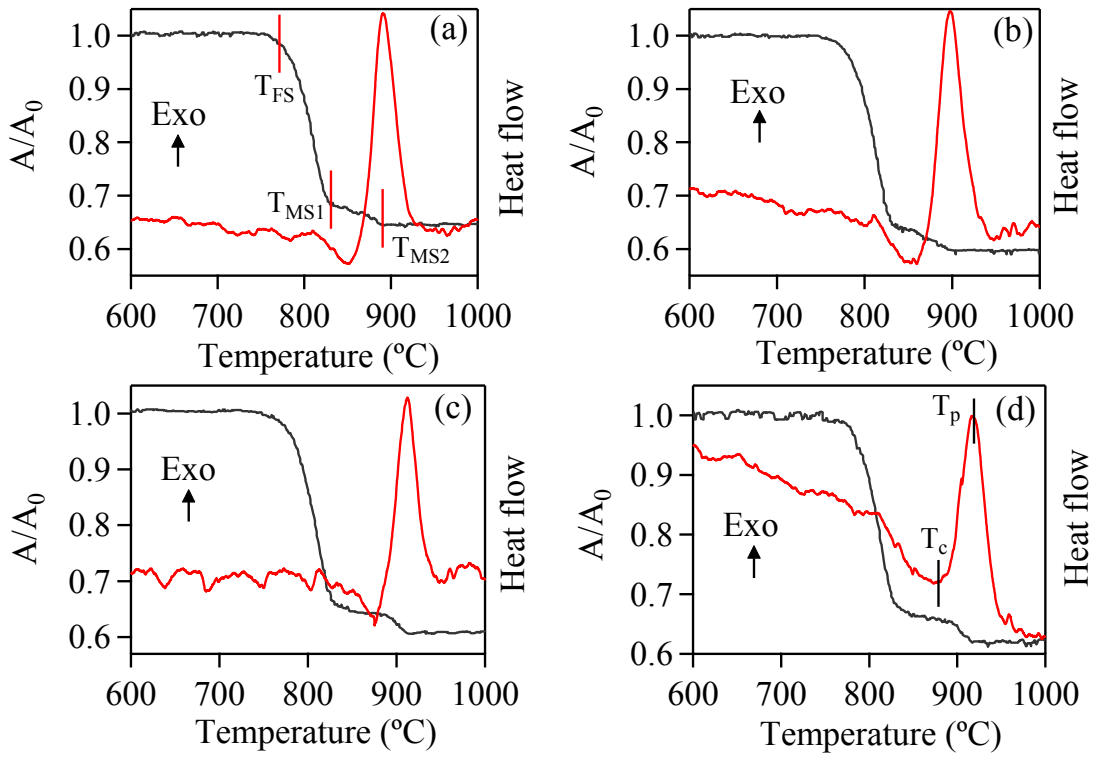

Fig.4.2.3: DTA–HSM thermo graphs of the investigated glasses at 5 $Kmin^{-1}$: (a) Sr–0.1; (b) Sr–0.2; (c) Sr–0.3; and (d) Sr–0.4.

Fig. 4.2.5 represents the viscosity curves for the present investigated glasses measured by least squares fitting of HSM characteristic points using the Vogel–Fulcher–Tammann (VFT) relation $log\,\eta = A + B/(T - T_0)$ [120, 121, 149] where η is the viscosity and T is the temperature. The coefficients A, B and T_0 deduced from the fitting are reported in Table 4.2.4

Table 4.2.3: Thermal parameters measured from DTA and HSM (ºC)

	Sr–0.0	*Sr–0.1*	*Sr–0.2*	*Sr–0.3*	*Sr–0.4*
T_g±2	753	744	744	744	748
T_{FS}±8	770	767	772	773	781
T_{MS1}±5	837	831	835	847	848
T_{MS2}±5	882	892	902	913	916
T_C±2	844	850	859	876	883
T_P±2	883	891	898	912	917
S_c (=T_c–T_{MS})	7	19	24	29	35
T_D±5	900	880	877	869	875
T_S±5	–	–	–	1213	900
T_{HB}±8	1305	1280	1258	1229	1207
T_F±10	1341	1327	1290	1260	1228
A/A_0 at T_{MS1}±0.02	0.65	0.68	0.64	0.65	0.67

It was depicting that addition of SrO enhances glass sintering ability considerably. The higher values of S_c (Table 4.2.3) correspond to delay in nucleation and thus provide a wider processing window for a glass composition to attain maximum densification. Moreover, characteristic temperatures T_D, T_S T_{HB} and T_F decreased with increment of SrO (Table 4.2.3) that correlates well with the trends observed from the corresponding viscosity curves (Fig. 4.2.5). Additionally, incorporation of SrO in the pyroxene glasses reduced the viscosity of glasses close to ~10^6 dPa.s at 900 ºC (Fig. 4.2.5). This is a quite decisive factor since within the temperature range of 850–900 ºC that is usually considered for joining of SOFC metallic/ceramic components by a glass/GC sealant [66, 150], glass viscosity must be low enough, e.g. ~10^6 dPa.s at 900 ºC.

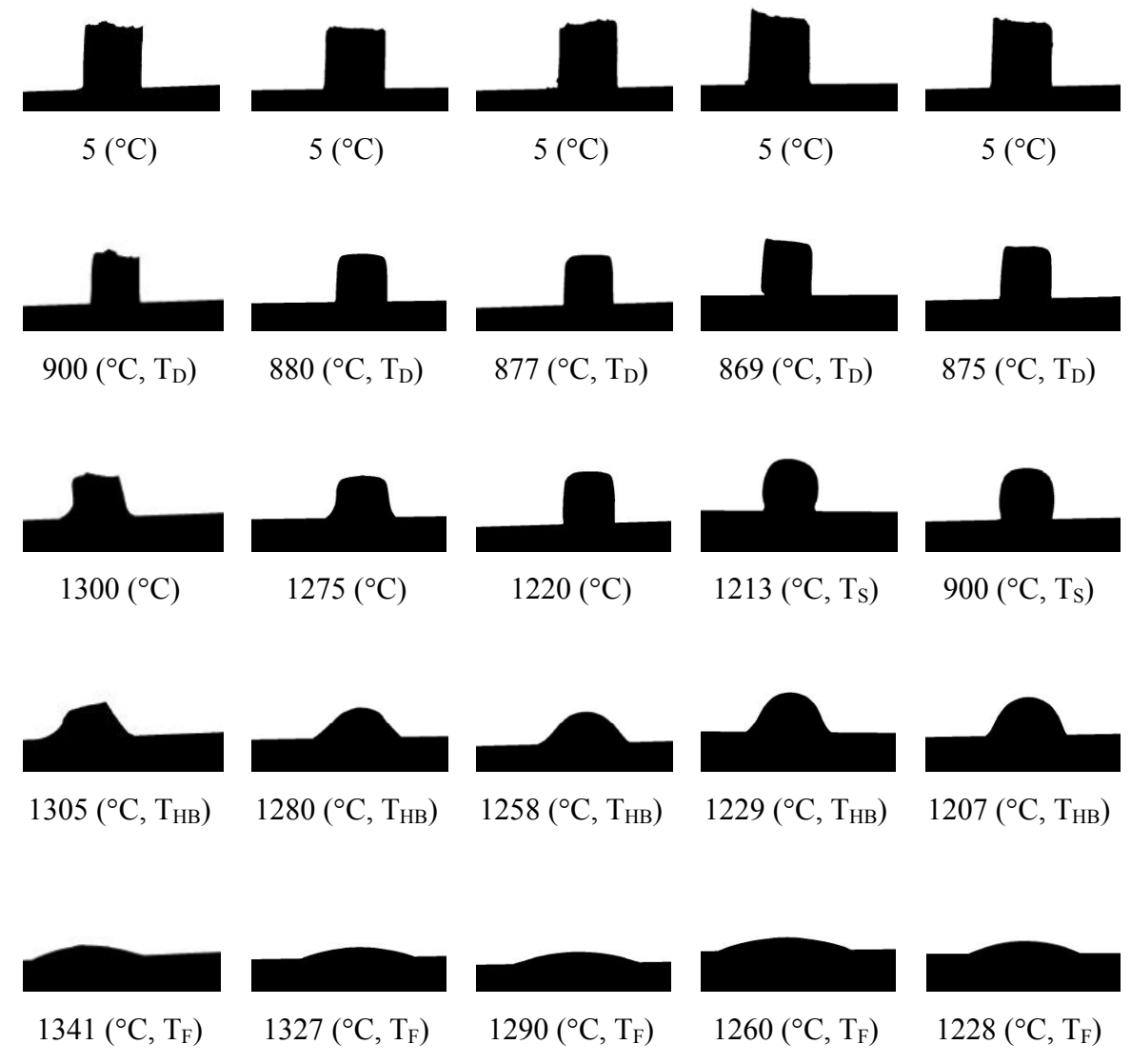

Fig. 4.2.4: HSM images of cylindrical glass–powder compact on alumina substrate at various stages of heating cycles.

Table 4.2.4: A, B and T_0 constants of the VFT equation, calculated from linear regression analysis, and viscosity at 900 ºC.

	A	*B*	T_0	$\log\eta$ *(dPas) at 900 ºC*
Sr–0.0	0.07	2182	773	6.5
Sr–0.1	0.38	1797	809	6.3
Sr–0.2	0.32	1735	824	6.3
Sr–0.3	0.15	1794	821	6.2
Sr–0.4	0.14	1667	846	6.2

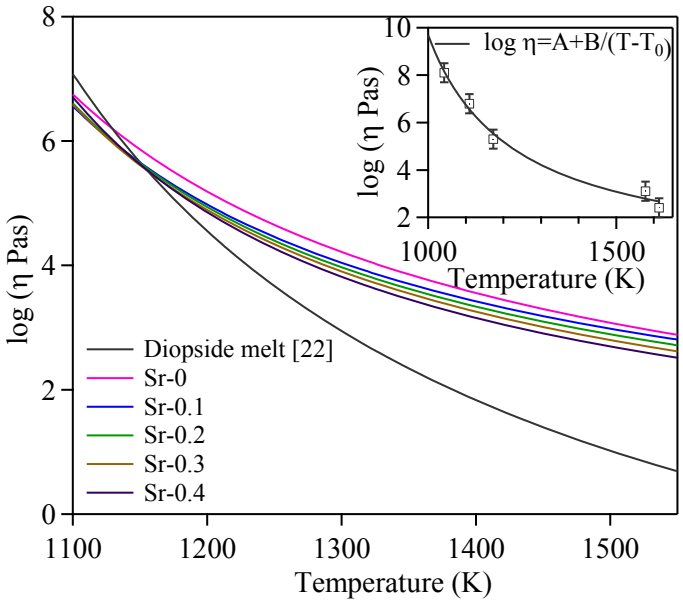

Fig. 4.2.5: Comparison of viscosity curves with diopside melt viscosity curve ($\log\eta$ = –4.27 +3961 K/(T–751K) [149]). Inset figure represents the viscosity curve derived from HSM characteristic viscosity points for Sr–0 glass.

4.2.2.4 Stability of crystalline phases

Fig. 4.2.6a presents X–ray diffractograms of the sintered glass powder compacts at 900 ºC for 1 h depicting the evolution of crystalline phases. Di solid solution (SS) crystallized as the only phase in the Sr–0 GC whilst Sr–containing glasses exhibited a tendency to form Sr–contain Di SS phases. The standard diffraction patterns of are also

presented for comparison in Fig. 4.2.6a. Detailed discussion regarding Sr occupancy at Ca sites in diopside crystal structure has been proposed for future work.

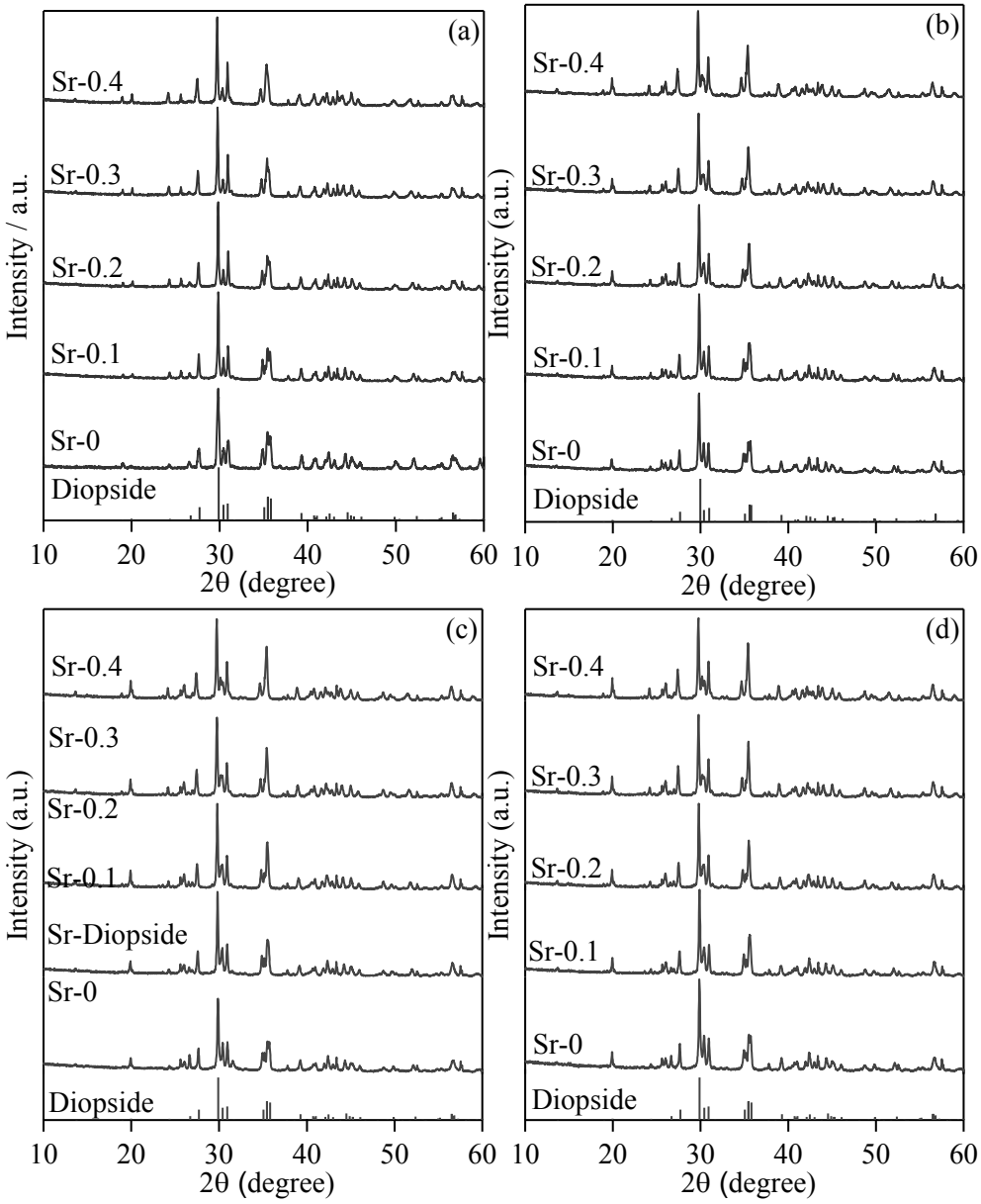

Fig. 4.2.6: XRD pattern of glass–ceramics sintered at 900 ºC for: (a) 1 h; (b) 250 h; (c) 500 h; and (d) 1,000 h.

The evolution of crystalline phases in the glass–powder compacts sintered at 900 ºC for 250 h, 500 h and 1,000 h is demonstrated in the X–ray diffractograms (Fig. 4.2.6 b–d). Table 4.2.5 presents the qualitative as well as quantitative analysis of the crystalline

phases present in all the investigated GCs as obtained from XRD analysis adjoined with Rietveld–R.I.R technique. The calculated diagrams are based on crystallographic structure models, which also take into account specific instrument and sample effects.

Table 4.2.5: Results of Rietveld R.I.R. technique

	Di/Sr–contain Di SS	*Amorphous*	χ^2
1 h			
Sr–0	95.6	4.4	3.67
Sr–0.1	84.5	15.5	1.87
Sr–0.2	79.4	20.6	2.35
Sr–0.3	79.7	15.3	2.52
Sr–0.4	83.7	16.3	2.74
250 h			
Sr–0	97.3	2.7	3.86
Sr–0.1	98.0	2.0	3.63
Sr–0.2	92.3	7.7	5.52
Sr–0.3	94.6	5.4	4.87
Sr–0.4	92.3	7.7	5.90
500 h			
Sr–0	98.0	2.0	4.37
Sr–0.1	94.1	5.9	4.73
Sr–0.2	91.4	8.6	6.05
Sr–0.3	93.4	6.6	5.7
Sr–0.4	93.2	6.8	5.8
1,000 h			
Sr–0	99.7	0.3	3.89
Sr–0.1	78.8	21.2	5.38
Sr–0.2	99.2	0.8	6.59
Sr–0.3	90.1	9.9	7.14
Sr–0.4	86.3	13.7	6.64

The parameters of this model have been refined simultaneously using least–squares methods in order to obtain the best fit to all measured data. By least–squares refinement, a so–called figure–of–merit function R has been defined, which describes the residual (agreement) between observed and calculated data [151]. It is noteworthy that many different statistical R factors have been proposed for judging the quality of a Rietveld refinement. The R factors show the mean deviation in accordance with the model used in per cent. The ‘‘profile R–factor”, R_p, and ‘‘weighted profile R–factor”, R_{wp}, for all the refinements are well within the limits of experimental accuracy.

Prolonged heat treatment at 250, 500 and 1,000 h resulted Di SS as the major crystalline phase in Sr–0 GC. Introduction of SrO in the glasses resulted in Sr–contain Di SS. No other impurity crystalline phases were developed in both Sr−free and Sr−contain glasses during heat treatment at 850 ºC for 1000 h. Irrespective of sintering time, increasing SrO content in the glasses initiated growth of the glassy phase in all the GCs. The residual glassy phase is highest for GCs Sr–0.2 (20.6 wt. % for 1 h, 7.7 wt. % for 250 h, and 8.6 wt. % for 500 h) and Sr–0.1 glass (21.2 wt. % for 1,000 h). Sintered Sr–0 GCs contain the lowest amount of glassy phase except samples sintered at 900 ºC for 250 h. The positive feature of these GCs is their stable phase assemblage with 85% crystallized fraction after 250 h of heat treatment and stability of crystalline phase up to 1000 h. Whereas the SrO–containing glasses reported by Chou et al. [77, 114] underwent a continuous crystallization process along the aging time up to 2000 h. The non–variable phase assemblage of the investigated glasses ensures their thermal stability and suitability as sealing materials.

4.2.2.5 Glass–ceramic properties

According to the values summarized in Table 4.2.6 glass powders in which crystallization precedes sintering result in porous and mechanically weak GCs exhibit a small shrinkage. In the present scenario, the values of shrinkage varied between 12.5% and ~16% and confirm the good densification of glass powder compacts. Shrinkage decreases after first addition of SrO in the parent glass and then increases reaching the maximum for Sr–0.4 composition. In general, SrO–free parent composition exhibited the

highest value of shrinkage among investigated compositions independent on the dwell time.

Table 4.2.6 presents the mechanical strength of the produced GCs with respect to the sintering time. In general, bending strengths of the GCs decreased with increasing SrO and as well as sintering time that may be due to the formation of higher amount of residual glassy phase (Table 4.2.5). Thus, Sr–0 GCs attained maximum bending strength values varied between 156–172 MPa whilst Sr–0.4 GCs demonstrates minimum values of 125–115 MPa. However, compared to parent (SrO–free) GCs SrO–containing compositions exhibited remarkable stability in retaining mechanical strength after prolonged heat treatments. Thus, after 1,000 h heat treatment at 900 ºC decrease in bending strength attained 9.3 % for Sr–0, 6.3% for Sr–0.1, 4.0%, for Sr–0.2, 2.9 %, for Sr–0.3 and 4.8% for Sr–0.4. The values of average flexural strengths for all the GCs are about 1.5–2.5 times higher than those reported for G–18 glass (51 MPa) [106], GC–9 glass (41–78 MPa) [36], H–sintered bar (55 MPa) [152] and B–sintered bar (91 MPa) [152].

The CTE values of the GCs sintered at 900 ºC for 1 h, 250 h, 500 h and 1,000 h are presented in Table 4.2.6. Sr–0.3 GC exhibited highest CTE (11.2×10^{-6} K^{-1}) among GCs sintered at 900 ºC for 1 h. No significant changes in thermal expansion were observed in SrO–containing GCs after long heat treatment at 900 ºC for 1,000 h compared to the parent GCs. Except for Sr–0 heat treated for 250–1,000 h and Sr–0.3 sintered for 1 h, the CTE values vary in the narrow range of $(9.8–10.8)\times10^{-6}$ K^{-1}, which are compatible with those of common SOFC components.

To minimize thermal stresses during cell operation the differences in CTEs between interconnect and the seal glass should not exceed, in general, 1×10^{-6} K^{-1}. All the studied SrO–containing GCs exhibited their CTE in the range $(9.6–11.2)\times0^{-6}$ K^{-1} that are nearly equal to CTE of parent glasses $(10–11.3)\times10^{-6}$ K^{-1}. Considering CTE values for metallic interconnect (Crofer22APU; SanergyHT) varying in the range $(11–12)\times10^{-6}$ K^{-1}, and ceramic electrolyte (i.e. 8YSZ) to be $(10–12)\times10^{-6}$ K^{-1} both the parent glasses and corresponding GC composition Sr–0.2, Sr–0.3 and Sr–0.4 (Table 4.2.6) should be suitable for rigid glass/GC seals.

Table 4.2.6: Shrinkage (%), density (gcm^{-3}), bending strength (MPa) and CTE (±0.1) × 10^{-6} K^{-1} (200–700 ºC) data measured for the glass–powder compacts after sintering at 900 ºC for 1 h, 250 h, 500 h and 1,000 h.

	1 h	*250 h*	*500 h*	*1,000 h*
Shrinkage				
Sr–0.0	15.8±0.1	15.7±0.5	15.9±0.3	15.3±0.3
Sr–0.1	12.8±0.2	13.9±0.2	13.9±0.4	13.8±0.3
Sr–0.2	12.5±0.3	14.0±0.1	13.7±0.3	13.9±0.2
Sr–0.3	13.7±0.3	14.6±0.1	14.0±0.1	14.2±0.1
Sr–0.4	13.7±0.1	13.8±0.2	14.2±0.2	14.2±0.1
Density				
Sr–0	2.96±0.001	3.08±0.004	3.09±0.005	3.08±0.006
Sr–0.1	3.10±0.006	3.08±0.003	3.09±0.003	3.09±0.002
Sr–0.2	3.15±0.005	3.12±0.001	3.14±0.006	3.13±0.002
Sr–0.3	3.23±0.007	3.22±0.004	3.22±0.005	3.21±0.002
Sr–0.4	3.25±0.001	3.22±0.002	3.23±0.005	3.23±0.005
Bending Strength				
Sr–0.0	172±4	162±7	161±9	156±8
Sr–0.1	160±5	158±4	154±1	150±4
Sr–0.2	150±7	141±3	150±7	144±5
Sr–0.3	137±7	125±3	133±5	133±8
Sr–0.4	125±3	123±4	122±3	115±3
CTE				
Sr–0.0	10.4	9.2	10.4	9.60
Sr–0.1	10.8	10.6	10.0	10.1
Sr–0.2	10.2	10.8	9.8	10.8
Sr–0.3	11.2	9.9	10.0	10.4
Sr–0.4	10.3	10.5	10.4	10.7

4.2.2.6 Interaction studies

All the GC seals bonded well to SanergyHT/Crofer22APU metallic interconnect as well 8YSZ ceramic plate, no gaps were observed, and the investigated interfaces showed homogeneous microstructures over their entire cross–sections of the joint. Fig. 4.2.7a and 4.2.8a shows the SEM image of the interfaces between Sanergy HT/GC and 8YSZ/GC for Sr–0.3 glasses, along with the corresponding EDS mapping of the relevent

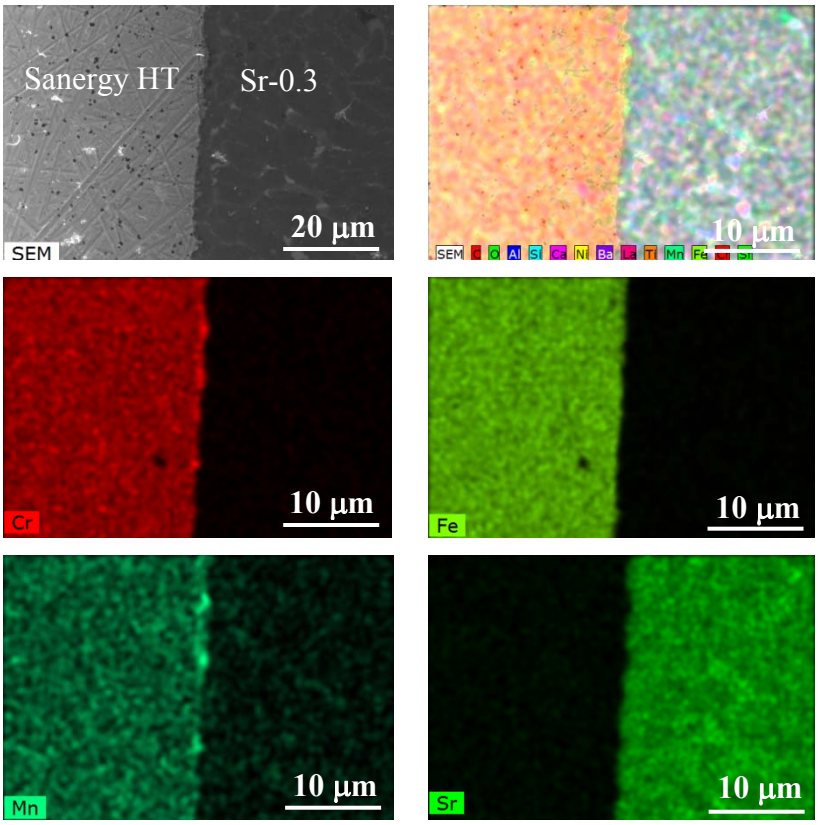

Fig. 4.2.7: SEM image and EDS element mappings for Cr, Fe, Mn and Sr at the interface between Sr–0.3 and Sanergy HT after heat treatment at 900 ºC for 1 h.

elements existing at the interface after heat treatment at 900 ºC for 1 h in air. Fig. 4.2.7b and 4.2.8b presents the elemental distribution profiles for Cr, Fe, Mn, Ni, Ba, La, Ca, Ti, Si, Al and Sr elements along the interface of Sr–0.3/SanergyHT and Y, Zr, Ba, La, Ca, Si, Al and Sr along the interface of Sr–0.3/8YSZ. Neither diffusion layers were detected at the interfaces by SEM/EDS analyses (Fig. 4.2.7c–f), within the limits of experimental uncertainty. Figure 4.2.9 shows the SEM images of the interfaces between Crofer22APU/GC and SanergyHT/GC for Sr–0.3 glass, along with the corresponding EDS elemental line profiles of the relevant elements existing at the interface after heat treatment at 850 ºC for 250 h in humidified atmosphere. The analysis of element mapping (not shown) and elemental profiles confirmed formation of a smooth interface between investigated GC seals and SOFCs Crofer22APU and Sanergy HT metallic plate. Neither spinel nor a chromium oxide layer and any other interfacial reactions were detected at the

interfaces by SEM/EDS analyses, within the limits of experimental uncertainty as was observed in case of SrO–containing glasses [25, 77, 114]. Further, no negative influence with respect to adhesion and cracking at the interface was observed for the Sr–containing GC sealants. Thus it can be concluded that the Sr–containing diopside glasses could be used within an SOFC stack for hermetic sealing.

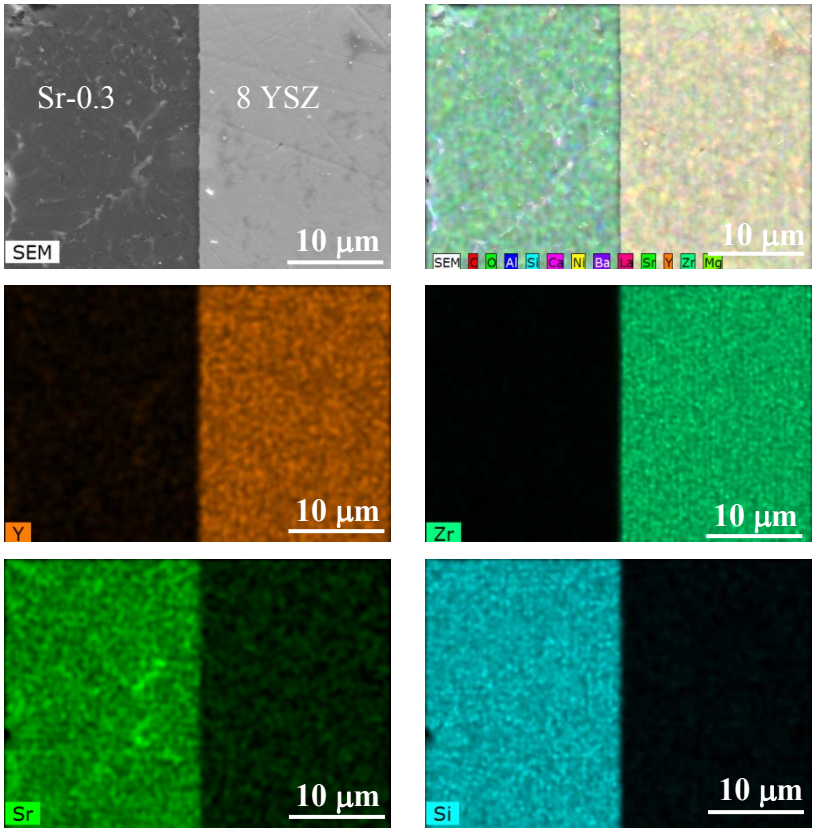

Fig. 4.2.8: SEM image and EDS element mappings for Y, Zr, Sr, and Si at the interface between Sr–0.3 and 8YSZ after heat treatment at 900 ºC for 1 h.

4.2.2.7 Electrical properties of the sealants

For all studied GCs, the Arrhenius dependencies of the total conductivity (Fig. 4.2.10) are linear, confirming that no phase changes take place after sintering at 900 ºC. Increasing strontium concentration leads to a higher conductivity, whilst the activation energy decreases from 246±7 down to 162±3 kJmol^{-1} (Fig. 4.2.11).

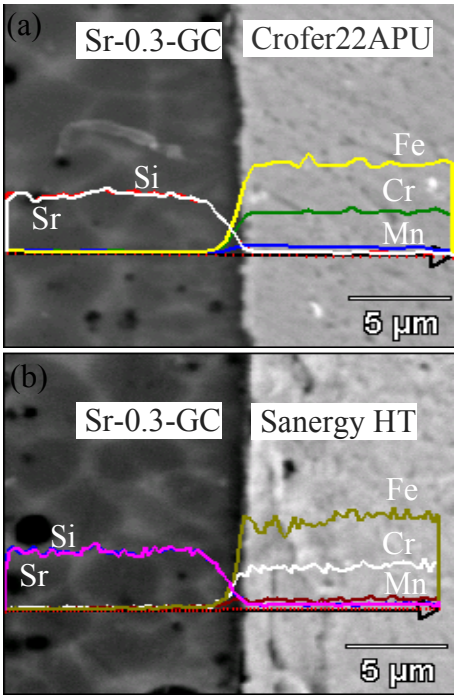

Fig. 4.2.9: (a) SEM image and elemental line profile at the interface of Sr–0.3 and Crofer22APU. And (b) SEM image and elemental line profile at the interface of Sr–0.3 and SanergyHT.

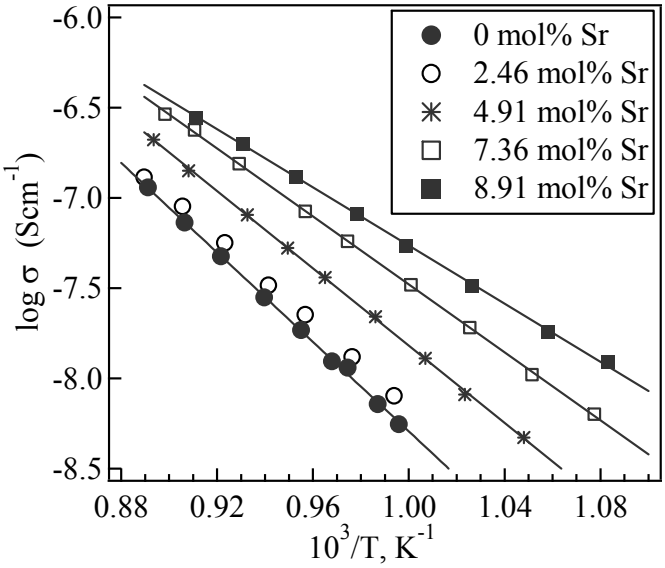

Fig. 4.2.10: Temperature dependencies of the total electrical conductivity in atmospheric air.

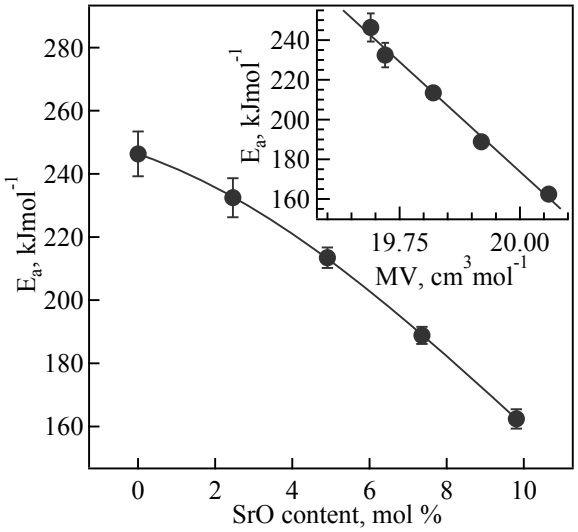

Fig. 4.2.11: Activation energy for the electrical conductivity of the studied glass–ceramics Inset shows the relationship between the total conductivity activation energy and molar volume.

Nonetheless, all the sealants possess excellent insulating properties; in the temperature range necessary for SOFC operation; their electrical resistivity is higher than 2 MOhm×cm. The linear relationship between the molar volume and conductivity activation energy (inset in Fig. 4.2.11) may suggest a dominant role of ionic charge carriers. Indeed, the ion transference numbers estimated by the electromotive force (EMF) method under air/ 10% H_2–90% N_2 gradient were found close to unity within the limits of experimental uncertainty. In accord with the very high level of the electrical resistance, this finding shows that NiO additive provides no significant electronic contribution to the conductivity. Although the EMF technique makes it impossible to determine the type of ionic charge carriers, the conductivity does not change when hydrogen or water vapour are present in the gaseous phase (Fig. 4.2.12b), thus indicating that protonic contribution is negligible. Furthermore, the oxygen permeation tests revealed no leakage fluxes through sintered gas–ceramics, again in agreement with their high electrical resistivity. The results on electrical resistivity of the Sr–0.3/8YSZ diffusion couples showed that no time degradation occurs at the SOFC operation temperatures, such as 800 ºC. One example is presented in Fig. 4.2.12a; except for data

scattering associated with high resistivity of the GC sealant (±2%), the electrical resistance exhibits no changes with time, within the limits of experimental error.

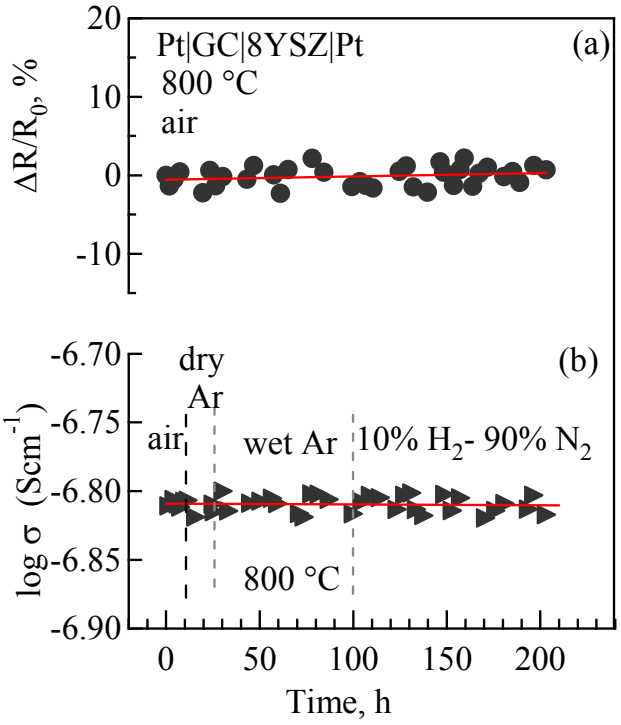

Fig. 4.2.12: Time dependencies of the relative variations of electrical resistance of Sr–0.3/8YSZ couple (a) in air and (b) total conductivity of Sr–0.3 glass–ceramics in various atmospheres, at 800 ºC.

4.2.2.8 Thermal shock resistance and oxygen leakage measurements

The thermal shock resistance tests performed using the Sr–0.3 glass demonstrated the good suitability of this composition for sealing of zirconia–based ceramics. However, further optimization would be required in the case of other electrolytes (CGO or LSGM). For the YSZ electrolyte, a good adhesion and a relatively low CTE mismatch provide sufficient stability during over 15 air–quenching cycles (Table 4.2.7) [153]. SEM showed no visible cracks at the GC/YSZ interfaces; as an example, Figure 4.2.13a presents one SEM image of Sr–0.3/YSZ assembly, which was partly cut and then fractured after 3 air–quenching cycles with T_{max} = 800 ºC. For gadolinia–doped ceria, however, the CTE is substantially higher, leading to excessive thermal stresses and failure under identical conditions (Table 4.2.7 and Figure 4.2.13b). A similar behaviour is observed for LSGM

electrolyte, although its average CTE is lower than that of doped ceria. Most likely, cracking in the latter case originates from structural transitions of the LSGM perovskite phase; the mechanical properties of LSGM ceramics are also, in general, worse compared to those of YSZ and ceria (e.g., see [127] and references cited). Thermal cycling of LSGM/Sr–0.3/CGO assemblies resulted in relatively large cracks (Figure 4.2.13c), followed by failure.

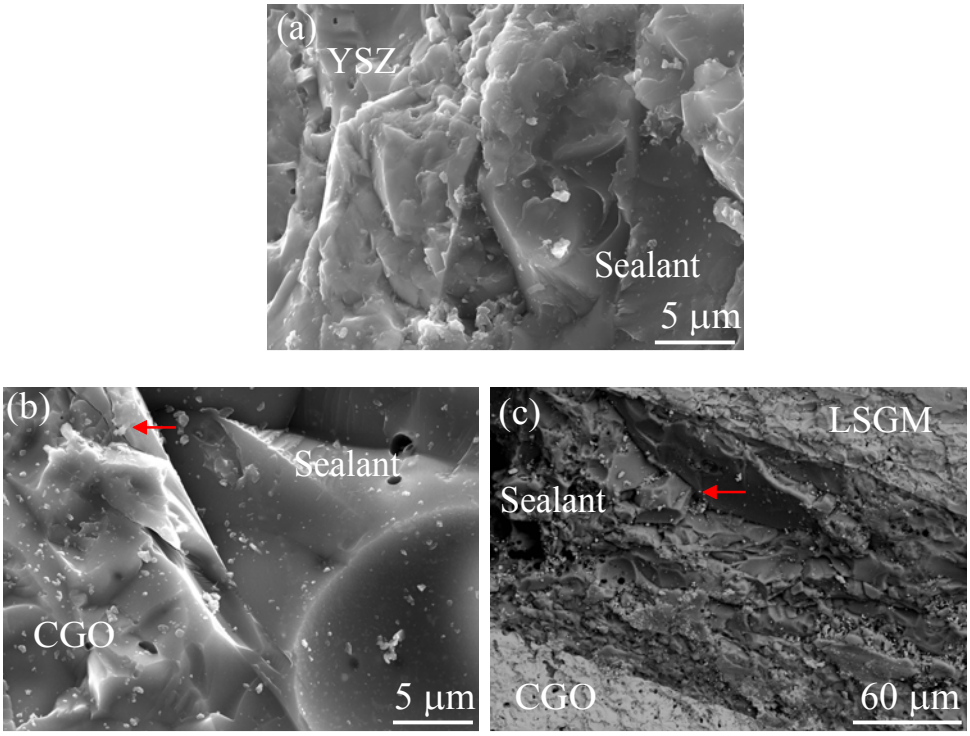

Fig. 4.2.13: (a)–(b) Typical SEM images of the interfaces between Sr–0.3 glass–ceramics sealant and various solid oxide electrolyte ceramics after 3 air–quenching cycles. The arrows show largest cracks developed at the interfaces.

Table 4.2.7: Average CTEs of solid oxide electrolyte (SOE) ceramics and thermal shock stability of SOE / glass–ceramics / YSZ assemblies sealed by Sr–0.3 glass–ceramics at 900 ºC.

Electrolyte	*Average thermal expansion coefficients*		*Number of*
	T ºC	*$\alpha \times 10^6$ K^{-1}*	*air–quenching cycles*
YSZ	25–1000	10.0	>15*
CGO	50–1000	12.5	4
LSGM	100–1000	11.1	3

* The cell remained gastight after 15 air–quenching cycles (T_{max} = 800 ºC)

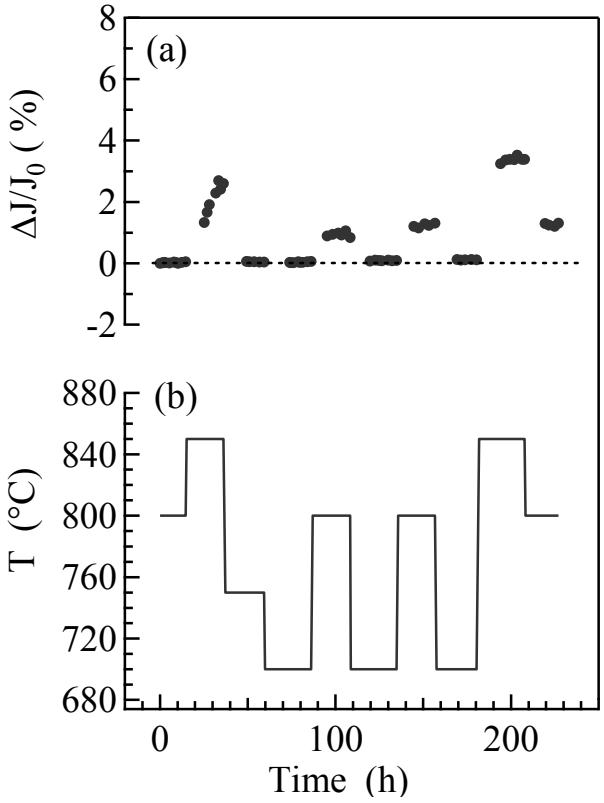

Fig. 4.2.14: Time dependence of the relative changes in oxygen leakage flux during thermal cycling of an electrochemical cell with dense YSZ membrane and Sr–0.3 sealant (a), and corresponding temperature variations (b).

The oxygen leakage tests were performed for the model cells comprising a dense YSZ membrane sealed by Sr–0.3 GCs onto tubular support of the same composition. The

experiments were carried out in the regime of periodic temperature variations in the range 700–850 ºC under large oxygen partial pressure gradient simulating the SOFC operation conditions, 0.21 atm / (10^{-21} –10^{-19}) atm. The results showed that the overall level of oxygen permeation is very low, close to the detection limit. For example, at 800 ºC the oxygen fluxes were lower than 5×10^{-13} $mols^{-1}$, which is comparable to the experimental error. One should also note that the measured fluxes correspond to the sum of physical leakages originating from micro cracks and pores, electrolytic leakage through YSZ due to minor electronic conductivity of stabilized zirconia [127], and oxygen transport in the sintered sealant layer separating zirconia ceramics [128, 134]. This combination makes it impossible to estimate area–specific contributions of the components. Consequently, Figure 4.2.14a shows the relative variations of the total oxygen flux with time; the corresponding temperature variations are displayed in Figure 4.2.14b. The leakage tends to increase with temperature, indicating important roles of possible morphological changes in the sealant at 850 ºC and electrolytic permeability increasing with temperature. The significance of the former factor is indicated by the fact that no Arrhenius dependence of the oxygen fluxes is observed; on the contrary, heating up to at 850 ºC leads to a drastic, essentially irreversible increase of the permeability. Nonetheless, thermal cycling does not induce critical degradation. For example, the resultant increase of the oxygen leakage at 800 ºC during 230 h is <2%, i.e., within the limits of experimental uncertainty. This confirms a relatively high quality of the Sr–0.3 GCs as the sealant for high–temperature electrochemical devices with stabilized zirconia electrolytes; the operation temperature should be limited, however, to 750–800 ºC.

4.3 Effect of strontium–to–calcium ratio on the structure, crystallization behaviour and functional properties of diopside–based glasses

4.3.1 Introduction

A series of glasses in which partial substitution of Ca by Sr up to 40 mol% in a diopside–$BaSi_2O_5$ boron–containing glass system were proposed and their suitability for sealing applications was investigated in the previous section (Chapter 4.2) [154, 155]. The resultant GC materials were revealed to be suitable candidates for rigid based GC sealants, as sufficient electrical resistivity coupled with an absence of oxygen leakage could be measured through dense GCs. Moreover, good thermal stability of Sr–diopside and a maximum CTE value (~10.7×10^{-6} K^{-1}) were obtained when 40 mol% Sr^{2+} ion substituted for Ca^{2+} ions. These further interesting features stimulated us to investigate the effects of higher levels of Sr–substitutions. The present work focuses on the extension of Sr for Ca substitution up to 90 % in diopside–based glass compositions, and evaluation of the effects of the Sr/Ca ratio on the structure, crystallization behaviour and functional properties. Table 4.3.1 presents the chemical composition of the experimental glasses.

Table 4.3.1: Nominal batch compositions of the glasses (mol %)

	CaO	*MgO*	*BaO*	*SrO*	*Al_2O_3*	*La_2O_3*	*SiO_2*	*NiO*
Sr/Ca=3/6	15.00	25.02	0.56	7.50	1.25	1.25	48.60	0.85
Sr/Ca=5/4	9.98	24.96	0.59	12.49	1.25	1.25	48.60	0.88
Sr/Ca=7/2	4.99	24.93	0.61	17.46	1.25	1.25	48.59	0.92
Sr/Ca=9/0	–	24.92	0.63	22.43	1.24	1.25	48.58	0.95

4.3.2 Results

4.3.2.1 Sintering/crystallization behaviours of glass–powder compacts by DTA and HSM

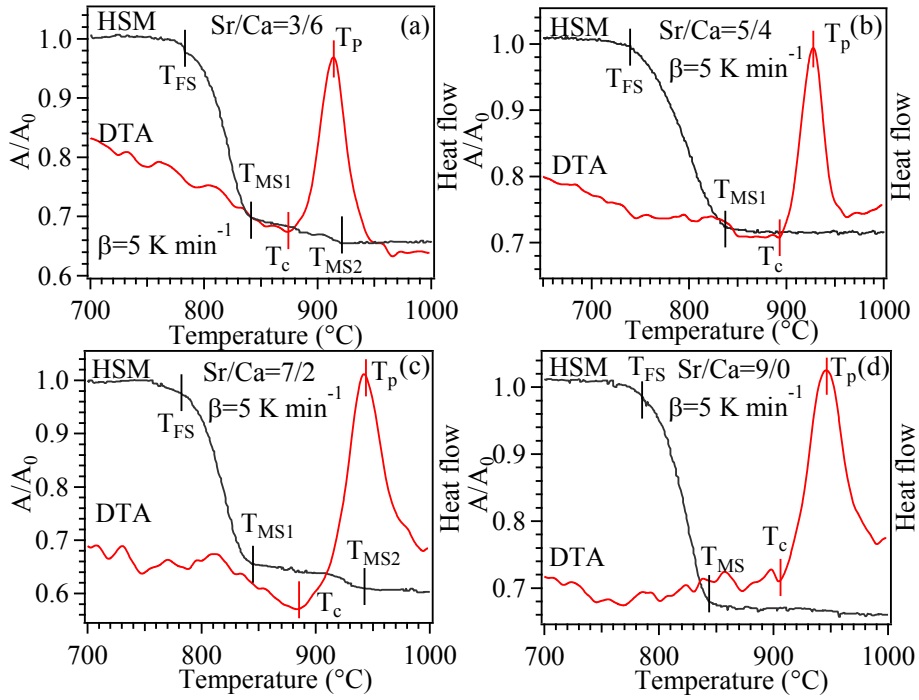

Fig. 4.3.1: DTA and HSM thermographs of the investigated glasses

Fig. 4.3.1 shows the HSM and DTA curves recorded at a heating rate of 5 Kmin^{-1}, and Table 4.3.2 summarizes the temperature values corresponding to the main thermal events as obtained from the HSM and DTA data. From Fig. 4.3.1 and Table 4.3.2, the following general trends have been revealed:

1. T_{FS} decreased from 787 to 731 ºC with increasing substitution from 30 to 50 mol% and then increased to ~782 ºC again with further incremental substitutions of Sr for Ca.
2. Fig. 4.3.2a reveals a two–stage sintering process for the Sr/Ca=3/6 glass with the first and the second sintering stages being accomplished at T_{MS1} and at T_{MS2}, respectively. It should be noted that the first sintering stage dominates over the second one. Further increasing the substitution ratio to 9/0 resulted in a single–stage sintering behaviour with $T_{MS}<T_c$ (Fig. 4.3.2b –d). This demonstrates that sintering precedes crystallization in all SrO–containing glasses.
3. The parameter S_c (=T_C–T_{MS}) is a measure of the sintering ability *vs* crystallization: the greater this difference is, the more independent are the

kinetics of both processes. The values of S_c varied in the interval 34–51 ºC. The highest S_c value was observed for Sr/Ca=9/0, while the lowest one was obtained for Sr/Ca=3/6. These results are in contradiction with findings reported elsewhere [156] that Sr/Ca >1 tended to degrade the sintering ability.

4. A single exothermic peak (Fig. 4.3.2) was recorded for all the glasses. The crystallization peak temperature (T_p) increased from 915 to 945 ºC with increasing Sr/Ca ratio.

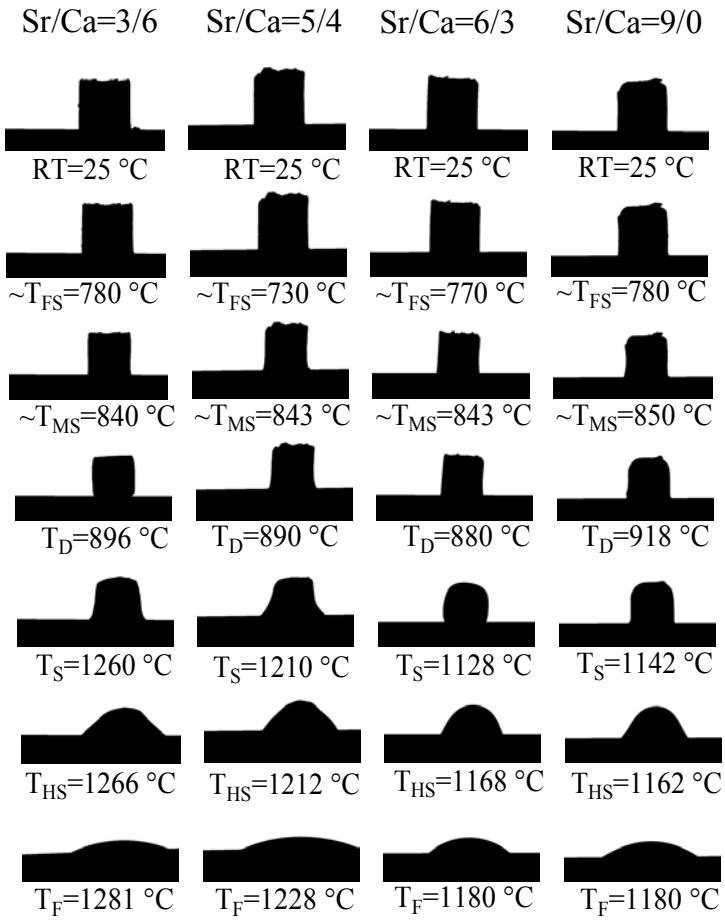

Figure 4.3.2: HSM images of various glass powder compacts of different Sr/Ca ratio on alumina substrates at various stages of heating cycle. (FS= first shrinkage; MS=maximum shrinkage; D=deformation; HS=hemi sphere; S=sphere; F=flow).

Table 4.3.2: Thermal parameters measured from DTA and HSM. (T_{FS}=First shrinkage, T_{MS}=Maximum shrinkage; T_C=onset of crystallization; T_P= peak temperature of crystallization; S_C=sintering ability)

	Sr/Ca=3/6	*Sr/Ca=5/4*	*Sr/Ca=7/2*	*Sr/Ca=9/0*
T_{FS} ±5(ºC)	787	731	772	782
T_{MS1} ±5 (ºC)	842	843	843	850
T_{MS2} ±5 (ºC)	920	–	–	–
T_C ±2 (ºC)	876	893	892	901
T_P ±2 (ºC)	915	928	942	945
S_c (=T_c–T_{MS})	34	50	49	51

4.3.2.2 Evolution of crystalline–phase composition on heat treatement

The XRD patterns of glass powder compacts sintered at 850 ºC for 1 h, 500 h and 1000 h are shown in Fig. 4.3.3, while Table 4.3.3 presents quantitative crystalline phase analysis data obtained via the Rietveld method for glasses sintered for 500 h [157]. Diopside–based phases ($Ca_{1-x}Sr_xMg_{1-y}Si_{2-y}Al_{2y}O_6$) and strontium akermanite (Sr–Akermanite: $Sr_2MgSi_2O_7$) precipitated upon heat treating for 1 h at 850 ºC. The diffraction lines corresponding to the standard files are also inserted at the bottom of Fig. 4.3.3a for comparison of the close matches. A common feature to all compositions sintered for 1 h is the relatively high fraction of amorphous phase, which can be seen in Fig. 4.3.3a. Additionally, Di was formed as single crystalline phase for the lower Sr/Ca ratios (3/6 and 5/4), while small amounts of akermanite also crystallized for higher Sr/Ca ratios (7/2 and 9/0). On increasing the heat treatment time, a more complex crystalline phase composition [Di–based phases ($Ca_{1-x}Sr_xMg_{1-y}Si_{1-y}Al_{2y}O_6$), Sr–Akermanite, and magnesium silicate ($MgSiO_3$)] formed at the expense of the glassy phase (Table 4.3.3). After 500 h at 850 ºC, the dominant crystalline phase changed from Di–like (lower Sr/Ca ratios) to Sr–Akermanite (higher Sr/Ca ratios) accompanied with magnesium silicate. Further structural details of the system after 500 h of treatment at 850 ºC using a wide array of structural characterization techniques are currently under study.

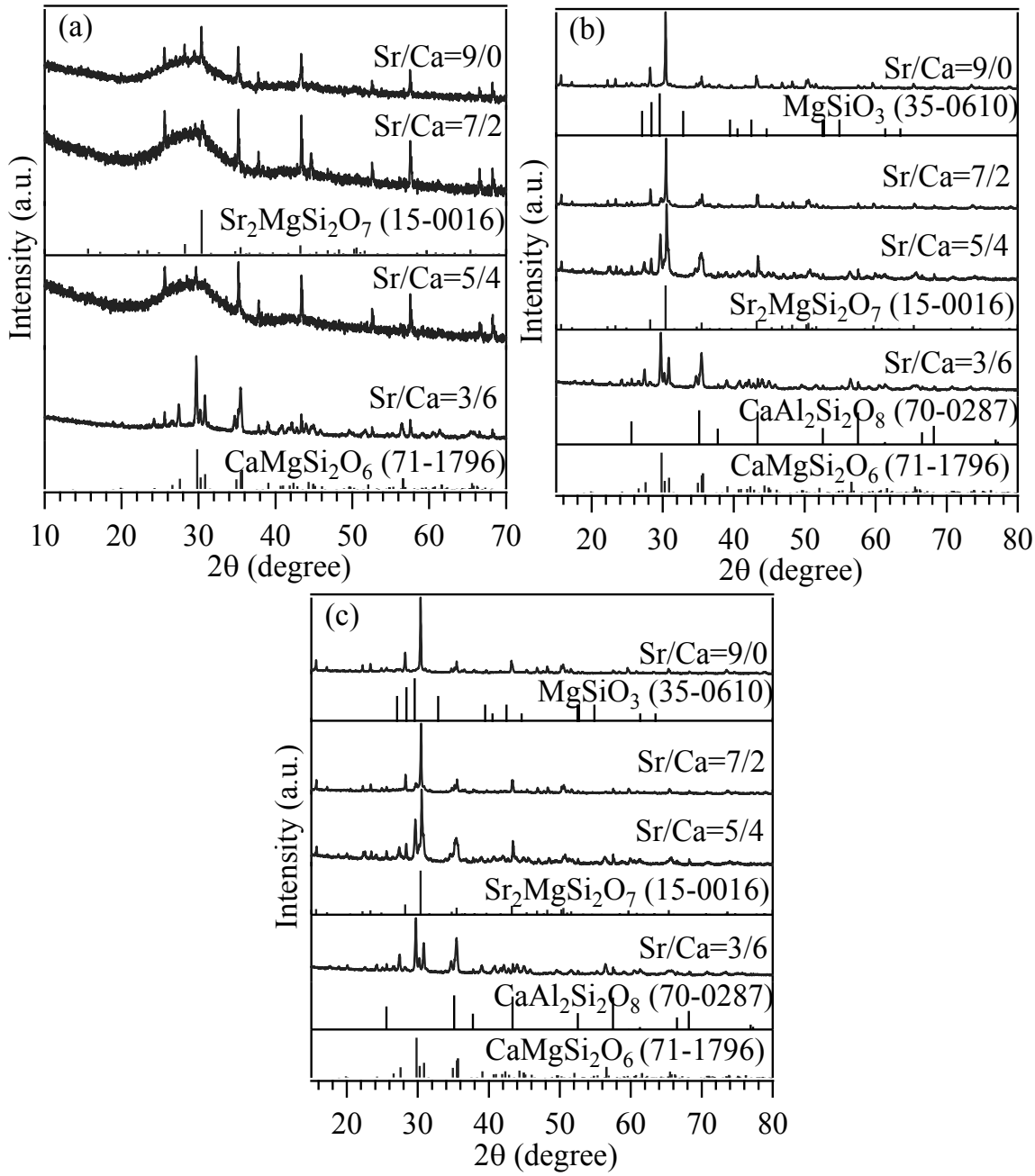

Fig. 4.3.3: XRD patterns of GCs sintered at 850 ºC for: (a) 1 h; (b) 500 h; and (c) 1000 h.

Table 4.3.3: Results of quantitative Rietveld refinement of glasses treated at 850 ºC for 500 h (wt %)

Glass	*Di–based phase*	*Anorthite*	$SrSiO_3$	$Sr_2MgSi_2O_7$	$MgSiO_3$	*Amorphous*	χ^2
Sr/Ca=3/6	68	4	1	–	–	27	1.9
Sr/Ca=5/4	62	–	–	4	–	34	1.7
Sr/Ca=7/2	29	–	–	32	–	39	1.6
Sr/Ca=9/0	–	–	–	28	15	57	1.9

The interesting feature of these GCs inferred from the XRD data is the stability in terms of crystalline–phase assemblage with further increasing the heat treatment time to 1000 h (Fig. 4.3.3). This thermal stability fares well in comparison with that of GCs seals reported in the literature [158]. The results reveal that with increasing the heat treatment time and the Sr/Ca ratio, Sr–akermanite along with a Di–based phase are preferentially formed. These changes in the crystallization behaviour behaviour are likely to have consequences on the intrinsic properties of materials, as will be discussed below.

4.3.2.3 MAS–NMR study of sintered glass–powder compacts

Fig. 4.3.4a shows ^{29}Si MAS–NMR spectra of GCs heat treated at 850 ºC for 1000 h. The position of the peak maximum reflects the predominance of certain silicate species [159]. The ^{29}Si NMR spectrum of Sr/Ca=3/6 GC exhibits a sharp peak centred at –85 ppm while that of Sr/Ca=5/4 shows an additional peak centred at –76 ppm. With further increasing the Sr/Ca ratio, the intensity of the peak at –76 ppm increased in comparison to that of the peak at –85 ppm. This latter peak corresponds to Q^2–silicate species (i.e. inosilicates) such as a diopside–based phase whilst the peak at –76 ppm indicates the presence of Q^1–silicate structural units such as those found in Sr–Akermanite [159]. The deconvolution of MAS–NMR spectra was attempted using the common assumption of a Gaussian distribution of isotropic chemical shifts for each type of Q^n unit to yield the percentages of Q^n species reported in Table 4.3.4. The best fitting parameter, i.e, a coefficient of determination R^2 = ~1, was achieved between the global simulation curve (superposition of Gaussian shapes) and the measured curve for all the GCs with the

considered number of Gaussian shapes for a specific glass composition. The fitting procedure was performed using Originpro version 8. Figures 4.3.4b and 4.3.4c present the deconvolution curves for GCs Sr/Ca=5/4 and Sr/Ca=9/0, respectively. Table 4.3.4 reveals that Q^2 species predominated in all the GCs. However, increasing the Sr/Ca ratio led to a redistribution of the chemical shifts of the peaks with Q^4 and Q^1 units growing at the expense of Q^2. The Q^4 species are seemingly derived from a residual amorphous phase since no corresponding crystalline phase was detected by XRD analysis. Moreover, the amount of Q^4 species listed in Table 4.3.4 scales well with the amorphous phase content presented in Table 4.3.3.

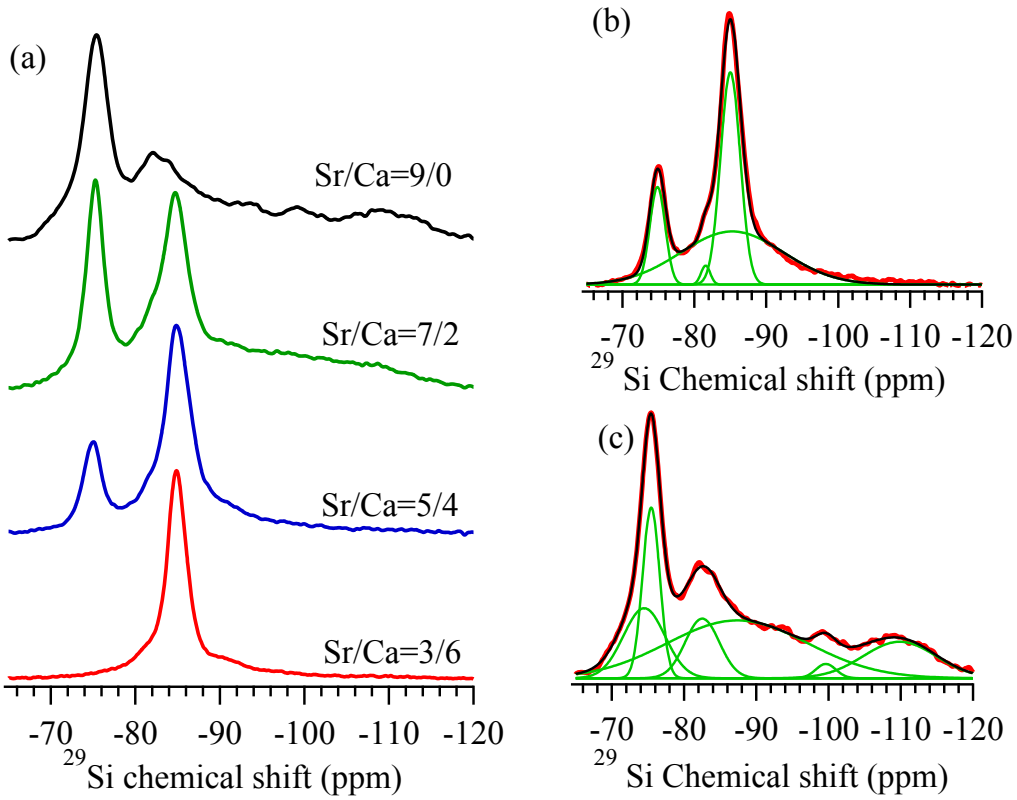

Fig. 4.3.4: (a) ^{29}Si MAS–NMR spectra of glass–ceramics heat treated at 850 ºC for 1000 h. Spectral deconvolutions of the ^{29}Si MAS spectra of glass–ceramics heat treated at 850 ºC for 1000 h: (b) Sr/Ca=5/4; (c) Sr/Ca=9/0. The red line represents experimental curve, (superposition of Gaussian shapes) and the green lines represent the Gaussian shapes.

Table 4.3.4: Quantification of the deconvoluted silicon components

	Chemical Shift (ppm)	*Area (a.u.)*	*Percentage area (%)*
Sr/Ca=3/6	-85.1–Q^2	2460	51.1
	-84.9–Q^2	2354	48.9
Sr/Ca=5/4	-85.3–Q^2	1848	48.2
	-85.0–Q^2	1419	37.0
	-81.6–Q^2	59	1.5
	-74.9–Q^1	509	13.3
Sr/Ca=7/2	-101.5–Q^4	1370	26.0
	-84.7–Q^2	890	16.9
	-82.49–Q^2	2181	41.5
	-75.2–Q^1	821	15.6
Sr/Ca=9/0	-109.8–Q^4	236	14.1
	-99.6–Q^4	26	1.6
	-87.4–Q^2	718	42.8
	-82.5–Q^2	180	10.7
	-75.4–Q^1	260	15.5
	-74.5–Q^1	257	15.3

The ^{27}Al MAS NMR spectra of the GCs heat–treated at 850 ºC for 1000 h are shown in Fig. 4.3.5. All the GCs exhibited chemical shifts within the 53–57 ppm range, characteristic of Al^{IV} species. A tail at about −5 ppm, typical of an AlO_6 environment, is well resolved in Sr/Ca=3/6, Sr/Ca=5/4 and Sr/Ca=7/2 samples, while the broad ^{27}Al spectra of the Sr/Ca=9/0 sample implies a wider distribution of Q^n (Al) structural units [160]. Moreover, there is a tendency for the ^{27}Al MAS NMR spectra of the GCs to become more asymmetric and similar to that of an amorphous glass on increasing the Sr/Ca ratio. This is due to the gradual re–formation of Al^V species in the GCs (Fig. 4.3.5). In fact, the ^{27}Al MAS–NMR spectra of the Sr/Ca=9/0 GC is very similar to the spectra of the glassy sample (inset at Fig. 4.3.5). This is consistent with the trend of an increasing

amount of residual glassy phase with increasing Sr content in the sintered samples (Table 4.3.3).

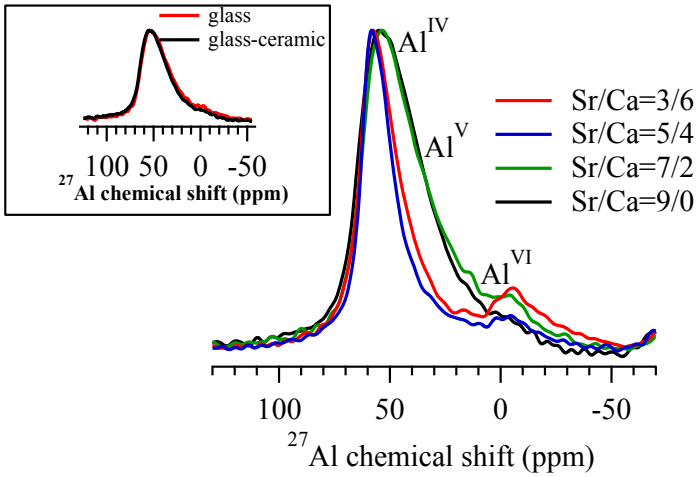

Fig. 4.3.5: ^{27}Al MAS–NMR spectra of glass–ceramics heat treated at 850 ºC for 1000 h. The inset compares the ^{27}Al MAS–NMR spectra for Sr/Ca=9/0 glass and Sr/Ca=9/0 glass–ceramic heat treated at 850 ºC for 1000 h.

4.3.2.4 Thermal, mechanical and electrical properties of sintered glass–ceramic samples

The CTE values of the GCs heat treated at 850 ºC for different time intervals are presented in Table 4.3.5. After 1 h, the CTE values are in the range of (9.0–9.4) × 10^{-6} K^{-1}. Systematic slight increases in the CTE of GCs were observed with increasing the heat treatment time up to 1000 h, irrespective of the Sr/Ca ratio. Such increases in the CTE are consistent with the higher fractions of crystalline phases (Table 4.3.3). These small variations are not expected to have any severe implications concerning the final intended application. It is noteworthy that the CTE of a GC seal decides the stability and hermeticity of the joins with other components of the SOFC, as the glass seal is prone to crystallize during joining. The CTE values measured for our GC compositions (9.0–10.3)×10^{-6} K^{-1} appear to be suitable for sealing joints with solid oxide electrolytes (i.e., 8YSZ,CTE = (10–11)×10^{-6} K^{-1}) and of metallic interconnects (Crofer22APU; SanergyHT, CTE = (11–12)×10^{-6} K^{-1}).

Table 4.3.5: Bending strength (MPa) and CTE (±0.1) × 10^{-6} K^{-1} (200–700 ºC) data measured for the glass–powder compacts after sintering / heat treated at 900 ºC for 1 h, 500 h and 1000 h.

	1 h	*500 h*	*1000 h*
Bending strength			
Sr/Ca=3/6	133±11	139±15	135±11
Sr/Ca=5/4	97±11	123±14	113±12
Sr/Ca=7/2	102±12	146±7	130±11
Sr/Ca=9/0	108±13	132±10	120±12
CTE			
Sr/Ca=3/6	9.2	9.6	10.2
Sr/Ca=5/4	9.2	9.7	9.8
Sr/Ca=7/2	9.4	9.7	9.8
Sr/Ca=9/0	9.0	9.0	9.1

The data on mechanical strength as functions of the Sr/Ca ratio and heat–treatment time are reported in Table 4.3.5. A general trend of increasing strength between 1 h and 500 h of thermal treatment is apparent, suggesting that structural defects in the samples tend to level off during the heat treatment, probably facilitated by the increasing amount of glassy phase, which, in turn, becomes enriched in Q^4–silicate structural units (Fig. 4.3.4). However, firm conclusions on the dependence of the mechanical strength on the Sr/Ca ratio and heat treatment time cannot be drawn because the mechanical performance also strongly depends on structural defects introduced on processing of the glass powders.

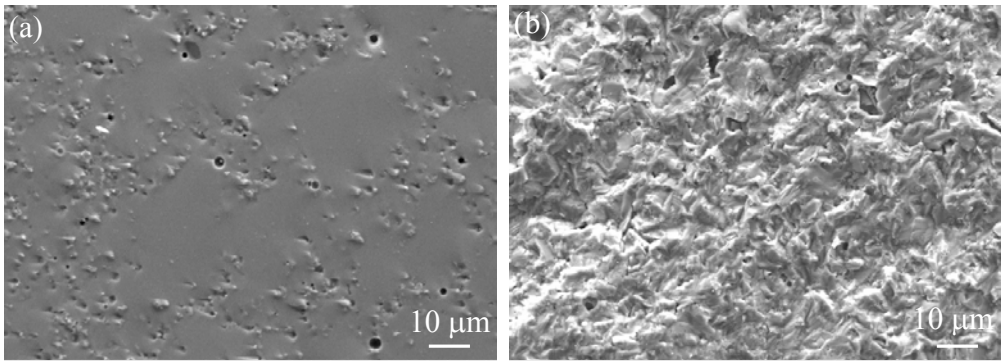

Fig. 4.3.6: Fracture surfaces of glass–powder compacts heat treated at 850 ºC (a) Sr/Ca=9/0, 1 h; (b) Sr/Ca=9/0, 1000 h.

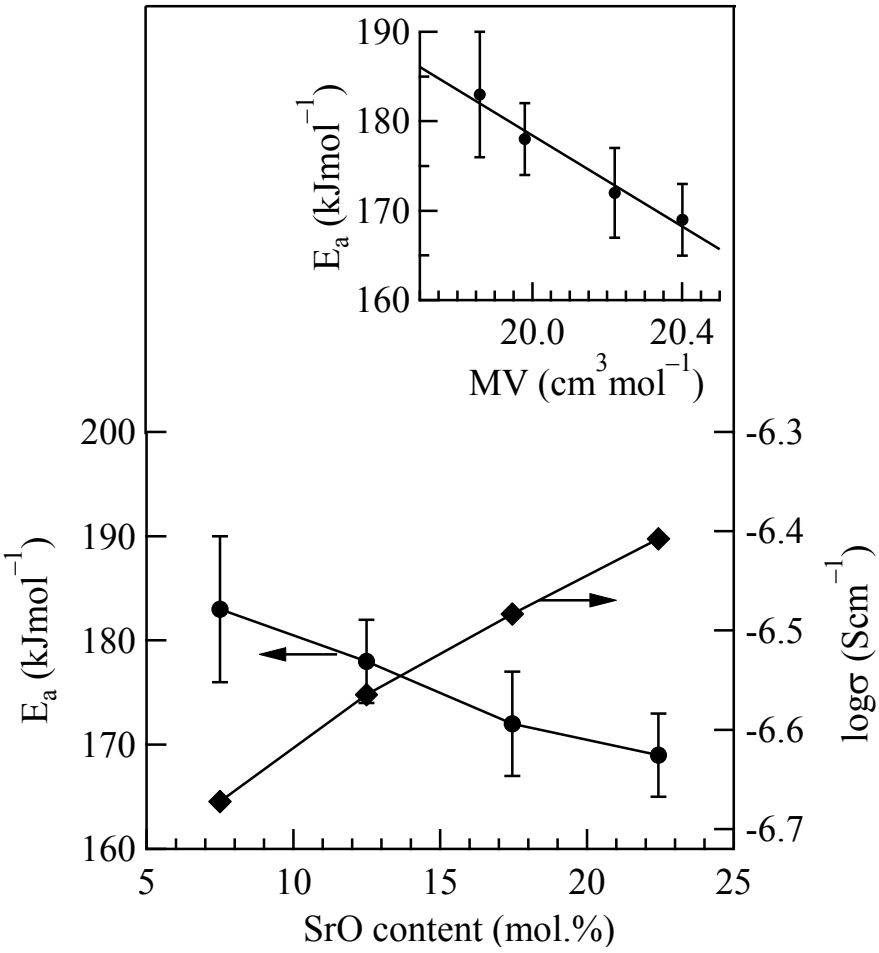

Fig. 4.3.7: Electrical conductivity at 800 ºC and the conductivity activation energy, calculated by the standard Arrhenius equation in the temperature range 600–830 ºC, as a function of strontium content in the studied glass–ceramics materials. The inset shows the relationship between the activation energy and molar volume.

The SEM micrographs shown in Figs. 4.3.6a and b reveal typical fracture surfaces after the bending strength test for the Sr/Ca=9/0 GC sintered at 850 ºC for 1 h and after further heat treating at this temperature for 1000 h. The relatively high amount of glassy phase of the sample sintered for 1 h is apparent in Fig. 4.3.6a, while Fig. 4.3.6b (1000 h of heat treatment) reflects a more crystalline structure.

Impedance–spectroscopy analysis showed that all GCs studied in this work exhibit excellent insulating properties. At 800 ºC, their electrical resistivity is higher than 2 MOhm×cm (Fig. 4.3.7). The apparent activation energies (E_a) calculated by the standard Arrhenius equation vary in the narrow range 169–183 kJmol^{-1}. The electrical conductivity was moderately enhanced with increasing Sr/Ca ratio, whilst the activation energy variations displayed the opposite trend, in correlation with the molar volume (inset in Fig. 4.3.7). The latter result is indicative of a dominant role of ionic charge carriers in the studied materials, as for the B_2O_3–containing GCs (Chapter 4.2) [155]. The electrical properties are stable and independent of oxygen and water–vapour partial pressure (Fig. 4.3.8).

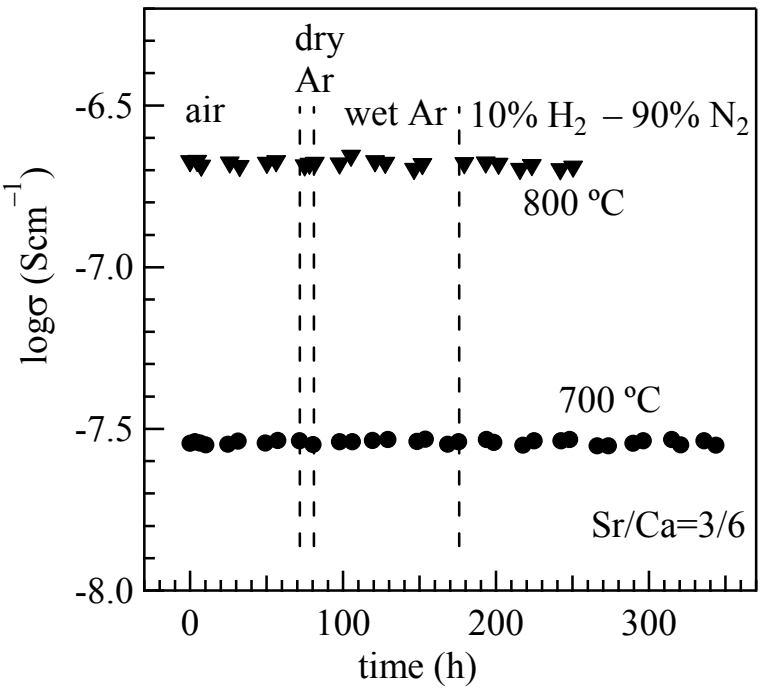

Fig. 4.3.8: Time dependencies of the total electrical conductivity of Sr/Ca–3/6 glass–ceramics in various atmospheres at 700 and 800 ºC.

4.3.2.5 Wetting and chemical interaction

Examples of elemental–mapping analyses are shown in, Figs. 4.3.9a–c, confirming that all the GC seals bonded well to the Crofer22APU metallic plate. Furthermore, no interfacial problems of adhesion, cracking and layer formation could be observed for the Sr–containing, GC sealants. Figs. 4.3.9d and 4.3.9e show X–ray diffractograms after the reactions between Cr_2O_3/glass and MnO/glass powders at 850 ºC for 100 h under air atmosphere. The crystalline phases developed in all the glasses are similar to 500 h and 1000 h heat–treated samples except for the addition of Cr_2O_3 and Mn_2O_3. No further unwanted crystalline phase, such as $SrCrO_4$, was developed [69]. This behaviour confirms the high thermal stability and chemical compatibility of the title GCs with the metallic interconnects.

In the case of 8YSZ ceramics, the adhesion of the studied GC sealants was, however, substantially worse compared to their B_2O_3–doped analogues (Chapter 4.2) [154, 155]. In fact, whilst thermal treatments at 850–900 ºC were insufficient to achieve gas–tight sealing with zirconia ceramics, annealing at 950 ºC led to inhomogeneities in the GC layer in the vicinity of 8YSZ/GC interface, as illustrated in Fig. 4.3.10. These in–homogeneities lead, in turn, to a poor mechanical stability. For comparison, testing the thermal–shock resistance of model 8YSZ cells sealed by B_2O_3–containing, diopside–based GCs (Chapter 4.2) [154, 155] showed no failure after 15 air–quenching cycles. Similar cells sealed with the Sr/Ca=3/6 GC were mechanically disaggregated on the first quenching. In addition to relatively poor adhesion, the lower CTE values of the materials studied in the present work (cf. Table 4.2.7 and Ref. [154, 155]) may have also contributed to this behaviour, resulting in high mechanical stresses upon temperature variations.

A similar conclusion was drawn on testing the microhardness of the GC layers applied onto 8YSZ. The Vicker's hardness of the Sr/Ca=3/6 layers (thickness of ~100 μm) deposited on 8YSZ was as low as 0.3±0.1 GPa; the value measured for the B_2O_3–doped analogue was >0.5 GPa. This makes the introduction of extra additives for improving the adhesion of the GCs to the surface of stabilized–zirconia electrolytes necessary.

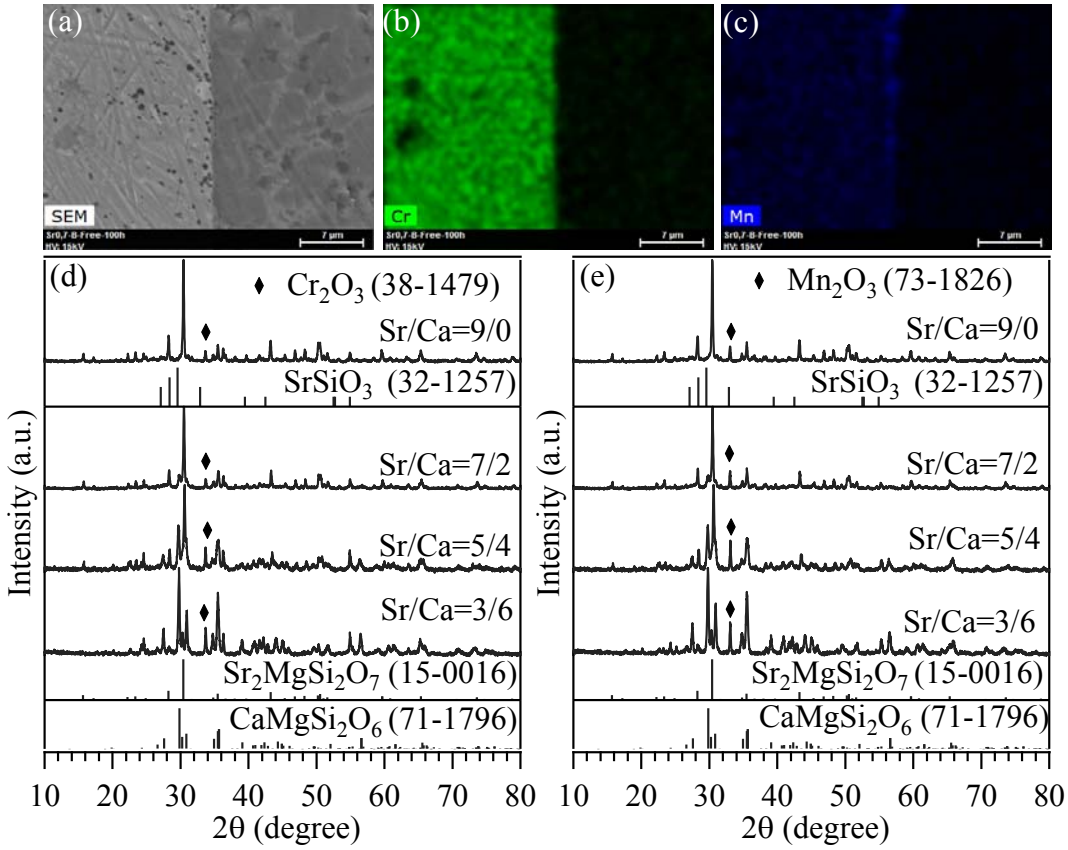

Fig. 4.3.9: a) SEM image and EDS element mappings for (b) Cr and (c) Mn, at the interface between Sr/Ca=7/2 and Crofer22APU after heat treatment at 850 ºC for 1 h. XRD pattern of (d) glass + 10 wt.% Cr_2O_3 and (e) glass + 10 wt.% MnO mixtures after 100 h heat treatment at 850 ºC.

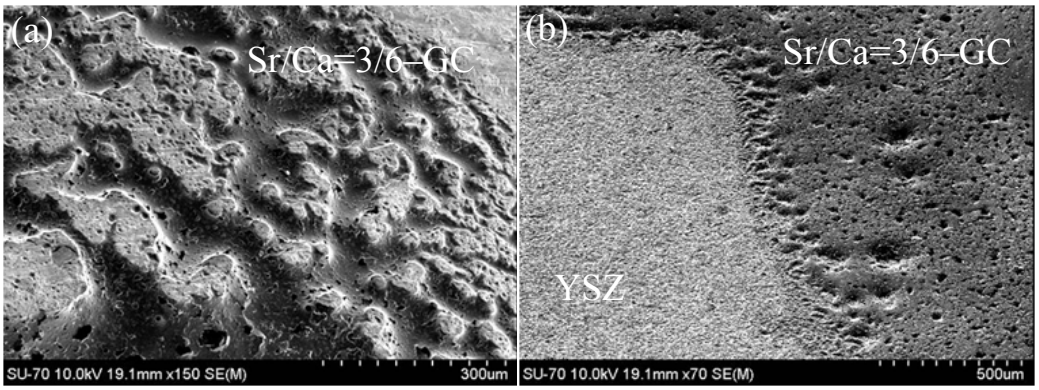

Fig. 4.3.10: Typical morphologies of the Sr/Ca–3/6 glass–ceramics layer deposited onto 8YSZ ceramics after heat treatment at 950 ºC: (a) glass–ceramics layer surface, (b) edge of glass–ceramics deposited on 8YSZ.

4.3.3 Discussion

The obtained results clearly show how the Sr/Ca ratio affects the structure, crystallization behaviour and properties of Di–based glasses and GCs. Similar evidence has not yet been reported according to the best of our knowledge.

Both CaO and SrO are well–known network modifiers. However, the larger Sr cation and the resulting weaker Sr–O bond strength lead to a decrease in the glass viscosity. This more accentuated disruption of the glass–network on increasing the Sr content is further depicted from the increased CTE values with increasing Sr/Ca ratio (Table 4.3.5). It is well known that sintering of glass powders may be strongly affected by phase transformations i.e., nucleation and growth of crystalline phases occurring upon heating. Hill et al. [161] reported that strontium substitution for calcium affects the nucleation and crystallization behaviour of the glass. However, the data of Rietveld analyses for the GCs sintered for 500 h (Table 4.3.3), reveal that higher Sr/Ca ratios tend to hinder crystallization. These results suggest that increasing the Sr/Ca ratio up to 5/4 promotes sintering behaviour (Table 4.3.2) by decreasing the viscosity of the glass. The flow point also decreased from 1281 ºC to 1228 ºC with increasing Sr/Ca ratio from 3/6 to 5/4, Fig. 4.3.1. This interpretation is consistent with the findings reported elsewhere [162, 163] that adding BaO as glass–network modifier decreases the glass viscosity. The further increase in Sr/Ca ratio has negligible influence on the sintering behaviour, probably due to the growth of Sr–akermanite crystalline phase. It has also been revealed from the quantitative Rietveld XRD and ^{29}Si MAS–NMR results that increasing the Sr/Ca ratio increases the fraction of Q^1 units over Q^2 units, consistent with the disruption of the network. Therefore, the growth of Sr–akermanite might hinder any further densification with increasing Sr/Ca ratio (Fig. 4.3.1). In any case, the maximum densification has been achieved well before the initiation of crystallization in all the GCs.

The XRD (Table 4.3.3) and the MAS–NMR data of GCs revealed that increasing the Sr/Ca ratio favours the formation of Q^1 structures in Sr–akermanite at the expense of Q^2 diopside structural units. According to Lee et al. [101], who studied the chemical order of mixed–cation silicate glasses, especially in $BaMgSi_2O_6$ glass, when a pair of mixed cations with identical charges but different ionic radii are mixed, the low–field–strength cation prefers bonding to both bridging and NBOs. This kind of

strong preference among network–modifying cations is solely due to the difference in ionic radii of the alkaline–earth metals. This indicates that increasing the Sr/Ca ratio perturbs the glass network more effectively and allows new crystalline phases to be formed when heated to sufficiently high temperature. Gillot et al. [164] reported that around T_g, Di glasses crystallize as akermanite in preference to diopside due to the decoupled mobility of network–modifying and network–forming cations. The formation of Sr–akermanite crystalline phase throughout the Di solid solution has also been observed previously [165]. Thus, the formation of Sr–akermanite along with the Di crystalline phase seems inevitable on increasing the ratio of Sr to Ca.

From the sintering behaviour and DTA thermographs (Fig.4.3.2), one would expect that 100% Sr–substituted glass would hinder crystallization more readily than in any of the other Ca–containing glasses. Consequently, the quantitative XRD results revealed retarded crystallization upon isothermal heating of the glass powder compacts at 850 ºC for 500 h (Table 4.3.3). The broadening of the NMR patterns in both the ^{29}Si MAS–NMR and ^{27}Al MAS–NMR spectra (Fig. 4.3.4a and Fig. 4.3.5) with increasing Sr/Ca ratio are also consistent with higher contents of amorphous phase (Table 4.3.3). This behaviour may be due to higher entropy of mixing that stabilizes the disordered glassy state. Increasing the entropy of mixing enhances the energy barrier for crystallization and delays the atomic rearrangement to form critical–size nuclei. It has been reported recently [156] that the substitution of Sr for Ca in multi–component glass compositions reduces the glass transition temperature and lowers the activation energy for crystallization whilst increasing the onset temperature of crystallization. The similar behaviour observed in the present glass system can be explained on the basis of the ion–diffusion coefficient, according to the findings of Nakamura [166], who measured the diffusivities of Ba and Sr elements in Di melts. They found that diffusion coefficients (DC) of divalent ions decrease with increasing ionic radii at constant pressure and temperature (~2.2×10^{-6} cm^2 sec^{-1} and ~2.6×10^{-6} for Sr and Ca, respectively). According to Lee et al. [167], low–field–strength, charge–balancing cations in aluminosilicate glasses decrease the thermodynamic configurational entropy and increase the structural disorder. Further detailed experimental analysis is required to better understand the effects of Sr/Ca ratio over long–run heat treatments.

It is known that variations of crystalline volume fractions and phase assemblage in GCs upon isothermal treatments influence the mechanical strength and the CTE of the seal. For example, a greater flexural strength was reported for the GC–9 glass sample aged for 1000 h at 750 ºC in comparison to a non–aged sample due to the increase of crystalline fraction [168]. On the other hand, a decrease of the CTE from 11.7×10^{-6} K^{-1} to 9.1×10^{-6} K^{-1} with increasing the heat treatment time from 5–100 h at 1000 ºC was attributed to the formation of a different crystalline–phase assemblage [169]. These cases contrast with the good stability of the present glass systems in terms of phase assemblage and properties as revealed from quantitative Rietveld analysis (Table 4.3.3) after 500 h at 850 ºC. This enhanced general stability with increasing Sr/Ca ratio is counterbalanced by a slight decrease in CTE, which is probably due to the formation of Sr–akermanite phase ($\alpha_a = 3.663 \times 10^{-6}$ K^{-1} and $\alpha_c = 6.666 \times 10^{-6}$ K^{-1}) at the expense of Di–based phase (diopside – ~9.5×10^{-6} K^{-1}) [138]. In any case, all the CTE values fit within the suitability range for applicability as SOFC seals. Moreover, the enhancement of mechanical strength during prolonged heat treatments resulted in higher values than those obtained for G–18 glass (~35 MPa) and GC–9 glass (49 MPa) after heat treating at 800 ºC for 1000 h [44, 168]. According to the Griffith crack theory, when a propagating crack in the compound encounters a crystal with high strength and elastic modulus, the crack direction is deviated by the crystal, thereby enhancing the fracture strength. As a result, a higher energy will be required for crack propagation. The fracture surface of the sample heat treated at 850 ºC for 1000 h, shown in Fig. 4.3.6d, is rougher in comparison to that of a sample sintered at the same temperature for 1 h (Fig. 4.3.6c).

One of the most arduous tasks in the development of SOFC seals is achieving good bonding and wetting ability with the SOFC components without forming any undesirable phases at the interfaces. It has been observed by Chou et al. [77] and Zhang et al. [103] that a significant amount of SrO in sealant–glass compositions leads to the formation of $SrCrO_4$ crystalline phase on interacting with the Cr–containing metallic plates. Pure $SrCrO_4$ is orthorhombic and highly anisotropic in CTE with $\alpha_a = 16.5 \times 10^{-6}$ K^{-1}, $\alpha_b = 33.8 \times 10^{-6}$ K^{-1}, and $\alpha_c = 20.4 \times 10^{-6}$ K^{-1} [170]. Such high CTE values will create unwanted stresses in the microstructure of the GCs, which consequentially affects the

mechanical strength of the seal. $SrCrO_4$ will generally form when high SrO–containing glasses react with Cr_2O_3 powders upon heat treating in air up to at least 800 ºC. One possible path for the formation of $SrCrO_4$ is: SrO (glass) + ½ Cr_2O_3 (solid) + ¾ O_2 ↔ $SrCrO_4$ (solid). However, in contrast to the sealants proposed by Chou et al. [77] and Zhang et al. [103], the materials studied in the present work did not form $SrCrO_4$. Their stability has, most likely, a kinetic nature and correlates with the low DC values given above (in this section). The results of XRD analysis and of the interaction studies (Fig. 4.3.9) reveal good chemical compatibility between the investigated glasses and GCs and SOFC components, making them suitable for sealant applications.

The presence of 30–40 % glassy phase in GCs, even after prolonged heat treatment, is expected to confer them some ability to flow and limit or close cracks formed during SOFC operation. Such self–healing behaviour of sealants has great interest in the present era. In general, all the studied GCs (i) exhibited a CTE in the range (9.2–10.2) × 10^{-6} K^{-1}, (ii) good mechanical strength compared to commercial glass G–18, (iii) good thermal stability up to 1000 h at 850 ºC and (iv) good wetting and chemical compatibility with the SOFC components which are desirable for their application as a sealing material in SOFCs.

4.4 Sintering behaviour of lanthanide–containing glass–ceramic sealants for solid oxide fuel cells

4.4.1 Introduction

Sintering behaviour plays a crucial role in the development of seals for SOFCs because the glass paste (glass powder mixed with a suitable binder) is usually applied on the surface (ceramic or metallic) components to be sealed, undergoing sintering before a continuous glassy phase layer forms, which might then be transformed into a GC layer. The literature survey revealed that apart from La_2O_3, no other lanthanide oxides have been investigated aiming at designing glass seals [23]. Therefore, the present study is dedicated towards investigating the influence of lanthanides (La^{3+}, Nd^{3+}, Gd^{3+}, Yb^{3+}) on sintering behaviour of GC–seals for SOFC. A total of 13 glasses with different lanthanide concentrations were designed and synthesized in the primary crystallization field of Di with the following theoretical compositions: $Ca_{0.7}Sr_{0.3}Mg_{0.9}Al_{0.1}Ln_{0.1}Si_{1.9}O_6$; $Ca_{0.7}Sr_{0.3}Mg_{0.85}Al_{0.1}Ln_{0.2}Si_{1.85}O_6$ and $Ca_{0.7}Sr_{0.3}Mg_{0.8}Al_{0.1}Ln_{0.3}Si_{1.8}O_6$, where Ln: La, Nd, Gd and Yb. Also a lanthanide free glass with composition $Ca_{0.7}Sr_{0.3}Mg_{0.95}Al_{0.1}Si_{1.95}O_6$ was synthesized in order to understand the influence of lanthanide oxides on different properties of glasses. These BaO–free glass compositions were selected to minimize the possibility of any detrimental chemical interactions between the seal and the metallic interconnect, as well as to avoid the formation of monoclinic celsian in the GC [23]. Further, Al_2O_3 was added in relatively small amounts so as to control the devitrification behaviour of glasses [171], while 2 wt.% B_2O_3 was added to all the glass compositions to tailor their flow behaviour [26]. The partial substitution of SiO_2 and MgO with lanthanides Ln_2O_3 ($Si^{4+} + Mg^{2+} \leftrightarrow 2\ Ln^{3+}$) has been made considering the fact that both silica and magnesia tend to decrease the CTE and increase the viscosity of glasses which might affect the flow as well as joining behaviour of glass seals to SOFC components. Table 4.4.1 presents the detailed compositions of all the investigated glasses.

Table 4.4.1: Glass compositions (Ln refers to lanthanide cation present in the glass).

		MgO	*CaO*	*SrO*	*SiO_2*	*Al_2O_3*	*B_2O_3*	*Ln_2O_3*
Ln–0	wt%	16.25	16.66	13.20	49.73	2.16	2.0	–
	mol%	23.64	17.42	7.47	48.54	1.24	1.68	–
La–0.1	wt%	14.68	15.89	12.58	46.20	2.06	2.0	6.59
	mol%	22.66	17.63	7.55	47.85	1.26	1.79	1.26
La–0.2	wt%	13.25	15.18	12.02	42.98	1.97	2.0	12.60
	mol%	21.66	17.84	7.64	47.14	1.27	1.89	2.55
La–0.3	wt%	11.94	14.53	11.51	40.04	1.89	2.0	18.10
	mol%	20.63	18.05	7.74	46.42	1.29	2.00	3.87
Nd–0.1	wt%	14.65	15.85	12.55	46.09	2.06	2.0	6.79
	mol%	22.67	17.63	7.55	47.84	1.26	1.79	1.26
Nd–0.2	wt%	13.19	15.12	11.97	42.80	1.96	2.0	12.96
	mol%	21.66	17.84	7.64	47.14	1.27	1.90	2.55
Nd–0.3	wt%	11.87	14.45	11.44	39.80	1.88	2.0	18.58
	mol%	20.63	18.05	7.73	46.41	1.29	2.01	3.87
Gd–0.1	wt%	14.57	15.77	12.49	45.85	2.05	2.0	7.28
	mol%	22.66	17.63	7.55	47.84	1.26	1.80	1.26
Gd–0.2	wt%	13.06	14.96	11.85	42.37	1.94	2.0	13.82
	mol%	21.66	17.83	7.64	47.13	1.27	1.92	2.55
Gd–0.3	wt%	11.69	14.24	11.28	39.22	1.85	2.0	19.72
	mol%	20.62	18.05	7.74	46.40	1.29	2.04	3.87
Yb–0.1	wt%	14.48	15.67	12.41	45.55	2.03	2.0	7.86
	mol%	22.66	17.63	7.55	47.83	1.26	1.81	1.26
Yb–0.2	wt%	12.90	14.78	11.71	41.85	1.92	2.0	14.84
	mol%	21.65	17.83	7.64	47.12	1.27	1.94	2.55
Yb–0.3	wt%	11.49	13.99	11.08	38.55	1.82	2.0	21.07
	mol%	20.61	18.04	7.73	46.39	1.29	2.08	3.87

4.4.2. Results

4.4.2.1 Glass forming ability

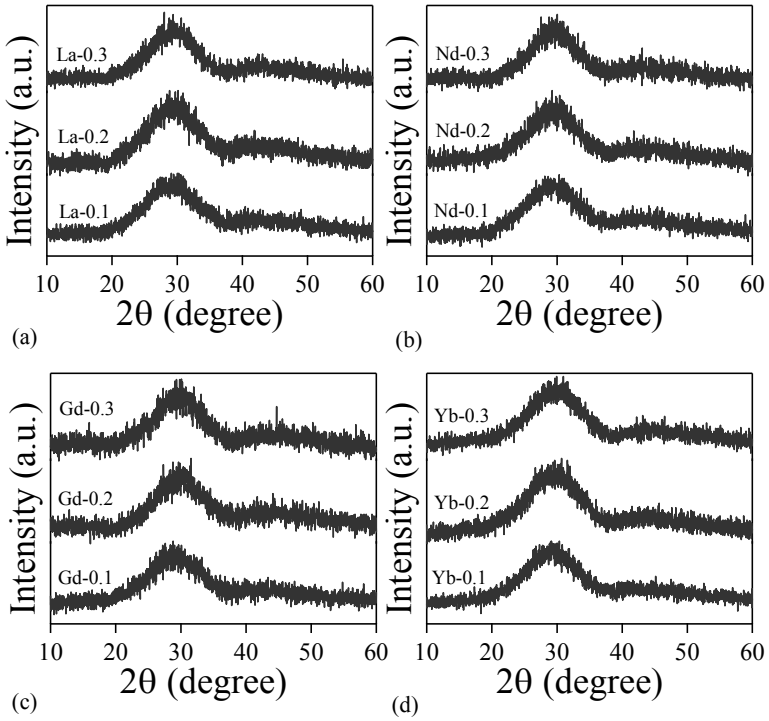

Fig. 4.4.1: X–ray diffractograms of as synthesized glasses depicting their amorphous nature.

For all the investigated compositions, melting at 1550 ºC for 1 h was sufficient to obtain bubble–free, homogeneous transparent glasses. Table 4.4.2 presents the experimental compositions for some of the glasses as determined by ICP–OES analysis. Negligible changes were observed in the chemical composition of the glasses after melting the glass batch as 1550 ºC. The absence of crystalline inclusions was confirmed by XRD analysis (Fig. 4.4.1). Although it has been reported that the upper limit for the amount of lanthanide oxides that can be incorporated into the aluminosilicate glasses decreases in accordance with lanthanide contraction [172], no such concern was observed in the present study. This might be due to the relatively lower concentrations of lanthanide oxides added in the present work in comparison to those used by Makishima et al. [172]. With respect to the colour, all the glasses except those containing Nd were colorless. Nd–containing glasses exhibited blue–purple colouration characteristic of Nd^{3+} ($4f^3$) ions f–f transitions: this is the most stable oxidation state of neodymium [173].

Also, according to Loiseau et al. [173], the colorless state of Gd and Yb containing glasses refers to the occurrence of the most stable trivalent oxidation state for these ions under normal conditions in air: Gd^{3+} ($4f^7$) ions absorb in the ultra–violet range whereas Yb^{3+} ($4f^{13}$) ions absorb in the near infrared range.

Table 4.4.2: Glass composition (wt%) of some glasses as determined by ICP–OES analysis

	MgO	*CaO*	*SrO*	SiO_2	Al_2O_3	B_2O_3	Ln_2O_3
Ln–0	15.25	16.49	13.94	50.42	2.36	1.55	–
La–0.2	12.06	15.30	12.67	43.10	2.06	1.88	12.93
Nd–0.2	11.27	15.67	14.03	42.79	2.12	1.85	12.28
Gd–0.2	11.41	15.29	13.39	42.32	2.08	1.79	13.73
Yb–0.2	11.21	15.06	12.62	41.71	1.94	1.78	15.68

4.4.2.2 Coefficient of thermal expansion (CTE)

Table 4.4.3 presents the CTE values for all the investigated glasses and GCs (after sintering at 850 ºC for 1 h). All the studied glasses exhibited their CTE values in the range $(9 – 10.5) \times 10^{-6}$ K^{-1} while the CTE of GCs varied between $(9.4 – 11.1) \times 10^{-6}$ K^{-1} which are desirable for their application as a sealing materials in SOFCs. The introduction of 1.26 mol% of lanthanide oxides in glasses led to an increase in the CTE of glasses except for glass La–0.1 which has a CTE value similar to that for parent glass Ln–0. Further, all the glasses containing La, Nd, Gd, and Yb exhibited an almost similar trend as their CTE values decreased with increase in lanthanide concentration from 1.26 mol% to 2.55 mol% and then increased with increasing lanthanide content to 3.87 mol%. At any particular concentration of lanthanides, CTE of glasses was lowest for La containing glass compositions and the highest for Yb–containing glasses (except for glass Yb–0.2). These results are in contradiction with those reported for lanthanide containing aluminosilicate glasses [174] and soda–lime–silica [175] glasses where CTE values have been shown to decrease linearly with the ionic field strength of the lanthanide ions (lanthanide contraction). This may be attributed to the compositional complexity of the

investigated glasses which consequentially affects their atomic and molecular structure and might lead to a variety of phenomena depending upon the nature and amount of lanthanides (i.e. lanthanide clustering, or network modifying effect/charge compensating effect) [175-179], thus, affecting their thermal expansion behaviour. For example: in alkali/alkaline–earth silicates, the addition of lanthanides beyond a certain amount leads to the phenomenon of concentration quenching and phase separation. However, incorporating Al_2O_3 in these glasses has been shown to increase the solubility limit of lanthanides, thus allowing the homogeneous dissolution of lanthanide oxides in amounts much higher than otherwise possible [180]. Therefore, a detailed structural evaluation of these glasses depicting the silicon, aluminum and boron coordination along with the local structural environment of various lanthanide cations is required in order to provide a reasonable justification for their thermal expansion behaviour.

Table 4.4.3: CTE ($\times 10^{-6}$ K^{-1}) of glasses (200 – 500 ºC) and glass–ceramics (200 – 700 ºC).

	Glass	*Glass–ceramic*
Ln–0	9.46	10.85
La–0.1	9.46	10.84
La–0.2	9.03	10.42
La–0.3	9.71	11.09
Nd–0.1	9.65	10.83
Nd–0.2	9.41	11.12
Nd–0.3	9.79	10.48
Gd–0.1	9.65	10.32
Gd–0.2	9.32	10.38
Gd–0.3	10.06	9.38
Yb–0.1	10.21	10.50
Yb–0.2	9.09	10.06
Yb–0.3	10.01	9.79

With respect to the CTE variation for GCs, their thermal expansion behaviour depends on the nature and amount of crystalline phase present in the GC system. As will be discussed in *section 4.4.2.4*, diopside–based crystalline phases comprise the majority of the crystalline content in the investigated GCs. It has been shown previously that mono–mineral GCs containing augite (Al–containing diopside) as the only crystalline phase exhibit a CTE value of ~9.5 × 10^{-6} K^{-1} [181]. Since the glass compositions being investigated in the present study also comprise of Sr^{2+} and Ln^{3+} ions, therefore an increase in the CTE of resultant GCs in inevitable. It is noteworthy that in a crystallized glass seal, the CTE of GC decides the stability and hermeticity of join between metal–ceramic or ceramic–ceramic components of SOFC as the glass seal is prone to crystallize during joining. In the present case, considering the CTE value of ceramic electrolyte (i.e. 8YSZ) to be ~10 × 10^{-6} K^{-1} and for metallic interconnect (Crofer22 APU; Sanergy HT) varying between (11 – 12 × 10^{-6} K^{-1}), the GC compositions with their CTE values ≥ 10.5 × 10^{-6} K^{-1} should be suitable for rigid GC seals. However, long term thermal stability of these GCs is yet to be investigated.

4.4.2.3 Sintering behaviour of glass powders

4.4.2.3.1 *In situ* hot–stage scanning electron microscopy

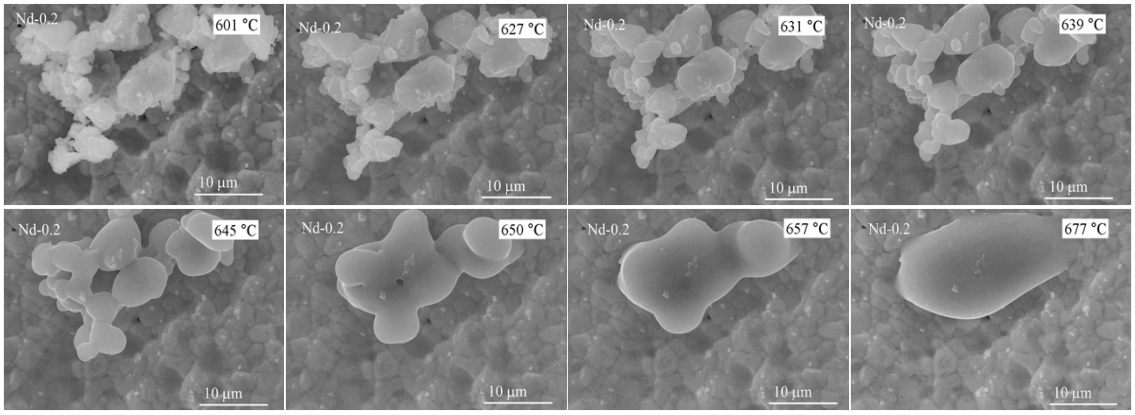

Fig. 4.4.2: HT–ESEM images for glass Nd–0.2 obtained *in situ* during heat treatment of glass powder in the temperature range of 600 – 680 ºC.

Fig. 4.4.2, 4.4.3, and 4.4.4 present the SEM images of the glasses Nd–0.2, Gd–0.2 and Yb–0.2, respectively at temperatures varying between 600 – 750 ºC. As per the observations made in HT–ESEM, the glass particles started to move and rotate in the temperature range of 500 – 600 ºC without depicting any changes in their morphology. A gradual increase in temperature to 620 – 630 ºC led to the slight softening of the glass particles (typically characterized by a smoothening of their edges). This temperature range is almost equivalent to the softening point of glasses as observed from thermal expansion curves of the investigated glasses. A dwell for 5–7 min at this stage initiated the neck formation between the particles (i.e. beginning of sintering). Further increase in temperature to 640 – 650 ºC led to the growth in neck formation among the glass particles resulting in a string of particles. The neck formation was observed to shift towards higher temperature with decrease in ionic radii of lanthanide cation. In the temperature interval of 650 – 670 ºC, the as formed string of particles merges into a single droplet of glass. Beyond this point, the apparition of very light, rounded shadows (darker areas) on the surface of glass droplets might suggest an amorphous phase separation. This phenomenon was observed in case of glass Yb–0.2 at 680 ºC (Fig. 4.4.4) while glass Nd–0.2 exhibited phase separation at comparatively higher temperature i.e. 720 ºC (not shown). A macroscopic shrinkage is observed around 750 ºC.

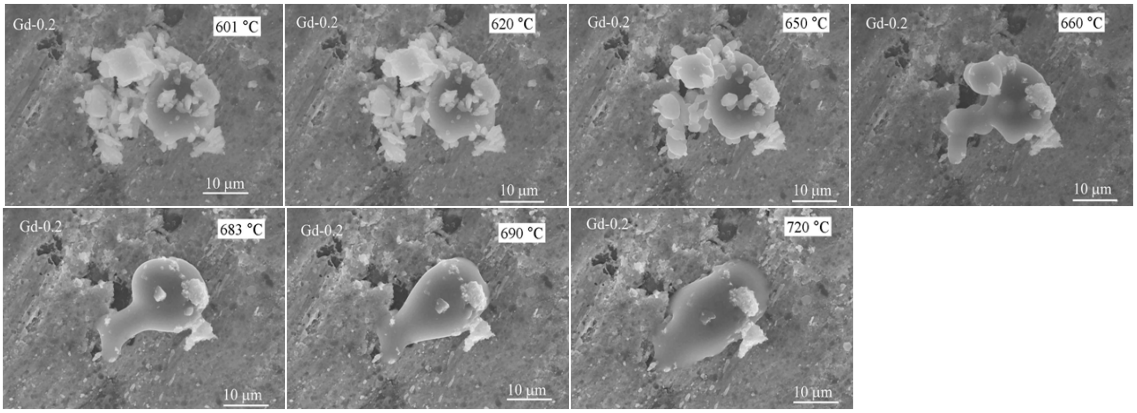

Fig. 4.4.3: HT–ESEM images for glass Gd–0.2 obtained *in situ* during heat treatment of glass powder in the temperature range of 600 – 720 ºC.

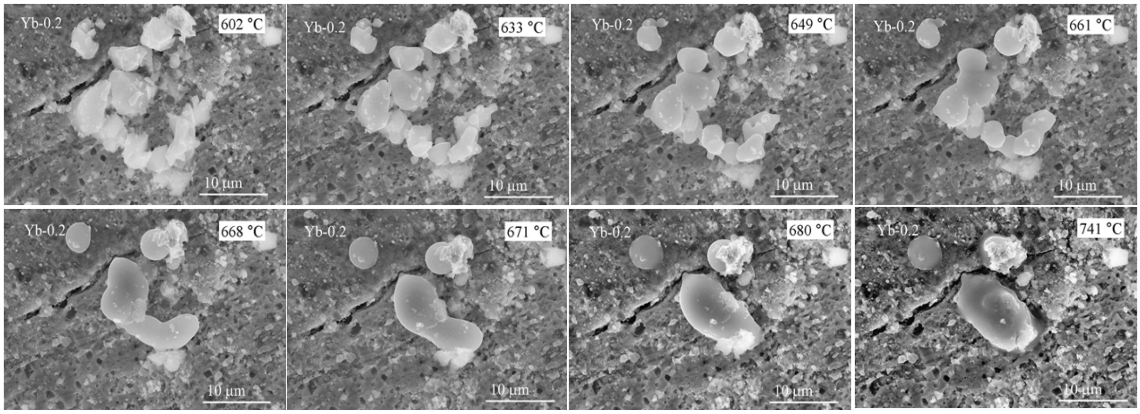

Fig. 4.4.4: HT–ESEM images for glass Yb–0.2 obtained *in situ* during heat treatment of glass powder in the temperature range of 600 – 750 ºC.

4.4.2.3.2 HSM–DTA

Fig. 4.4.5 presents the data as obtained from DTA and HSM (β = 5 $Kmin^{-1}$) pertaining to sintering and devitrification behaviour of glasses that allow observation of the following trends:

1. Fig. 4.4.5a–e presents the variation in the relative area obtained from the HSM measurement and differential temperature (from DTA) with respect to temperature for glass Ln–0 (Fig. 4.4.5a), La–0.3 (Fig. 4.4.5b), Nd–0.3 (Fig. 4.4.5c), Gd–0.2 (Fig. 4.4.5d) and Yb–0.2 (Fig. 4.4.5e), respectively. The DTA thermographs of all the glasses exhibited a single crystallization exothermic curve. This signifies that the GC is formed either as a result of single phase crystallization or of an almost simultaneous precipitation of different crystalline phases.
2. The temperature of first shrinkage (T_{FS}; $\log\eta = 9.1 \pm 0.1$, η is viscosity; dPa s) as obtained from HSM (Fig. 4.4.6a) varied between 750 – 794 ºC depending on the nature and amount of lanthanide content in glasses (Fig. 4.4.6).
3. Increasing La_2O_3 and Yb_2O_3 concentration in glasses showed a monotonic increase in T_{FS} (Fig. 4.4.6a and 4.4.6d) while glasses containing Nd_2O_3

and Gd_2O_3 exhibited a dip in their respective T_{FS} values for glasses Nd–0.1 and Gd–0.1 in comparison to lanthanide free glass Ln–0. Further increment in lanthanide content in Nd– and Gd–containing glasses shifted their T_{FS} temperature to higher side.

4. As is evident from Fig. 4.4.5a, lanthanide free glass Ln–0 exhibited a single stage shrinkage behaviour. Although, a slight tendency towards exhibiting a two–stage sintering behaviour can be seen in glass Ln–0 but it is not as evident as in the case of lanthanide containing glasses.
5. The two stage shrinkage behaviour was observed for all the glasses as is evident from Fig. 4.4.5. The conclusion of first sintering stage is characterized with temperature of first maximum shrinkage (T_{MS1}; $\log\eta = 7.8 \pm 0.1$) while the end of second sintering stage is characterized with temperature of second maximum shrinkage (T_{MS2}). Fig. 4.4.6 presents the variation in the values of T_{MS1} and T_{MS2} with respect to the lanthanide content in glasses. In all the glass compositions the $T_{MS1}<T_c$ (onset of crystallization) which demonstrates that sintering precedes crystallization in all the glasses (including Ln–0) and therefore, well sintered and mechanically strong glass powder compacts should be expected.
6. The value for T_{MS2} was higher than T_c in all the investigated glasses (Fig. 4.4.6) depicting that shrinkage continued in the glass powders even after onset of crystallization possibly due to the presence of residual glassy phase in the GC.
7. The values for T_p varied between 838 – 928 ºC for La–containing glasses; 838 – 918 ºC for Nd–containing glasses; 838 – 931 ºC for Gd–containing glasses and 838 – 935 ºC for Yb–containing glasses. As is evident from Fig. 4.4.6, the lowest value of T_p was observed for glass Ln–0 and the introduction of lanthanides (1.26 mol%) in this glass resulted in a considerable increase in peak temperature of crystallization. Further increase in lanthanide content in glasses (>1.26 mol%) did lead to an

increase in their T_p; however, this shift was less significant in comparison to that observed between glasses Ln–0 and Ln–0.1, respectively.

8. The value of sintering ability parameter S_c (= $T_c - T_{MS1}$) for the lanthanide free glass, Ln–0 (S_c = 17), was considerably lower (~ 2 times) in comparison to its lanthanide containing counterparts (Fig. 4.4.5), thus depicting that addition of lanthanides (~1 mol% – 4 mol%) in aluminosilicate glasses enhances their sintering ability considerably [182]. In general, increasing the lanthanide content in glasses between 1 – 4 mol% (approximately) improved their sintering ability. Among all the lanthanide containing glasses, the lowest value of S_c was observed for glass Gd–0.2 (S_c = 33) while the highest was obtained for glass Yb–0.3 (S_c = 56).

9. Fig. 4.4.7 and Fig. 4.4.8 present the photomicrographs of all the investigated glasses depicting the changes in geometric shape of the glasses with respect to temperature as obtained from HSM. The deformation temperature (temperature at which the first signs of softening are observed; generally shown by the disappearance or rounding of the small protrusions at the edges of the sample; $\log\eta = 7.8 \pm 0.1$) of all the glasses varied between 870 – 890 ºC while sphere formation in almost all the glasses occurred at ~900 ºC. This temperature range (850 – 900 ºC) is usually considered for joining of SOFC metallic/ceramic components by a glass/GC sealant. In fact, attempts have been made to accomplish the joining of SOFC metallic interconnect with ceramic electrolyte at higher temperatures (950 – 1050 ºC) [66, 150]. However, sealing at temperatures >900 ºC usually degrades the metallic interconnect and thus affects the performance of SOFC in a detrimental manner [183].

10. The half ball temperature ($\log\eta = 4.1 \pm 0.1$) and flow temperature ($\log\eta = 3.4 \pm 0.1$) for all the glasses varied between 1190 – 1260 ºC and 1200 – 1270 ºC, respectively (Fig. 4.4.7 and Fig. 4.4.8). The highest half ball and flow temperatures were observed for glass Ln–0 depicting its highly refractory nature. However, introduction of lanthanide in glass Ln–0 (0.05

Mg^{2+} + 0.05 Si^{4+} ↔ 0.1 Ln^{3+}) led to a significant decrease in both the temperature values (i.e. half ball and flow) irrespective of the nature of lanthanide cation which exhibits the influence of lanthanide oxides on the viscosity of aluminosilicate glasses.

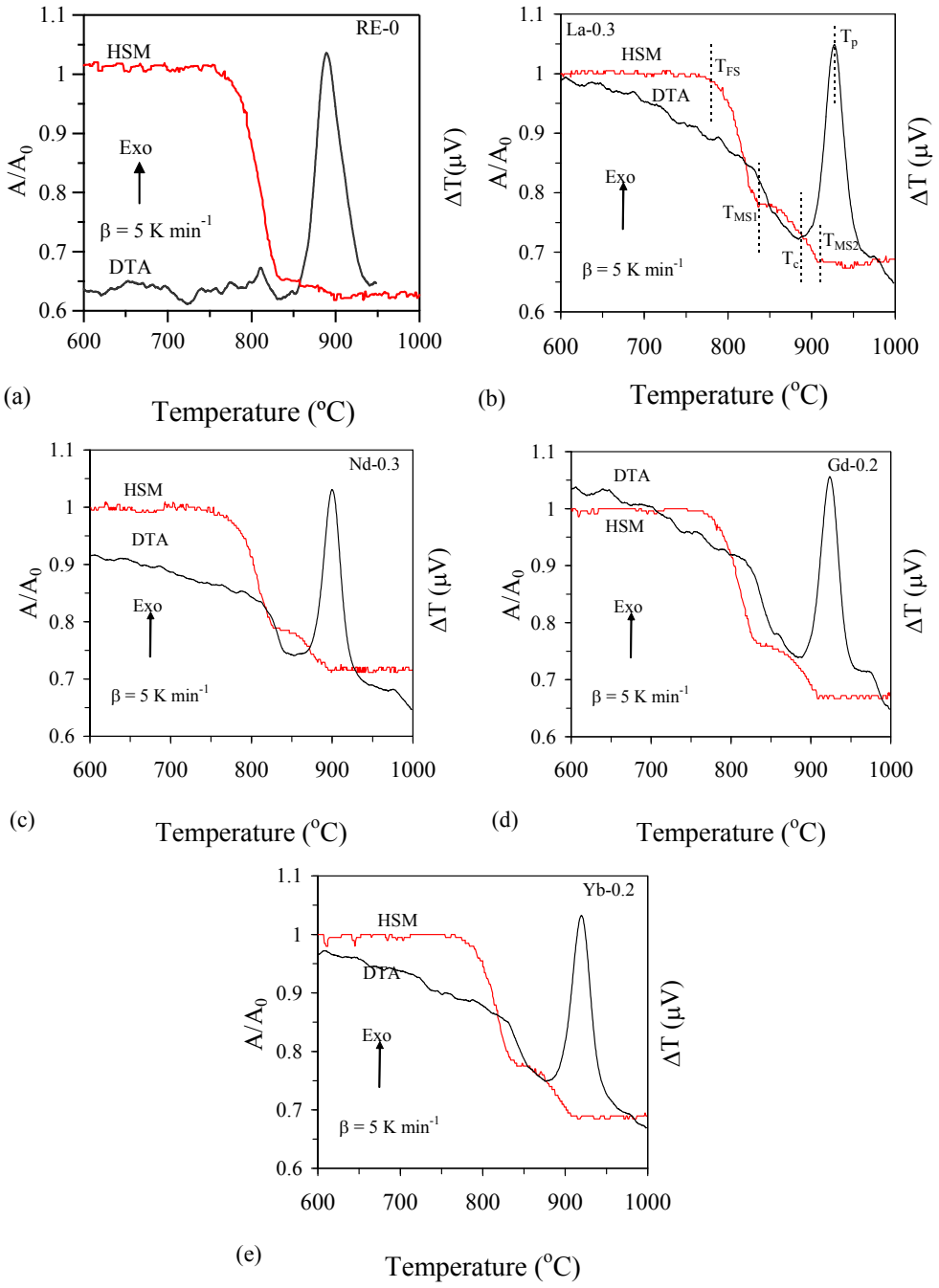

Fig. 4.4.5: Comparison of DTA and HSM curves on the same temperature scale for glasses: (a) Ln–0, (b) La–0.3, (c) Nd–0.3, (d) Gd–0.2, and (e) Yb–0.2 at heating rate of 5 $Kmin^{-1}$.

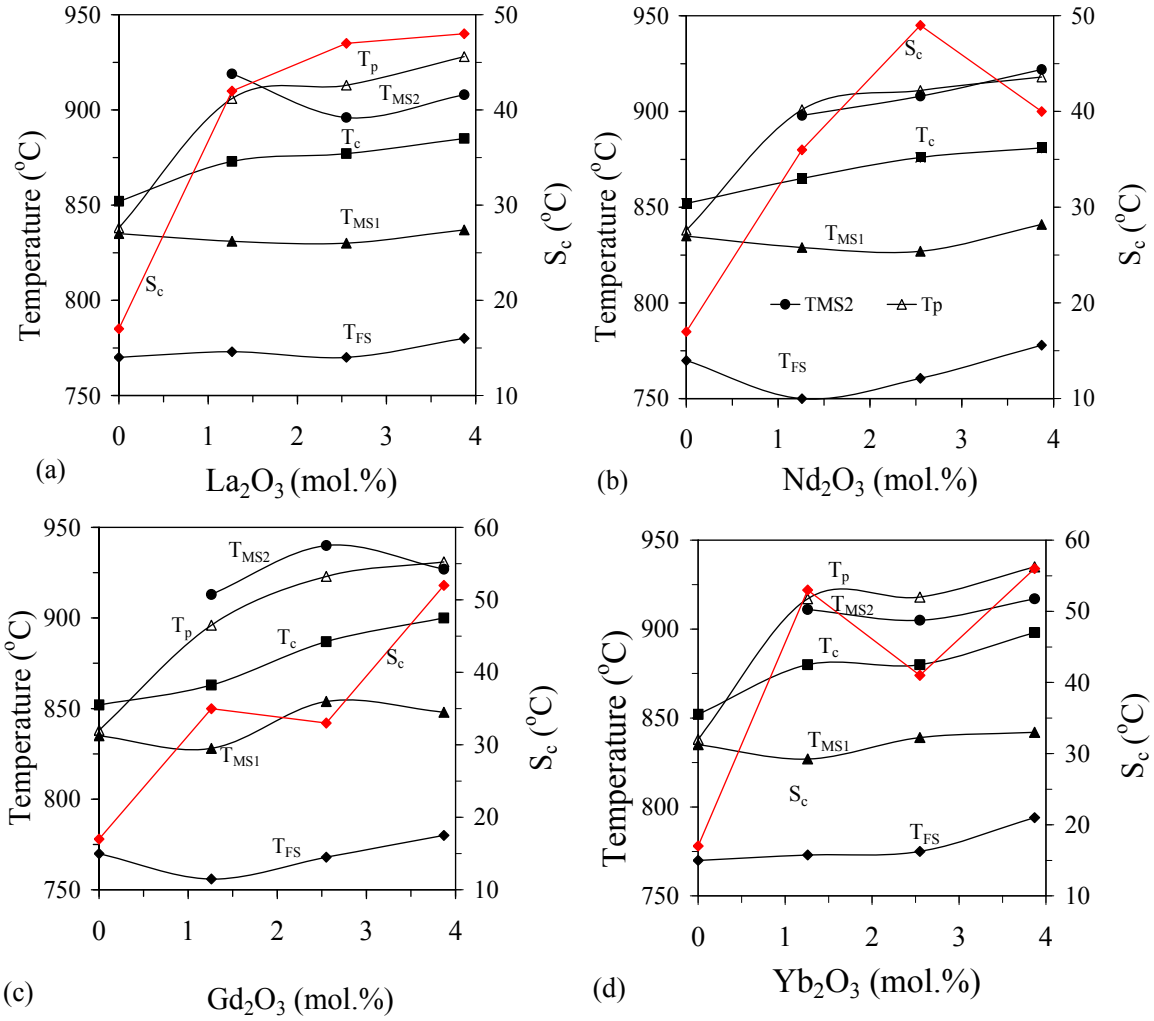

Fig. 4.4.6: The variation in different thermal parameters for glasses obtained from DTA and HSM with respect to (a) La_2O_3, (b) Nd_2O_3, (c) Gd_2O_3, and (d) Yb_2O_3 content in glasses. The error bars have been masked by the data points.

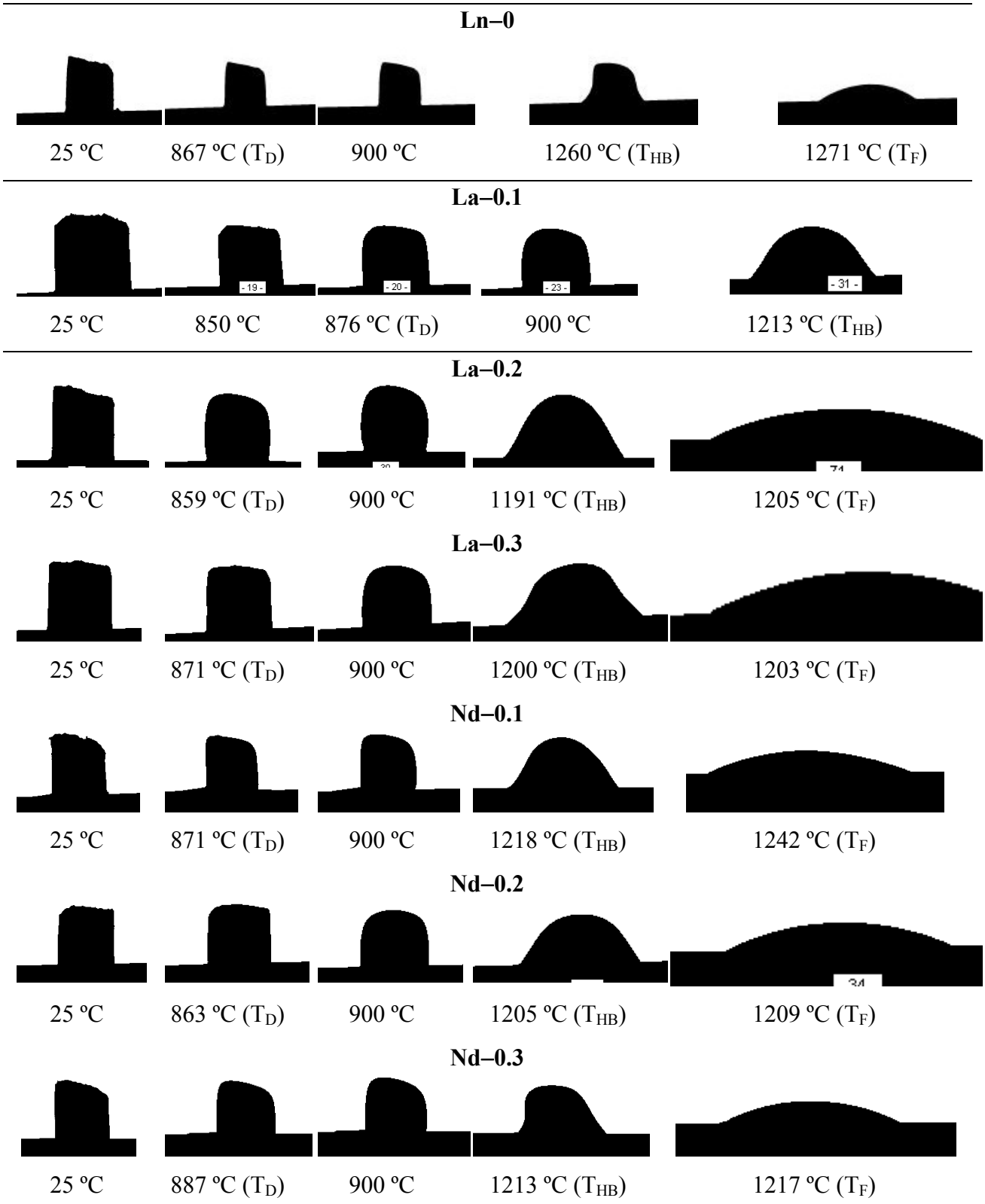

Fig. 4.4.7: HSM images of lanthanide free glass (Ln–0) along with La_2O_3 and Nd_2O_3 containing glass powder compacts on alumina substrates at various stages of heating cycle.

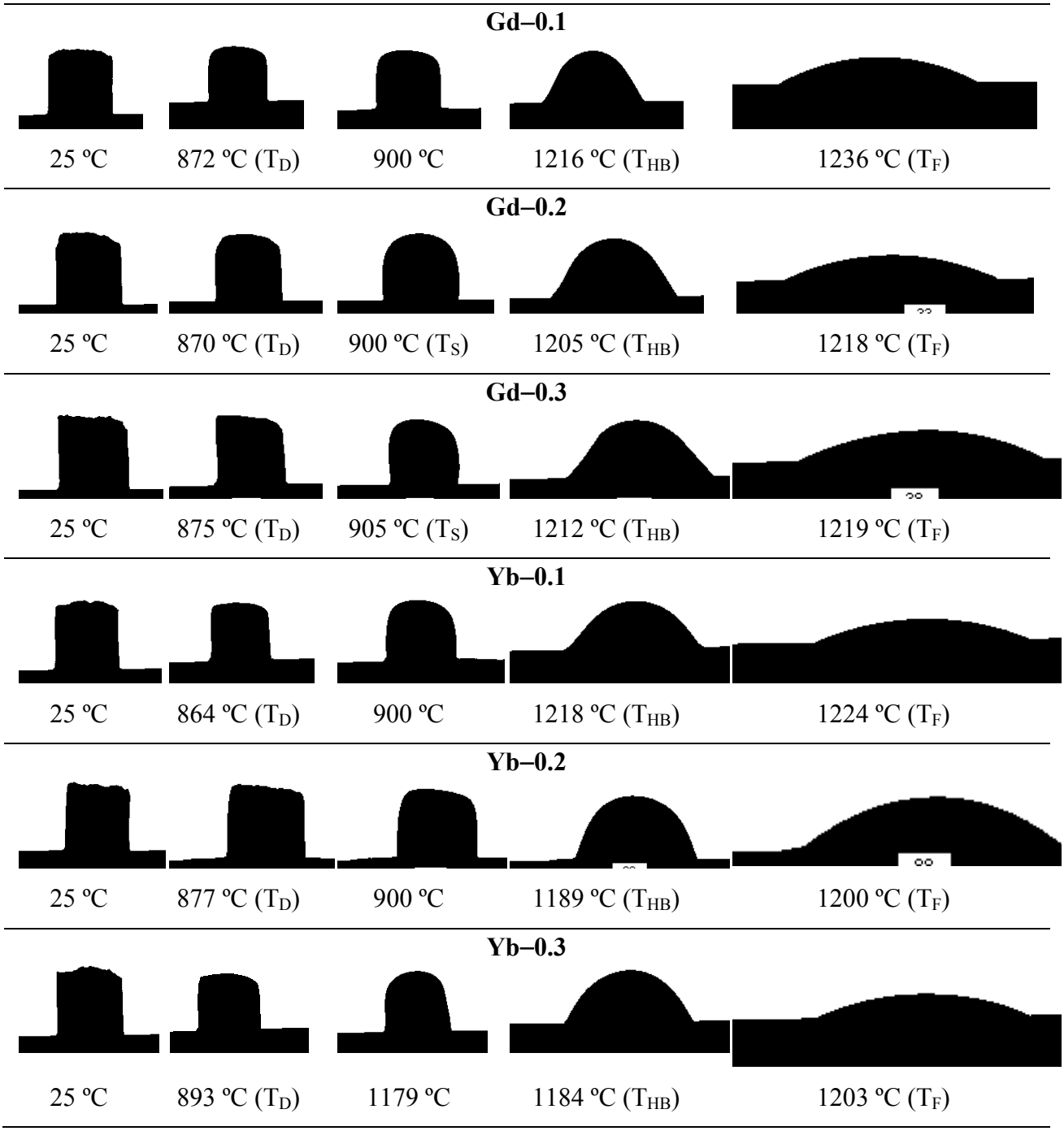

Fig. 4.4.8: HSM images of Gd_2O_3 and Yb_2O_3 containing glass powder compacts on alumina substrates at various stages of heating cycle.

4.4.2.4 Crystalline phase evolution

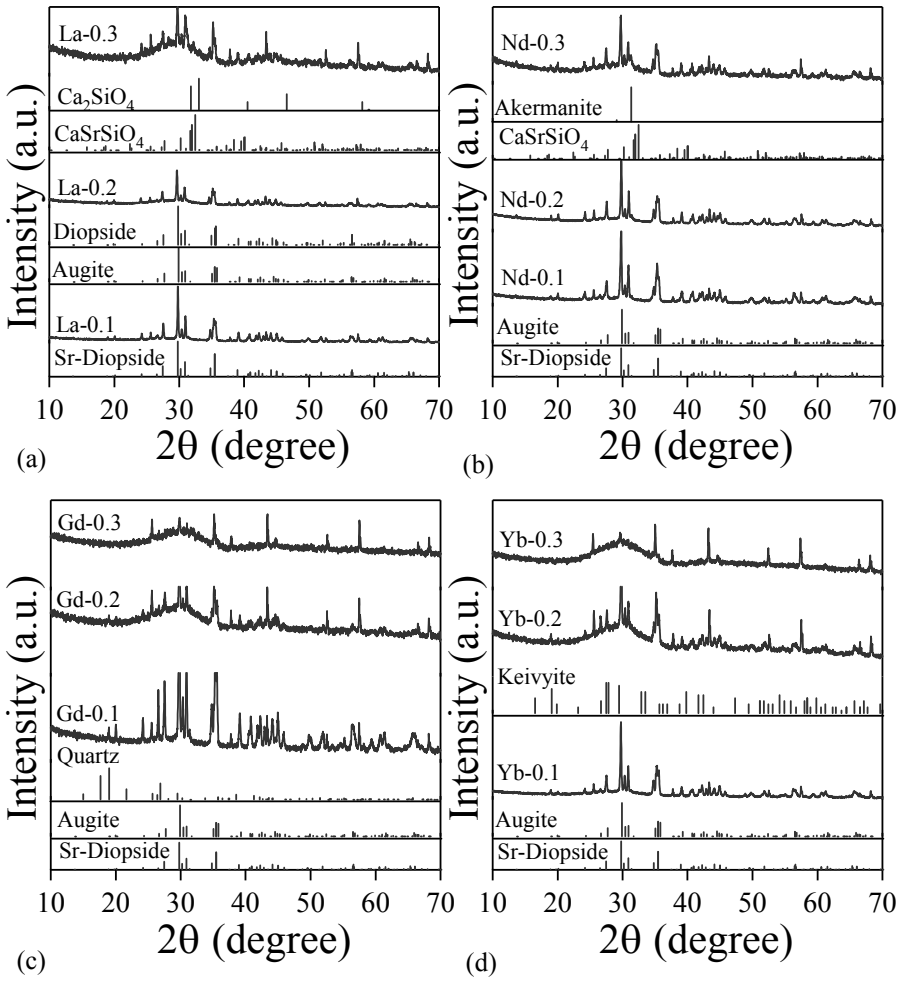

Fig. 4.4.9: X–ray diffractograms of glass powder compacts after sintering at 850 ºC for 1 h.

Fig. 4.4.9 presents the X–ray diffractograms of the sintered GCs while Table 4.4.4 presents the quantitative analysis of the crystalline phases present in all the investigated GCs as obtained from XRD analysis adjoined with Rietveld–R.I.R technique. Fig. 4.4.10 shows the fit of a measured XRD pattern of a sintered GC Ln–0 by using the TOPAS software. The fitting to the measured X–ray diagram has been performed by a least–square calculation. The calculated diagram (Fig. 4.4.9) is based on crystallographic structure models, which also take into account specific instrument and sample effects. The parameters of this model have been refined simultaneously using least–squares methods in order to obtain the best fit to all measured data. By

least–squares refinement, a so–called figure–of–merit function R has been defined, which describes the residual (agreement) between observed and calculated data [151]. The R factors show the mean deviation in accordance with the model used in per cent. The values of *R* factor (not shown) as obtained in the present investigation are well within the limits of experimental accuracy. The difference plot in Fig. 4.4.10 does not show any significant misfits. The differences between the main peaks of augite, Sr–diopside and corundum are caused by adjustment difficulties based on the crystallinity of the phases.

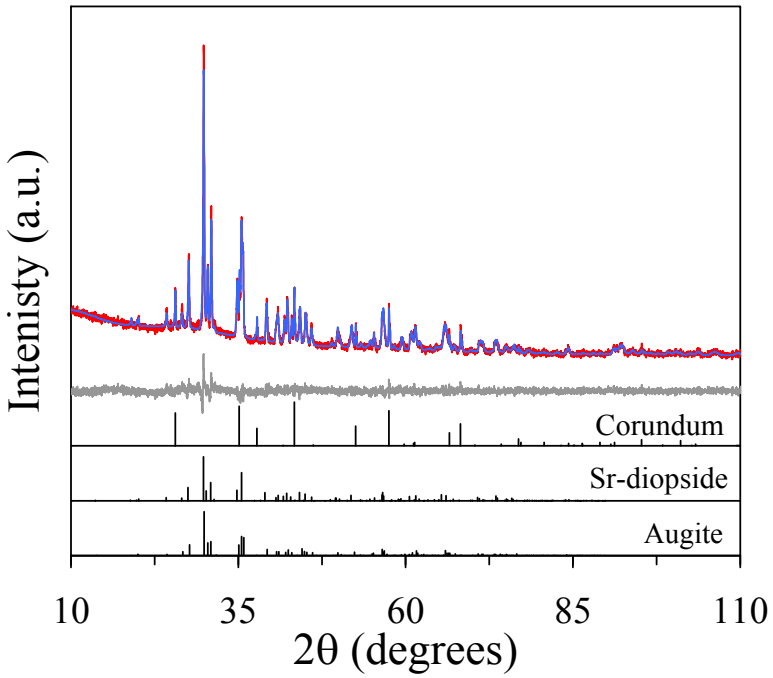

Fig. 4.4.10: Observed (red), calculated (blue), and difference curve from the Rietveld refinement of GC Ln–0 after sintering at 850 ºC for 1 h.

Sr–containing Di ($Ca_{0.8}Sr_{0.2}MgSi_2O6$; ICSD: 68178) crystallized as the primary phase in all the GCs followed by an Al–containing Di [augite; $(Ca(Mg_{0.70}Al_{0.30})(Si_{1.70}Al_{0.30})O_6$; ICSD: 62547] as the second most dominant crystalline phase except for compositions La–0.2 and Yb–0.2 (Table 4.4.4). While augite dominated the crystalline phase assemblage of GC La–0.2 followed by Sr–diopside as the secondary phase; Yb–containing keivyite ($Yb_2Si_2O_7$; ICSD: 65363) crystallized as the primary

phase in composition Yb–0.2 followed by augite and Sr–diopside as the secondary phases. Some other alkaline earth silicate based crystalline phases including Ca_2SiO_4 (ICSD: 39124), $CaSrSiO_4$ (ICSD: 20544), akermanite (Ca_2MgSi_2O7; ICSD: 50066) and low–quartz (SiO_2; ICSD: 75657) crystallized as minor phases in the GCs as presented in Table 4.4.5. Increasing lanthanide content in glasses (in particular glasses containing Gd and Yb) retarded their tendency towards devitrification as is evident from Table 4.4.5. The residual amorphous content in GCs is highest for GCs Gd–0.3 (96 wt.%) and Yb–0.3 (96 wt.%). The high amount of residual glassy phase along with the flow behaviour of these compositions as exhibited by XRD and HSM, respectively, makes the investigated glasses as potential candidates for self–healing GC seals.

Table 4.4.4: Quantitative crystalline phase analysis of glass–ceramics produced at 850 ºC for 1 h from Rietveld–R.I.R. analysis (wt.%)

	Amorphous	*Augite*	*Sr-Di*	Di	Ak	$CaSrSiO_4$	Ca_2SiO_4	Quartz	Keivyite
RE-0	52.43	23.86	23.71	-	-	-	-	-	-
La-0.1	53.43	-	46.57	-	-	-	-	-	-
La-0.2	55.48	26.32	-	18.20	-	-	-	-	-
La-0.3	56.78	8.50	16.74	-	0.00	16.44	1.55	-	-
Nd-0.1	48.89	10.68	40.43	-	-	-	-	-	-
Nd-0.2	54.09	1.47	44.44	-	-	-	-	-	-
Nd-0.3	68.14	-	27.74	-	2.00	2.12	-	-	-
Gd-0.1	31.53	7.27	58.85	-	-	-	-	2.35	-
Gd-0.2	86.24	0.00	13.43	-	-	-	-	0.33	-
Gd-0.3	96.19	0.00	3.81	-	-	-	-	-	-
Yb-0.1	52.86	17.73	29.41	-	-	-	-	-	-
Yb-0.2	56.70	12.56	6.76	-	-	-	-	-	23.99
Yb-0.3	95.97	-	4.03	-	-	-	-	-	-

3.5 Electrical conductivity of glass-ceramics

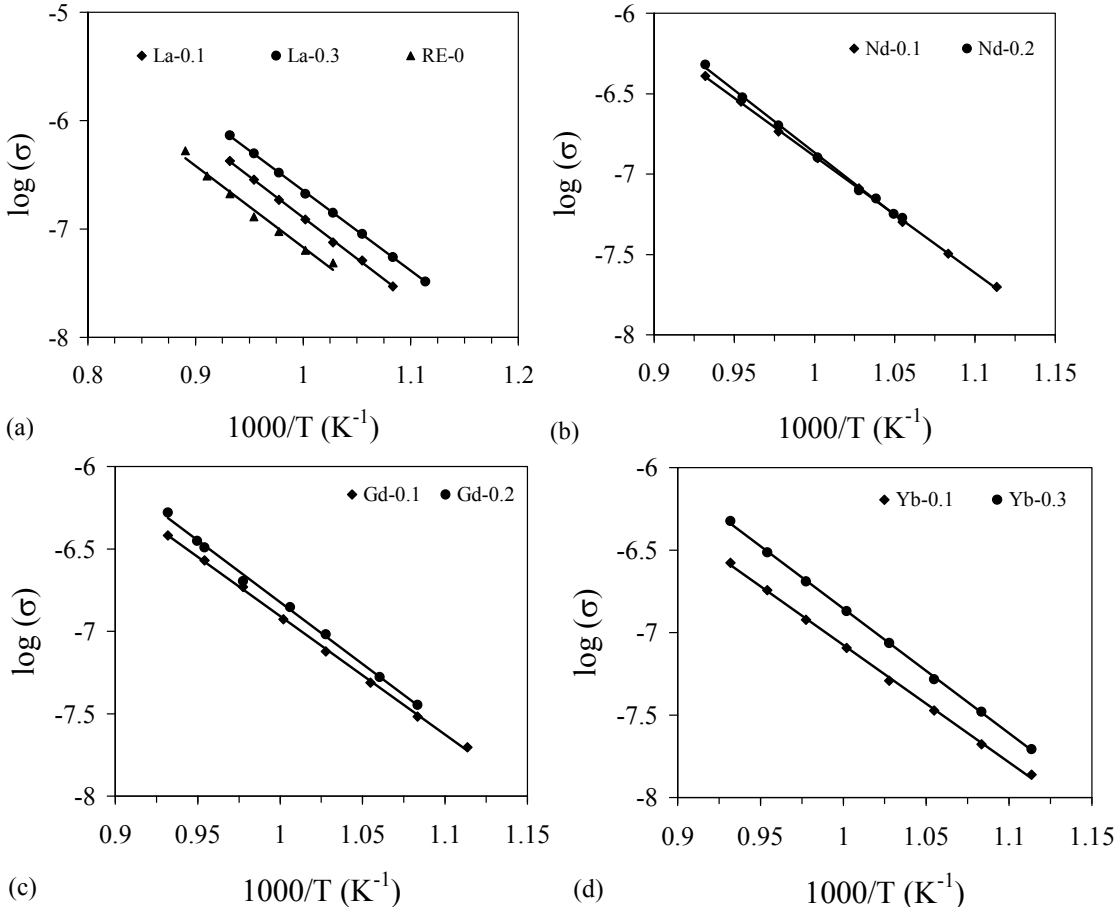

Fig. 4.4.11: Total electrical conductivity (σ) of dense glass–ceramics in air in the temperature range of 625 – 800 ºC: (a) La–, (b) Nd–, (c) Gd, (d) Yb–containing glass–ceramics.

Fig. 4.4.11 presents the variation in the electrical conductivity (σ) of GCs with respect to temperature. The conductivity of all the GCs varied between (1.19 – 7.33) × 10^{-7} Scm^{-1} (750 – 800 ºC). The electrical conductivity of the GCs increased with increasing temperature due to the higher diffusion of network modifying cations. In order for a material to qualify for sealing application in SOFC, it should behave as an electrical insulator with its total electrical conductivity lower than 10^{-5} Scm^{-1} so as to avoid parasitic currents which decrease the efficiency of the system. The electrical conductivity

of investigated glass compositions is considerably lower in comparison to its desired value which makes them suitable material for sealing. Further, the electrical conductivity was observed to increase with increasing lanthanide content in GCs. Also, decreasing ionic radii (increasing ionic field strength) of lanthanide cations decreased the total electrical conductivity of the GCs as La containing GCs exhibited the highest electrical conductivity while the lowest conductivity was observed for Yb– containing GCs.

The electrical conductivity of a seal glass depends on the glass network formers, modifiers and intermediates. Although, a lot of literature has been published with reference to the role of various glass components on their electrical conductivity, the additive effect is still uncertain because of the different roles played by these ions in varying concentrations. In particular, there is a considerable dearth of data on the effect of lanthanide cations on the electrical conductivity of glasses/GCs. As a rule of thumb, it is generally accepted that the electrical conductivity should increase with decreasing ionic radii (i.e. La–containing glasses should exhibit lower electrical conductivity in comparison to Yb containing glasses) [21]. However, it should be noted that this rule might not stand valid in glasses with high compositional complexity, as has been seen in the present study. Therefore, a detailed structural evaluation of the investigated glass system is required with special emphasis on their tendency towards glass–in–glass phase separation and lanthanide clustering as both of these phenomenon control the electrical conductivity in glasses to a greater extent. Further, it should be noted that in a GC system, the electrical conductivity is decided by the nature and amount of crystalline phase formed along with the chemical composition of residual glassy matrix [21].

4.4.3. Discussion

The sintering and crystallization processes play an important role in determining the properties and applications of GC sealants for SOFC. For example, an installation process for the Siemens–SOFC stack required that the sealing glass be partially viscous at 950 ºC for 2 – 3 h to allow small displacements of the single stack elements after joining at 1000 ºC [115]. This can be achieved by using a slowly crystallizing glass. Therefore, sintering stage should be completed before significant crystallization occurs in order to get a fully dense material suitable for SOFC seal. Uncontrolled crystallization

during the initial sintering process can lead to the formation of a porous sealing layer that can adversely affect the SOFC operation.

During the sintering of a glass–powder compact with a size distribution of glass particles, small particles get sintered first as shown by Prado et al. [184]. Thus, sintering kinetics at first shrinkage is dominated by the neck formation among smallest particles by viscous flow and is best described by the Frenkel model of sintering [32]. Maximum shrinkage is reached when larger pores (pores formed from cavities among larger particles) have disappeared due to viscous flow that reduces their radii with time. This region of sintering kinetics may be described by the Mackenzie–Shuttleworth model of sintering [185]. However, various physical processes (entrapped insoluble gases, crystallization) occurring at the very end of sintering process might affect the densification kinetics.

In accordance with the above discussed theory, the following sintering and devitrification stages were observed in the present study with increment in temperature: (i) the initiation of sintering took place with neck formation in the temperature range of 620 – 650 ºC followed by the formation of string of particles which further converted into a single glass droplet with increasing temperature; (ii) the glass droplet exhibited glass–in–glass phase separation whose tendency increased with decreasing ionic radii of lanthanide cation; (iii) macroscopic shrinkage as observed under HT–ESEM which is the temperature range of first shrinkage (T_{FS}) as detected by HSM; (iv) two–step sintering behaviour (as observed in HSM) most probably due to the presence of glass–in–glass phase separation; (v) onset of crystallization (T_c) after the termination of first sintering step (T_{MS1}), thus, resulting in well sintered and dense glass powder compacts.

Liquid–liquid phase separation is a well–known and common phenomenon in silicate liquids, and can be observed in high–silica regions of many alkaline–earth silicate glass systems, at temperatures either above or below the liquidus [186]. Adding few mole percent of Al_2O_3 inhibits the phase separation to a significant extent in these glasses but still the nano–sized domains which are either rich in silica or in alkaline–earth aluminosilicate do exist [186]. According to De Veckey et al. [187], in glasses located in $CaO–MgO–Al_2O_3–SiO_2$ system, phase separation is caused by segregation of calcium and magnesium ions. It is probably due to this reason that a single stage–sintering

behaviour has been observed for glass Ln–0. However, addition of lanthanides in the glasses shifted the sintering behaviour from one–stage to two–stage owing to the phase separation induced by them as has also been explained by McGahay and Tomozawa [180] on the basis of theory of corresponding states. Also, the temperature values obtained from HSM are considerably higher than those obtained from *in situ* HT–ESEM (Fig. 4.4.2–4.4.4) for the initiation of sintering. This discrepancy can be explained on the basis of different magnifications of the two instruments being used to study the sintering behaviour of these glasses. While the sintering behaviour of glass powders in ESEM has been observed at a magnification of 3000x, the magnification for the lens being used in HSM is ~10x. Therefore, although, the sintering in glass powders starts at considerably lower temperatures as has been observed by HT–ESEM (Fig. 4.4.2 – 4.4.4), it can be observed in HSM only at higher temperatures in the terms of total area shrinkage (Fig. 4.4.5).

All the glass powders exhibited good sintering ability (as demonstrated by linear shrinkage data) resulting in well sintered GCs after heat treatment at 850 ºC for 1 h with varying degree of crystallinity. The influence of different lanthanides on sintering ability of investigated alkaline–earth aluminosilicate glasses has been elucidated by the sintering ability parameter ($S_c = T_c - T_{MS1}$). The parameter S_c is the measure of ability of sintering versus crystallization: the greater this difference, the more independent are the kinetics of both processes [182]. The variation in the S_c values with increasing lanthanide content in glasses as presented in Fig. 4.4.5 depict that glass compositions Gd–0.3 and Yb–0.3 exhibit better sintering behaviour ($S_c > 50$) among all the investigated glass compositions (Fig. 4.4.6d).

All the resultant GCs (except Gd–0.1) comprise of ≥ 50 wt.% residual glassy phase along with appropriate flow behaviour (Fig. 4.4.7 and 4.4.8), thus showing their ability to demonstrate self–healing behaviour at SOFC operation temperature (800 – 900 ºC). In particular, the glass compositions La–0.1, La–0.2, Nd–0.1, Nd–0.2 are suitable for GC sealing in SOFC mainly owing to their appropriate CTE values along with the absence of any undesired crystalline phases. Although, Ln–0 possess similar traits but it does lack behind due to its high refractory nature. Also, the GC compositions Gd–0.3 and

Yb–0.3 might be considered as potential candidates for self–healing glass seals as they comprise of > 95 wt.% residual glassy phase and are mono–mineral in nature (i.e. possess only one crystalline phase) which is a highly desirable feature for self–healing seals. The concept of self–healing glass seals can help alleviate some of the expansion mismatch and still be able to form a functioning seal between materials with significant mismatch by healing the cracks formed during thermal transients. Although, good sintering ability, low devitrification tendency, appropriate thermal expansion, good flow behaviour and low electrical conductivity, make these GCs (in particular Gd–0.3 and Yb–0.3) to be potential candidates for self–healing glass seals in SOFC; still the GCs have to prove their efficacy during long term thermal treatments (~1000 h). The positive feature of these GCs is that they contain Sr–diopside as the only crystalline phase which possesses high CTE (~9 × 10^{-6} K^{-1}) and does not exhibit polymorphism during long term heat treatments as is usually seen in case of $BaO–Al_2O_3–SiO_2$ based glass seals (hexacelsian → celsian) [41]. Also, the absence of BaO from the glasses will ensure minimal interfacial reactions with metallic interconnect [43].

4.5 Thermal and mechanical stability of lanthanide–containing glass–ceramic sealants for solid oxide fuel cells

4.5.1 Introduction

A major issue with the glass based seals is related with their long–term chemical and thermal stability. Since the current design of SOFCs requires them to operate at temperatures varying between 800 – 1000 ºC, most of the aluminosilicate based glass seals are prone to devitrification in this temperature range, especially during long–term operation. Although good sintering behaviour along with controlled devitrification are the prerequisites for a suitable sealing glass composition, the formation of some undesirable crystalline phases in the glass seal can severely affect the performance of SOFC stack. For instance, the barium – rich aluminosilicate based glass seals [36, 44] are known to exhibit appropriate CTE and sintering behaviour required for their operation in SOFC. However, these glasses tend to devitrify at 800–850 ºC resulting in the appearance of hexacelsian ($BaAl_2Si_2O_8$) crystalline phase in the GC which during gradual SOFC operation transforms to its monoclinic polymorph with low CTE, lowering the CTE values for the GC seal along with deterioration of its mechanical properties [188]. Similarly, severe chemical interaction has been observed at the interface between BaO–containing or alkali–containing glass seals when joined with metallic interconnects of SOFCs [189, 190]. A vast amount of literature available in this area depicting the failure of glass seals during long–term operation warrants a thorough investigation of long–term thermal and chemical stability of any proposed glass composition for high temperature sealing application. In this pursuit, the present chapter is focused upon investigating the long–term (up to 1000 h) thermal and chemical stability of lanthanide containing GC sealants proposed in the previous chapter for SOFC (Table 4.4.1). However, for this study we have choosen four specific glass compositions, namely La–0.2, Nd–0.2, Gd–0.3 and Yb–0.3, considering the results obtained in our previous study depicting the sintering and flow behaviour of lanthanide containing aluminosilicate GC sealants (chapter 4.4). The main criteria for choosing the investigated glass compositions were: (i) good sintering ability; (ii) high amorphous/crystalline ratio; and (iii) appropriate CTE.

4.5.2. Results and Discussion

4.5.2.1 Structural transformations and shape deformation during sintering of glass powders

Fig. 4.5.1 presents HT–XRD patterns of the investigated glasses observed from room temperature to 850 ºC. All the glasses were amorphous until 800 ºC as is evident from Fig. 4.5.1. Further, with gradual increase in temperature from 800 to 850 ºC, crystals started to precipitate in La–0.2 (Fig. 4.5.1a) and Nd–0.2 (Fig. 4.5.1b) while glasses Gd–0.3 (Fig. 4.5.1c) and Yb–0.3 (Fig. 4.5.1d) still exhibited an amorphous halo. The observed XRD phase reflections for samples La–0.2 and Nd–0.2 correspond to diopside ($CaMgSi_2O_6$ chemical formula; ICDD: 71–1497). Moreover, dwell at 850 ºC for 1 h led to an increase in the intensity of phase reflections for diopside in both samples (La–0.2 and Nd–0.2) along with the appearance of phase reflections corresponding to low–quartz (SiO_2; ICDD: 77–8626) while glasses Gd–0.3 and Yb–0.3 still exhibited a broad amorphous halo depicting their non–crystalline nature. The HT–XRD data on all the glass compositions are in good agreement with the room temperature XRD data obtained from glass powder compacts sintered at 850 ºC for 1 h (Fig. 4.4.9), except that some low–intensity reflections corresponding to diopside–based phases could be observed in the room temperature patterns of compositions Gd–0.3 and Yb–0.3.

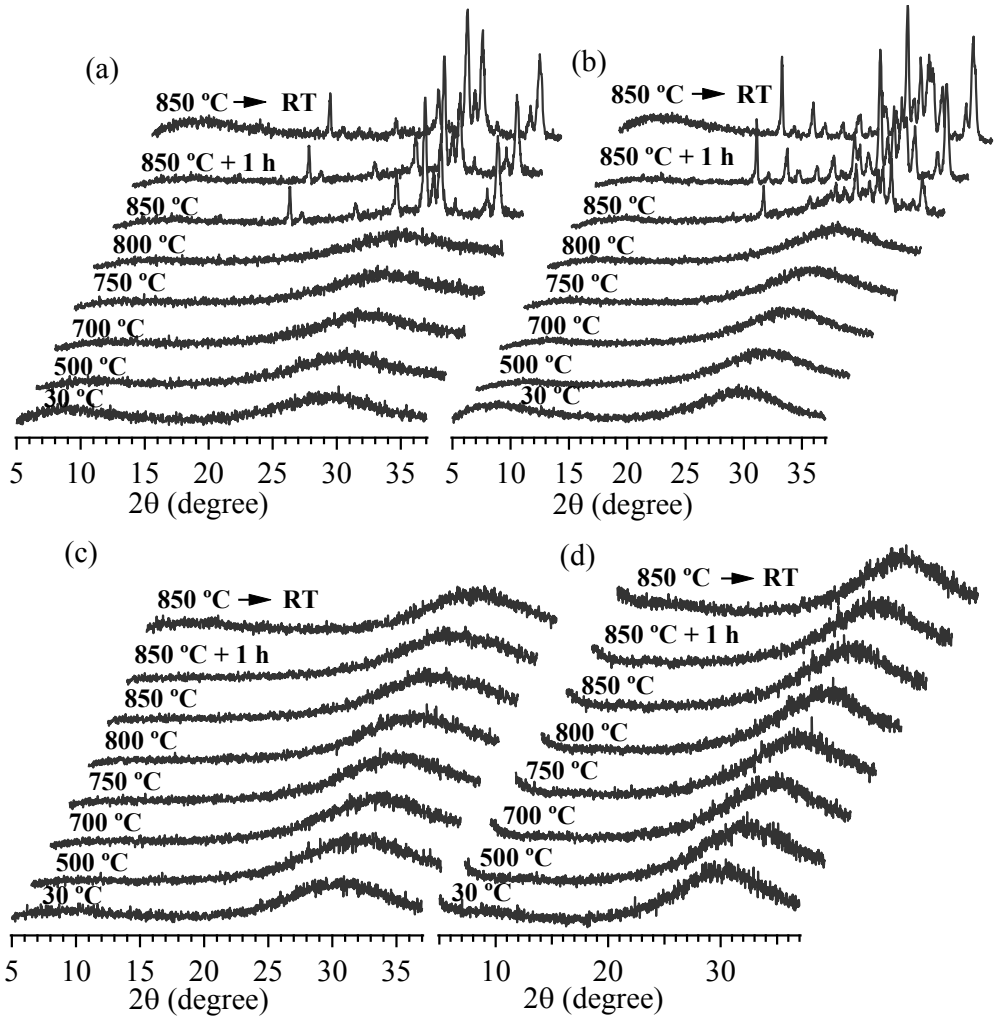

Fig. 4.5.1: *In–situ* XRD patterns observed from room temperature to 850 ºC temperature for (a) La–0.2; (b) Nd–0.2; (c) Gd–0.3 and (d) Yb–0.3 glass.

The sluggish crystallization behaviour of glasses Gd–0.3 and Yb–0.3 in comparison to their lanthanum and neodymium containing analogues may be attributed to the structural role of these ions in aluminosilicate glasses which is further determined by their ionic radii (which controls their coordination number) and by their ionic field strength (=Z/r^2; Z is the charge on cation, r is its ionic radius; La^{3+}: 2.82 $Å^{-2}$; Nd^{3+}: 3.10 $Å^{-2}$; Gd^{3+}: 3.41 $Å^{-2}$; Yb^{3+}: 3.98 $Å^{-2}$) [174]. The lanthanide ions, due to their size, are able to occupy octahedral sites in the glass structure (instead of tetrahedral sites), in which the bonds between Ln^{3+} and surrounding oxygen are the weakest links in the glass structure

compared to Al–O and Si–O bonds. The stronger the Ln–O bonds (i.e. higher the ionic field strength of Ln^{3+}), higher the glass transition (T_g) and crystallization temperature, suggesting that Ln^{3+} cations act alike to Al^{3+} in these glasses [174]. The structural characterization of the investigated glasses and GCs will be discussed in *section* 4.5.*2.2*.

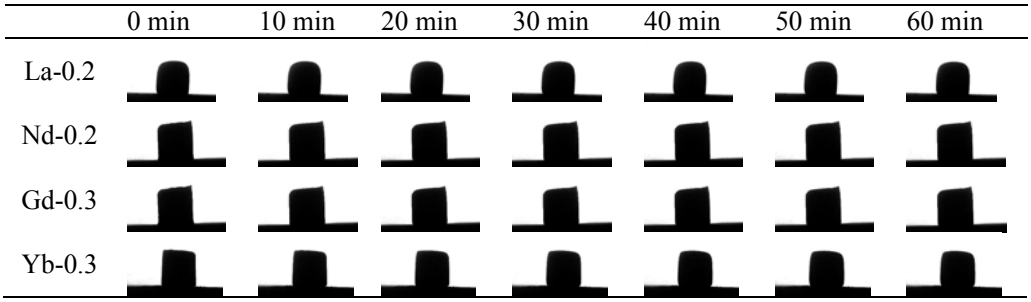

Fig. 4.5.2: HSM images of glass–powder compacts upon holding at 850 ºC for 1 h.

The HSM micrographs of glass powder compacts obtained at various time intervals during sintering at 850 ºC for 1 h are shown in Fig. 4.5.2. The glass powder La–0.2 exhibited deformation in its shape (as is evident from the rounding of edges) by the time it reached 850 ºC. However, further changes in the morphology of the sample could not be observed over 1 h dwell time. The remaining three glass samples (Nd–0.2, Gd–0.3 and Yb–0.3) although well sintered, did not exhibit such an evident deformation in their shape, thus, exhibiting their refractory nature.

From SOFC viewpoint, during sealing of SOFC stack, typically some fraction of the original glass sealant sinters and then devitrifies or begins to undergo crystallization and forms a composite of nano– and micro–scale ceramic crystalline phases. This time dependent phenomenon raises the material's viscosity and sets the seal. Although the resulting composite can be stronger than the starting glass, extensive devitrification before achieving maximum densification of glass powder often leads to the formation of pores and cracks, and poor adherence of the seal. Such an observation can be negated for the studied glass compositions since well sintered and dense glass powder compacts with appropriate thermal expansion coefficients and high mechanical strength were obtained after sintering at 850 ºC for 1 h, as will be discussed later.

4.5.2.2. Structural transformations in glasses during long term thermal treatments

4.5.2.2.1 X–ray diffraction

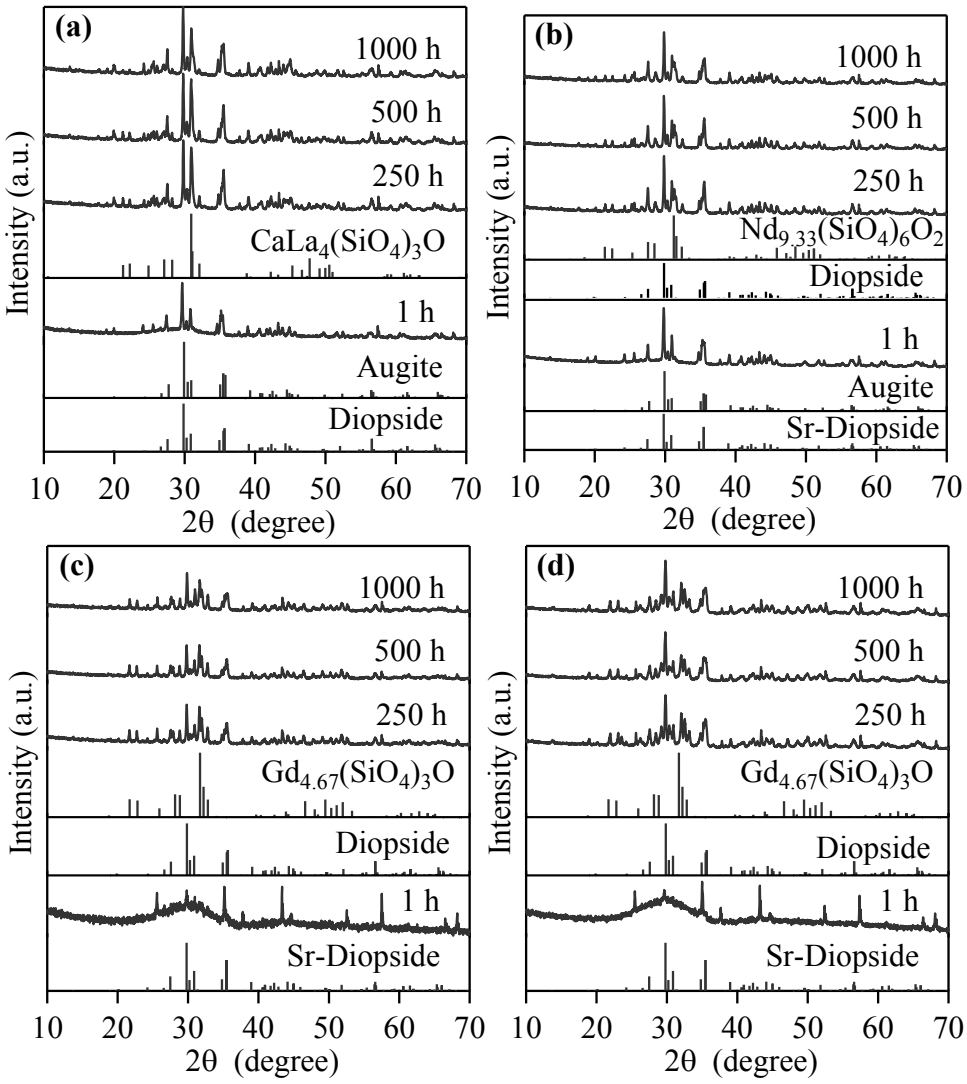

Fig. 4.5.3: XRD patterns of (a) La–0.2 (b) Nd–0.2 (c) Gd–0.3 and (d) Yb–0.3 GCs sintered at 850 ºC for various periods of time.

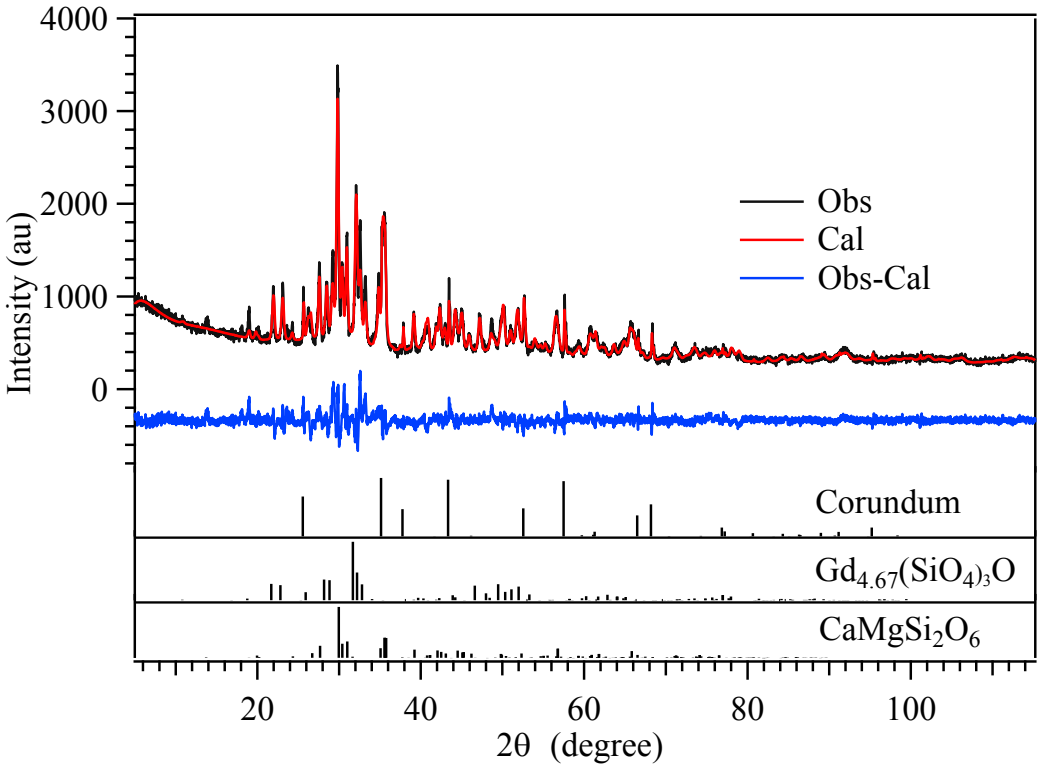

Fig. 4.5.4: Observed, calculated, and difference curve from the Rietveld refinement of the Yb–0.3 GC heat treated at 850 ºC for 1000 h in air atmosphere.

Fig. 4.5.3 presents the X–ray diffractograms of the glass powder compacts sintered at 850 ºC for a time period varying between 1–1000 h while Table 4.5.1 presents the quantitative phase analysis depicting the amorphous/crystalline content in the GCs as obtained from Rietveld–R.I.R. analysis of the XRD data. Additionally, Fig. 4.5.4 presents the difference between the measured and calculated XRD pattern fits for GC Yb – 0.3 sintered at 850 ºC for 1000 h by using the GSAS–EXPGUI software. The calculated diagrams are based on crystallographic structure models, which also take into account specific instrument and sample effects. The parameters of this model have been refined simultaneously using least–squares methods in order to obtain the best fit to all measured data. By least–squares refinement, a so–called figure–of–merit function R has been defined, which describes the residual (agreement) between observed and calculated data [135]. The R factors show the mean deviation in accordance with the model used in percent. The ‘‘profile R–factor”, R_p, and ‘‘weighted profile R–factor”, R_{wp}, for all the refinements are well within the limits of experimental accuracy. The differences between

the main peaks of diopside and $Gd_{4.67}(SiO_4)_3O$ were due to adjustment difficulties based on the crystallinity of the phases. It should be noted that the Rietveld–refinement on the XRD data of GC Yb–0.3 has been made by using the structural models corresponding to $Gd_{4.67}(SiO_4)_3O$ as we could not identify a relevant crystalline phase containing ytterbium for this sample. Since the reflections from GC Yb–0.3 exhibit good match with those corresponding to Gd–containing oxyapatite, it has been presumed that the crystalline phase formed in GC Yb–0.3 (apart from diopside) is a Yb–containing oxyapatite with its structural features similar to that of $Gd_{4.67}(SiO_4)_3O$.

All glass powder compacts exhibited the highest content of residual glassy phase after sintering at 850 ºC for 1 h with Gd–0.3 and Yb–0.3 GCs comprising ~95 wt.% amorphous content. Clinopyroxene based phases in the crystallization field of diopside ($CaMgSi_2O_6$) dominated the phase assemblage in all the GCs irrespective of heat treatment time duration. The most plausible diopside based crystalline phases that have been identified in the GCs based on the best fit between experimental and as generated XRD data during the Rietveld refinement are: diopside ($CaMgSi_2O_6$; ICDD: 78–1390); augite ($CaMg_{0.7}Al_{0.6}Si_{1.77}O_6$; ICDD: 78–1392) and Sr–diopside ($Ca_{0.8}Sr_{0.2}MgSi_2O_6$; ICDD: 80–0386). However, it is difficult to identify any of these individual phases in GCs in a precise manner as the phase reflections for all them overlap with each other (Intensity = 100%, $2\theta \approx 29.8^{\circ}$). These observations have been supported and resolved in a better manner by the results obtained from structural studies on GCs as discussed in the next section.

Prolonged heat treatment at 850 ºC for 1000 h caused some insignificant changes in the crystalline phase assemblages as minor amounts (~10 wt.%) of lanthanide–containing silicate oxyapatites crystallized, while diopside based phases predominance (Table 4.5.1). However, significant changes were observed in the total amorphous/ crystalline content in the GCs with the residual glassy phase decreasing from ~96% to ~41% and ~96% to ~19% (after heat treatment for 250 h) for compositions Gd–0.3 and Yb–0.3, respectively.

Table 4.5.1: XRD – Rietveld refinement results (wt%)

Time (h)	Di	Sr-Di	Augite	$(CaLa_4(SiO_4)_3O)$	$(Nd_{9.33}(SiO_4)_6O_2)$	$(Gd_{4.67}(SiO_4)_3O)$	Glass	$\chi 2$
				La-0.2				
1	33	-	11	-	-	-	56	3.00
250	64	-	9	8			19	4.08
500	69	-	11	7	-	-	13	4.92
1000	66	-	15	5	-	-	14	5.14
				Nd-0.2				
1	-	26	24	-	-	-	50	4.12
250	56	-	6	-	5	-	33	2.19
500	59	-	9	-	7	-	25	2.88
1000	57	-	8	-	8	-	27	3.18
				Gd-03				
1	-	3	-	-	-	-	97	2.12
250	44	-	4	-	-	11	41	2.02
500	46	-	7	-	-	12	35	2.18
1000	45	-	6	-	-	10	39	2.45
				Yb-03				
1	-	4	-	-	-	-	96	2.33
250	63	-	6	-	-	12	19	3.12
500	77	-	5	-	-	13	5	4.29
1000	76	-	8	-	-	12	4	3.06

The crystallization of small fraction of lanthanide containing silicate apatite phase is highly expected in lanthanide– and SiO_2–rich aluminosilicate glass compositions. Similar observations have also been reported by Quiantas et al., [191] in lanthanide containing aluminoborosilicate nuclear waste glasses and by Sohn et al., [192] in BaO–containing GC sealants with 5 mol% La_2O_3 content. In the present study, minor amounts

of apatite phases have been observed after long term heat treatments for time period varying between 250–1000 h. Moreover, the fraction of these phases was nearly constant (~7 wt.% of $CaLa_4(SiO_4)_3O$ in La–0.2, ~7 wt.% of $Nd_{9.33}(SiO_4)_6O_2$ in Nd–0.2, ~11 wt.% of $Gd_{4.67}(SiO_4)_3O$ in Gd–0.3, ~12 wt.% of $Yb_{4.67}(SiO_4)_3O$ in Yb–0.3) and did not increase significantly with increasing thermal treatment time. The lanthanide containing silicate apatites as observed in the present study are basically quasi–binary phases and are the members of a solid solution series with general formula $Ln_{9.33+2x}(Si_{1-x}Al_xO_4)_6O_2$ (with x varying between 0–0.33) [193]. For example: the crystalline phase $Gd_{9.33}(SiO_4)_6O_2$ has been shown to dissolve up to 10 mol% Al_2O_3 in its crystal structure which consequentially is accompanied by an increase of the lattice parameters *a* and *c* [193].

The noticeable conclusion from the XRD data is that no significant changes could be observed in crystalline phase assemblage or in amorphous/crystalline content of GCs after 250 h of heat treatment at 850 ºC. This behaviour exhibits the high thermal stability of GC seals under investigation in comparison to other prominent glass/GC seals reported in the literature. For example: the barium calcium aluminosilicate glass seals are prone to crystallization at temperatures as low as 700 ºC and metastable hexacelsian phase ($BaAl_2Si_2O_8$) crystallizes in this glass at 750 ºC which on prolonged heat treatment starts transforming to its monoclinic polymorph [158]. The formation of monoclinic celsian phase is, however, undesirable for SOFC sealing application due to its lower CTE of ~2.29×10^{-6} K^{-1} (30–1000 ºC) in comparison to its hexagonal polymorph (~8×10^{-6} K^{-1}) [194]. Therefore, this hexagonal → monoclinic transformation not only lowers the overall CTE of the GC seal but also creates unwanted stresses in the microstructure of the GC which consequentially affects the mechanical strength of the seal. Similarly, the absence of any boron containing crystalline phases in the investigated GCs during prolonged heat treatments is another feature that provides their superiority over high boron containing seals[108, 195] particularly in relation with thermal stability under humidified reducing environments.

In order to obtain good flow behaviour along with self–healing ability and appropriate viscosity ($\log \eta \approx 5$ at 850 ºC; η in dPas [50]) required for the glass/GC seal to join and bond to the SOFC components, it is mandatory to achieve an equilibrium between the crystalline content and residual glassy phase in the GC. From our previous

observations and experiences on similar glass compositions [137, 138], a GC composition with an ability to maintain crystalline/amorphous content ratio of ~60/40 (wt.%) during long run along with a stable crystalline phase assemblage should be suitable as a self–healing sealant for SOFC. Accordingly, on the basis of the data obtained from quantitative crystalline phase analysis of GCs (Table 4.5.1) after heat treatment at 850 ºC for time durations up to 1000 h, glass composition Gd–0.3 seems to be the most promising candidate for this task.

4.5.2.2.2 Solid–state NMR

Through inspection of the NMR line widths present in the spectra, one can access the crystallinity of the GCs since sharper lines are characteristic of crystalline systems and broad lines are usually associated with amorphous samples. The samples not containing a paramagnetic species (La–0.2) produced better–resolved spectra, enabling the observation of otherwise masked resonance lines. Therefore, the chemical information obtained from ^{29}Si, ^{27}Al, and ^{11}B spectra of La–0.2 samples may be transferrable to the other systems, as they are all isostructural in nature owing to their compositional similarities with the exception of the lanthanide ion that varies between La^{3+}, Nd^{3+}, Gd^{3+}, Yb^{3+} (Table 4.4.1). In addition, the relative areas between the NMR resonances provide important information about the nature of crystalline phases that allows us to corroborate the spectroscopic results with those obtained from quantitative crystalline phase analysis using XRD data, as evidenced in the following discussion.

^{29}Si MAS NMR

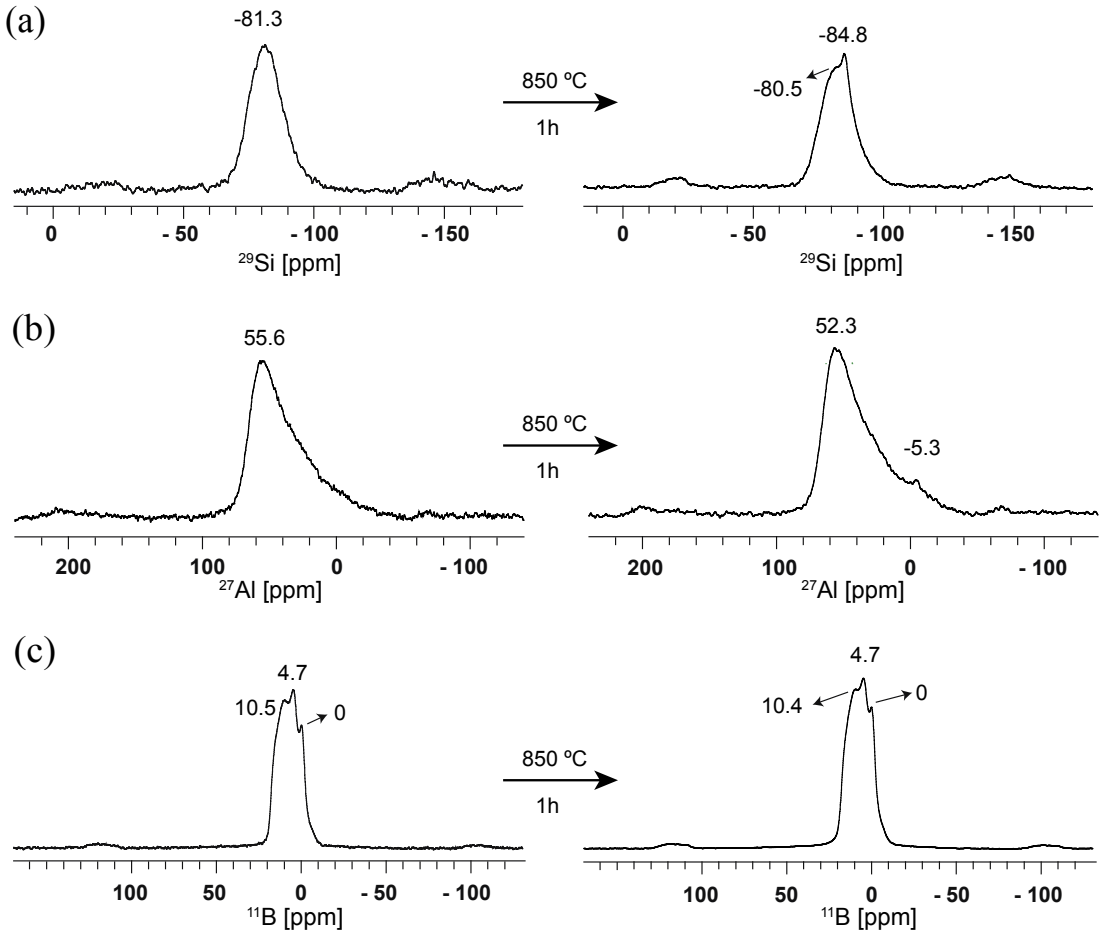

Fig 4.5.5: MAS NMR spectra of (a) ^{29}Si, (b) ^{27}Al and (c) ^{11}B nuclides for the La–0.2 glass (left) and GCs sintered at 850 ºC for 1 h (right).

Fig. 4.5.5 presents the ^{29}Si, ^{27}Al and ^{11}B multinuclear solid–state NMR data of glass La–0.2 and its corresponding GC obtained after heating the glass powder compacts at 850 ºC for 1 h depicting the structural transformations occurring in the glasses during sintering. Most glass and GC (Fig. 4.5.5a and 4.5.7a) samples display single broad resonance Q (Si) site distributions characteristic for glassy systems centered at –81 to –85 ppm. ^{29}Si NMR chemical shift of diopside is typically centered at around –82 ppm for glasses and at –84 ppm for GCs and assigned to Q^2 environments [159, 190, 196], which explains the single resonance observed in all glasses and GCs for Nd–0.2 and La–0.2 (Fig. 4.5.7a), since their compositions exhibit diopside as the primary phase (according to

Fig. 4.5.1 and Table 4.5.1). In the case of the Yb–0.3 sample, the resonance at ca. –85 ppm is absent or difficult to observe. This observation also fits with the very low amount of diopside quantified by the X–ray diffraction analysis (~ 4 %, Table 4.5.1).

With an increase in the heat treatment time (500 h and 1000 h), no significant changes could be seen between the NMR spectra of GCs as is evident from Fig. 4.5.8. This observation is in agreement with Table 4.5.1, showing approximately the same qualitative and quantitative crystalline and glassy phase composition, derived from Rietveld R.I.R results. Regarding the La–0.2 sample, the formation of the crystalline phase (~ –85 ppm, diopside) is already observable in Fig. 4.5.7a, where two components are detected. As the sintering time increases to 500 and 1000 h (Fig. 4.5.8), the *ca*. –85 ppm resonance, associated with the crystalline phase, is predominant and the other component at ca. –81 ppm (due to the amorphous phase) tends to disappear (cf. Fig. 4.5.6 and Fig. 4.5.8). Similarly, in the case of Nd–containing GCs, loss of amorphous phase (in comparison to parent glass) is clearly observed when the samples are sintered for 500 and 1000 h (considering the width of the resonance; Fig. 4.5.8 and Fig. 4.5.6a). ^{29}Si NMR spectra show that the diopside phase dominates the NMR spectrum with a small amount of the initial glass present. This observation helped to obtain the glassy composition described in Table 4.5.1.

^{27}Al MAS NMR

The ^{27}Al MAS NMR spectra of glass samples (Fig. 4.5.5b and 4.5.6b) display broad and, in some cases, asymmetric line shapes with a typical tailing profile due to ^{27}Al sites in disordered materials [197-199]. Conversely, the spectra of GCs La–0.2 and Nd–0.2 obtained after heat treatment at 850 ºC for 1 h (Fig. 4.5.5b for La–0.2 glass) and its comparison with other glasses (Fig. 4.5.6b with Fig. 4.5.7b) show an emerging resonance at –5 to –8 ppm, typical of AlO_6 environments ($^{[6]}$Al). This is attributed to an increase in augite/glass ratio in samples sintered at 850 ºC for 1 h. Augite is the only source of AlO_6 species among the other phases present in Table 4.5.1 and thus, NMR clearly shows that augite is present in these GCs.

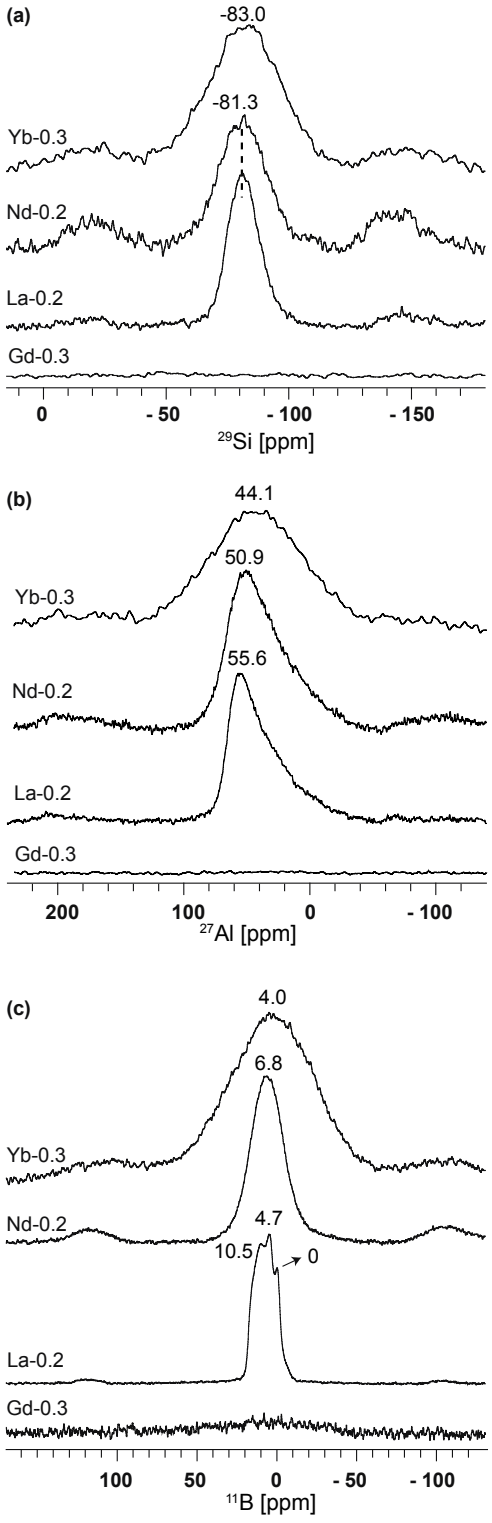

Fig. 4. 5.6: MAS NMR spectra of (a) ^{29}Si, (b) ^{27}Al and (c) ^{11}B nuclides for the glass powders.

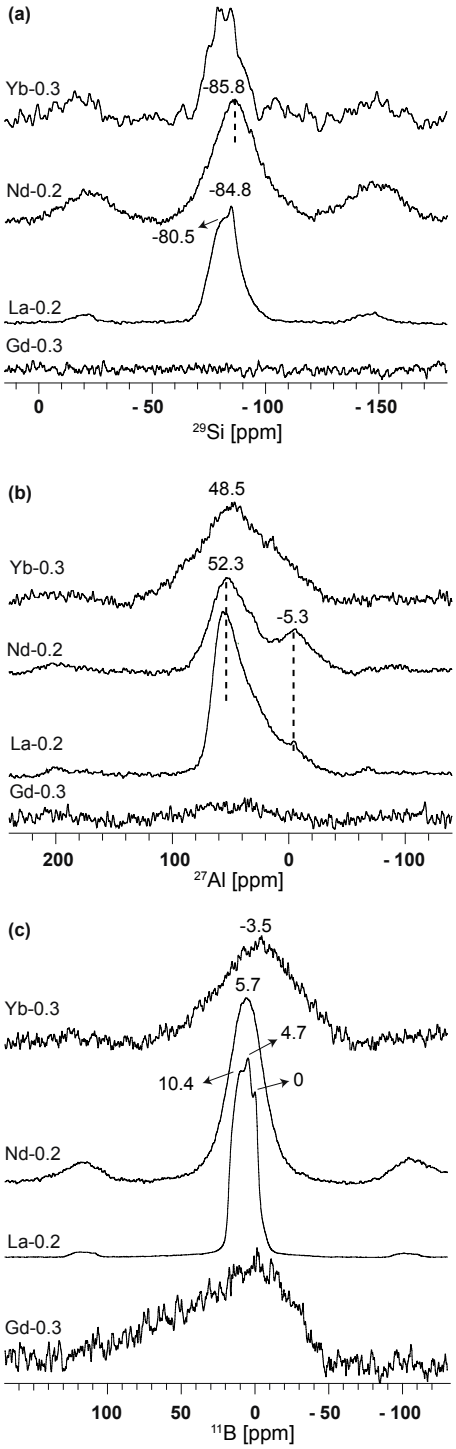

Fig. 4.5.7: MAS NMR spectra of (a) ^{29}Si, (b) ^{27}Al and (c) ^{11}B nuclides for the glass–ceramics sintered at 850 ºC for 1 h.

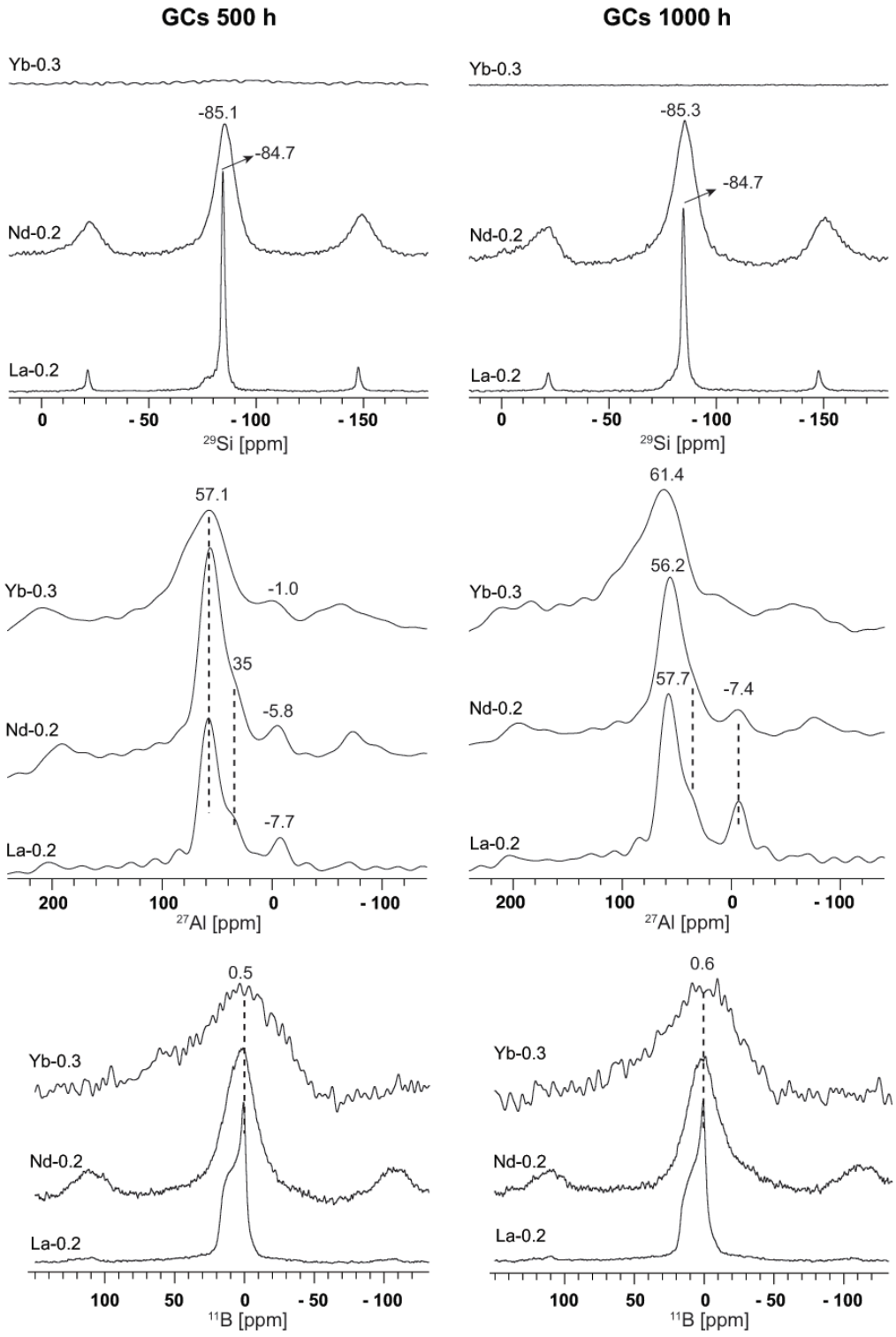

Fig. 4.5.8: MAS NMR spectra of ^{29}Si, ^{27}Al and ^{11}B nuclides of the glass–ceramics heat treated at 850 ºC for 500 h and 1000 h

In addition, ^{27}Al MAS–NMR spectra of La–0.2 and Nd–0.2 GCs also show that augite/glass ratio must be higher in the latter GC sample as the AlO_6 peak at ca. –5.3 ppm (augite) is significantly more intense than the broad ^{27}Al resonance, at ca. 52 ppm, arising from the glass phase as compared to the La–0.2 GC sample (Fig. 4.5.7b). As has been mentioned in *Section 4.5.2.2.1*, it is difficult to unambiguously estimate quantitatively the proportions of augite, diopside and Sr–diopside as all these three crystalline phases result in a similar X–ray diffraction patterns. Indeed, it is possible to obtain many different relative amounts of distinct crystalline phases or distinct crystalline/amorphous ratios that fit well the X–ray diffraction pattern. In this context, ^{27}Al NMR was a valuable and highly selective method to estimate the augite crystalline phase and is thus a powerful technique to help tuning the R.I.R quantifications toward the real composition of our GC. For example, R.I.R results for GCs heated at 850 ºC for 1 h, frequently report crystalline/glass ratios close to 1 with augite present as one of the main crystalline phases (particularly in the case of the La–0.2 and Nd–0.2 GCs). Therefore, ^{27}Al NMR was essential to validate RIR results. The resonance at –5 to –8 ppm was also observed in the ^{27}Al MAS NMR spectra of GCs after heat treatment at 850 ºC for 500 h and 1000 h (Fig. 4.5.8) depicting the favorable environment for $^{[6]}$Al species, assigned to the augite phase as discussed previously. An additional shoulder centered at ~35 ppm, observed for the La–0.2 and Nd–0.2 GCs (500 and 1000 h, Fig. 4.5.8), is likely to be associated with 5–coordinated Al species ($^{[5]}$Al), more pronounced in the La–0.2 samples.

^{11}B MAS NMR

The 1D ^{11}B Hahn–echo MAS NMR experiments clearly show the presence of BO_4 ($^{[4]}$B) species yielding a Gaussian shape centered at 0 ppm (Fig. 4.5.5c and 4.5.6c). The amount of these $^{[4]}$B species increases as the sintering time increases (Fig. 4.5.7c and Fig. 4.5.8) probably due to the crystallization of silica–rich phases rendering the borate and alumina rich residual glassy phase component. The other site present in these spectra is assigned to assymetric BO_3 ($^{[3]}$B) units giving rise to the typical second–order quadrupolar line shapes ranging from 20 to –5 ppm. Because it is not possible to resolve the number of $^{[3]}$B and $^{[4]}$B species present in each sample by means of 1D ^{11}B Hahn–echo experiments, and often several $^{[3]}$B or $^{[4]}$B species may also overlap, we have

performed 3QMAS experiments for the samples where singularities are observed (glass La–0.2 and La–0.2 GC, 1000 h), which could be associated to multiple resonances (Fig. 4.5.9). The ^{11}B 3QMAS spectra of glass La–0.2 and La–0.2 GCs 1000 h samples both confirm the presence of two boron environments (a single $^{[3]}B$ and a single $^{[4]}B$ site).

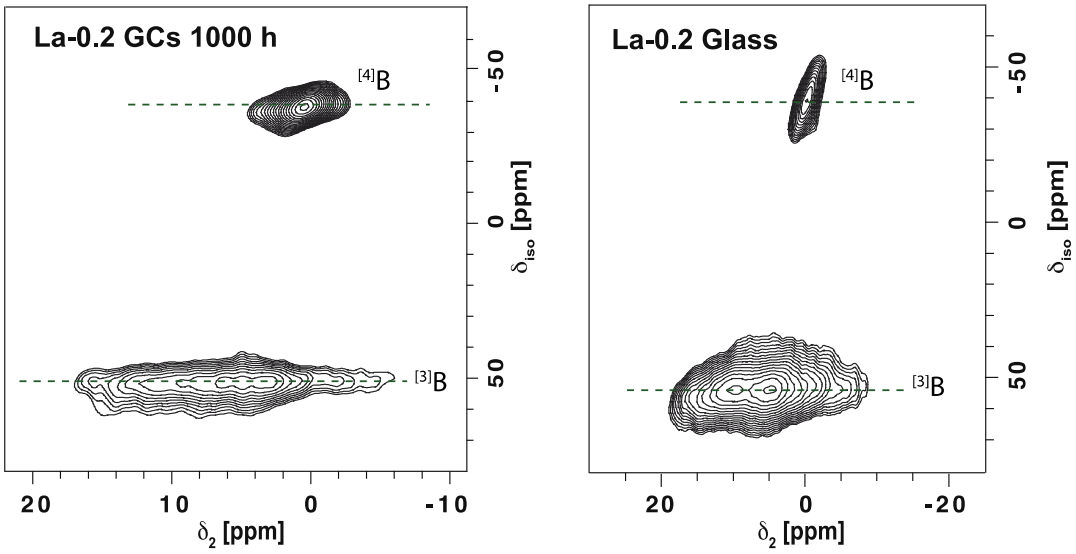

Fig 4.5.9: ^{11}B 3QMAS spectra of the GC heat treated at 850 ºC for 1000 h (left) and the glass powder (right) corresponding to the La–0.2 sample.

As described above, the structure of lanthanide containing aluminosilicate glasses depends markedly on the Ln^{3+} cation field strength over both short and intermediate length scales. A detailed study involving the elucidation of the effect of lanthanide cations on the structure of these glasses will form the basis of our forthcoming article where a wide array of structural characterization techniques (for example: Extended X–ray absorption fine spectroscopy, MAS NMR and UV–Visible spectroscopy), will be employed.

4.5.2.3. Thermomechanical behaviour of sintered glass–ceramics

4.5.2.3.1 Linear shrinkage, mechanical properties and thermal expansion

In accordance with the HSM results [138] and the shrinkage values summarized in Table 4.5.2, well sintered and dense GCs were obtained after sintering/heat treatment

of glass powders at 850 ºC for various periods of time. The values of linear shrinkage for all the GCs varied between 11.7–16.3 % over 1000 h of heat treatment time. Interestingly, all the GCs exhibited a gradual increase in the linear shrinkage during 1000 h of heat treatment irrespective of their lanthanide content. With respect to the influence of lanthanide type on shrinkage behaviour, GCs derived from composition Nd–0.2 showed highest shrinkage followed by La–0.2, Gd–0.3 and Yb–0.3. It is noteworthy that GC Yb–0.3 glass exhibited the smallest variation in shrinkage (0.8 %) over 1000 h of time period while the highest (2.01%) was observed for La–0.2.

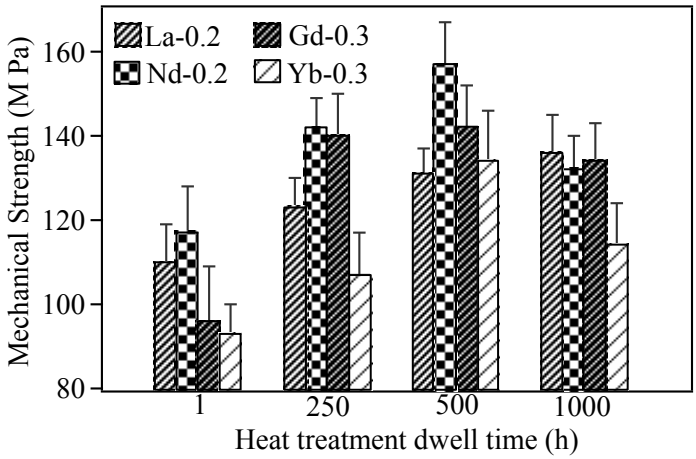

Fig. 4.5.10: Variation of mechanical strength with respect to the GCs heat treatment dwell time.

Fig. 4.5.10 presents the mechanical strength of the produced GCs with respect to the heat treatment time. In general, the mechanical strength of ytterbium containing GCs was lower in comparison to its lanthanide containing counterparts. This is not surprising considering the high residual glassy phase in Yb–0.3 after 1 h of sintering at 850 ºC and low linear shrinkage values over heat treatment time. The flexural strength of lanthanum–containing GC showed an increasing trend from 110 MPa to 139 MPa with heat treatment time. However, for GCs Nd–0.2, Gd–0.3 and Yb–0.3, the flexural strength values demonstrated an increasing trend only up to 500 h of heat treatment time and then initiated to decrease with further increase in heat treatment. This is attributable to a greater extent of crystallization through a longer thermal heat treatment.

Generally, crystalline phases in the glass and GC can enhance mechanical strength. In agreement with this statement a larger amount of crystalline fraction in 250, 500 and 1000 h heat treated GCs reinforced the mechanical strength to a greater extent compared to the 1 h sintered compacts. Similar results were also observed in case of 0–40 BaO, 0–15 B_2O_3, 0–10 Al_2O_3, 0–40 SiO_2, 0–15 CaO, 0–15 La_2O_3, and 0–5 ZrO_2 (mol%) (GC–9) glass composition reported by Chang et al., [93]. However, apart from the crystalline fraction and type of crystalline phase, another important factor which can influence the mechanical strength is the microstructure of GCs. According to Griffith crack theory, when a propagating crack in the compound encounters a crystal with high strength and elastic modulus, the crack direction is deviated by the crystal leading to an increase of the cleavage of the surface. As a result, a higher fracture surface energy is required for crack propagation. As observed from Fig. 4.5.11, fracture surfaces of specimens heat treated for 500 h are apparently rougher than those of 1000 h heat treated samples. This means that more energy is lost during crack propagation, explaining the enhanced mechanical strength measured for GCs heat treated for 500 h. Except Yb–0.3, the falls in mechanical strength of GCs upon heat treating at 850 ºC for time durations within 250 – 1000 h are in ±10 – ±15 MPa range. These standard deviation values are in the limits of experimental errors and therefore, the mechanical strengths can be considered to be fairly constant. The measured values (110 – 140 MPa) for the 1000 h heat treated GCs are considerably higher than those reported for barium calcium aluminosilicate glass ((15CaO–35BaO–5Al_2O_3–10B_2O_3–35SiO_2 (mol%)) (~35 MPa)) (~35 MPa) and GC–9 glass (49 MPa) after heat treatment at 800 ºC for 1000 h [44, 168].

Weibull statistics [122] is commonly used to describe the fracture behaviour of brittle materials. The two–parameter Weibull distribution of flexural strengths for the investigated GCs heated over 1000 h of time period at room temperature are shown in Fig. 4.5.12. Table 4.5.3 lists the Weibull characteristic strength σ_0 (corresponding to F = 63.2%) and Weibull modulus m for the studied GCs. A larger Weibull modulus, called the shape factor m, relates to the uniformity of the distribution of flaws in a brittle material: a high value of m implies a highly uniform distribution of defect sizes and therefore a low level of variability of seal strengths. Conversely, a low value of m implies highly variable flaw sizes and a large spread of measured strengths.

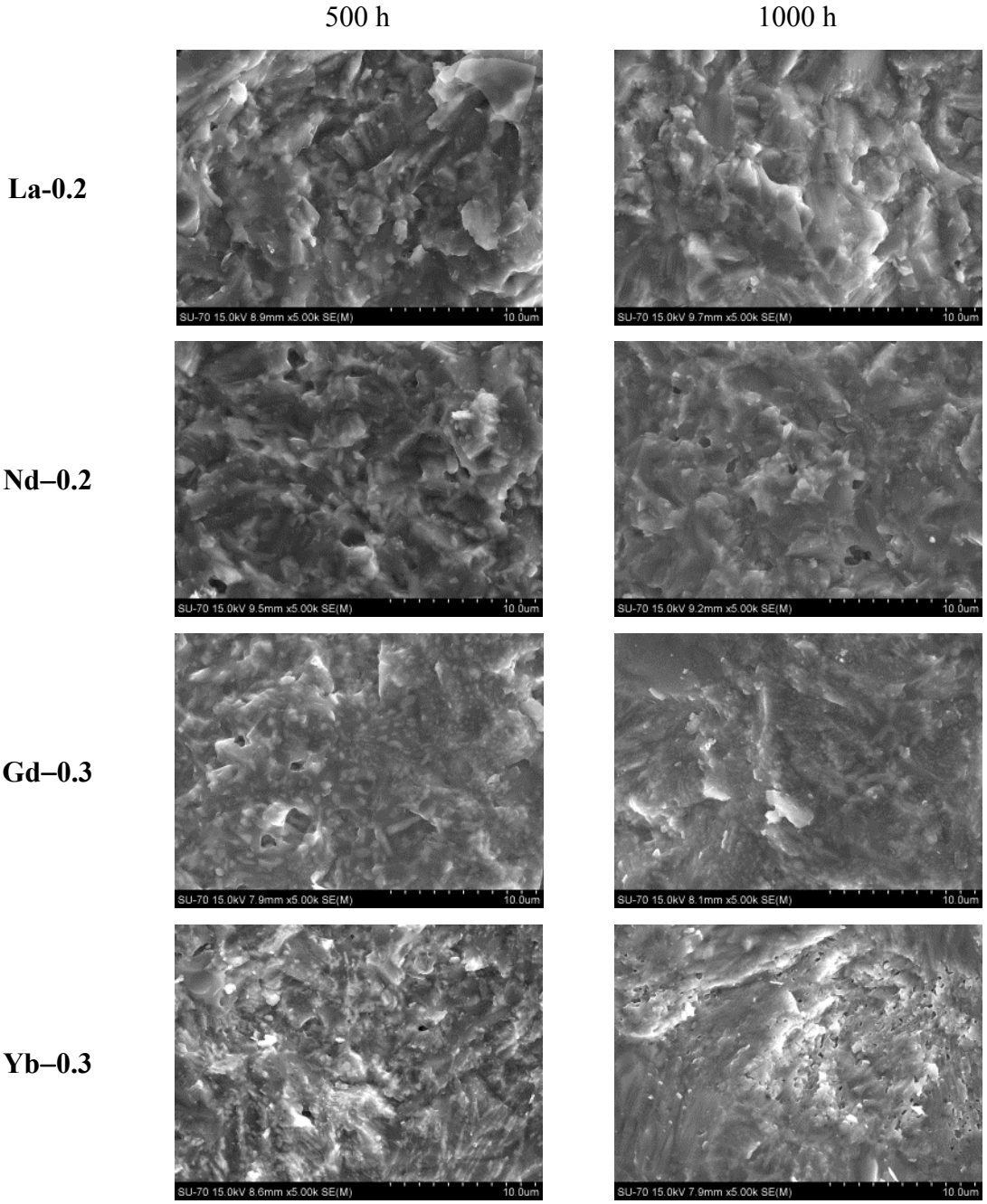

Fig 4.5.11: Fractured surfaces of glass–powder compacts heat treated at 850 ºC for 500 h and 1000 h after the 3 point bending strength measurement.

In general, irrespective of heat treatment higher *m* values were calculated for lanthanum containing GCs (*m* = 16.2–21.5) followed by Nd–0.2 (10.9–16.6), Gd–0.3

(9.9–15.6) and Yb–0.3 (8.5–10.6) GCs. The relatively high Weibull modulus, *m* ~7–21.5 (Table 4.5.3), means good mechanical reliability for the sealants. Higher values of Weibull modulus were observed for the long term heat treated GCs as compared to 1 h heat treated GCs indicating highly uniform distribution of defect sizes and therefore a low level of variability of seal strengths with prolonged heat treatment (Fig. 4.5.11). Good mechanical reliability and suitable Weibull strength (112–163 MPa) for the GCs produced after the prolonged heat treatment indicates that the lanthanide GC sealants present strong resistance against the thermal shocks.

In general, a CTE varying between $(9 - 12) \times 10^{-6}$ K^{-1} is considered desirable for a stable glass/GC sealant for SOFC application [25]. The CTE values of the GCs sintered at 850 ºC for various hours are presented in Table 4.5.2. GCs produced at 850 ºC for 1 h exhibited CTE values of $(9.7–10.1) \times 10^{-6}$ K^{-1}. Irrespective of the type of lanthanide oxide incorporated in the glass, an increase in the CTE of GCs was observed with increase in heat treatment time up to 500 h at 850 ºC. On increasing the heat treatment time to 1000 h, a decrease in CTE of GCs within the range of $\pm 0.5 \times 10^{-6}$ K^{-1} was observed. This small variation in CTE is not likely to have any severe implication concerning the intended final applications. In general, prolonged thermal treatment significantly affects the CTE of GCs due to structural rearrangement and formation of new crystalline phases with different CTE values, as reported by Ojha et al., [169] for a glass composition in (mol%) 25.7 SrO–4.1 La_2O_3–13.1 Al_2O_3–12.8 B_2O_3–44.3 SiO_2. The CTE value increased from 11.1 to 11.7×10^{-6} K^{-1} when the heat treatment time increased form 1–5 h, and then decreased down to 9.1×10^{-6} K^{-1} with continuous heat treatment time up to 100 h at 1000 ºC. However, in the present scenario, as revealed from ssNMR analysis, our glasses did not exhibit any structural rearrangement during prolonged heat treatment time up to 1000 h at 850 ºC. Moreover, from XRD along with RIR quantitative analysis (Table 4.5.1) all the GCs are confined to only two crystalline phases, diopside and lanthanum silicate phases, throughout their long term heat treatment.

Table 4.5.2: Shrinkage (%) and CTE ($\times 10^{-6}$) K^{-1} measured for the glass–powder compacts after sintering at 850 ºC for 1 h, 250 h, 500 h and 1000 h.

	1 h	*250 h*	*500 h*	*1000 h*
Shrinkage				
La–0.2	12.6±0.4	12.7±0.3	12.9±0.3	14.7±0.2
Nd–0.2	14.7±0.4	15.5±0.1	15.8±0.3	16.3±0.5
Gd–0.3	13.0±0.3	13.5±0.3	13.8±0.2	14.1±0.7
Yb–0.3	11.7±0.4	11.7±0.2	11.8±0.3	12.5±0.1
CTE				
La–0.2	9.7±0.2	10.0±0.1	10.4±0.1	9.8±0.1
Nd–0.2	10.1±0.1	10.1±0.2	9.9±0.1	9.7±0.2
Gd–0.3	9.9±0.1	10.8±0.1	11.1±0.1	10.6±0.2
Yb–0.3	9.8±0.1	10.6±0.3	10.9±0.1	10.3±0.1

Table 4.5.3: Weibull modulus (m) and Weibull strength (σ_0, MPa) extracted from the flexural strength data for the glass–powder compacts sintered at 850 ºC for 1 h, 250 h, 500 h and 1000 h.

	1 h	*250 h*	*500 h*	*1000 h*
Weibull modulus				
La–0.2	11.5	17.1	21.5	16.2
Nd–0.2	6.6	12.7	10.9	16.6
Gd–0.3	6.8	13.0	9.9	15.6
Yb–0.3	10.6	10.6	8.5	8.9
Weibull strength				
La–0.2	114	126	134	140
Nd–0.2	133	147	163	136
Gd–0.3	103	145	149	139
Yb–0.3	97	112	141	116

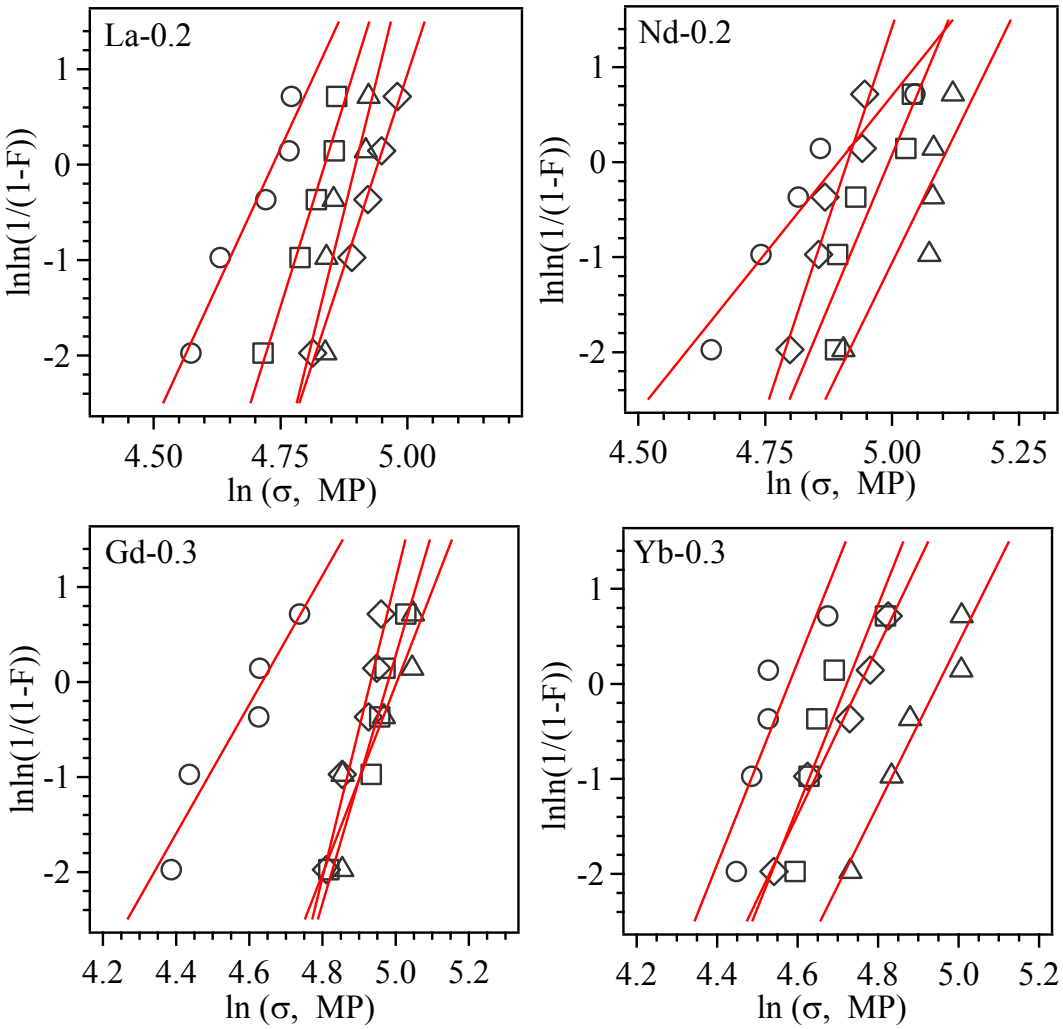

Fig. 4.5.12: Weibull distribution of flexural strength for glass–powder compacts annealed at 850 ºC for various dwell times. (○–1h; □–250 h; Δ –500 h; ◊ –1000 h)

This indicates thermal stability of lanthanide contain glasses and their suitability for applications in SOFCs as stable sealants. However, the observed tiny variations in CTE may have occurred due to small variations in crystalline fractions of two developed crystalline phases (Table 4.5.1).

4.5.2.3.2 Electrical and thermal shock resistances

The thermal shock resistance tests demonstrated that the Gd–0.3 and Yb–0.3 sealants are suitable for hermetization of stabilized zirconia membranes. For the model cells sealed by these compositions, no visible cracks or detectable leakages at room temperature were observed after 7 and 10 air–quenching cycles, respectively. In the case of La–0.2 and Nd–0.2 GCs, the thermal shock resistance was worse, probably due to lower CTEs (Table 4.5.2). For comparison, the La–0.2 sealant joining YSZ ceramics was fractured after two quenching cycles in air. Taking into account the lower mechanical strength of Yb–0.3 (Table 4.5.3) and higher cost of Yb–containing precursors that may limit practical applications, the composition Gd–0.3 was selected for further experimentation.

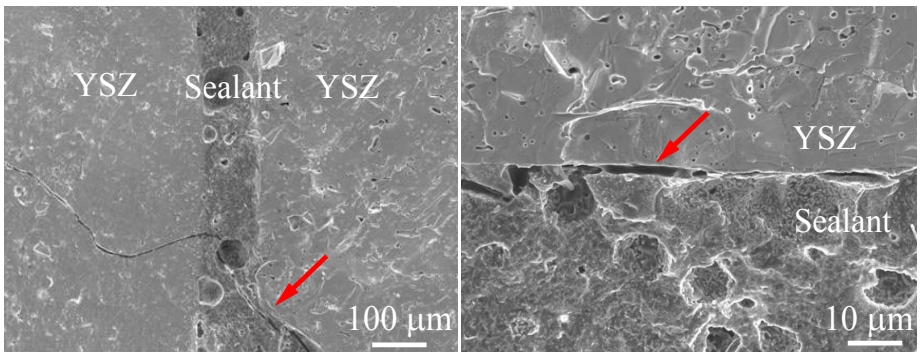

Fig. 4.6.13: Typical SEM images of the interface between Gd–0.3 GC sealant and YSZ solid electrolyte ceramics after 7 air–quenching cycles and final quenching in water. Arrows show the largest cracks developed at the interface.

As expected, quenching in water led to the formation of large cracks and mechanical disintegration in all cases. SEM inspections showed that the crack development occurred primarily in the interfacial layers of the sealant (Fig. 4.5.13), suggesting that the minor CTE mismatch between the sealant and stabilized zirconia may still play an important role. Such a mismatch can be suppressed by incorporating nano– or submicron–sized zirconia additives into the GC composition. In any case, the thermomechanical compatibility of Gd–0.3 GCs and zirconia solid electrolytes is very good (e.g., see Table 4.5.3 and Ref [44][127]), enabling both long–term operation and startup/shutdown regimes as confirmed by the successful air–quenching tests.

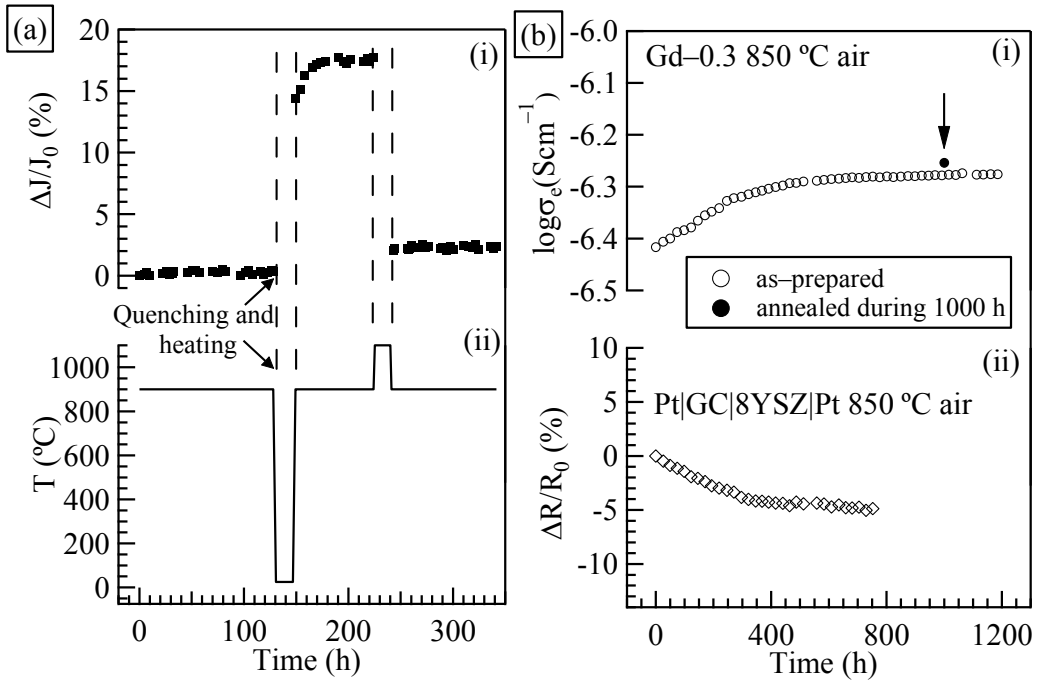

Fig. 4.5.14: (a) Time dependence of the relative changes in oxygen leakage flux during thermal cycling of an electrochemical cell with dense YSZ membrane and Gd–0.3 sealant (i), and corresponding temperature variations (ii). (b) Time dependencies of total electrical conductivity (σ_e) of Gd–0.3 GCs (i) and relative variations of electrical resistance of Gd–0.3/8YSZ couple (ii), at 850 ºC in air. The arrow shows the conductivity value obtained after heat treatment of Gd–0.3 compact during 1000 h at 850 ºC and subsequent deposition of Pt electrodes, followed by the measurement.

Similar conclusion was also drawn from the oxygen leakage measurements at elevated temperatures (Fig. 4.5.14a). These tests were performed for the model cells comprising a dense 8YSZ membrane sealed by Gd–0.3 GCs onto tubular zirconia support of the same composition. The data on oxygen permeation fluxes were collected during approximately 350 h at 900 ºC under large oxygen partial pressure gradient simulating the SOFC operation conditions, 0.21 atm / (10^{-21} –10^{-19}) atm. It should be mentioned that the measured oxygen fluxes correspond to the sum of physical leakages originating from microcracks and closed porosity, electrolytic leakage through YSZ due to minor electronic conductivity of stabilized zirconia [127], and oxygen transport in the sintered

sealant layer separating zirconia ceramics [128, 134]. This combination makes it impossible to estimate area–specific contributions of the components. Consequently, Fig. 4.5.14a(i) shows the relative variations of the total oxygen flux with time induced by ageing and thermal cycling; the corresponding temperature variations are displayed in Fig. 4.5.14a(ii). The measurement regime included one temperature cycle between 900 and 25 ºC with cooling/heating rates of 5–6 ºCmin^{-1}, and an additional treatment at 1100 ºC introduced in order to assess possible self–healing behaviour of the sealant. The results showed a very low initial level of the oxygen leakage fluxes, $<5\times10^{-12}$ mols^{-1}, comparable to the limit of experimental uncertainty. The leakage remains essentially unchanged in the isothermal regime, but increases by approximately 17–18% after fast cooling down to room temperature and subsequent heating up to 900 ºC, probably due to microcracks formation at the sealant/electrolyte interface. Further annealing at 1100 ºC made it possible to decrease oxygen permeation down to the values close to its initial level. Whatever the microscopic mechanism, this type of behaviour suggests the possibility of re–hermetization of SOFCs and other electrochemical cells after prolonged operation, although the relevant temperature regimes need careful optimization. Another necessary comment is that, despite the moderate increase of the oxygen leakage after temperature cycling, the leakage fluxes remain low, acceptable for the application in SOFCs.

Finally, the impedance spectroscopy studies of sintered GCs showed their good insulating properties. As an example, Fig. 4.5.14b(i) presents the time dependence of the total electrical conductivity of as–prepared Gd–0.3 sintered during 1 h. For the sake of comparison, the conductivity of Gd–0.3 GC after thermal treatment at 850 ºC during 1000 h and subsequent deposition of Pt electrodes is also shown. The crystallization processes, in particular the formation of apatite phases having substantially high oxygen–ionic conductivity [127], lead to a moderate increase of the total conductivity with time. In the case of Gd–0.3 (Fig. 4.5.14b(i)), such an increase corresponds to approximately 40% during 1000 h and occurs mainly during initial 300–500 h. A similar behaviour was observed for other studied GCs, where the conductivity increments after 1000 h heat treatment at 850 ºC varied from approximately 20% (La–0.2) up to 75%

(Yb–0.3). Nonetheless, the high concentration of amorphous phase (Table 4.5.1) preserves high electrical resistance (>1 MOhm×cm), sufficient for SOFC applications.

4.5.2.4 Chemical compatibility

Interconnect/seal glass interface plays a crucial role in the sealing reliability. This can be discussed from several aspects: gas leakage, structural integrity, and electrical performance. Cracks and pores at the interface are potential gas leakage sources. These defects form due to the CTE difference among the seal glass and the metallic interconnect and newly formed interfacial species from the reactions. The cracking of the seal layer is one of the important causes for seal failure. Thus, to minimize thermal stresses during cell operation the differences in CTEs between interconnect, solid electrolyte and the seal glass should not exceed, in general, 1×10^{-6} K^{-1} [25]. Considering CTE values for metallic interconnect (Crofer22 APU; Sanergy HT) varying in the range $(11–12) \times 10^{-6}$ K^{-1}, and ceramic electrolytes (i.e. 8YSZ) to be 10.5×10^{-6} K^{-1}, lanthanide containing diopside GCs should be suitable for rigid glass/GC seals for their applications in SOFCs. This hypothesis is supported by the absence of gaps in all GC seals bonded to Sanergy HT metallic interconnect, by the homogeneous microstructures of all investigated interfaces over their entire cross–sections of the joints and by stable electrical resistivity of the 8YSZ/GC assemblies. As an illustration, Fig. 4.5.14b(ii) shows time dependence of the relative variations of electrical resistance of Gd–0.3/8YSZ couple in air. Whilst the formation of cracks at the interface should increase resistance, an opposite behaviour is observed due to crystallization (cf. Fig. 4.5.14b(ii), Fig.4.5.15a and Table 4.5.1). Figs. 4.5.15 and 4.5.16 show the SEM images of the interfaces between Sanergy HT/GC/Sanergy HT for La–0.2 and Nd–0.2 glass, respectively, along with their corresponding EDS elemental scans depicting the diffusion of Cr, Fe, and Mn elements from Sanergy HT to GC after heat treatment at 850 ºC for 500 h in air. The interface SEM images reveal a low fraction of closed pores in the GCs region. As explained before, remnant closed porosity in the GCs region is very common. According to Karamanovt al., [200] enlosed porosity did not compromised the functionality of diopside–albite GC sealant. This was confirmed in the present study by the results of thermal shock resistance and oxygen leakage measurements.

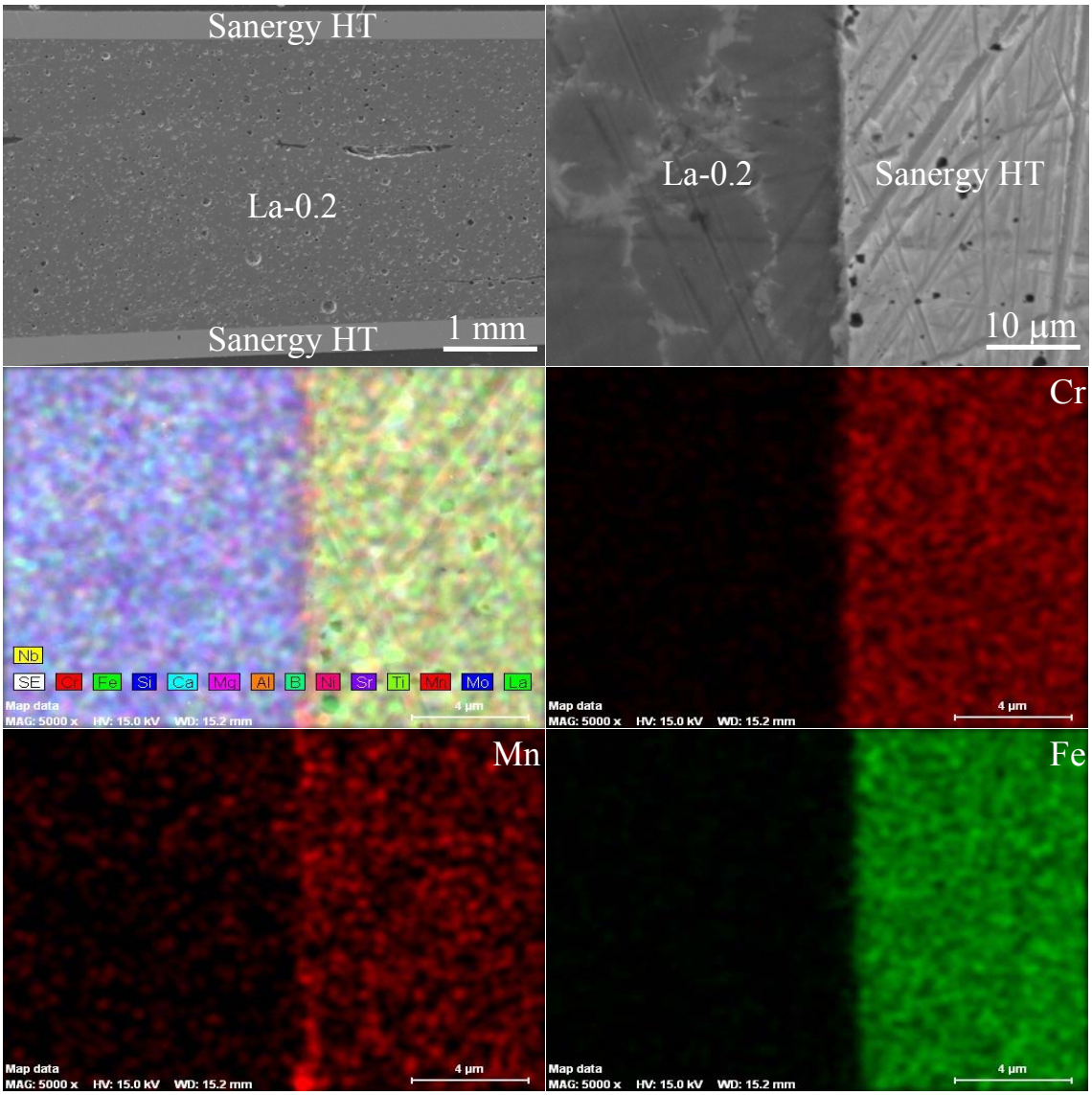

Fig. 4.5.15: Microstructure (SEM) and EDS element mapping of Cr, Fe, Mn, Si and Sr at the interface between SanergyHT/La–0.2–GC/SanergyHT after the heat treatment at 850 ºC for 500 h.

The crack observed in the Nd–0.2 GC region (Fig. 4.5.16a) might have been originated by the mechanical stresses applied at the interface during grinding and polishing, and/or any small thermal mismatch between the glass and the as developed crystalline phases during the prolonged heat treatment. As evidenced from element mapping, a rather smooth interface was obtained between the investigated GC seals and metallic interconnect Sanergy HT without the presence of iron–rich oxide products. However, a

thin reaction zone (<0.5 μm thick) of Mn and Cr–rich oxide layer was formed at the steel side of the interface, indicating the formation of manganese–chromium spinel. The formation of spinel phase at the glass and interconnect interface under air atmosphere is a general process [201] and in the present scenario, formation of an inter diffusion distance between seal glass and interconnect, *ca.* 5 μm, was in a limit of its applicability [25]. Further, formation of Mn and Cr–rich oxide layer on the steel surface is expected to offer the following benefits: (i) Mn and Cr–rich oxide layer limits chromium volatilization rate under the prospective operating conditions knowing the fact that Mn and Cr–rich oxide layer was less reactive and more stable than chromia [66]; and (ii) the CTE of Mn and Cr–rich oxide layer (10.7×10^{-6} K^{-1}) is closer to those of electrodes, electrolyte, and seal (Table 4.5.1) and thus the thermal stress can be reduced and the durability of cell can be improved. It should be noted that an interfacial reaction zone of thickness varying between 10–75 μm has been reported during chemical interaction between barium calcium borosilicate glass and Crofer22APU after thermal treatment in air at 750 ºC for 200 h [202]. Further, it has been observed by Chou et al., [77] and T. Zhang et al., [103] that a significant amount of SrO in sealant glass composition will lead to the formation of $SrCO_4$ crystalline phase when interacting with the Cr–containing metallic plates. Pure $SrCrO_4$ is orthorhombic and highly anisotropic in CTE with $\alpha_a = 16.5\times10^{-6}$ K^{-1}, $\alpha_b = 3.8\times10^{-6}$ K^{-1}, and $\alpha_c = 20.4\times10^{-6}$ K^{-1} [170]. Such high coefficient values will create unwanted stresses in the microstructure of the GC which consequentially affect the mechanical strength of the seal. $SrCrO_4$ will generally form when high SrO–containing glasses react with Cr_2O_3 powders upon heat treating in air up to at least 800 ºC. One possible path for the formation of $SrCrO_4$ is SrO (glass) + ½ Cr_2O_3 (solid) + ¾ O_2 ↔ $SrCrO_4$ (solid). According to the findings of Nakamura, [166] who measured the diffusivities of M^{2+} elements in diopside melts, diffusion coefficients (DC) of divalent ions decrease with increasing ionic radii at constant pressure and temperature (~2.2×10^{-6} cm^2 sec^{-1} and ~2.6×10^{-6} for Sr and Ca, respectively). Therefore, the crystallization of the poisoning $SrCrO_4$ phase from the present lanthanide containing glass compositions could be neglected. Contrary to the sealants proposed by Chou et al.,[77] and T. Zhang et al., [103] the materials studied in the present work did not form $SrCrO_4$.

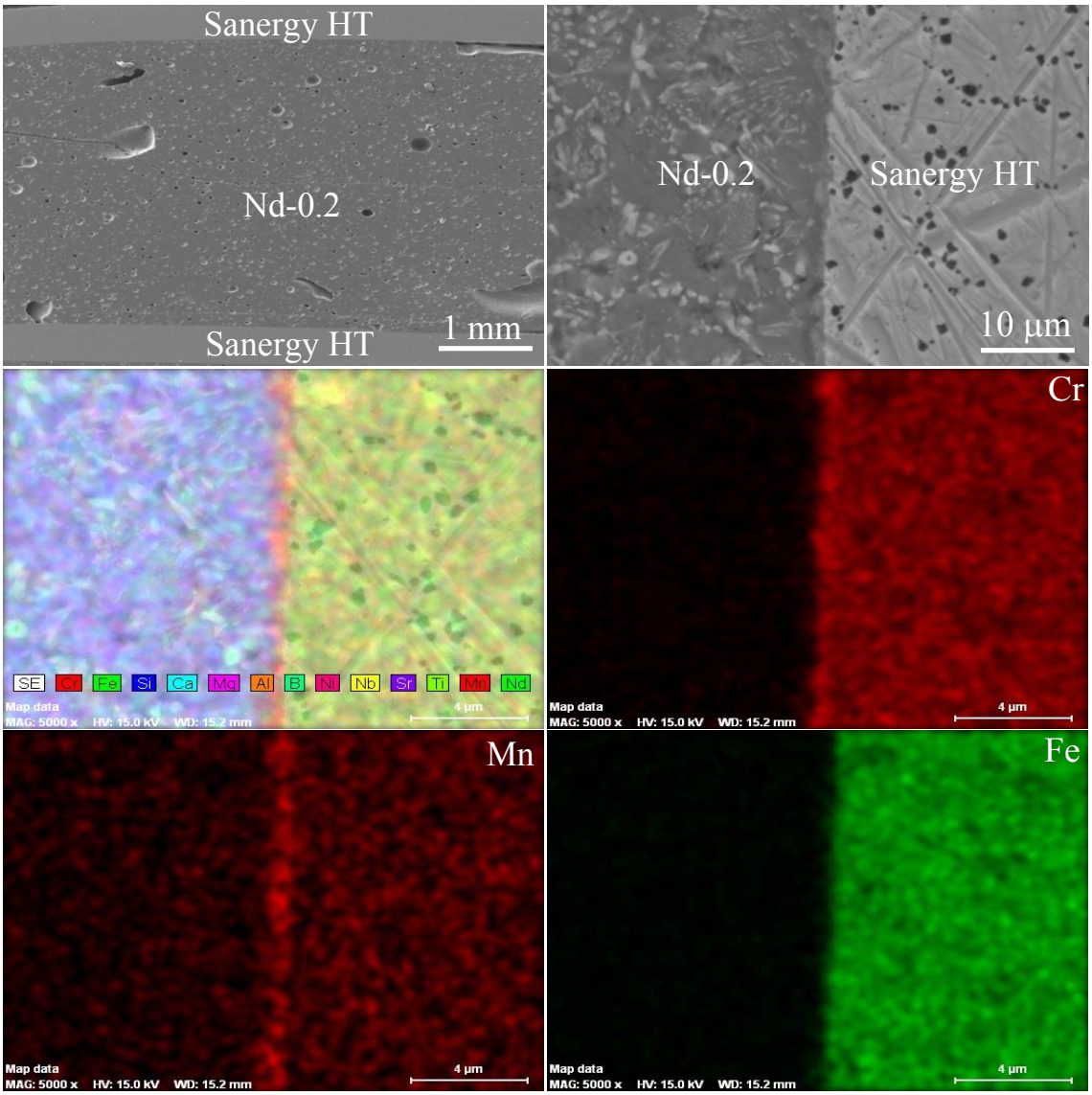

Fig. 4.5.16: Microstructure (SEM) and EDS element mapping of Cr, Fe, Mn, Si and Sr at the interface between Sanergy HT/Nd–0.2–GC/Sanergy HT after the heat treatment at 850 ºC for 500 h.

4.6 Bi–layer glass–ceramic sealant for solid oxide fuel cells

4.6.1 Introduction

To date, a number of rigid glasses and GCs sealants have been tested; in most cases, however, the stability of seals was insufficient due to: (i) coefficient of thermal expansion (CTE) mismatch; (ii) chemical interactions with SOFC components; and (iii) continuous devitrification behaviour [44, 69, 95, 103, 114]. Therefore, along with the design of new and more suitable glasses, new additional concepts/modifications are required to conquer the challenges being faced by the existing sealing technology.

In an attempt to adress these issues, two different series of diopside–based glass systems were selected for applications as sealants for SOFCs (chapter 4.2, 4.4 and 4.5) [138, 154, 155]. Among those, the systems designated as Gd–0.3 (in mol%: 20.62 MgO–18.05 CaO–7.74 SrO–46.40 SiO_2–1.29Al_2O_3–2.04 B_2O_3–3.87Gd_2O_3) and Sr–0.3 (in mol%: 24.54 MgO–14.73 CaO–7.36 SrO–0.55 BaO–47.73 SiO_2–1.23 Al_2O_3–1.23 La_2O_3–1.79 B_2O_3–0.84 NiO) presented superior properties (Table 4.6.1). Namely, both glasses revealed excellent thermal stability along a period of 1,000 h and bonded well to the Sanergy HT metallic interconnect and 8 mol% yttrium stabilized zirconium (8YSZ) ceramic electrolyte without forming undesirable interfacial layers at the joints of SOFC components and GC. From Table 4.6.1 we can observe that both GCs exhibit similar properties, while differing in their amorphous fractions. Thus, using these glasses in the form of layer on layer i.e., a bi–layer approach instead of a single layer between the metallic and ceramic plate of SOFCs might provide the following additional benefits: (i) a small gradient in the CTE that will lead to a lower thermal expansion mismatch between the sealing layers and the other SOFC components, thus providing enhanced mechanical reliability for the stack; (ii) cracks produced due to minor thermal stresses might be healed by the Gd–0.3 GC due to its sufficient amorphous content. In order to obtain good flow behaviour along with self–healing ability and appropriate viscosity (η), $\log \eta \approx 5$ at 850 ºC (η in dPa s) is required [50]. GC compositions with crystalline/amorphous ratios of ~60/40 and with an ability to maintain stable crystalline phase assemblage during long runs have been considered suitable as a self–healing

sealant for SOFC [138, 154, 155, 203]. This communication presents the results and discusses the suitability of the Gd–0.3 and Sr–0.3 bi–layer approach for the application in SOFC stacks. The microstructural variations at the interface of the bi–layered GCs were assessed by micro–Raman spectroscopy.

Table 4.6.1: Properties of Gd–0.3 and Sr–0.3 glasses and glass–ceramics (Chapter 4.2, 4.4, and 4.5).

	Gd–0.3	*Sr–0.3*
T_g (ºC)	770	744
CTE $\times 10^{-6}$ K^{-1} (200–500 ºC)	10.06±0.1	11.2±0.1
T_p (ºC)	931	912
Sintering ability S_c (=T_c–T_{MS})	52	29
T_D (ºC)	875	869
glass–ceramics produced after 1 h		
CTE $\times 10^{-6}$ K^{-1} (200–700 ºC)	9.9±0.1	11.2±0.1
Shrinkage (%)	13.1	13.7
Mechanical strength (MPa)	96±8	137±7
Crystalline fraction (vol. %)	4	85
glass–ceramics produced after 1000 h		
CTE $\times 10^{-6}$ K^{-1} (200–700 ºC)	10.6±0.1	10.4±0.2
Shrinkage (%)	14.1	14.2
Mechanical strength (MPa)	134±4	133±5
Crystalline fraction (vol. %)	60	90

4.6.2 Results and Discussion

Figures 4.6.1 and 4.6.2 (a & b) show SEM cross–sections with different magnifications of the bi–layered GCs after sintering for 1 h and after further heat treating for 100 h at 850 ºC, respectively. From the hot–stage microscopy tests performed for

Sr–0.3 and Gd–0.3 compositions it was observed that heat treating the glass powder compacts at 850 ºC was enough for obtaining fully dense GCs [138, 154, 155, 203]. SEM micrographs revealed the smooth and voids free nature of the interfaces between the two glassy layers, indicating their good joining behaviour. This is further confirmed by the elemental mapping analysis for Gd, Sr and La elements, which enables differentiating the two glassy layers (Fig. 4.6.1d & Fig. 4.6.2d). Fig. 4.6.1c and Fig. 4.6.2c show the Raman spectra at the interfaces of the bi–layered GC structures sintered for 1 h (Fig. 4.6.1c) and further heat treated for 100 h (Fig. 4.6.2c). Micro–Raman allows getting complementary information by analyzing different points at the interface within the micrometric range, not assessible by XRD. Both layers exhibit similar structural features (Fig. 4.6.3). However, the peaks are quite sharp in the case of Sr–0.3, whereas in Gd–0.3 they are much broader.

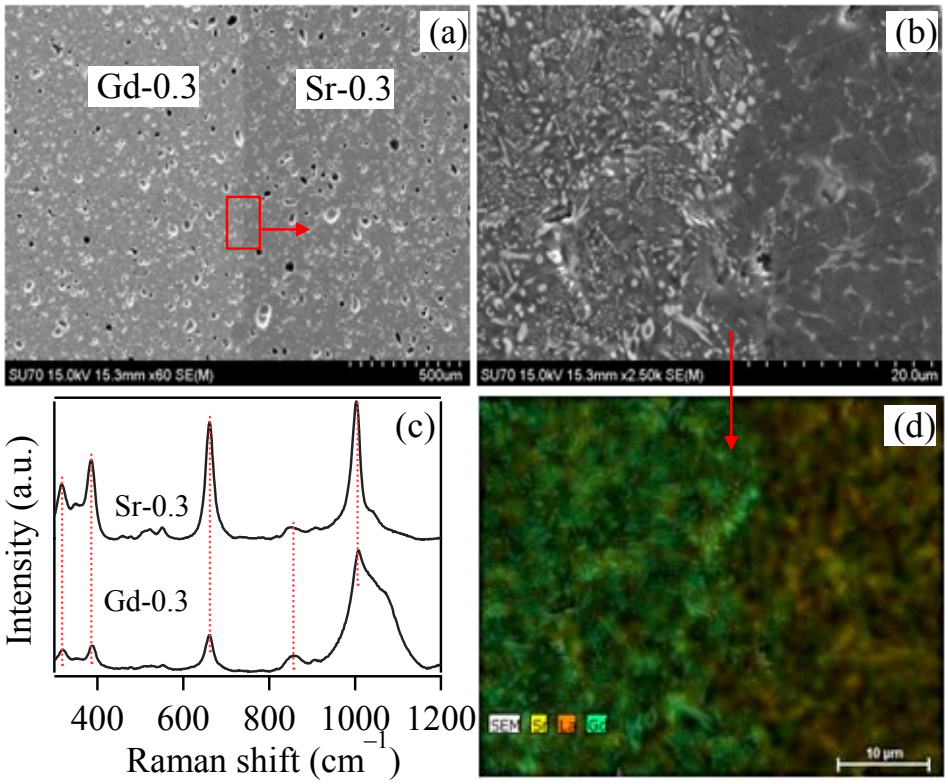

Fig. 4.6.1: Interface between Gd–0.3 and Sr–0.3 glass–ceramics after heat treating at 850 ºC for 1 h: (a) and (b) SEM images; (c) Raman spectra; (d) elemental mapping.

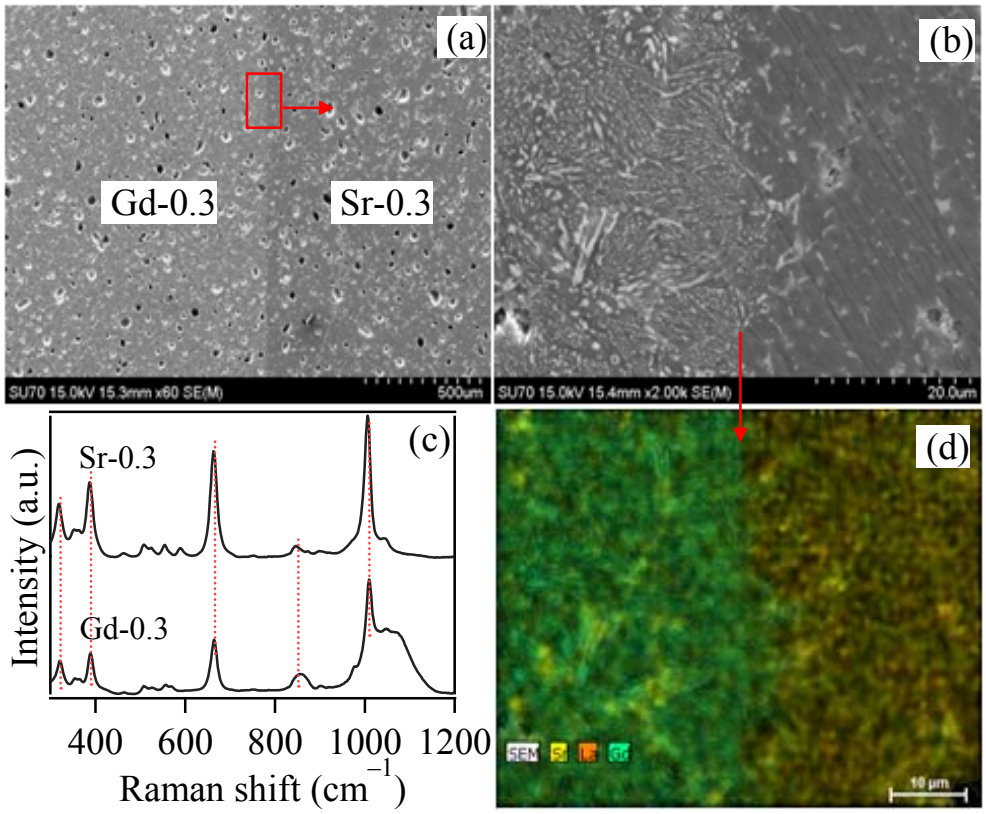

Fig.4.6.2: Interface between Gd–0.3 and Sr–0.3 glass–ceramics after heat treating at 850 ºC for 100 h: (a) and (b) SEM images; (c) Raman spectra; (d) elemental mapping.

The above mentioned difference in peaks' definition can be understood based on the quantity of crystalline and glassy fractions present in the respective glasses. In general, broad Raman peaks are indicative of the glassy nature of materials. Thus, it is worth mentioning at this point that the high fraction of amorphous material presented in Gd–0.3 GC may be playing a crucial role in achieving the strong interaction and in the formation of the smooth interface between the two bi–layers. On the other hand, it is worthy mentioning that vibrational Raman bands observed for both Sr–0.3 and Gd–0.3 GCs were similar to those of synthetic diopside (Fig. Fig. 4.6.4) reported by Rcihet et al.[204]. Micro–Raman analysis at the interface of bi–layered GC revealed that no further structural variations occurred during the further 100 h of heat treatment, except in intensity and full width half–maximum of the peaks. These changes were due to the

partial conversion of glassy phase into crystalline phase (namely to the diopside [138, 154, 155, 203]) along the heat treatment period. Micro–Raman mapping (Fig. 4.6.3) provides additional clearer information about this phase transition. These initial studies prove the suitability of the proposed glasses for the bi–layer approach, encouraging the application of this concept as sealant systems for SOFCs.

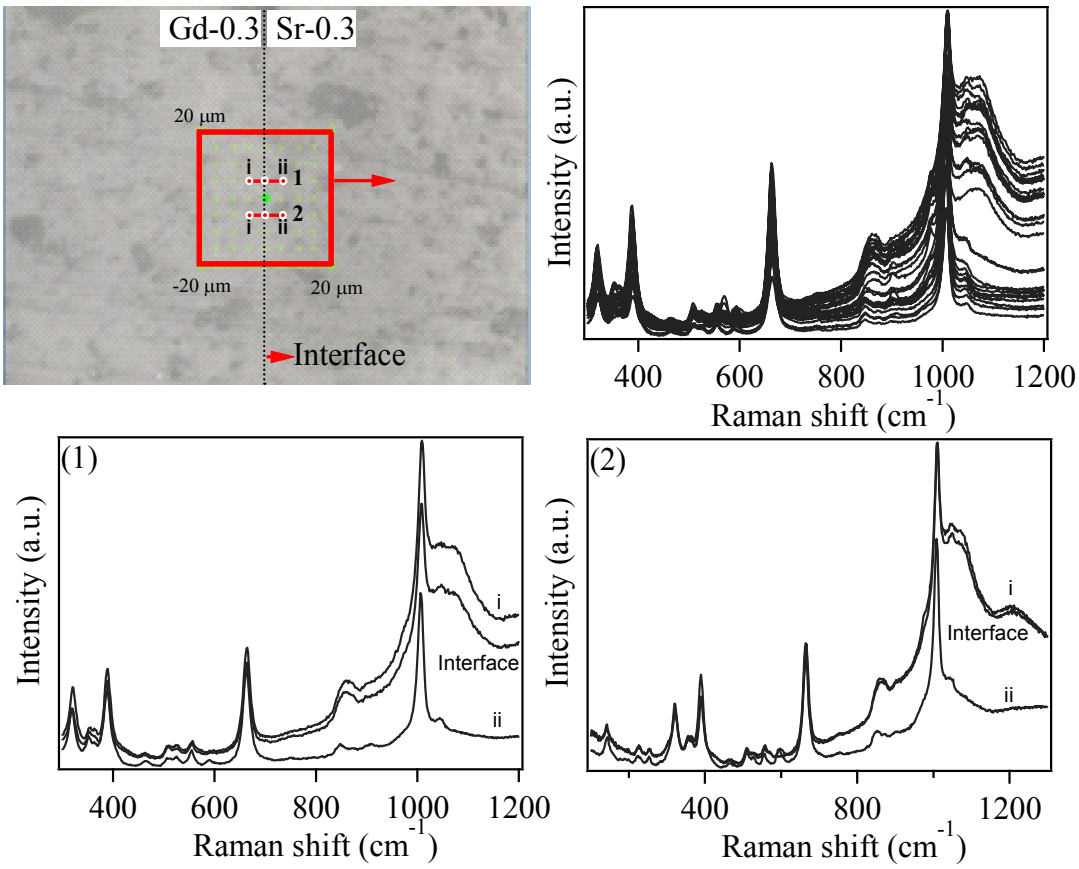

Fig. 4.6.3: SEM image and micro–Raman spectra collected in the square area (identified in the SEM image) at the interface between Gd–0.3 glass–ceramic/Sr–0.3 glass–ceramic after heat treatment at 850 ºC for 100 h. The figures (1) and (2) below show Raman spectra at 3 different places with 5 μm interval along the interface.

The mechanical strength values measured for the bi–layered GCs after sintering at 850 ºC for 1 h, and after further heat treating for 100 h, were 105±5 MPa and 118±7 MPa, respectively. In order to characterize the quality of the bi–layer GCs, the two–

parameter Weibull statistics was implemented based on the measured mechanical strength values. The obtained plots are presented in Fig. 4.6.5a. According to Weibull statistics [122], the increasing probability of failure (F) for a brittle material can be expressed by $F=1-exp\ (-\sigma/\sigma_0)^m$, where F is the failure probability for an applied stress (σ), σ_0 is a normalizing parameter known as Weibull characteristic strength, and m is the Weibull modulus. Here, the Weibull modulus m is a measure of the degree of strength data dispersion. It can be observed that the failure probability function provides a reasonable fit to the experimental data. The obtained mechanical strength values for all the GCs being within the limits (22–150 MPa) required for SOFCs sealants make them suitable for this specific application [205]. The increase in mechanical strength of bi–layered GCs from 105±5 MPa to118±7 MPa with increasing heat treatment time from 1 to 100 h is attributable to a greater extent of crystallization as can be deduced from the sharper Raman peaks after the longer thermal heat treatment. It is known that phase assemblage variations (types and volume fractions of crystalline/amorphous phases) in GCs upon isothermal treatments influence the mechanical strength of the seal. For example, a greater flexural strength was reported for the aged GC–9 glass sample in comparison to a non–aged one due to the increase of crystalline fraction [93].

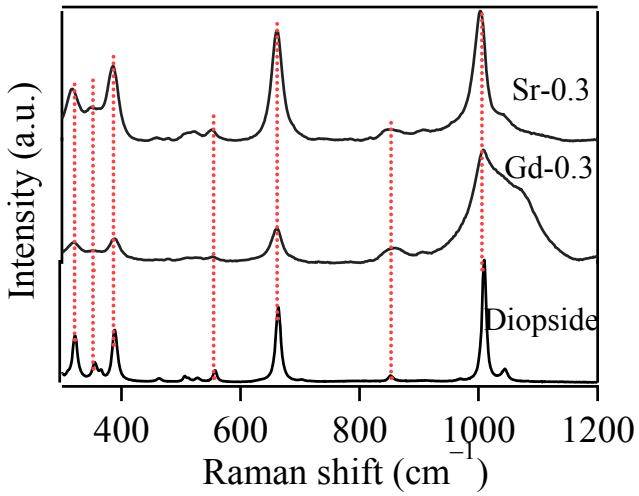

Fig. 4.6.4: Comparison of Raman spectra for Sr–0.3 and Gd–0.3 glass–ceramics with the pure diopside crystalline phase (Ref. [204]).

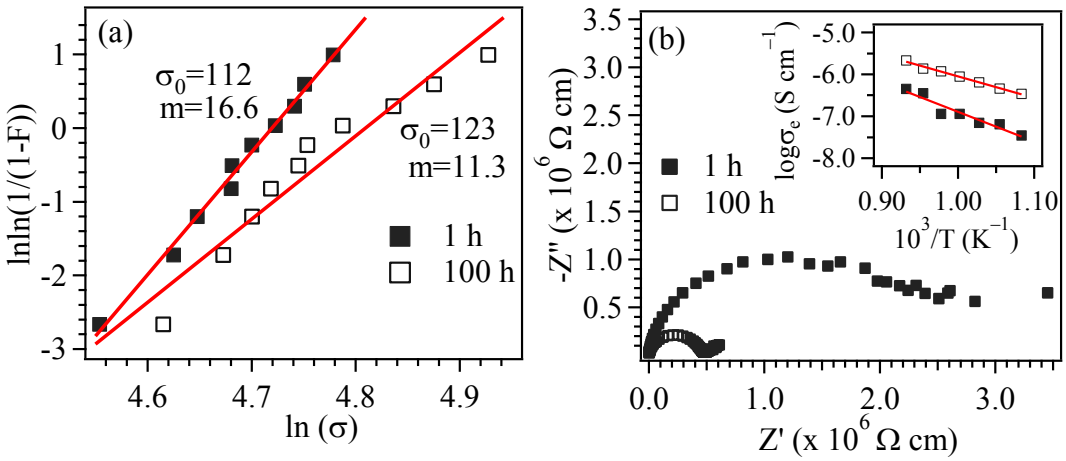

Fig. 4.6.5: (a) Weibull distributions of flexural strength values for the Gd–0.3/Sr–0.3 bi–layered glass–ceramics heat treated at 850 ºC for 1 h, and (b) Impedance spectra obtained at 800 ºC in air of bi–layered glass–ceramics. The inset in (b) shows the temperature dependence of the electrical conductivity.

A potential problem in multi–/bi–layered materials is the crack growth between the continuous layers. Cracks can derive from residual stresses generated at the interface due to large differences in the CTE and phase transitions. Thus, a close match of the CTEs of all components is essential for the mechanical integrity of the join between metal–ceramic or ceramic–ceramic components of SOFC. Apart from this, different shrinkage behaviours of the layers will also lead to delamination of the multi–/bi–layers. However, linear decreasing/increasing thermal expansion gradients with increasing number of layers will result in smaller residual stresses and, intuitively, one would expect that this would increase the crack growth energy in the layered materials [206].

The CTE values of the glasses and GCs sintered at 850 ºC for 1 h are presented in Table 4.6.1. Sr–0.3 exhibits the highest CTE (11.2 × 10^{-6} K^{-1}) and shrinkage (13.7 %) values. After the heat treatment period of 1,000 h, both GCs exhibited the nearly equal CTE (10.4× 10^{-6} K^{-1}) and shrinkage (14.2%). Considering these observations and the CTE values of metallic interconnects (Crofer22APU, Crofer22H) [(11–12) × 10^{-6} K^{-1}] and of ceramic electrolytes (i.e. 8YSZ) [(10–12) × 10^{-6} K^{-1}], the following bi–layer approach: ceramic electrolyte – Gd–0.3 glass – Sr–0.3 glass – interconnect, was adopted

aiming at reducing the thermal stresses at the interfaces. Nevertheless, the stability of the bi–layered GC/interconnect couple might be deteriorated upon further prolonging the heat treatment due to the propensity of Gd–0.3 glass to continuous devitrification (Table 4.6.1).

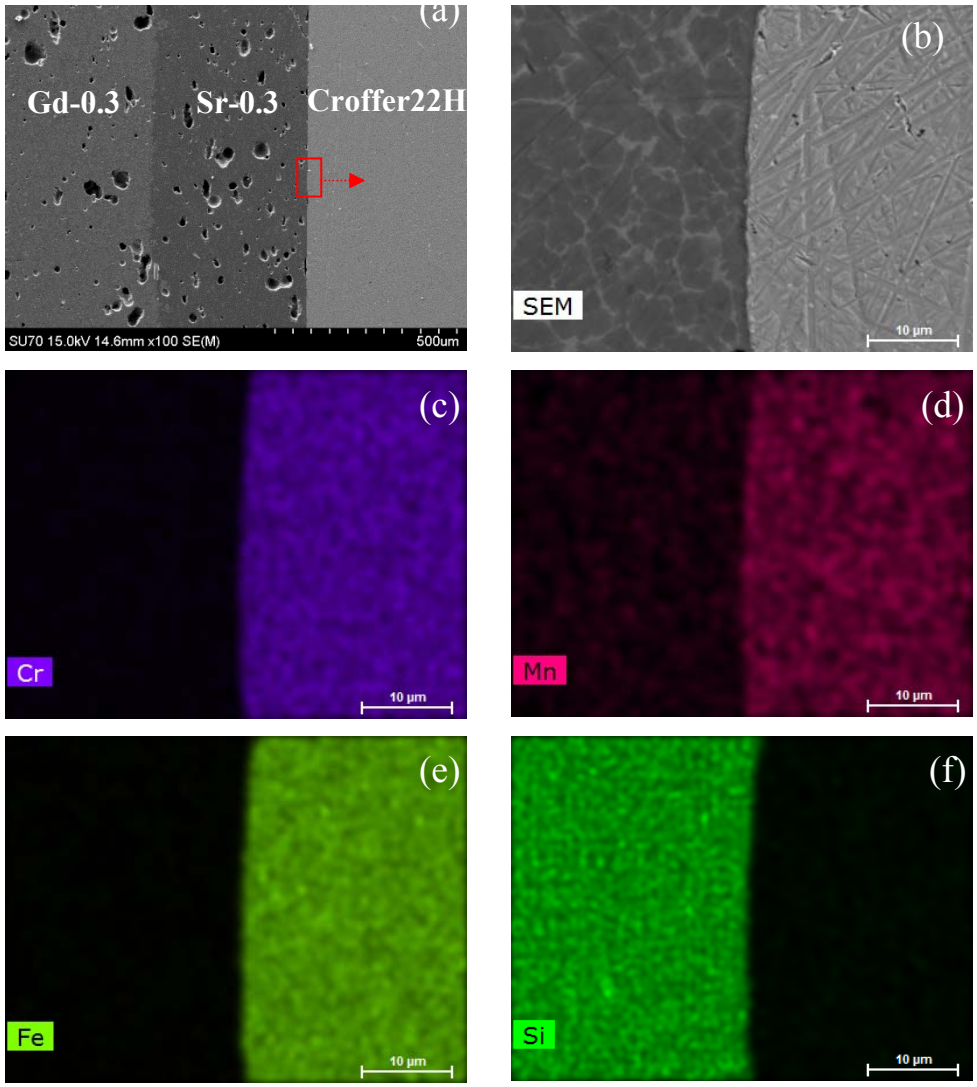

Fig. 4.6.6: SEM image and elemental mappings at the interfaces between Gd–0.3 glass–ceramic/Sr–0.3 glass–ceramic/Crofer22H after heat treatment at 850 ºC for 1 h.

Bi–layered GC seals bonded well to Crofer22H and Crofer22APU metallic interconnects since the investigated interfaces show homogeneous microstructures without any gaps being observed over their entire cross–sections of the joint. Fig.

4.6.6a–b and Fig. 4.6.7a–b show SEM images of the interfaces between bi–layered GCs and Crofer22H after 1 h and 100 h heat treatment at 850 ºC, respectively. The corresponding EDS mapping for the relevant elements (Cr, Mn, Fe, and Si) existing at the Sr–0.3 GC/ interconnect interface are also shown in Fig. 4.6.6 and Fig. 4.6.7. No diffusion layers were detected at the interfaces by SEM/EDS analyses within the limits of experimental uncertainty.

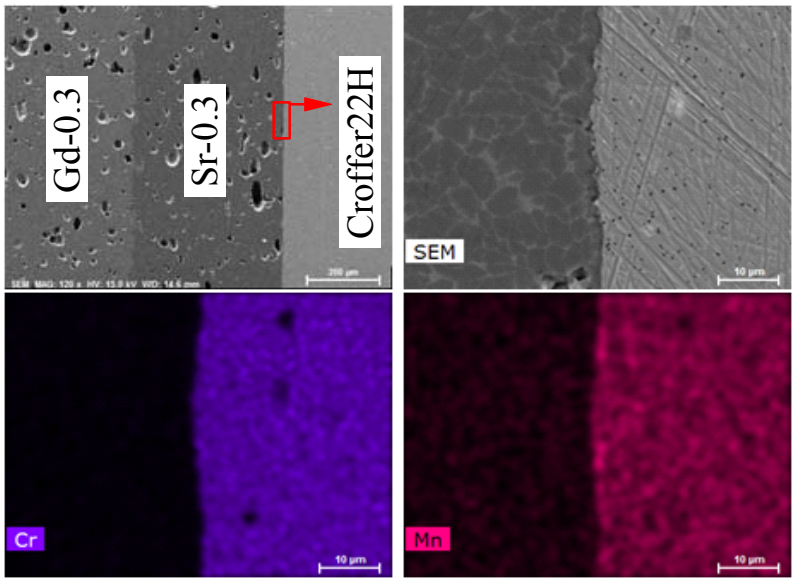

Fig 4.6.7: SEM image and elemental mappings at the Interface between Gd–0.3 GC/Sr–0.3 GC/Crofer22H after heat treating at 850 ºC for 100 h.

Representative impedance spectra obtained in air at 800 ºC for the bi–layered samples annealed at 850 ºC either for 1 h or for 100 h, are shown in Fig. 4.6.5b. The spectrum of a sample sintered at 850 ºC for 1 h shows a large and depressed arc covering almost the entire frequency range which suggests the contribution from different phases with distinct relaxation frequencies, maybe also some interfacial impedance between the seal layers, given their distinct composition and crystallinity. This is coherent with the analysis of the phase content of each layer, where both crystalline and glassy phases are present, and one of the layers is mostly amorphous (Table 4.6.1). At low frequency the spectrum is poorly defined, but a very small electrode tail can be assumed at such low

frequencies. Considering the composition of these glasses, alkaline–earth ions are the most likely charge carriers.

In the case of samples sintered at 850 ºC for 100 h the Nyquist plot obtained under the same conditions shows an almost regular semicircle which indicates the dominant contribution from a single phase. Considering the prolonged thermal treatment, the most likely explanation consists on the extensive crystallization of the glassy phases, providing a continuous ionic pathway throughout the entire bi–layer. If the glassy phases are still present, as suggested in Table 4.6.1, they are likely to provide only a parallel but least conductive pathway, since the conductivity of parallel arrangements is dominated by the most conductive element. This also means that this global conductivity is certainly a function of the thickness ratio of both layers, representing an average performance of the specific characteristics of this bi–layer assembly. The low frequency electrode tail is better defined in the case of samples annealed for 100 h, which indeed confirms the presence of dominant ionic conductivity in these samples. The possibility of a continuous ionic pathway throughout the entire bi–layer is a consequence of the layers composition, including common alkaline–earth cations.

The global bi–layer resistivity shows a considerable variation for samples annealed for 1 h or 100 h. For instance, at 800 ºC the former sample has a resistivity 1.2 MΩ cm while the later has a resistivity of 0.2 MΩ cm. Irrespective of the already suggested dominant ionic transport through these bi–layer seals, the overall resistivity values are still high enough for the functional requirements of SOFC seals, enabling a good isolation between fuel cell components. As reference, in a SOFC, amongst electrolyte, cathode and anode, the least conductive cell component is the electrolyte with a target resistivity lower than 10 Ω cm at operating temperatures. In the worst case scenario (seal after 100 h), this means that the conductivity of the electrolyte is still four orders of magnitude higher than found for the seal. If we also consider the surface area/thickness ratios for currents crossing the electrolyte (high ratio) and sealant (extremely low ratio), we find an even more impressive relation between the cell output current and any internal parasitic current through the seal.

The temperature dependent electrical conductivity is shown in Fig. 4.6.5b inset. The activation energy calculated from the slope of the ln (σ_eT) versus 1/T plots is around 130 kJmol^{-1} and 98 kJmol^{-1} for samples annealed for 1 h and 100 h, respectively. The lower activation energies for the samples annealed for longer periods of time again suggest an easier ionic pathway through the bi–layer. This can be the result of enhanced crystallization in these samples (not only volume fraction but also average crystal/grain size), hypothesis coherent with the XRD results and involved process kinetics. Indeed, at constant temperature, interfaces and amorphous phases are expected to involve higher activation energies for ionic migration than crystalline phases.

5. Conclusions

5.1 Diopside – Ba disilicate glass–ceramics for sealing applications in SOFC: sintering and chemical interactions studies

The results gathered, presented and discussed along this work enable the following conclusion to be drawn:

1. The combination of diopside phase with crystalline phases exhibiting high CTE, such as barium aluminosilicates, revealed to be a promising strategy to increase and stabilize the CTE of the diopside based GCs, and to increase their electrical resistivity.
2. The CTE values of investigated GCs are relatively stable under different heat treatment schedules and correlated quite well with those of ceramic electrolyte, 8YSZ (~10×0^{-6} K^{-1}) and metallic interconnect, Crofer22APU (~$11.4–12.5\times10^{-6}$ K^{-1}).
3. In all experimental glass powders the sintering proceded in two stages, but most of the densification (95–98 %) occurred along the first stage and was thus accomplished at T_{MS1}, i.e., before the onset of crystallization, therefore, resulting in well sintered and dense glass powder compacts.
4. Stability of the main Augite phase after prolonged isothermal heat treatment was achieved and no formation of other detrimental phases were detected.
5. The investigated GCs showed good insulating properties. At 1073 K the resistivity varied in the range 5–10 MOhm × cm, enabling good isolation to be achieved between the fuel cell components.
6. The investigated interfaces showed: (i) homogeneous microstructures over the entire cross–sections of the joints without gaps formation; (ii) no appreciable diffusion of elements from GCs towards Crofer22APU and vice–versa; (iii) absence of any detrimental Cr– or Ba–rich layers, at least after sealing.

5.2 Diopside–Ba disilicate glass–ceramic sealants for SOFCs: enhanced adhesion and thermal stability by Sr for Ca substitution

From this work the following conclusions might be drawn:

1. Strontium for calcium substitution in diopside–Ba disilicate GC revealed to be a promising strategy for stabilizing the thermal parameters and enhancing the adhesion of GCs seals to interconnect material of SOFCs.
2. Systematic substitution Sr for Ca in pyroxene structure decreases the viscosity of glasses at temperatures close to T_g and within the range of 850–900 ºC that is usually considered for joining of SOFC metallic/ceramic components by a glass/glass–ceramic sealant.
3. All the studied SrO–containing glasses exhibited higher CTE compared to the SrO–free parent glass. Their CTE values varied in the range $(10.0–11.3)\times10^{-6}$ K^{-1} and are nearly equal to CTE of corresponding GCs $(9.6–11.2)\times10^{-6}$ K^{-1}. CTE of investigated glass–ceramics are relatively stable under different heat treatment schedules and correlated quite well with those of ceramic electrolyte, 8YSZ and metallic interconnect, Sanergy HT.
4. The sintering precedes crystallization resulting in well sintered and dense glass powder compacts. Although densification occurred in two stages, the first stage contributed in 95–98 % to the total shrinkage and was accomplished at T_{MS1}, i.e., before the onset of crystallization.
5. Precipitation and mutual transformation of pyroxene based phases, i.e. solid solutions of diopside, after prolonged isothermal heat treatment was revealed and no formation of other detrimental phases were detected. This feature ensured stability of CTE under various heat treatment conditions.
6. Glass–ceramics demonstrated excellent insulating properties. Their specific electrical resistivity is higher than 5 MOhm×cm at 800 ºC, and is independent of the oxygen and water vapor partial pressures. This enables isolation between the fuel cell components. No oxygen leakage fluxes through dense glass–ceramics were detected.

7. Homogeneous microstructures over the entire cross–sections of the GC–interconnect joints (a) without gaps formation, (b) no appreciable diffusion of elements from GC toward Sanergy HT and vice–versa, and (c) absence of any detrimental Cr or Ba–rich layers were observed.
8. The thermal shock resistance tests demonstrated that sealants are suitable for sealing of zirconia–based ceramics. Further optimization will be required for SOFC stacks involving other electrolytes (CGO or LSGM).

5.3 Effect of strontium–to–calcium ratio on the structure, crystallization behaviour and functional properties of diopside–based glasses

The data presented and discussed within this part of the work enable the following conclusions to be drawn:

1. The Sr/Ca ratio influences on the sintering behaviour of glass–powder compacts and on the structure and properties of glass–ceramics in diopside–based glasses. High Sr/Ca ratios tend to enhance the sintering ability of glass–powder compacts.
2. The conversion of structural units from Q^2 to Q^1+Q^4 indicates that increasing the Sr/Ca ratio perturbs the glass network more effectively and allows new crystalline phases to be formed when heated to sufficiently high temperature. Diopside–based crystalline phase was dominant at lower Sr/Ca ratios whilst Sr–akermanite phase emerged at higher Sr/Ca ratios.
3. The crystalline phase assemblage evolved up to 500 h heat treatment and then remained essentially unchanged with further heat treatment up to 1000 h.
4. The thermal and mechanical properties of the glass–ceramics produced under various heat–treatment conditions are well correlated with the structure and crystalline phase assemblages.
5. Although their adhesion to the surface of stabilized–zirconia electrolytes and metallic interconnects needs to be improved, the overall functional properties of these glass–ceramics qualify them for further experimentations as sealants for SOFC.

5.4 Sintering behaviour of lanthanide–containing glass–ceramic sealants for solid oxide fuel cells

A detailed investigation dedicated towards evaluating the influence of lanthanides on sintering behaviour of alkaline–earth aluminosilicate glass/GCs has been carried out with an aim to develop suitable GC sealant for solid oxide fuel cells. The following conclusions can be drawn from the discussed results:

1. All the glasses exhibit CTE in range of (9 – 10.5) x 10^{-6} K^{-1} while the sintered GCs exhibit CTE in the range of (9.8 – 11.12) x 10^{-6} K^{-1} which is appropriate for sealing applications in SOFC.
2. The sintering initiates in all the glasses in the temperature range of 620 – 650 ºC followed by glass–in–glass phase separation consequentially leading to two stage sintering behaviour .
3. Well sintered and dense GCs were obtained after sintering of glass powders at 850 ºC for 1h with crystalline phase assemblage dominated primarily by diopside based crystalline phases.
4. The electrical conductivity of the investigated GCs varied between (1.19 – 7.33) x 10^{-7} S cm^{-1} (750 – 800 ºC). La–containing GCs exhibit highest electrical conductivity while Yb–containing GCs exhibited the lowest value.
5. The as developed GCs possess high amount of residual glassy phase (~30 – 96 wt.%) along with appropriate flow behaviour and CTE matching at SOFC operating temperatures (850 – 900 ºC), thus making them suitable candidates for self–healing GC seals for SOFC. In particular, GCs La–0.1, La–0.2, Nd–0.1 and Nd–0.2 are potential materials for sealing applications in SOFC. Also, GCs Gd–0.3 and Yb–0.3 demonstrate high sintering ability, mono–mineral crystalline phase assemblage and > 95 wt.% residual amorphous phase, thus, making them suitable candidates for self–healing glass seals.

5.5 Thermal and mechanical stability of lanthanide–containing glass–ceramic sealants for solid oxide fuel cells

The data presented and discussed along this part of the work enable drawing the following conclusions:

1. The glasses Gd–0.3 and Yb–0.3 demonstrated a sluggish crystallization behaviour in comparison to their lanthanum and neodymium containing analogues and, consequently, featured high residual glassy phase contents after sintering for 1 h at 850 ºC.
2. Prolonged heat treatment at 850 ºC for 250–1000 h caused intensive crystallization of pyroxene based phases and lanthanide–containing silicate oxyapatites that was accompanied by a significant drop of the residual amorphous glassy phase content. These processes are accompanied with a moderate increase of the electrical conductivity, which remains, however, low enough for SOFC applications.
3. All the GC seals bonded well to Sanergy HT metallic interconnects and 8YSZ solid electrolyte, without the formation of gaps or deleterious phases.
4. The investigated GCs featured good mechanical reliability with flexural strength values within the range of 110–140 MPa and Weibull modulus, m ~8.9–16.6 after heat treatment at 850 ºC for 1000 h.
5. The glass composition Gd–0.3 appears as the most promising candidate for self–healing sealants for SOFC due to its ability to maintain a relatively high crystalline/amorphous ratio of ~60/40 (wt.%) along with a stable crystalline phase assemblage during long run, and good performance in terms of mechanical reliability, electrical and thermal–shock resistances, oxygen leakage and thermal expansion. Long–term tests of electrical resistivity and oxygen permeation did not reveal essential degradation of this sealant.

5.6 Bi–layer glass–ceramic sealant for solid oxide fuel cells

1. Smooth and void free bi–layered GCs were successfully obtained. The high amount of glassy phase (96 vol.%) presented in Gd–0.3 glass enabled the formation of smooth interface and strong bonding with the Sr–0.3.

2. The as developed bi–layered GCs possess good mechanical reliability and wetting ability with Crofer22APU and Crofer22H, while having enough electrical resistivity.

3. Irrespective of the partial conversion of amorphous to crystalline phases with annealing at working temperatures, the global electrical conductivity of these GC bi–layers was at least four orders of magnitude lower than target values for the electrolyte layer. This low conductivity, presumably dominated by ionic transport, is clearly compatible with the electrical functional requirement imposed to efficient SOFC sealing materials.

4. Despite the interesting results achieved in this study, further experiments are needed for better evaluating the stability of the crystalline phase assembly of Gd–0.3 composition and its implications concerning the sealing performance at the SOFC's stack operation temperature.

Future plan

In order to overcome the challenges being faced by SOFCS community, we have developed a bi–layered GC sealing system. Based on the results obtanied, a new concept i.e., ***multilayer seal*** can be proposed. The inspiration behind the multilayer seal material is as follows: In general, glass materials are chemically stable when exposed to the hydrogen fuel gas or other metallic or ceramic fuel cell components. In addition, if the glass (i) does not crystallize at the elevated temperatures of normal operation of SOFCs and its T_g is below and T_s is above the SOFCs working temperature, it behaves as a self–healing material. Apart from this, it is known that ceramic materials have excellent long term chemical and thermal stability. Therefore, the development of SH–GC seals adjoined with rigid GC seals in a multi–layered fashion where rigid GC will be sandwiched between SH–GCs may provide a better solution. The rationale behind this idea is to develop two GC compositions with varying amorphous/crystalline content and their CTE matching to SOFC ceramic/metallic components. While the first and third GC layers in contact with SOFC components will have higher amorphous content (70–80 vol.%), the second GC layer sandwiched between first and third GC layers will have an amorphous content varying between 20–30 wt.%. The presence of 20–30 % crystalline content in SH–glass controls the viscosity at operating temperature and stuck with in the stack. Whilst, the presence 20–30 wt.% glass content in layer 2 helps in making strong bond with the layers of 1 and 3rd. In addition, the second GC layer as a core of the whole system will impart mechanical integrity for the sandwiched layers along with the assurance of zero gas permeability.

From the present study Sr–0.3 GCs could be used as a rigid GC layer in a multilayer seal due to the following reasons: (i) good sintering ability suitable for SOFC sealants; (ii) stable phase assemblage with >85 % crystallized fraction after 250 h of heat treatment, (iii) excellent thermal stability properties such as CTE and mechanical strength along a period of 1,000 h at 900 ºC, (iv) well bonding to the Sanergy HT metallic interconnect and 8YSZ ceramic electrolyte without forming any undesirable interfacial layers at the joints of SOFC components and GC both in air and reduced atmosphere

condition, (v) the stability of electrical conductivity in various atmosphere during the period of 250 h and (vi) has the good thermal shock resistance with 8YSZ ceramic plate. On the other hand, Gd–0.3 glass can be used as starting point to develop a self–healing GC layer fulfilling all the required properties, including the following:

1. Stable and higher amorphous quantity after prolong heat treatment (~3000 h) at 850 ºC.
2. Self–healing behaviour at temperatures slightly above the SOFCs working temperature range.

After the successful development of self–healing glass/GC layer from the Gd–0.3 glass, future work in this area may be addressed to the following issues:

a) The interfacial strength between SHGC and rigid GC layers can be studied by nano–indentation technique.
b) Diffusion of elements across the interface between SHGC and rigid GC layer should be addressed.
c) The chemical interaction between SH–GC sealants and SOFC components should be studied after prolonged heat treatments (~3000 h) at SOFC operating conditions.
d) Temperature dependence of viscosity is another concern which should be addressed while improving the properties of sealant.
e) Self–healing behaviour should be studied by *in–situ* SEM.
f) Thickness dependence properties of multilayer seal should be studied
g) Also, it will be necessary to study the influence of seal design on the thermal stresses in SOFC stack using finite elemental analysis technique which will include the development of three–dimensional model of SOFC stack.
h) Before the final application of Di based GC sealant in SOFC stack, its performance should be evaluated in model cells. After successful experimentation in model cells, this sealant should be applied to SOFC stacks.

References

[1] Wachsman ED, Lee KT. Lowering the temperature of solid oxide fuel cells. Science 2011;334:935-9.

[2] Wachsman ED, Marlowe CA, Lee KT. Role of solid oxide fuel cells in a balanced energy strategy. Energy & Environmental Science 2012;5:5498.

[3] Fuel cell annual report-2012, Office of Fossil Energy Fuel Cell Program, NETL.

[4] Minh NK, Takahashi T. Science-and-Technology-of-Ceramic-Fuel-Cells. The Netharland: Elsevier; 1995.

[5] Larminie J, Dicks A. Fuel Cell Systems Explained. second ed. West Sussex, England: John Wiley & Sons Ltd,; 2003.

[6] Stolten D, Emonts B. Fuel Cell Science and Engineering: Materials, Processes, Systems and Technology. Weinheim, Germany: wiley-VCH Verlag Gmbh &Co. KGaA; 2012.

[7] Haile S, Dane A. Boysen D, Chisholm C, Merle R. Solid acids as fuel cell electrolytes. Nature 2001;410:910-4.

[8] Adams TA, Nease J, Tucker D, Barton PI. Energy Conversion with Solid Oxide Fuel Cell Systems: A Review of Concepts and Outlooks for the Short- and Long-Term. Industrial & Engineering Chemistry Research 2013;52:3089-111.

[9] Singhal SC. Solid oxide fuel cells for power generation. Wiley Interdisciplinary Reviews: Energy and Environment 2014;3:179-94.

[10] Ellen I-T, Andre W, Dirk H. Materials and technologies for SOFC-components. . Journal of the European Ceramic Society 2001;21:1805–11.

[11] Freiman S, Mecholsky Jr J. The fracture of brittle materials: testing and analysis,. USA: American Ceramic Society and John Wiley & Sons.,; 2012.

[12] Refi J. Fiber Optic Cable - A lightguide. USA: abc TeleTraining, Inc.; 1991.

[13] Zhao Y, Xia C, Jia L, Wang Z, Li H, Yu J, et al. Recent progress on solid oxide fuel cell: Lowering temperature and utilizing non-hydrogen fuels. International Journal of Hydrogen Energy 2013;38:16498-517.

[14] Fuel cell handbook. EG&G Technical Services, Science Applications International Corporation, . 6th ed. U.S. Department of Energy Office of Fossil Energy, Morgantown, West Virginia. : Springfield; 2002.
[15] Minh NQ, Takahashi T. Science and Technology of Ceramic Fuel Cells. Amsterdam: Elsevier; 1995.
[16] Sammes N. Fuel Cell Technology: Reaching Towards Commercialization. London: Springer; 2006.
[17] Perfilyev MV, Demin AK, Kuzin BL, Lipilin AS. High-Temperature Electrolysis of Gases. Nauka, Moscow1988.
[18] Tsipis EV, Kharton VV. Electrode materials and reaction mechanisms in solid oxide fuel cells: a brief review. III. Recent trends and selected methodological aspects. Journal of Solid State Electrochem 2011;15:1007-40.
[19] Gellings PJ, Bouwmeester HJM. Handbook of Solid State Electrochemistry. . Boca Raton: CRC Press; 1997.
[20] Kharton VV. Solid State Electrochemistry I: Fundamentals, Materials and their Applications. Weinheim: Wiley-VCH; 2009.
[21] Mahapatra MK, Lu K. Glass-based seals for solid oxide fuel and electrolyzer cells – A review. Materials Science and Engineering: R: Reports 2010;67:65-85.
[22] Basu RN, Blass G, Buchkremer HP, Stöver D, Tietz F, Wessel E, et al. Simplified processing of anode-supported thin film planar solid oxide fuel cells. Journal of the European Ceramic Society 2005;25:463-71.
[23] Fergus JW. Sealants for solid oxide fuel cells. Journal of Power Sources 2005;147:46-57.
[24] Jacobson AJ. Materials for Solid Oxide Fuel Cells. Chemistry of Materials 2010;22:660-74.
[25] Mahapatra MK, Lu K. Seal glass for solid oxide fuel cells. Journal of Power Sources 2010;195:7129-39.
[26] Lessing PA. A review of sealing technologies applicable to solid oxide electrolysis cells. Journal of Materials Science 2007;42:3465-76.
[27] Xue LA, Yamanis J, Piascik J, Ong ET. Alkali-free composite sealant materials for solid oxide fuel cells. US Patent 75213872009.

[28] Warrier SG, Yamanis J, Tulyani S, Benn RC. Compliant seals for solid oxide fuel cell stack. US Patent 79770042011.

[29] Yoo YS, Han YH, Kang TK. Single cell and stack structure for solid oxide fuel cell stack. US Patent 68640092005.

[30] Badding EM, Cortright EJ, Ketcham TD, Lineman MD, Julien JD, Sun Y. Solid oxide fuel cell stack and packet designs. Eur. Patent 14468472002.

[31] Draper R, Zhang G, Ruka RJ, Litzinger KP, Zafred PR, R.A. Basel Solid oxide fuel cell generator including a glass sealant. US Patent 80973812012.

[32] Ko HJ, Lee HW, Lee JC, Lee JH, Song HS, Kim JS, et al. Solid oxide fuel cell sealant comprising glass matrix and ceramic fiber and method of manufactoring the same. US patent 0147866 A12005.

[33] Goel A, Shaaban ER, Tulyaganov DU, Ferreira JMF. Study of Crystallization Kinetics in Glasses along the Diopside-Ca-Tschermak Join. Journal of the American Ceramic Society 2008;91:2690-7.

[34] Tong J, Han M, Singhal SC, Gong Y. Influence of Al_2O_3 addition on the properties of Bi_2O_3–BaO–SiO_2–R_xO_y (R=K, Zn, etc.) glass sealant. Journal of Non-Crystalline Solids 2012;358:1038-43.

[35] Smeacetto F, Chrysanthou A, Salvo M, Moskalewicz T, D'Herin Bytner F, Ajitdoss LC, et al. Thermal cycling and ageing of a glass-ceramic sealant for planar SOFCs. International Journal of Hydrogen Energy 2011;36:11895-903.

[36] Chang H-T, Lin C-K, Liu C-K, Wu S-H. High-temperature mechanical properties of a solid oxide fuel cell glass sealant in sintered forms. Journal of Power Sources 2011;196:3583-91.

[37] Zachariasen WH. The atomic arrangement in glass. Journal of American Chemical Society 1932;54:3841-51.

[38] Larsen PH, Poulsen FW, Berg RW. The influence of SiO_2 addition to 2MgO-Al_2O_3-3.3P_2O_5 glass. Journal of Non-Crystalline Solids 1999;244:16-24.

[39] Ghosh S, Das Sharma A, Kundu P, Mahanty S, Basu RN. Development and characterizations of BaO–CaO–Al_2O_3–SiO_2 glass–ceramic sealants for intermediate temperature solid oxide fuel cell application. Journal of Non-Crystalline Solids 2008;354:4081-8.

[40] Bansal NP, Gamble EA. Crystallization kinetics of a solid oxide fuel cell seal glass by differential thermal analysis. Journal of Power Sources 2005;147:107-15.
[41] Meinhardt KD, Kim DS, Chou YS, Weil KS. Synthesis and properties of a barium aluminosilicate solid oxide fuel cell glass–ceramic sealant. Journal of Power Sources 2008;182:188-96.
[42] Ghosh S, Kundu P, Das Sharma A, Basu RN, Maiti HS. Microstructure and property evaluation of barium aluminosilicate glass–ceramic sealant for anode-supported solid oxide fuel cell. Journal of the European Ceramic Society 2008;28:69-76.
[43] Yang Z. Chemical interactions of barium–calcium–aluminosilicate-based sealing glasses with oxidation resistant alloys. Solid State Ionics 2003;160:213-25.
[44] Stephens EV, Vetrano JS, Koeppel BJ, Chou Y, Sun X, Khaleel MA. Experimental characterization of glass–ceramic seal properties and their constitutive implementation in solid oxide fuel cell stack models. Journal of Power Sources 2009;193:625-31.
[45] Meinhardt KD, Vienna JD, Armstrong TR, Pederson LR. Glass-Ceramic Material and method of making. United states2002.
[46] Larsen PH, james PF. Chemical stability of MgO/CaO/Cr_2O_3–Al_2O_3–B_2O_3–phosphate glasses in solid oxide fuel cell environment. Journal of Materials Science 1998;33:2499-507.
[47] Liu WN, Sun X, Koeppel B, Khaleel M. Experimental Study of the Aging and Self-Healing of the Glass/Ceramic Sealant Used in SOFCs. International Journal of Applied Ceramic Technology 2010;7:22-9.
[48] Liu WN, Sun X, Khaleel MA. Study of geometric stability and structural integrity of self-healing glass seal system used in solid oxide fuel cells. Journal of Power Sources 2011;196:1750-61.
[49] Gross SM, Federmann D, Remmel J, Pap M. Reinforced composite sealants for solid oxide fuel cell applications. Journal of Power Sources 2011;196:7338-42.
[50] Pascual MJ, Guillet A, Durán A. Optimization of glass–ceramic sealant compositions in the system MgO–BaO–SiO_2 for solid oxide fuel cells (SOFC). Journal of Power Sources 2007;169:40-6.
[51] Donald IW, Metcalfe BL, Gerrard LA. Interfacial Reactions in Glass–Ceramic-to-Metal Seals. Journal of the American Ceramic Society 2008;91:715-20.

[52] Coillot D, Méar FO, Podor R, Montagne L. Autonomic Self-Repairing Glassy Materials. Advanced Functional Materials 2010;20:4371-4.
[53] Govindaraju N, Liu WN, Sun X, Singh P, Singh RN. A modeling study on the thermomechanical behavior of glass-ceramic and self-healing glass seals at elevated temperatures. Journal of Power Sources 2009;190:476-84.
[54] Singh RN. Sealing technology for solid oxide fuel cells (sofc). International Journal of Applied Ceramic Technology 2007;4:134-44.
[55] Zhang T, Tang D, Yang H. Can crystalline phases be self-healing sealants for solid oxide fuel cells? Journal of Power Sources 2011;196:1321-3.
[56] Zhang T, Zou Q, Zhang J, Tang D, Yang H. Development of ceramic sealant for solid oxide fuel cell application: Self-healing property, mechanical stability and thermal stability. Journal of Power Sources 2012;204:122-6.
[57] Donald IW, Mallinson PM, Metcalfe BL, Gerrard LA, Fernie JA. Recent developments in the preparation, characterization and applications of glass- and glass–ceramic-to-metal seals and coatings. Journal of Materials Science 2011;46:1975-2000.
[58] Shelby JE. Introduction to glass science and technology. Cambridge: The Royal Society of Chemistry; 1997.
[59] Ganster P, Benoit M, Kob W, Delaye JM. Structural properties of a calcium aluminosilicate glass from molecular-dynamics simulations: a finite size effects study. Journal of Chemical Physics 2004;120:10172-81.
[60] Kaur B, Singh K, Pandey OP. Microstructural study of Crofer 22 APU-glass interface for SOFC application. International Journal of Hydrogen Energy 2012;37:3839-47.
[61] Chou Y-S, Thomsen EC, Choi JP, Stevenson JW. Compliant alkali silicate sealing glass for solid oxide fuel cell applications: Combined stability in isothermal ageing and thermal cycling with YSZ coated ferritic stainless steels. Journal of Power Sources 2012;197:154-60.
[62] Chou Y-S, Thomsen EC, Williams RT, Choi JP, Canfield NL, Bonnett JF, et al. Compliant alkali silicate sealing glass for solid oxide fuel cell applications: Thermal cycle stability and chemical compatibility. Journal of Power Sources 2011;196:2709-16.

[63] Coillot D, Méar FO, Nonnet H, Montagne L. New viscous sealing glasses for electrochemical cells. International Journal of Hydrogen Energy 2012;37:9351-8.
[64] Smeacetto F, Salvo M, Ferraris M, Casalegno V, Asinari P. Glass and composite seals for the joining of YSZ to metallic interconnect in solid oxide fuel cells. Journal of the European Ceramic Society 2008;28:611-6.
[65] Smeacetto F, Salvo M, D'Hérin Bytner FD, Leone P, Ferraris M. New glass and glass–ceramic sealants for planar solid oxide fuel cells. Journal of the European Ceramic Society 2010;30:933-40.
[66] Smeacetto F, Salvo M, Ferraris M, Cho J, Boccaccini AR. Glass–ceramic seal to join Crofer 22 APU alloy to YSZ ceramic in planar SOFCs. Journal of the European Ceramic Society 2008;28:61-8.
[67] Smeacetto F, Chrysanthou A, Salvo M, Zhang Z, Ferraris M. Performance and testing of glass-ceramic sealant used to join anode-supported-electrolyte to Crofer22APU in planar solid oxide fuel cells. Journal of Power Sources 2009;190:402-7.
[68] Smeacetto F, Salvo M, Ferraris M, Casalegno V, Asinari P, Chrysanthou A. Characterization and performance of glass–ceramic sealant to join metallic interconnects to YSZ and anode-supported-electrolyte in planar SOFCs. Journal of the European Ceramic Society 2008;28:2521-7.
[69] Zhang T, Zou Q, Zeng F, Wang S, Tang D, Yang H. Improving the chemical compatibility of sealing glass for solid oxide fuel cells: Blocking the reactive species by controlled crystallization. Journal of Power Sources 2012;216:1-4.
[70] Liu W, Sun X, Khaleel M. Predicting Young's modulus of glass/ceramic sealant for solid oxide fuel cell considering the combined effects of aging, micro-voids and self-healing. Journal of Power Sources 2008;185:1193-200.
[71] Heydari F, Maghsoudipour A, Hamnabard Z, Farhangdoust S. Mechanical properties and microstructure characterization of zirconia nanoparticles glass composites for SOFC sealant. Materials Science and Engineering: A 2012;552:119-24.
[72] Heydari F, Maghsoudipour A, Hamnabard Z, Farhangdoust S. Evaluation on Properties of CaO–BaO–B2O3–Al2O3–SiO2 Glass–Ceramic Sealants for Intermediate Temperature Solid Oxide Fuel Cells. Journal of Materials Science & Technology 2013;29:49-54.

[73] Arora A, Singh K, Pandey OP. Thermal, structural and crystallization kinetics of SiO2–BaO–ZnO–B_2O_3–Al_2O_3 glass samples as a sealant for SOFC. International Journal of Hydrogen Energy 2011;36:14948-55.

[74] Arora A, Kumar V, Singh K, Pandey OP. Structural, thermal and crystallization kinetics of ZnO–BaO–SiO_2–B_2O_3–Mn_2O_3 based glass sealants for solid oxide fuel cells. Ceramics International 2011;37:2101-7.

[75] Chou YS, Stevenson JW, Xia GG, Yang ZG. Electrical stability of a novel sealing glass with (Mn,Co)-spinel coated Crofer22APU in a simulated SOFC dual environment. Journal of Power Sources 2010;195:5666-73.

[76] Chou Y-S, Stevenson JW, Meinhardt KD. Electrical Stability of a Novel Refractory Sealing Glass in a Dual Environment for Solid Oxide Fuel Cell Applications. Journal of the American Ceramic Society 2010;93:618-23.

[77] Chou Y-S, Stevenson JW, Singh P. Effect of pre-oxidation and environmental aging on the seal strength of a novel high-temperature solid oxide fuel cell (SOFC) sealing glass with metallic interconnect. Journal of Power Sources 2008;184:238-44.

[78] Wang S-F, Hsu Y-F, Lu H-C, Lo S-C, Cheng C-S. B_2O3-free SiO_2–Al_2O_3–SrO–La_2O_3–ZnO–TiO_2 glass sealants for intermediate temperature solid oxide fuel cell applications. International Journal of Hydrogen Energy 2012;37:5901-13.

[79] Sharma K, Kothiyal GP, Montagne L, Méar FO, Revel B. A new formulation of barium–strontium silicate glasses and glass-ceramics for high-temperature sealant. International Journal of Hydrogen Energy 2012;37:11360-9.

[80] Tiwari B, Dixit A, Kothiyal GP. Study of glasses/glass-ceramics in the SrO–ZnO–SiO_2 system as high temperature sealant for SOFC applications. International Journal of Hydrogen Energy 2011;36:15002-8.

[81] Ananthanarayanan A, Kothiyal GP, Montagne L, Tricot G, Revel B. The effect of P_2O_5 on the structure, sintering and sealing properties of barium calcium aluminum boro-silicate (BCABS) glasses. Materials Chemistry and Physics 2011;130:880-9.

[82] Kaur G, Pandey OP, Singh K. Interfacial study between high temperature SiO_2–B_2O_3–AO–La_2O_3 (A = Sr, Ba) glass seals and Crofer 22APU for solid oxide fuel cell applications. International Journal of Hydrogen Energy 2012;37:6862-74.

[83] Kumar V, Rupali, Pandey OP, Singh K. Thermal and crystallization kinetics of yttrium and lanthanum calcium silicate glass sealants for solid oxide fuel cells. International Journal of Hydrogen Energy 2011;36:14971-6.

[84] Kumar V, Sharma S, Pandey OP, Singh K. Thermal and physical properties of $30SrO–40SiO_2–20B_2O_3–10A_2O_3$ (A = La, Y, Al) glasses and their chemical reaction with bismuth vanadate for SOFC. Solid State Ionics 2010;181:79-85.

[85] Kumar V, Pandey OP, Singh K. Effect of A_2O_3 (A=La, Y, Cr, Al) on thermal and crystallization kinetics of borosilicate glass sealants for solid oxide fuel cells. Ceramics International 2010;36:1621-8.

[86] Kumar V, Arora A, Pandey O, Singh K. Studies on thermal and structural properties of glasses as sealants for solid oxide fuel cells. International Journal of Hydrogen Energy 2008;33:434-8.

[87] Ojha PK, Rath SK, Chongdar TK, Gokhale NM, Kulkarni AR. Physical and thermal behaviour of Sr–La–Al–B–Si based SOFC glass sealants as function of SrO content and B_2O_3/SiO_2 ratio in the matrix. Journal of Power Sources 2011;196:4594-8.

[88] Jin T, Lu K. Thermal stability of a new solid oxide fuel/electrolyzer cell seal glass. Journal of Power Sources 2010;195:195-203.

[89] Mahapatra MK, Lu K. Interfacial study of Crofer 22 APU interconnect-SABS-0 seal glass for solid oxide fuel/electrolyzer cells. Journal of Materials Science 2009;44:5569-78.

[90] Lu K, Mahapatra MK. Network structure and thermal stability study of high temperature seal glass. Journal of Applied Physics 2008;104:074910.

[91] Lin C-K, Chen J-Y, Tian J-W, Chiang L-K, Wu S-H. Joint strength of a solid oxide fuel cell glass–ceramic sealant with metallic interconnect. Journal of Power Sources 2012;205:307-17.

[92] Chang H-T, Lin C-K, Liu C-K. High-temperature mechanical properties of a glass sealant for solid oxide fuel cell. Journal of Power Sources 2009;189:1093-9.

[93] Chang H-T, Lin C-K, Liu C-K. Effects of crystallization on the high-temperature mechanical properties of a glass sealant for solid oxide fuel cell. Journal of Power Sources 2010;195:3159-65.

[94] Hao J, Zan Q, Ai D, Ma J, Deng C, Xu J. Structure and high temperature physical properties of glass seal materials in solid oxide electrolysis cell. Journal of Power Sources 2012;214:75-83.
[95] Gödeke D, Dahlmann U. Study on the crystallization behaviour and thermal stability of glass-ceramics used as solid oxide fuel cell-sealing materials. Journal of Power Sources 2011;196:9046-50.
[96] Wang S-F, Lu C-M, Wu Y-C, Yang Y-C, Chiu T-W. La_2O_3–Al_2O_3–B_2O_3–SiO_2 glasses for solid oxide fuel cell applications. International Journal of Hydrogen Energy 2011;36:3666-72.
[97] Sun T, Xiao H, Guo W, Hong X. Effect of Al_2O_3 content on BaO–Al_2O_3–B_2O_3–SiO_2 glass sealant for solid oxide fuel cell. Ceramics International 2010;36:821-6.
[98] Wang S-F, Wang Y-R, Hsu Y-F, Chuang C-C. Effect of additives on the thermal properties and sealing characteristic of BaO-Al_2O_3-B_2O_3-SiO_2 glass-ceramic for solid oxide fuel cell application. International Journal of Hydrogen Energy 2009;34:8235-44.
[99] Widgeon SJ, Corral EL, Spilde MN, Loehman RE. Glass-to-Metal Seal Interfacial Analysis using Electron Probe Microscopy for Reliable Solid Oxide Fuel Cells. Journal of the American Ceramic Society 2009;92:781-6.
[100] Laorodphan N, Namwong P, Thiemsorn W, Jaimasith M, Wannagon A, Chairuangsri T. A low silica, barium borate glass–ceramic for use as seals in planar SOFCs. Journal of Non-Crystalline Solids 2009;355:38-44.
[101] Lee S, Mysen B, Cody G. Chemical order in mixed-cation silicate glasses and melts. Physical Review B 2003;68:214206.
[102] Kharton VV, Naumovich EN, Vecher AA. Research on the electrochemistry of oxygen ion conductors in the former soviet union. I ZrO_2-based ceramic materials. Journal of Solid State Electrochemistry 1999;3:61-81.
[103] Zhang T, Brow RK, Fahrenholtz WG, Reis ST. Chromate formation at the interface between a solid oxide fuel cell sealing glass and interconnect alloy. Journal of Power Sources 2012;205:301-6.
[104] Zhang T, Fahrenholtz WG, Reis ST, Brow RK. Borate Volatility from SOFC Sealing Glasses. Journal of the American Ceramic Society 2008;91:2564-9.

[105] Zhang T, Zhang H, Li G, Yung H. Reduction of chromate formation at the interface of solid oxide fuel cells by different additives. Journal of Power Sources 2010;195:6795-7.

[106] Choi SR, Bansal NP, Garg A. Mechanical and microstructural characterization of boron nitride nanotubes-reinforced SOFC seal glass composite. Materials Science and Engineering: A 2007;460-461:509-15.

[107] Zhao Y, Malzbender J, Gross SM. The effect of room temperature and high temperature exposure on the elastic modulus, hardness and fracture toughness of glass ceramic sealants for solid oxide fuel cells. Journal of the European Ceramic Society 2011;31:541-8.

[108] Mahapatra MK, Lu K, Bodnar RJ. Network structure and thermal property of a novel high temperature seal glass. Applied Physics A 2008;95:493-500.

[109] Chang CYS, Wei WCJ, Hsueh CH. Viscosity of Ba–B–Si–Al–O glass measured by indentation creep test at operating temperature of IT-SOFC. Journal of Non-Crystalline Solids 2011;357:1414-9.

[110] Ojha PK, Chongdar TK, Gokhale NM, Kulkarni AR. Investigation of crystallization kinetic of $SrO–La_2O_3–Al_2O_3–B_2O_3–SiO_2$ glass and its suitability for SOFC sealant. International Journal of Hydrogen Energy 2011;36:14996-5001.

[111] Mahapatra MK, Lu K, Liu X, Wu J. Compatibility of a seal glass with $(Mn,Co)_3O_4$ coated interconnects: Effect of atmosphere. International Journal of Hydrogen Energy 2010;35:7945-56.

[112] Peng L, Zhu Q. Thermal cycle stability of $BaO–B_2O_3–SiO_2$ sealing glass. Journal of Power Sources 2009;194:880-5.

[113] Brown GE, Gibbs GV. Stereochemistry and ordering in the tetrahedral portion of silicates. American Mineralogist 1970;55:1587-607.

[114] Chou Y-S, Stevenson JW, Singh P. Novel refractory alkaline earth silicate sealing glasses for planar solid oxide fuel cells. Journal of The Electrochemical Society 2007;154:B644.

[115] Zhang T, Brow RK, Reis ST, Ray CS. Isothermal crystallization of a solid oxide fuel cell sealing glass by differential thermal analysis. Journal of the American Ceramic Society 2008;91:3235-9.

[116] Volf MB. Glass science and technology. Amsrerdam: Elsevier; 1984.
[117] Goel A, Tulyaganov DU, Kharton VV, Yaremchenko AA, Ferreira JMF. Electrical behavior of aluminosilicate glass-ceramic sealants and their interaction with metallic solid oxide fuel cell interconnects. Journal of Power Sources 2010;195:522-6.
[118] Batfalsky P, Haanappel VAC, Malzbender J, Menzler NH, Shemet V, Vinke IC, et al. Chemical interaction between glass–ceramic sealants and interconnect steels in SOFC stacks. Journal of Power Sources 2006;155:128-37.
[119] Story C, Lu K, Reynoldsjr W, Brown D. Shape memory alloy/glass composite seal for solid oxide electrolyzer and fuel cells. International Journal of Hydrogen Energy 2008;33:3970-5.
[120] Scholze H. Ver: Dtsch Kerom Ges, 1962;391:63.
[121] Pascual MJ, Duran A, Prado MO. A new method for determining fixed viscosity points of glasses. Physical Chemistry Glasses 2005;46:512-21.
[122] Waloddi A W, Stockholm S. A stastical distrubution function of wide applicability. Journal of appled Mechanics 1951;18:293-9.
[123] Larson AC, Dreele VRB. GSAS: General Structure Analysis System LANSCE, MS-H805;. Los Alamos National Laboratory, Los Alamos, NM, 1998.
[124] Toby BH. EXPGUI, a graphical user interface for GSAS. Journal of Applied Crystalography 2001;34:210-3.
[125] Crofer 22 APU, Material data sheet no. 4046, December 2006, Thyssen Krupp VDM, Germany.
[126] Sanergy HT, Material data sheet, Sandvik Materials Technology, Sandvik, Sweden.
[127] Kharton V, Marques F, Atkinson A. Transport properties of solid oxide electrolyte ceramics: a brief review. Solid State Ionics 2004;174:135-49.
[128] Pascual MJ, Kharton VV, Tsipis E, Yaremchenko AA, Lara C, Durán A, et al. Transport properties of sealants for high-temperature electrochemical applications: RO–BaO–SiO_2 (R=Mg, Zn) glass–ceramics. Journal of the European Ceramic Society 2006;26:3315-24.
[129] Chase MW. NIST-JANAF thermochemical tables, fourth edition. Journal of Physical Chemistry Reference Data 1998:1–1951.

[130] Goel A, Tulyaganov DU, Agathopoulos S, Ribeiro MJ, Basu RN, Ferreira JMF. Diopside–Ca-Tschermak clinopyroxene based glass–ceramics processed via sintering and crystallization of glass powder compacts. Journal of the European Ceramic Society 2007;27:2325-31.

[131] Goel A, Tulyaganov DU, Kharton VV, Yaremchenko AA, Ferreira JMF. The effect of Cr_2O_3 addition on crystallization and properties of La_2O_3-containing diopside glass-ceramics. Acta Materialia 2008;56:3065-76.

[132] Goel A, Ferrari AM, Kansal I, Pascual MJ, Barbieri L, Bondioli F, et al. Sintering and crystallization behavior of $CaMgSi_2O_6$–$NaFeSi_2O_6$ based glass-ceramics. Journal of Applied Physics 2009;106:093502.

[133] Goel A, Tulyaganov DU, Goel IK, Shaaban ER, Ferreira JMF. Effect of BaO on the crystallization kinetics of glasses along the Diopside–Ca-Tschermak join. Journal of Non-Crystalline Solids 2009;355:193-202.

[134] Goel A, Tulyaganov DU, Kharton VV, Yaremchenko AA, Eriksson S, Ferreira JMF. Optimization of La_2O_3-containing diopside based glass-ceramic sealants for fuel cell applications. Journal of Power Sources 2009;189:1032-43.

[135] Goel A, Tulyaganov DU, Pascual MJ, Shaaban ER, Muñoz F, Lü Z, et al. Development and performance of diopside based glass-ceramic sealants for solid oxide fuel cells. Journal of Non-Crystalline Solids 2010;356:1070-80.

[136] Goel A, Tulyaganov DU, Ferrari AM, Shaaban ER, Prange A, Bondioli F, et al. Structure, Sintering, and Crystallization Kinetics of Alkaline-Earth Aluminosilicate Glass-Ceramic Sealants for Solid Oxide Fuel Cells. Journal of the American Ceramic Society 2010;93:830-7.

[137] Goel A, Pascual MJ, Ferreira JMF. Stable glass-ceramic sealants for solid oxide fuel cells: Influence of Bi_2O_3 doping. International Journal of Hydrogen Energy 2010;35:6911-23.

[138] Goel A, Reddy AA, Pascual MJ, Gremillard L, Malchere A, Ferreira JMF. Sintering behavior of lanthanide-containing glass-ceramic sealants for solid oxide fuel cells. Journal of Materials Chemistry 2012;22:10042.

[139] Kerstan M, Rüssel C. Barium silicates as high thermal expansion seals for solid oxide fuel cells studied by high-temperature X-ray diffraction (HT-XRD). Journal of Power Sources 2011;196:7578-84.
[140] Buesser B, Gröhn A, Pratsinis S. Sintering Rate and Mechanism of TiO2 Nanoparticles by Molecular Dynamics. The journal of physical chemistry C, Nanomaterials and interfaces 2011;115:11030-5.
[141] Xu J, Sakanoi R, Higuchi Y, Ozawa N, Sato K, Hashida T, et al. Molecular Dynamics Simulation of Ni Nanoparticles Sintering Process in Ni/YSZ Multi-Nanoparticle System. The Journal of Physical Chemistry C 2013;117:9663-72.
[142] Pascual MJ, Duran A, Pascual L. Sintering process of glasses in the system Na_2O-B_2O_3-SiO_2. Journal of Non-Crystalline Solids 2002;306:58-69.
[143] Lara C, Pascual MJ, Durán A. Glass-forming ability, sinterability and thermal properties in the systems RO–BaO–SiO2 (R=Mg, Zn). Journal of Non-Crystalline Solids 2004;348:149-55.
[144] Mahapatra MK, Lu K. Sealing Evaluation of an Alkaline Earth Silicate Glass for Solid Oxide Fuel/Electrolyser Cells. Fuel Cells 2011;11:436-44.
[145] Xiang Y, Du J. Effect of Strontium Substitution on the Structure of 45S5 Bioglasses. Chemistry of Materials 2011;23:2703-17.
[146] Marcio LFN, Cristina A. Viscosity of strong and fragile glass-forming liquids investigated by means of principal component analysis. Journal of Physics and Chemistry of Solids 2007;68:104-10.
[147] Fujikura K, Karpukhina N, Kasuga T, Brauer DS, Hill RG, Law RV. Influence of strontium substitution on structure and crystallisation of Bioglass® 45S5. Journal of Materials Chemistry 2012;22:7395.
[148] O'Donnell MD, Candarlioglu PL, Miller CA, Gentleman E, Stevens MM. Materials characterisation and cytotoxic assessment of strontium-substituted bioactive glasses for bone regeneration. Journal of Materials Chemistry 2010;20:8934.
[149] Reinsch S, Nascimento MLF, Müller R, Zanotto ED. Crystal growth kinetics in cordierite and diopside glasses in wide temperature ranges. Journal of Non-Crystalline Solids 2008;354:5386-94.

[150] Chou Y-S, Stevenson JW, Gow RN. Novel alkaline earth silicate sealing glass for SOFC. Journal of Power Sources 2007;170:395-400.
[151] Young RA. Introduction to the Rietveld method. In: R. A. Young, editor. The Rietveld method. International Union of Crystallography Monographs on Crystallography. Oxford: Oxford University Press 1993;5:1–39.
[152] Malzbender J, Zhao Y. Flexural Strength and Viscosity of Glass Ceramic Sealants for Solid Oxide Fuel Cell Stacks. Fuel Cells 2012;12:47-53.
[153] Shaula AL, Kharton VV, Marques FMB, Kovalevsky AV, Viskup AP, Naumovich EN. Oxygen permeability of mixed-conducting composite membranes: effects of phase interaction. Journal of Solid State Electrochemistry 2005;10:28-40.
[154] Reddy A, Tulyaganov D, Pascual M, Kharton V, Tsipis EV, Kolotygin V, et al. SrO-Containing diopside glass-ceramic sealants for solid oxide fuel cells: mechanical reliability and thermal shock resistance. Fuel Cells 2013;13:689–94.
[155] Reddy AA, Tulyaganov DU, Pascual MJ, Kharton VV, Tsipis EV, Kolotygin VA, et al. Diopside–Ba disilicate glass–ceramic sealants for SOFCs: Enhanced adhesion and thermal stability by Sr for Ca substitution. International Journal of Hydrogen Energy 2013;38:3073-86.
[156] Lotfibakhshaiesh N, Brauer DS, Hill RG. Bioactive glass engineered coatings for Ti_6Al_4V alloys: Influence of strontium substitution for calcium on sintering behaviour. Journal of Non-Crystalline Solids 2010;356:2583-90.
[157] Reddy AA, Tulyaganov DU, Kapoor S, Goel A, Pascual MJ, Kharton VV, et al. Study of melilite based glasses and glass-ceramics nucleated by Bi_2O_3 for functional applications. RSC Advances 2012;2:10955.
[158] Oliveira J, Corria R, Fernandes M, Rocha J. Influence of the CaO/MgO ratio on the structure of phase separated glasses: a solid state 29Si and 31P MAS NMR study. Journal of Non-Crystalline Solids 2000;265:221-9.
[159] James B. Murdoch, Stebbins JF. High-resolution ^{29}Si NMR study of silicate and aluminosilicate glasses: the effect of network-modifying cations. American Mineralogist 1985;70:332-43.
[160] Lee SK, Yi YS, Cody GD, Mibe K, Fei Y, Mysen BO. Effect of Network Polymerization on the Pressure-Induced Structural Changes in Sodium Aluminosilicate

Glasses and Melts:^{27}Al and^{17}O Solid-State NMR Study. The Journal of Physical Chemistry C 2012;116:2183-91.

[161] Hill RG, Stamboulis A, Law RV, Clifford A, Towler MR, Crowley C. The influence of strontium substitution in fluorapatite glasses and glass-ceramics. Journal of Non-Crystalline Solids 2004;336:223-9.

[162] M. O. Prado, E. B. Ferreira, E. D. Zanotto. Sintering Kinetics of Crystallizing Glass Particles. A Review Hoboken, NJ, USA: John Wiley & Sons, Inc.; 2006.

[163] Reddy AA, Tulyaganov DU, Goel A, Kapoor S, Pascual MJ, Ferreira JMF. Sintering and devitrification of glass-powder compacts in the akermanite–gehlenite system. Journal of Materials Science 2013;48:4128-36.

[164] Gillot J, Roskosz M, Leroux H, Capet F, Roussel P. Crystallization of amorphous silicates far from equilibrium part II: Experimental insight into the key role of decoupled cation mobilities. Journal of Non-Crystalline Solids 2011;357:3467-73.

[165] Benna P. Ca-Sr Substitution in Clinopyroxenes Along the Join $CaMgSi_2O_6$ - $SrMgSi_2O_6$. TMPM Tschermaks Mineralogische und Petrographische 1982;30:37-46.

[166] Nakamura E, Kushiro I. Trace element diffusion in jadeite and diopside melts at high pressures and its geochemical implication. Geochimica et Cosmochimica Acta 1998;62:3151-60.

[167] Lee SK, Stebbins JF. The Structure of Aluminosilicate Glasses: High-Resolution ^{17}O and ^{27}Al MAS and 3QMAS NMR Study. The Journal of physical Chemistry B 2000;104:4091-100.

[168] Lin C, Lin K, Yeh J-H, Shiu W-H, Liu C-K, Lee R-Y. Aging effects on high-temperature creep properties of a solid oxide fuel cell glass-ceramic sealant. journal of Power Sources 2013;241:12-9.

[169] Ojha PK, Chongdar TK, Gokhale NM, Kulkarni AR. Accelerated devitrification of a strontiumlanthanumaluminoborosilicate based intermediate temperature solid oxide fuel cell glass sealant and its effect on thermophysical behaviour of the glass ceramics. Journal of Power Sources 2013;221:28-34.

[170] Carl WFTPu, Pistorius M. Lattice constants and thermal-expansion properties of the chromates and selenates of lead, strontium and barium. Z Kristallogr 1962;117:259-72.

[171] Goel A, Tulyaganov DU, Agathopoulos S, Ferreira JMF. The effect of Al_2O_3 on sintering and crystallization of $MgSiO_3$-based glass-powder compacts. Ceramics International 2008;34:505-10.

[172] Makishima A, Kobayashi M, Shimohira T, Nagata T. Formation of aluminosilicate glasses containing rare-earth oxides. Journal of American Ceramic Society 1982;65:C210-C1.

[173] Loiseau P, Caurant D, Baffier N, Mazerolles L, Fillet C. Glass–ceramic nuclear waste forms obtained from SiO_2–Al_2O_3–CaO–ZrO_2–TiO_2 glasses containing lanthanides (Ce, Nd, Eu, Gd, Yb) and actinides (Th): study of internal crystallization. Journal of Nuclear Materials 2004;335:14-32.

[174] Shelby J, Kohli J. Rare-Earth Aluminosilicate Glasses. Journal of American Ceramic Society 1990;73:39-42.

[175] Mi-tang W, Jin-shu C. Viscosity and thermal expansion of rare earth containing soda–lime–silicate glass. Journal of Alloys and Compounds 2010;504:273-6.

[176] Marchi J, Morais DS, Schneider J, Bressiani JC, Bressiani AHA. Characterization of rare earth aluminosilicate glasses. Journal of Non-Crystalline Solids 2005;351:863-8.

[177] Steimacher A, Barboza MJ, Farias AM, Sakai OA, Rohling JH, Bento AC, et al. Preparation of Nd_2O_3-doped calcium aluminosilicate glasses and thermo-optical and mechanical characterization. Journal of Non-Crystalline Solids 2008;354:4749-54.

[178] Iftekhar S, Leonova E, Edén M. Structural characterization of lanthanum aluminosilicate glasses by ^{29}Si solid-state NMR. Journal of Non-Crystalline Solids 2009;355:2165-74.

[179] Bonamartini Corradi A, Cannillo V, Montorsi M, Siligardi C, Cormack AN. Structural characterization of neodymium containing glasses by molecular dynamics simulation. Journal of Non-Crystalline Solids 2005;351:1185-91.

[180] McGahay V, Tomozawa M. Phase separation in rare-earth-doped SiO_2 glasses. Journal of Non-Crystalline Solids 1993;159:246-52.

[181] Goel A, Tulyaganov DU, Agathopoulos S, Ribeiro MJ, Ferreira JMF. Crystallization behaviour, structure and properties of sintered glasses in the diopside–Ca-Tschermak system. Journal of the European Ceramic Society 2007;27:3231-8.

[182] Lara C, Pascual M, Duran A. Glass-forming ability, sinterability and thermal properties in the system RO-BaO-SiO_2 (R = Mg, Zn). Journal of Non-Crystalline Solids 2004;348:149-55.

[183] Huczkowski P, Shemet V, Piron-Abellan J, Singheiser L, Quadakkers WJ, Christiansen N. Oxidation limited life times of chromia forming ferritic steels. Materials and Corrosion 2004;55:825-30.

[184] Prado M, Zanotto E, Muller R. Model for sintering polydispersed glass particles. Journal of Non-Crystalline Solids 2001;279:169-78.

[185] Mackenzie J, Shuttleworth R. A phenomenological theory of sintering. Proceedings of the Physical Society Section B 1949;62:833.

[186] Martel L, Allix M, Millot F, Sarou-Kanian V, Véron E, Ory S, et al. Controlling the size of nanodomains in calcium aluminosilicate glasses. The Journal of Physical Chemistry C 2011;115:18935-45.

[187] De Vekey R, Majumdar A. The effect of fabrication variables on the properties of cordierite based glass-ceramics. Glass tech 1974;15:71-80.

[188] Stebbins J, Oglesby J, Kroeker S. Oxygen triclusters in crystalline $CaAl_4O_7$ (grossite) and in calcium aluminosilicate glasses: ^{17}O NMR. American Mineralogist 2001;86:1307-11.

[189] Rodríguez JL, Baudín C, Pena P. Relationships between phase constitution and mechanical behaviour in MgO–CaZrO3–calcium silicate materials. Journal of the European Ceramic Society 2004;24:669-79.

[190] Schneider j, Mastelaro V, Panepucci H, Zanotto E. ^{29}Si MAS-NMR studies of Q^n structural units in metasilicate glasses and their nucleating ability. Journal of Non-Crystalline Solids 2000;273:8-18.

[191] Quintas A, Caurant D, Majérus O, Charpentier T, Dussossoy JL. Effect of compositional variations on charge compensation of AlO_4 and BO_4 entities and on crystallization tendency of a rare-earth-rich aluminoborosilicate glass. Materials Research Bulletin 2009;44:1895-8.

[192] Sohn S-B, Choi S-Y, Kim G-H, Song H-S, Kim G-D. Suitable glass-ceramic sealant for planar solid-oxide fuel cells. Journal of American Ceramic Society 2004;87:254-60.

[193] Kolitsch U, Seifert HJ, Aldinger F. Phase relationships in the systems RE_2O_3-Al_2O_3-SiO_2. Journal of Phase Equilibria 1998;19:426-33.
[194] Orman JAV, Grove TL, Shimizu N. Rare-earth element diffusion in diopside: influence of temperature, pressure, and ionic radius, and an elastic model for diffusion in silicates. Contributions to Mineralogy and Petrology 2001;141:687-703.
[195] Gatto Rotondo G. Micro-Raman and SEM Analysis of Minerals from the Darhib Mine, Egypt. Journal of Analytical Sciences, Methods and Instrumentation 2012;02:42-7.
[196] Sherriff BL, Grundy HD, Hartman JP. The relationship between ^{29}Si MAS NMR chemical shift and silicate mineral structure. European Journal of Mineralogy 1991;3:751-68.
[197] Xue X, Kanzaki M. Al coordination and water speciation in hydrous aluminosilicate glasses: direct evidence from high-resolution heteronuclear 1H-27Al correlation NMR. Solid State Nuclear Magnetic Resononance 2007;31:10-27.
[198] Stamboulis A, Matsuya S, Hill RG, Law RV, Udoh K, Nakagawa M, et al. MAS-NMR spectroscopy studies in the setting reaction of glass ionomer cements. Journal of dentistry 2006;34:574-81.
[199] Weber R, Sen S, Youngman R, Hart R, Benmore C. Structure of high alumina content Al_2O_3-SiO_2 composition glasses. Journal of Physical chemistry B 2008;112:16726-33.
[200] Karamanov A, Arrizza L, Matekovits I, Pelino M. Properties of sintered glass-ceramics in the diopside–albite system. Ceramics International 2004;30:2129-35.
[201] Mahapatra MK, Lu K. Seal glass compatibility with bare and $(Mn,Co)_3O_4$ coated Crofer 22 APU alloy in different atmospheres. Journal of Power Sources 2011;196:700-8.
[202] Ghaffari M, Alizadeh P, Rahimipour MR. Sintering behavior and mechanical properties of mica-diopside glass–ceramic composites reinforced by nano and micro-sized zirconia particles. Journal of Non-Crystalline Solids 2012;358:3304-11.
[203] Reddy AA, Goel A, Tulyaganov DU, Sardo M, Mafra L, Pascual MJ, et al. Thermal and mechanical stability of lanthanide-containing glass–ceramic sealants for solid oxide fuel cells. Journal of Materials Chemistry A 2014;2:1834.

[204] Richet P, Mysen BO, Ingrin J. High-temperature X-ray diffraction andRaman spectroscopy of diopside and pseudowollastonite. Physics and Chemistry of Minerals 1998;25:401-14.
[205] Reddy A, Goel A, Tulyaganov D, Kapoor S, Pradeesh K, Pascual M, et al. Study of calcium–magnesium–aluminum–silicate (CMAS) glass and glass-ceramic sealant for solid oxide fuel cells. Journal of Power Sources 2013;231:203-12.
[206] Sorensen B, Sarraute S, Jorgensen O, Horsewell A. Thermally induced delamination of multilayers. Acta Materialia 1998;46:2603-15.